Design Principles of Advanced Porous Materials for Efficient CO_2 Capture and Electrochemical Reduction

Ph.D. Thesis

By

KAHKASHA PARVEEN
(Roll Number: 2101151004)



DEPARTMENT OF PHYSICS
INDIAN INSTITUTE OF TECHNOLOGY INDORE

JULY, 2026

Design Principles of Advanced Porous Materials for Efficient CO_2 Capture and Electrochemical Reduction

A THESIS

Submitted in partial fulfillment of the requirements for the award of the degree

of

DOCTOR OF PHILOSOPHY

by

KAHKASHA PARVEEN
(Roll Number: 2101151004)



DEPARTMENT OF PHYSICS
INDIAN INSTITUTE OF TECHNOLOGY INDORE

JULY, 2026

INDIAN INSTITUTE OF TECHNOLOGY INDORE

I hereby certify that the work which is being presented in the thesis entitled **Design Principles of Advanced Porous Materials for Efficient CO_2 Capture and Electrochemical Reduction** in the partial fulfillment of the requirements for the award of the degree of **DOCTOR OF PHILOSOPHY** and submitted in the **DEPARTMENT OF PHYSICS, Indian Institute of Technology Indore**, is an authentic record of my own work carried out during the time period from May 2021 to June 2026 under the supervision of **Dr. Srimanta Pakhira, Associate Professor, Indian Institute of Technology, Indore.**

The matter presented in this thesis has not been submitted by me for the award of any other degree of this or any other institute

Kahkasha

23.10.2026

Signature of the student with date
(KAHKASHA PARVEEN)

This is to certify that the above statement made by the candidate is correct to the best of my/our knowledge.

Dr. Srimanta Pakhira, Ph.D.
Associate Professor
Department of Physics and
Centre for Advanced Electronics
Indian Institute of Technology Indore, M.P., India

23.10.2026

Signature of Thesis Supervisor with date

(DR. SRIMANTA PAKHIRA)

KAHKASHA PARVEEN has successfully given her Ph.D. Oral Examination held on 23.10.2026

Dr. Srimanta Pakhira, Ph.D.
Associate Professor
Department of Physics and
Centre for Advanced Electronics
Indian Institute of Technology Indore, M.P., India

23.10.2026

Signature of Thesis Supervisor with date

(DR. SRIMANTA PAKHIRA)

ACKNOWLEDGEMENTS

First and foremost, I express my deepest gratitude to Allah (SWT) for His infinite blessing, mercy, and guidance throughout my life. It is only through His grace that I have been granted strength, patience, and perseverance to complete this work.

I would like to express my deepest gratitude to my supervisor, ***Dr. Srimanta Pakhira****, for his invaluable guidance, continuous encouragement, insightful discussions, and unwavering support throughout my PhD journey. His vast knowledge, scientific vision, and dedication to research have greatly influenced my academic and professional development. I am truly fortunate to have worked under his mentorship, and I remain sincerely grateful for all the opportunities and confidence he has bestowed upon me.*

I extend my heartfelt gratitude to my PhD Student Progress Committee (PSPC) members, ***Prof. Somaditya Sen, Department of Physics,*** *and* ***Prof. Anjan Chakraborty, Department of Chemistry, Indian Institute of Technology Indore,*** *for their valuable suggestions, insightful comments, and constructive feedback throughout my doctoral research. Their guidance, encouragement, and critical evaluations have significantly contributed to the successful completion of this work.*

I sincerely thank my seniors, lab mates, and colleagues for their cooperation, support, and the many fruitful technical and non-technical discussions that made my doctoral journey both enjoyable and enriching. I am also grateful to my friends for their constant motivation and support during both the challenging and memorable moments of this journey. Their companionship and encouragement have contributed significantly to my growth as a researcher.

Finally, I express my deepest gratitude to my family. I owe this achievement to my beloved parents, ***Mr. Abdul Quddus Warsi*** *and* ***Lt. Sanjeeda****, whose unconditional love, sacrifices, blessings, and unwavering faith in me have been the foundation of my success. I am deeply grateful to my sisters,* ***Ms. Uzma Afreen and Ms. Adeeba Parveen,*** *and my brother,* ***Mr. Amir Suhail,*** *for their constant encouragement, affection, and support. I also extend my heartfelt gratitude to my grandfather,* ***Lt. Hafizullah Warsi,*** *whose blessings and good wishes have always inspired me to move forward. This accomplishment would not have been possible without their love, patience, and support.*

Kahkasha Parveen

Indian Institute of Technology Indore

Date: 23.10.2026

DEDICATED TO

My Beloved Family

Father, Mother, Sisters, and Brother for their love, sacrifices, and support

SYNOPSIS

1. Introduction

The rapid increase in atmospheric carbon dioxide (CO_2) concentration caused by excessive fossil fuel consumption, industrialization, and anthropogenic activities has emerged as one of the most critical environmental challenges of the twenty-first century.[1] Since the Industrial Revolution, atmospheric CO_2 levels have increased significantly from about 280 ppm to over 425 ppm in 2025 and are projected to reach approximately 950 ppm by the end of the century.[2–4] The continuous emission of greenhouse gases has significantly contributed to global warming, climate change, ocean acidification and ecological imbalance. Consequently, the development of sustainable technologies for carbon capture, utilization, and storage (CCUS) has become an urgent global priority. In recent decades, researchers have devoted significant efforts toward developing sustainable strategies to capture atmospheric CO_2 and convert it into valuable chemicals and fuels, thereby contributing to carbon neutrality and renewable energy technologies.[5,6]

Among the various classes of porous materials, metal-organic frameworks (MOFs) and covalent organic frameworks (COFs) have attracted significant attention due to their exceptionally high surface areas, tunable porosity, structural diversity, chemical stability, and functional tailorability.[7] MOFs are crystalline porous materials composed of metal ions or clusters interconnected by organic ligands.[8] In contrast, COFs are entirely organic porous crystalline frameworks constructed through strong covalent bonds between light elements such as C, H, B, N, and O.[9] The modular nature of these frameworks enables precise control over pore size, functionality, electronic structure, and catalytic activity, making them promising candidates for gas adsorption, separation, catalysis, sensing and energy conversion applications. Particularly, their unique structural flexibility and controllable electronic properties make MOFs and COFs attractive materials for CO_2 capture and electrochemical CO_2 reduction reaction (CO_2RR). In recent years, metallophthalocyanine (MPc)-based porous frameworks have emerged as promising electrocatalysts for electrochemical CO_2RR due to their tunable electronic structures, highly active metal centres, excellent charge-transport properties, and catalytic selectivity.[10] However, despite significant experimental and theoretical progress, several challenges remain unresolved, including

weak CO_2 adsorption, poor catalytic selectivity, high overpotentials, inefficient charge transfer, and limited understanding of structure-property relationships governing catalytic performance.[11]

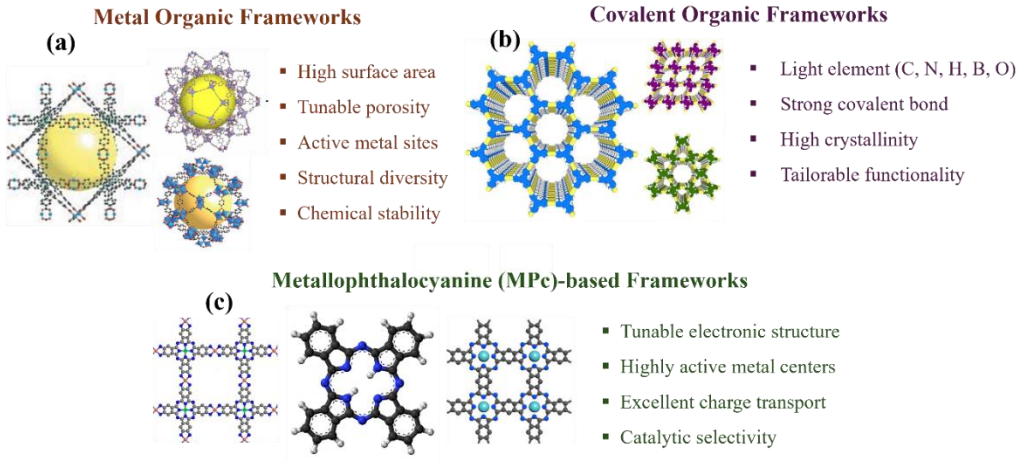


Figure 1. Schematic representation of: (a) metal-organic frameworks (MOFs), (b) covalent organic frameworks (COFs), and (c) metallophthalocyanine (MPc)-based frameworks, highlighting their structural features and key properties relevant to CO_2 capture and electrochemical CO_2 reduction.

In this thesis, porous MOFs and COFs have been theoretically designed and computationally investigated for CO_2 adsorption and electrochemical reduction applications using first principles-based density functional theory (DFT) methods. The work systematically explores the relationships among linker engineering, framework design, electronic structure, adsorption behavior, and catalytic activity. A special emphasis has been given to understanding the role of functionalization, sulfur-containing linkages, and metal-centred active sites in influencing the adsorption and catalytic conversion of CO_2 into value-added C_1 and C_2 products. The thesis primarily focuses on three important aspects: (i) understanding CO_2 adsorption on functionalized MOF linkers, (ii) investigating CO_2 electroreduction on sulfur-linked metallophthalocyanine-based COFs, and (iii) exploring catalytic pathways for C_1 and C_2 product formation on copper phthalocyanine-based MOFs. These studies provide fundamental insights into the rational design of advanced porous materials for sustainable CCUS technologies.

2. Motivation and objective of the work

The growing global demand for sustainable energy technologies and carbon-neutral processes has spurred extensive research into advanced porous materials capable of

efficient CO_2 capture and catalytic conversion. Although many MOFs and COFs have already been synthesized and investigated for gas adsorption and catalytic applications, understanding the relationship between framework structure, electronic properties, adsorption behavior, and catalytic performance remains a major scientific challenge. In particular, there is still limited theoretical and computational understanding regarding:

- The role of linker functionalization and metal decoration in enhancing CO_2 adsorption,
- The influence of frameworks containing linkages on catalytic activity,
- The electronic structure modulation in MPc-based frameworks,
- The mechanistic pathways governing selective CO_2 electroreduction toward C_1 and C_2 products.

Therefore, the primary motivation of the present work is to develop rational design strategies for porous MOFs and COFs with enhanced CO_2 adsorption and catalytic reduction performance, based on molecular-level theoretical investigations.

The main objectives of the present work are:

1. To investigate CO_2 adsorption on organic bridging linkers of MOFs through Li decoration and understand the interaction mechanisms governing the adsorption behavior. *(Published:* K. Parveen, S. Pakhira, Designing organic bridging linkers of metal-organic frameworks for enhanced carbon dioxide adsorption, New J. Chem. 48 (2024) 13700-13714.*)*

2. To investigate the structural and electronic properties of sulfur-linked MPc-based COFs for selective electrochemical CO_2 reduction to C_1 products. *(Published:* K. Parveen, S. Pakhira, Unveiling the electrocatalytic activity of metallophthalocyanine-based covalent organic frameworks toward CO_2 reduction reaction, J. Phys. Chem C 129 (2025) 2973-2987.*)*
3. To study the structural, electronic, and catalytic properties of CuPc-Cu-O MOF for electrochemical CO_2 reduction toward both C_1 and C_2 products. *(Published:* K. Parveen, S. Pakhira, Unveiling the electrocatalytic activity of metallophthalocyanine-based metal-organic frameworks toward CO_2 reduction reaction, ACS Appl. Energy Mater. 8 (2025) 17818-17830.*)*

3. Methodology of the work

The computational investigations carried out in this thesis are primarily based on first principles-based DFT and post-Hartree-Fock methods to understand the structural, electronic, adsorption, and catalytic properties of porous MOF and COF materials for CO_2 capture and electrochemical CO_2 reduction reactions. The non-periodic calculations carried out for the CO_2 adsorption studies on various pristine and Li-decorated MOF linkers were performed by using the unrestricted hybrid density functional theory (UDFT) method employing the B3LYP function with Grimme's third-order dispersion correction (B3LYP-D3).[12,13] To obtain accurate interaction and account for weak van der Waals (vdW) interactions, the correlation consistent triple-ζ quality Gaussian basis set (cc-pVTZ) was employed for all atoms.[14] Further, single-point energy calculations at the second-order Møller–Plesset perturbation theory (MP2) level were carried out using the optimized geometries obtained from the B3LYP-D3 method to validate the binding enthalpy. Frequency and thermodynamic calculations were also performed to confirm the stability of the optimized geometries and evaluate the binding enthalpy (ΔH) of the complexes. Frontier molecular orbital (FMO) analysis and localized molecular orbital energy decomposition analysis (LMO-EDA) were additionally employed to understand the stability and adsorption mechanism of the complexes. All non-periodic calculations were carried out using the Gaussian16[15] and GAMESS[16] suite codes, while the optimized structures and adsorption geometries were visualized using GaussView6.1[17] and ChemCraft[18] software packages.

Next, the periodic structural, electronic, and catalytic investigations of the sulfur-linked CoPc-based COFs and CuPc-based MOF monolayers were performed by using the hybrid periodic dispersion-corrected DFT method, as implemented in the *ab initio*-based CRYSTAL23 suite code.[19] The equilibrium geometries, electronic band structures, density of states (DOS), spin density distributions, adsorption energies, and catalytic reaction pathways associated with the CO_2 reduction reaction (CO_2RR) were systematically investigated using triple-ζ valence with polarization quality (TZVP) Gaussian basis sets for all atoms involved in the frameworks.[20] To accurately account for weak van der Waals interactions within the porous frameworks and layered monolayer systems, Grimme's third-order dispersion correction was incorporated with

the DFT (i.e., B3LYP-D3) method throughout the calculations.[21] The reciprocal space integrations were sampled using Monkhorst-Pack *k*-mesh grids with appropriate convergence criteria, while large vacuum regions (~500 Å) were introduced along the z-direction to model isolated two-dimensional monolayer slab structures and avoid interlayer interactions. The electronic properties, including band structures and total as well as partial density of states, were analyzed to understand the catalytic behavior and charge transfer characteristics of the frameworks. The catalytic mechanisms for CO_2 reduction toward C_1 and C_2 products were explored by evaluating the adsorption energies and Gibbs free energy profiles of the reaction intermediates on the active metal centers. All periodic crystal and monolayer structures, along with the catalytic intermediates, were visualized and analyzed using the VESTA package.[22]

4. Summary of the present work

First, we have computationally investigated the adsorption behavior of CO_2 on various organic bridging linkers of MOF using first principles-based DFT and MP2 methods. The study explored the interaction of CO_2 molecules with pristine and Li-decorated fluorinated and chlorinated organic linkers to understand the adsorption mechanism and improve the CO_2 binding strength. Chapter 3 describes the investigations of CO_2 adsorption on these linkers using molecular clusters, including the effects of Li-decoration on binding enthalpy and electronic interactions in detail. This chapter also includes the frontier molecular orbital (FMO) analysis to understand the stability of the complexes, and energy decomposition analysis (EDA) to analyze the interactions governing the adsorption process. Chapter 4 comprises the investigation of electrochemical CO_2 reduction using sulfur-linked cobalt phthalocyanine (CoPc)-based COFs. The structural, electronic, and catalytic properties of CoPc-DNDS and CoPc-DSDS COFs containing thiomorpholine and dithiine linkages, respectively, were systematically studied using periodic hybrid DFT calculations. This chapter includes the analysis of band structures, DOS, spin density distribution, and Gibbs free energy profiles associated with the CO_2RR toward C_1 products such as CO and CH_4. The role of sulfur-containing linkages and framework engineering in regulating catalytic activity and product selectivity has also been explored in detail. Chapter 5 includes the study of a copper phthalocyanine-based MOF, namely CuPc-Cu-O, for electrochemical CO_2RR toward C_1 and C_2 products. The equilibrium geometry, electronic properties, adsorption

behavior, and catalytic reaction mechanism of the CuPc MOF were investigated by using periodic DFT-D calculations. This chapter covers the mechanistic investigation of CO_2 adsorption, activation, and subsequent reduction pathways leading to CH_4, C_2H_4, and C_2H_5OH formation. The study further explores the role of Cu active sites, electronic interactions, and C-C coupling pathways in controlling catalytic selectivity toward higher value C_2 products, highlighting the potential of MPc-based porous materials as efficient electrocatalysts for CO_2RR.

4.1 Organic bridging linkers of MOFs for enhanced CO_2 adsorption

The first part of the thesis focuses on the non-periodic investigation of CO_2 adsorption on various linkers of MOF, namely BDC, FBDC, DFBDC-1, DFBDC-2, TFBDC, DClBDC-1, DClBDC-2, and NDC, using the molecular cluster model and first-principles based DFT and MP2 methods. The interaction of CO_2 molecules with pristine and Li-decorated linkers was systematically explored to understand the adsorption mechanism and improve the CO_2 binding strength. The results revealed that the center and side positions of the FBDC, DFBDC-1, DFBDC-2 and TFBDC linkers, the side position of the DClBDC-2 linker, and the center position of the NDC linker exhibit favorable physisorption behavior on CO_2 adsorption, with the values of binding enthalpy (ΔH) ranging from -12.05 kJ/mol to -14.09 kJ/mol. After Li-decoration, the CO_2 adsorption strength increased significantly, particularly at the center positions of the BDC, FBDC, and DClBDC-1 linkers and the side positions of the BDC, FBDC, DFBDC-1, and DFBDC-2 linkers, with the values of ΔH ranging from -34.64 kJ/mol to -35.30 kJ/mol. These values indicate strong physisorption behavior and remain below the chemisorption limit, thereby ensuring facile CO_2 desorption suitable for practical carbon capture. The high energy gap obtained from FMO analysis indicated the kinetic stability of Li-decorated linker physisorption behavior. Furthermore, the EDA revealed that the electrostatic (ΔE_{els}) and (ΔE_{pol}) interactions predominantly govern the adsorption mechanism.

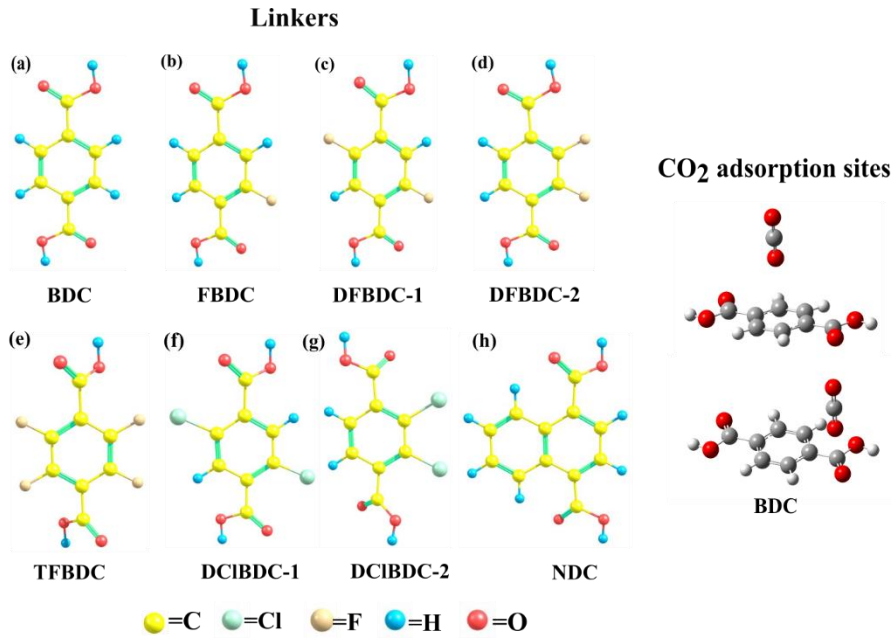


Figure 2. Molecular structures of the organic linkers considered for the CO_2 adsorption: (a) 1,4-benzene dicarboxylate (BDC), (b) 3-fluoro 1,4-benzene dicarboxylate (FBDC), (c) 3,6-difluoro 1,4-benzene dicarboxylate (DFBDC-1), (d) 2,3-difluoro 1,4-benzene dicarboxylate (DFBDC-2), (e) 2,3,5,6-tetrafluoro 1,4-benzene dicarboxylate (TFBDC), (f) 3,6-dichloro 1,4-benzene dicarboxylate (DClBDC-1), (g) 2,3-dichloro 1,4-benzene dicarboxylate (DClBDC-2), and (h) 1,4 naphthalene dicarboxylate (NDC), along with demonstration of the CO_2 molecule at the center and side positions of the BDC linker.

The present investigation demonstrates that Li-decoration enhances the interaction between CO_2 molecules and linkers, thereby providing an efficient strategy for designing advanced porous adsorbents for carbon capture technologies. Furthermore, the study focuses on the importance of developing chemically and thermally stable porous materials for practical CO_2 capture. Although the present investigations focus only on isolated organic MOF linkers, the favorable physisorption observed for fluorinated and chlorinated linkers, particularly after Li-decoration, demonstrates the potential of linker engineering in enhancing CO_2 adsorption affinity and hydrothermal stability. The findings of this work are expected to guide the future synthesis and design of stable porous MOFs with improved CO_2 capture performance for carbon capture applications. *(*K. Parveen, S. Pakhira, Designing organic bridging linkers of metal-organic frameworks for enhanced carbon dioxide adsorption, New J. Chem. 48 (2024) 13700-13714.*)*

4.2 Metallophthalocyanine-based covalent organic frameworks toward CO_2 reduction reaction

The second part of the thesis focuses on the electrochemical reduction of CO_2 into C_1 products using sulfur-linked cobalt phthalocyanine (CoPc) based COFs. The equilibrium geometry, electronic properties, spin density, and catalytic reaction pathways of two structurally analogous COFs, namely CoPc-DNDS-COF (DNDS) and CoPc-DSDS-COF (DSDS), containing thiomorpholine and dithiine linkages, respectively, were obtained using the periodic first-principles DFT-D (B3LYP-D3) calculations. The electronic structure calculations revealed that 3D DNDS and DSDS COFs possess small energy band gap (E_g) values of 0.35 eV and 0.44 eV, respectively, with significant DOS contributions near the Fermi energy level (E_F), indicating favorable electronic conductivity. To further investigate the CO_2RR mechanism, a 2D monolayer slab of both COFs was computationally designed and analyzed. The results showed that the DNDS monolayer exhibits an indirect band gap of 1.49 eV, whereas the DSDS monolayer possesses a slightly higher band gap of 1.49 eV, confirming the semiconducting nature of both the COFs. The sulfur-containing linkages significantly influence charge delocalization and facilitate efficient electron transfer during CO_2RR, thereby strongly affecting the catalytic activity and product selectivity of the COFs.

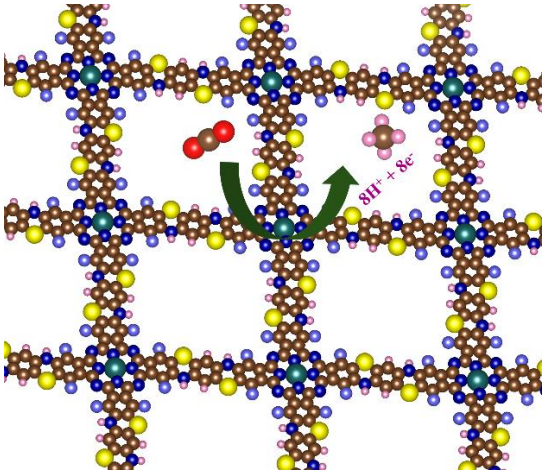


Figure 3. Schematic representation of electrochemical CO_2 reduction on the CoPc-DNDS-COF (DNDS) COF toward methane (CH_4) formation through proton-coupled electron transfer steps.

The catalytic performance of the 2D monolayer COFs was systematically explored by evaluating the change in Gibbs free energy (ΔG) profiles associated with the CO_2RR intermediates at the Co active sites. The electrocatalytic analysis revealed that the

DNDS efficiently reduces CO_2 to CH_4 with a favorable ΔG value of approximately -0.97 eV, whereas the DSDS preferentially favors the CO desorption with a value of ΔG about 0.68 eV. The enhanced catalytic activity of the DNDS COF originates from the sufficiently strong interaction between the reaction intermediates and the Co center attached to the MPc unit, which facilitates the protonation of *CO intermediates and promotes CH_4 formation, as further supported by the spin density analysis. The present investigation indicates the excellent potential of sulfur-linked MPc-based COFs as low-cost and efficient electrocatalysts for selective CO_2 reduction and demonstrates linkage engineering as an effective strategy for designing high-performance COF catalysts for CO_2 conversion applications. *(*K. Parveen, S. Pakhira, Unveiling the electrocatalytic activity of metallophthalocyanine-based covalent organic frameworks toward CO_2 reduction reaction, J. Phys. Chem C 129 (2025) 2973-2987.*)*

4.3 Metallophthalocyanine-based metal organic frameworks toward CO_2 reduction reaction

The final part of the thesis extends the catalytic investigation toward electrochemical CO_2 reduction using a dual copper phthalocyanine-based MOF, namely CuPc-Cu-O (in short CuPc), for the selective formation of both C_1 and C_2 products. The equilibrium geometry, electronic properties, structural stability, adsorption behavior, and catalytic reaction mechanisms of the CuPc were investigated using the periodic hybrid DFT-D (B3LYP-D3) method. The electronic band structure calculations revealed that the CuPc monolayer exhibits semiconducting behavior with a very small band gap of approximately 0.65 eV, indicating good electrical conductivity and efficient charge transfer required for catalytic activity. The DOS analysis demonstrated that the catalytic performance originates from the synergistic contributions of the Cu atoms and the nitrogen atom of the MPc unit. Furthermore, the negative binding energy (E_b = -3.59 eV) confirmed the thermodynamic stability and experimental feasibility of the CuPc MOF. The adsorption studies also revealed that the Cu-N_4 active site exhibits the lowest CO_2 adsorption energy, facilitating efficient proton/electron transfer during CO_2RR.

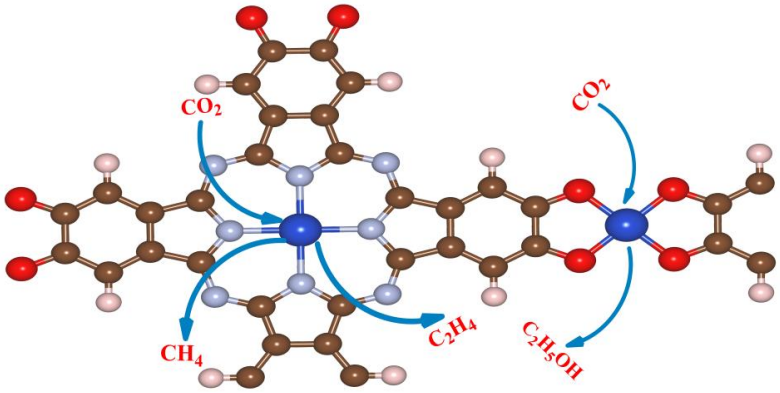


Figure 4. Schematic representation of electrochemical CO_2 reduction on the CuPc-Cu-O MOF leading to C_1 and C_2 products.

The catalytic performance of the CuPc toward CO_2RR was systematically explored through the evaluation of the relative change in adsorption energy (ΔE_{ads}) associated with various reaction intermediates leading to CH_4, C_2H_4 and C_2H_5OH formation. The results revealed that the *HCOOH pathway with a ΔE_{ad} value of -5.07 eV is energetically more favorable than the *CO pathway (-3.49 eV) for CO_2 reduction to CH_4, yielding a final ΔE_{ad} value of -2.28 eV after completing eight-electron transfer. More importantly, the CuPc framework preferentially promotes ethanol (C_2H_5OH) formation over ethylene (C2H4), with a significantly favorable ΔE_{ad} value of -2.76 eV compared to 2.11 eV for C_2H_4 formation, indicating efficient C-C coupling and enhanced selectivity toward C_2 products. These findings provide important mechanistic insights into multi-carbon product formation during electrochemical CO_2RR and highlight the crucial role of Cu active sites and framework engineering in regulating catalytic selectivity. *(*K. Parveen, S. Pakhira, Unveiling the electrocatalytic activity of metallophthalocyanine-based metal-organic frameworks toward CO_2 reduction reaction, ACS Appl. Energy Mater. 8 (2025) 17818-17830.*)*

5. Conclusions

In the present thesis, porous MOFs and COFs have been theoretically/computationally designed and investigated for carbon capture and electrochemical CO_2RR using first principles-based DFT methods. The study demonstrates that the metal decoration significantly enhances CO_2 adsorption behavior through strong electrostatic and polarization interactions while maintaining reversible adsorption. The results provide important molecular-level understanding of adsorption mechanisms and demonstrate

rational strategies for designing efficient CO_2 adsorbents. The investigation of sulfur-linked MPc-based COFs reveals that linker engineering plays a crucial role in modulating electronic properties and catalytic activity toward electrochemical CO_2 reduction. The sulfur-containing frameworks exhibit favorable catalytic activity toward methane formation due to efficient charge transfer and stabilization or reaction intermediates. Furthermore, the CuPc-Cu-O MOF demonstrates excellent catalytic potential for electrochemical CO_2 conversion toward C_1 and C_2 products, particularly ethanol formation. The study provides a detailed mechanistic understanding of C-C coupling pathways and highlights the importance of dual metal active centers in governing catalytic selectivity toward C_2 products.

Overall, this thesis presents a comprehensive theoretical investigation connecting adsorption behavior, electronic structure, and catalytic performance in porous crystalline materials. The systematic study of metal decoration, linker engineering and metal center activity significantly advances the understanding of MOFs and COFs for sustainable CCUS applications and provides valuable guidelines for the rational design of next-generation porous materials for carbon-neutral energy technologies.

6. References

[1] N. F. Attia, M. Jung, J. Park, H. Jang, K. Lee, H. Oh, Flexible nanoporous activated carbon cloth for achieving high H_2, CH_4, and CO_2 storage capacities and selective CO_2/CH_4 separation, Chem. Eng. J. 379 (2020) 122367.

[2] https://www.downtoearth.org.in/climate-change/carbon-dioxide-emissions-to-hit-4296-ppm-in-may-2025-highest-in-over-2-million-years.

[3] https://www.ipcc-data.org/observ/ddc_co2.html.

[4] M. Ding, R. W. Flaig, H. L. Jiang, O. M. Yaghi, Carbon capture and conversion using metal-organic frameworks and MOF-based materials, Chem. Soc. Rev. 48 (2019) 2783-2828.

[5] S. Samanta, R. Srivastava, Catalytic conversion of CO_2 to chemicals and fuels: the collective thermocatalytic/photocatalytic/electrocatalytic approach with graphitic carbon nitride, Mater. Adv. 1 (2020) 1506-1545.

[6] C. Ma, Y. Dai, G. Zhuang, H. Zhang, Catalytic conversion of carbon dioxide into

fuel chemicals: Progress, challenges, and future directions, J. Environ. Chem. Eng. 13 (2025) 117767.

[7] Y. Song, S. Ma, Pore engineering in metal-organic frameworks and covalent organic frameworks: strategies and applications, Chem. Sci. 16 (2025) 11740-11767.

[8] F. zohra Zeggai, Z. Ait-Touchente, K. Bachari, A. Elaissari, Investigation of Metal-Organic Frameworks (MOFs): Synthesis, Properties, and Applications - An In-Depth Review, Chem. Phys. Impact. 10 (2025) 100864.

[9] P. J. Waller, F. Gándara, O. M. Yaghi, Chemistry of Covalent Organic Frameworks, Acc. Chem. Res. 48 (2015) 3053-3063.

[10] C. Wang, Y. Zhang, F. Zhao, D. Zhao, J. Zhang, Design Principles of Metal Phthalocyanine for Electrochemical CO_2 Reduction: From Targeted Molecular Structures to Atomic-Level Active Sites, Small 21 (2025) 2502897.

[11] J. Han, X. Bai, X. Xu, X. Bai, A. Husile, S. Zhang, L. Qi, J. Guan, Advances and challenges in the electrochemical reduction of carbon dioxide, Chem. Sci. 15 (2024) 7870-7907.

[12] S. Grimme, J. Antony, S. Ehrlich, H. Krieg, A consistent and accurate *ab initio* parametrization of density functional dispersion correction (DFT-D) for the 94 elements H-Pu, J. Chem. Phys. 132 (2010) 154104.

[13] S. Grimme, S. Ehrlich, L. Goerigk, Effect of the damping function in dispersion corrected density functional theory, J. Comput. Chem. 32 (2011) 1456-1465.

[14] S. Pakhira, J. L. M. Cortes, Quantum nature in the interaction of molecular hydrogen with porous materials: Implications for practical hydrogen storage, J. Phys. Chem. C 124 (2020) 6454-6460.

[15] M. J. Frisch, G. W. Trucks, H. B. Schlegel, G. E. Scuseria, M. A. Robb, J. R. Cheeseman, G. Scalmani, V. Barone, B. Mennucci, G. A. Petersson, et al., Gaussian, Inc., Wallingford CT, (2016).

[16] M. W. Schmidt, K. K. Baldridge, J. A. Boatz, S. T. Elbert, M. S. Gordon, J. H. Jensen, S. Koseki, N. Matsunaga, K. A. Nguyen, S. Su, T. L. Windus, M. Dupuis,

J. A. Montgomery, General atomic and molecular electronic structure system, J. Comput. Chem. 14 (1993) 1347-1363.

[17] R. Dennington, T. Keith, and J. Millam, Semichem Inc., Shawnee Mission, KS, GaussView, Version 6.1.1, 2019.

[18] Chemcraft - graphical software for visualization of quantum chemistry computations. Version 1.8, build 682. https://www.chemcraftprog.com

[19] A. Erba, J. K. Desmarais, S. Casassa, B. Civalleri, L. Donà, I. J. Bush, B. Searle, L. Maschio, L. E. Daga, A. Cossard, C. Ribaldone, E. Ascrizzi, N. L. Marana, J. P. Flament, B. Kirtman, CRYSTAL23: A program for computational solid state physics and chemistry, J. Chem. Theory Comput. 19 (2023) 6891-6932.

[20] R. Nagaraj, S. Pakhira, K. Aruchamy, P. Thippeswamy, D. Mondal, K. Dharmalingm, N. S. Kotrappanavar, D. Ghosh, Catalyzing the intercalation storage capacity of aqueous zinc-ion battery constructed with Zn(II) preinserted organo-vanadyl hybrid cathode, ACS Appl. Energy Mater. 3 (2020) 3425-3434.

[21] H. Joshi, N. Sinha, K. Parveen, S. Pakhira, Unveiling the electrocatalytic activity of cobaloxime metallolinker in the UU-100(Co) metal-organic framework toward the H_2 evolution reaction: A DFT study, Energy Fuels 37 (2023) 19771-19784.

[22] K. Momma, F. Izumi, VESTA 3 for three-dimensional visualization of crystal, volumetric and morphology data, J. Appl. Cryst. 44 (2011) 1272-1276.

LIST OF PUBLICATIONS

Publications from the thesis

1. **K. Parveen,** S. Pakhira, Designing organic bridging linkers of metal-organic frameworks for enhanced carbon dioxide adsorption, ***New J. Chem.*** 48 (2024) 13700-13714.
2. **K. Parveen,** S. Pakhira, Unveiling the electrocatalytic activity of metallophthalocyanine-based covalent organic frameworks toward CO_2 reduction reaction, ***J. Phys. Chem. C***, 129 (2025) 2973-2987.
3. **K. Parveen,** S. Pakhira, Unveiling the electrocatalytic activity of metallophthalocyanine-based metal-organic frameworks toward CO_2 reduction reaction, ***ACS Appl. Energy Mater.***, 8 (2025) 17818-17830.

Publications other than the thesis

1. H. Joshi†, N. Sinha†, **K. Parveen**†, S. Pakhira, Unveiling the electrocatalytic activity of cobaloxime metallolinker in the UU-100(Co) metal-organic framework toward the H_2 evolution reaction: A DFT study, ACS ***Energy Fuels***, 37 (2023) 19771-19784. **(† Equal Contribution)**
2. N. Sinha†, **K. Parveen**†, S. Pakhira, Synergistic Ni-doping in 2D monolayer molybdenum disulfide for enhanced electrocatalytic H_2 evolution, ***Int. J. Hydrogen Energy***, 105 (2025) 1294-1308. **(† Equal Contribution)**
3. L. Yadav, V. Kumar, **K. Parveen**, S. Pakhira, Demystifying the dual-functional electrocatalytic activity of the 2D Co-doped NbSSe Janus transition metal dichalcogenide for O_2 reduction and H_2 evolution reactions, ***J. Mater. Chem. A***, 14 (2026) 16735-16753.
4. S. Patnaik, L. Yadav, **K. Parveen**, S. Pakhira, D. Pradhan, Synergistic Effect of a Bi_2MoO_6/-g-C_3N_4 Composite for Highly Selective Electrocatalytic Oxygen Reduction to Produce H_2O_2, ***ACS Appl. Mater. Interfaces*** 18 (2026), 29931-29945.

International Conferences and Workshops

1. **K. Parveen, S. Pakhira,** "Unveiling the electrocatalytic activity of metallophthalocyanine-based metal-organic frameworks toward CO_2 reduction reaction", 17th International Conference on Materials Chemistry (MC17 2025), Edinburgh, Scotland. **(Poster Presentation)**
2. **K. Parveen,** S. Pakhira, "Unveiling the electrocatalytic activity of metallophthalocyanine-based covalent organic frameworks toward CO_2 reduction reaction", International Conference and Workshop on Evolution of Electronic Structure Theory and Experimental Realization (EESTER 2025), SRM and IIT Madras. **(Poster Presentation)**
3. **K. Parveen**, S. Pakhira, Synergistic Ni-doping in 2D monolayer molybdenum disulfide for enhanced electrocatalytic H_2 evolution, International Symposium on Materials for Sustainable Development (ISMSD 2024), IIT Indore. **(Oral Presentation)**
4. **K. Parveen**, S. Pakhira, Synergistic Ni-doping in 2D monolayer molybdenum disulfide for enhanced electrocatalytic H_2 evolution, Society for Atomistic and Continuum Modeling (SACM 2024), Bhabha Atomic Research Center (BARC), Mumbai. **(Oral Presentation)**
5. **K. Parveen,** S. Pakhira, Designing organic bridging linkers of metal-organic frameworks for enhanced carbon dioxide adsorption, Atomistic Modeling of Molecules and Materials (AMMM 2023), Bhabha Atomic Research Center (BARC), Mumbai. **(Oral Presentation)**

TABLE OF CONTENTS

LIST OF FIGURES……xxi

LIST OF TABLES…… xxv

LIST OF ABBREVIATIONS AND SYMBOLS…… xxvii

ABSTRACT……xxxiii

Chapter 1: Introduction……...1

1.1 Global CO_2 emissions and environmental impact……...1

1.2 CO_2 capture, utilization, and storage……...2

1.3 Porous crystalline organic frameworks……...2

1.3.1 Metal organic frameworks…… 4

1.3.2 Covalent organic frameworks……..... 5

1.4 Role of linkers in forming MOFs and COFs……6

1.5 Properties of porous materials (COFs and MOFs) ……... 10

1.6 Applications of MOFs and COFs……. 13

1.7 Metallopthacyanine (MPc)……...16

1.8 CO_2RR on MPc-based MOFs and COFs……. 18

1.9 Research gap and motivation……... 20

1.10 Contribution from the present thesis……... 22

1.11 Organization of the thesis……..…… 23

1.12 References……. 24

Chapter 2: Theoretical Background and Computational Approaches..... 33

2.1 Fundamentals of quantum mechanics and electronic structure theory……. 33

2.1.1 Many-body Schrödinger equation…… 34

2.1.2 Born-Oppenheimer approximation……...36

2.1.3 Need for approximate solutions……37

2.2 Hartree and Hartree-Fock theory……. 38

2.3 Density functional theory (DFT)……...40

2.3.1 Hohenberg-Kohn theorems……...40

2.3.2 Kohn-Sham formalism…….. 41

2.3.3 Exchange-correlation functionals……..... 43

2.3.4 van der Waals interactions and dispersion corrections…… 45

2.3.5 Møller-Plesset second-order perturbation theory……. 46

2.3.6 Basis sets…….....47

2.4 Computational quantum chemistry calculations…….. 48

2.4.1 Hohenberg-Kohn theorems…… 49

2.4.2 Energy decomposition analysis (EDA)……. 49

2.4.3 Natural bond orbital (NBO) analysis……... 50

2.4.4 Computational hydrogen electrode (CHE) model……. 51

2.5 Software……. 53

2.5.1 Gaussian 16……...53

2.5.2 GAMESS……. 54

2.5.3 CRYSTAL 23……. 55

2.5.4 Chemcraft1.8……58

2.5.5 GaussView6.1……. 59

2.5.6 VESTA……60

2.6 References……61

Chapter 3: Organic Bridging Linkers of MOFs for Enhanced CO_2 Adsorption.....65

3.1 Introduction…… 65

3.2 Computational details……...67

3.3 Molecular systems design and adsorption sites…… 69

3.4 Results and discussion…… 71

3.4.1 Binding Enthalpy…… 71

3.4.2 Energy decomposition analysis (EDA)…… 79

3.4.3 Frontier molecular orbital (FMO)…… 80

3.5 Conclusions…… 83

3.6 References……84

Chapter 4: Metallophthalocyanine-based COFs for CO_2 Reduction Reaction…… 91

4.1 Introduction…… 91

4.2 Computational details……...93

4.3 Materials design……95

4.4 Results and discussion…… 96

4.4.1 Equilibrium geometries……96

4.4.2 Electronic properties…… 98

4.4.3 CO_2RR mechanisms…… 102

4.4.4 Spin density…… 109

4.5 Conclusions……110

4.6 References…… 111

Chapter 5: Metallophthalocyanine-based MOF for CO_2 Reduction Reaction……119

5.1 Introduction……119

5.2 Computational details…… 122

5.3 Material details……...123

5.4 Results and discussion……124

5.4.1 Equilibrium geometry, structural and electronic properties……124

5.4.2 Reaction mechanisms…… 128

5.4.3 Structural and chemical stability…… 140

5.5 Conclusions……...… 141

5.6 References…… 142

Chapter 6: Conclusions and Future Perspectives…… 149

6.1 Conclusions……... 149

6.2 Future Perspectives…… 150

LIST OF FIGURES

Figure 1.1 The structural illustration of MOF-5, showing coordination between the metal node and the organic linker……..……...5

Figure 1.2 The schematic representation of the formation and porous structures of COF-1 and COF-5, illustrating the constituent organic building units and their connectivity within the extended framework……...…...6

Figure 1.3 The MOFs with various structures, porosity and topology synthesized depending on the kinds of linkers……8

Figure 1.4 Various linkages formed by COFs linkers for the synthesis of COFs……..10

Figure 1.5 Properties of MOFs and COFs……13

Figure 1.6 Applications of MOFs and COFs……16

Figure 1.7 The molecular structure, features and advantages of metallophthalocyanine (MPc)……17

Figure 1.8 Possible pathways for CO_2 reduction into CH_4……...19

Figure 1.9 Possible pathways for CO_2 reduction into C_2H_4 and C_2H_5OH…….20

Figure 3.1 The equilibrium structures of the pure MOF's linkers: (a) 1,4-benzene dicarboxylate (BDC), (b) 3-fluoro 1,4-benzene dicarboxylate (FBDC), (c) 3,6-difluoro 1,4-benzene dicarboxylate (DFBDC-1), (d) 2,3-difluoro 1,4-benzene dicarboxylate (DFBDC-2), (e) 2,3,5,6-tetrafluoro 1,4-benzene dicarboxylate (TFBDC), (f) 3,6-dichloro 1,4-benzene dicarboxylate (DClBDC-1), (g) 2,3-dichloro 1,4-benzene dicarboxylate (DClBDC-2), and (h) 1,4 naphthalene dicarboxylate (NDC)…… 70

Figure 3.2 The adsorption of CO_2 molecule at the (a) center, and (b) side position of the BDC linker……..71

Figure 3.3 Equilibrium structures of both the pristine linkers and the adsorbed CO_2 at the center and side positions of the linkers: (a) BDC-Center, (b) BDC-Side, (c) FBDC-Center, (d) FBDC-Side, (e) DFBDC-1-Center, (f) DFBDC-1-Side, (g) DFBDC-2-Center, (h) DFBDC-2-Side, (i) TFBDC-Center, (j) TFBDC-Side, (k) DClBDC-1-Center, (l) DClBDC-2-Side, (m) DClBDC-2-Center, (n) DClBDC-2-Side, (o) NDC-Center, and (p) NDC-Side…… 73

Figure 3.4 Equilibrium structures of the Li-decorated linkers and the adsorbed CO_2 at the center and side positions: (a) BDC-Li-Center, (b) BDC-Li-Side, (c) FBDC-Li-Center, (d) FBDC-Li-Side, (e) DFBDC-1-Li-Center, (f) DFBDC-1-Li-Side, (g) DFBDC-2-Li-Center, (h) DFBDC-2-Li-Side, (i) TFBDC-Li-Center, (j) TFBDC-Li-Side, (k) DClBDC-1-Li-Center, (l) DClBDC-2-Li-Side, (m) DClBDC-2-Li-Center, (n) DClBDC-2-Li-Side, (o) NDC-Li-Center, and (p) NDC-Li-Side…….. 76

Figure 3.5 The binding enthalpy (ΔH) value of the adsorbed CO_2 molecule at the center and side positions of both the pure and Li-decorated linkers computed by the (a) B3LYP-D3, and (b) MP2 method…… 78

Figure 3.6 The Energy Decomposition Analysis (EDA) of CO_2 adsorption at the side position of the linkers. The electrostatic energy, polarization energy, dispersion energy, exchange energy, repulsion energy, and binding enthalpy are represented by ΔE_{els}, ΔE_{pol}, ΔE_{dis}, ΔE_{exc}, ΔE_{rep}, and ΔH_{bind} respectively. The units are expressed in kJ/mol……...80

Figure 3.7 The energy gap (E_g) between the HOMO and LUMO of both the pure and Li-decorated linkers. The energies are expressed in eV……82

Figure 3.8 The HOMO-LUMO projections of CO_2 adsorption at the side position of pure and Li-decorated linkers (a) BDC linker, (b) FBDC linker, (c) DFBDC-1 linker, (d) DFBFC-2 linker, (e) NDC linker, (f) BDC-Li-decorated linker, (g) FBDC-Li-decorated linker, (h) DFBDC-1-Li-decorated linker, and (i) DFBDC-2-Li-decorated linker, (j) NDC-Li-decorated linker……..83

Figure 4.1 Illustration of the chemical structure of the COF materials, where X stands for SH and NH_2 group. The R with NH group in the resultant COF stands for the CoPc-DNDS-COF and S group stands for the CoPc-DSDS-COF. The metallophthalocyanine (MPc) part of the COF materials is shown by the dotted blue color circle, and the organic bridging linker part is shown by the dotted red color rectangle……96

Figure 4.2 (a) Equilibrium geometry, (b) Electronic band structure, (c) Total DOS of the 3D CoPc-DNDS-COF, and Partial density of states (PDOS) of (d) Co atom, and (e) the contributing component of the DOS of ***d***-orbital of the Co atom……99

Figure 4.3 (a) Equilibrium geometry, (b) Electronic band structure, (c) Total DOS of the 3D CoPc-DSDS-COF, and Partial density of states (PDOS) of (d) Co atom, and (e) the contributing component of the DOS of ***d***-orbital of the Co atom……99

Figure 4.4 (a) Equilibrium geometry, (b) Electronic band structure, (c) Total DOS of 2D monolayer slab of the CoPc-DNDS-COF, and (d) Partial density of states (PDOS) of the Co atom……..101

Figure 4.5 (a) Equilibrium geometry, (b) Electronic band structure, (c) Total DOS of 2D monolayer slab of the CoPc-DSDS-COF, and (d) Partial density of states (PDOS) of the Co atom…… 102

Figure 4.6 The equilibrium geometries of the reaction intermediates for the most favorable path of CO_2RR into methane (CH_4) in the CO_2RR process on the surface of CoPc-DNDS-COF material computed by the DFT-D method……...105

Figure 4.7 The free energy diagram computed by the DFT-D method (i.e., Gibbs free energy (ΔG in eV) profile) of all the eight pathways followed in CO_2 reduction reaction (CO_2RR) into methane (CH_4) at the surface of CoPc-DNDS-COF material…….. 106

Figure 4.8 The equilibrium geometries of the reaction intermediates involved in the electrochemical reduction of CO_2 into carbon monoxide (CO) on the surface of CoPc-DNDS-COF material computed by the DFT-D method…… 107

Figure 4.9 The free energy diagram computed by the DFT-D method (i.e., Gibbs free energy (ΔG in eV) profile) of all the eight pathways followed in CO_2 reduction reaction (CO_2RR) into carbon monoxide (CO) and methane (CH_4) at the surface of CoPc-DNDS-COF material…… 108

Figure 4.10 Electron spin density of all the intermediates adsorbed on the DNDS surface during CO_2 reduction into CH_4; (a) CoPc-DNDS surface; (b) *CO_2; (c) *COOH; (d) *CO; (e) *CHO; (f) *OCH_2; (g) *CH_2OH; (h) *CH_3OH; and (i) *CH_3. The yellow region represents the positive part of the wave function i.e., α spin, while the sky blue region represents the negative part of the wave function i.e., β spin. The * asterisk represents that the species (intermediate) is adsorbed on the surface of CoPc-DNDS-COF……110

Figure 5.1 Illustration of the chemical structure of CuPc MOF material. The metal node and the linkage parts of the CuPc MOF are shown by the dotted red color rectangle and circle, respectively……..124

Figure 5.2 The (a) equilibrium geometry, (b) band structure, (c) total density of states (DOS), and (d) partial density of states (PDOS) of the Cu atom's d subshell of the CuPc……... 127

Figure 5.3 CO_2 adsorption at the various possible sites of CuPc…… 129

Figure 5.4 The equilibrium geometries of the possible reaction intermediates associated with the two-electron CO_2RR to *HCOOH intermediate on the CuPc surface, with (a) CuPc surface; and the intermediates: (b) *CO_2; (c) *HCOO; (d) *COOH; (e) *CO; and (f) *HCOOH…….. 131

Figure 5.5 The equilibrium geometries of the possible reaction intermediates associated with the subsequent six-electron reduction of *HCOOH to CH_4 on the CuPc surface with intermediates: (a) *HCOOH; (b) *COH; (c) *CHO; (d) *C; (e) *CHOH; (f) *OCH_2; (g) *CH; (h) *OCH_3; (i) *CH_2OH; (j) *CH_2; (k) *O; (l) *CH_3OH; (m) *OH; (n) *CH_3; and (o) *CuPc…….. 133

Figure 5.6 The potential energy surface (PES) diagram representing the ΔE_{ads} values for CO_2 reduction to CH_4 through various reaction intermediates on the CuPc surface at 0 V_{RHE}. The energies are expressed in eV……...134

Figure 5.7 The equilibrium geometries of the possible reaction intermediates associated with the first seven-electron reduction of CO_2 to *CHCO intermediate on the CuPc surface with (a) CuPc surface; and intermediates: (b) *2CO_2; (c) *2COOH; (d) *2CO; (e) *CHO + *CO; (f) *COH + *CO; (g) *CHOH + *CO; (h) *CCO; and (i) *CHCO……..136

Figure 5.8 The equilibrium geometries of the possible reaction intermediates associated with the subsequent five-electron reduction of *CHCO toward C_2 Products (C_2H_4 and C_2H_5OH) on the CuPc surface with intermediates: (a) *CHCO, (b) *CHCOH; (c) *CH_2CO; (d) *OCHCH; (e) *CHC; (f) *CH_2CHO; (g) *$OCHCH_2$; (h) *O; (i) *CHCH; (j) *CH_2CH_2O; (k) *OH; (l) *$CHCH_2$; (m) *CH_2CH_2OH; and (n) CuPc surface……... 137

Figure 5.9 The potential energy surface (PES) diagram representing the ΔE_{ads} values for CO_2 reduction to C_2H_4 and C_2H_5OH through various reaction intermediates on the CuPc surface at 0 V_{RHE}. The energies are expressed in eV…… 139

LIST OF TABLES

Table 3.1 The charge transfer (C_T) of CO_2 molecule at the center and side positions of the pristine and Li-decorated linkers…… 74

Table 3.2 Some IRMOFs with their constituent linkers, and pore parameters (Brunauer-Emmett-Teller (BET) and Langmuir surface area, and pore volume)……...79

Table 4.1 The equilibrium structural parameters (lattice constants and interfacial angles), space group symmetry, bandgap (E_g), and material state of the bulk 3D crystal structure and 2D monolayer of the DNDS and DSDS COFs…… 97

Table 5.1 The equilibrium structural parameters (lattice constants and interfacial angles), space group symmetry, bandgap (E_g), and material state of the 2D monolayer slab of the CuPc……..…….... 125

LIST OF ABBREVIATIONS AND SYMBOLS

ABBREVIATIONS

0D	Zero-dimensional
1D	One-dimensional
2D	Two-dimensional
3D	Three-dimensional
AOs	Atomic orbitals
B3LYP	Becke three-parameter Lee-Yang-Parr
BDC	1,4-Benzenedicarboxylate
BET	Brunauer-Emmett-Teller
BFs	Bloch functions
BTC	Benzenetricarboxylate
CB	Conduction band
CCUS	Carbon capture, utilization, and storage
CGFs	Contracted Gaussian functions
CHE	Computational Hydrogen Electrode
CN	Coordination number
COFs	Covalent organic frameworks
CO_2RR	Carbon dioxide reduction reaction
Cos	Crystalline orbitals
CT	Charge transfer
DClBDC-1	3,6-Dichloro-1,4-benzenedicarboxylate
DClBDC-2	2,3-Dichloro-1,4-benzenedicarboxylate
DFBDC-1	3,6-Difluoro-1,4-benzenedicarboxylate
DFBDC-2	2,3-Difluoro-1,4-benzenedicarboxylate
DFT	Density functional theory
DOS	Density of states
ECPs	Effective core potentials
EDA	Energy decomposition analysis
eV	Electron volt
FBDC	3-Fluoro-1,4-benzenedicarboxylate
FMO	Frontier molecular orbitals

GAMESS	General Atomic and Molecular Electronic Structure System
GFs	Gaussian functions
GGA	Generalized Gradient Approximation
GPW	Gaussian and plane wave
GTFs	Gaussian-type functions
GTOs	Gaussian-type orbitals
HER	Hydrogen evolution reaction
HF	Hartree-Fock
HK	Hohenberg-Kohn
HOMO	Highest occupied molecular orbital
IPCC	Intergovernmental Panel on Climate Change
IRC	Intrinsic reaction coordinate
LCAO	Linear combination of atomic orbitals
LDA	Local Density Approximation
LMO-EDA	Localized molecular orbital energy decomposition analysis
LMP2	Local second-order Møller-Plesset
LSDA	Local Spin Density Approximation
LUMO	Lowest unoccupied molecular orbital
MOFs	Metal–organic frameworks
MP2	Second-order Møller-Plesset
MPA	Mulliken population analysis
MPc	Metallophthalocyanine
NBO	Natural Bond Orbital
NDA	1,4-Naphthalenedicarboxylate
ORR	Oxygen reduction reaction
PCET	Proton-coupled electron transfer
PDOS	Partial density of states
PES	Potential energy surface
POPs	Porous organic polymers
ppm	Parts per million
Pz	Pyrazine
QM	Quantum mechanical
RI-MP2	Resolution-of-identity second-order Møller-Plesset

SACs	Single-atom catalysts
SBUs	Secondary building units
SCF	Self-consistent field
STOs	Slater-type orbitals
TDDFT	Time-dependent density functional theory
TFBDC	2,3,5,6-Tetrafluoro-1,4-benzenedicarboxylate
TS	Transition state(s)
TZVP	Triple-ζ valence with polarization
UDFT	Unrestricted density functional theory
VB	Valence band
vdW	Van der Waals
VESTA	Visualization for Electronic and Structural Analysis
XC	Exchange-correlation

SYMBOLS

Å	Ångström
*	Adsorbed species (asterisk denotes adsorption site)
°	Degree
°C	Degree Celsius
β	Beta
ħ	Reduced Planck constant
μ	Chemical potential
Ψ(r)	Wave function
Φ({R})	Nuclear wave function
ε_0	Permittivity of free space
ε_i	Orbital energy
∇^2_i	Laplacian operator acting on electronic coordinates
∇^{2I}	Laplacian operator acting on nuclear coordinates
ρ(r)	Electron density
n(r)	Electron density
V(r)	Potential
$V_n(r_i)$	Potential due to the nuclei acting on the electrons

$V_{ext}(r)$	External potential
V_h	Hartree potential
$V_s(r)$	Effective potential
$V_{XC}(r)$	Exchange-correlation potential
U	Electron-electron interaction
$\hat{H}$	Hamiltonian operator
$\hat{H}_e$	Electronic Hamiltonian operator
$\hat{H}_n$	Nuclear Hamiltonian operator
$\hat{F}$	Fock operator
$\hat{T}$	Kinetic energy operator
$\hat{V}$	Potential energy operator
E	Energy eigenvalue
E_b	Binding energy
ΔE_b	Change in binding energy
ΔE	Energy change
ΔE_{ads}	Adsorption energy
ΔE_{dis}	Dispersion energy
ΔE_{els}	Electrostatic interaction energy
ΔE_{exc}	Exchange energy
ΔE_{int}	Total interaction energy
ΔE_{pol}	Polarization energy
ΔErep	Repulsion energy
E_{coh}	Cohesive energy
E_g	Energy gap (band gap)
E_F	Fermi energy level
E_{tot}	Total energy
$E_{XC}[\rho]$	Exchange-correlation energy functional
$E_{XC}[n]$	Exchange-correlation energy functional
$T_s[n]$	Kinetic energy functional of non-interacting electrons
$T[\rho]$	Kinetic energy functional
$V_{ee}[\rho]$	Electron-electron interaction functional
ρ_{GS}	Ground-state electron density
ΔG	Gibbs free energy change
ΔH	Binding enthalpy

ΔH_{ads}	Adsorption enthalpy
ΔH_{bind}	Total binding enthalpy
Q_{st}	Heat of adsorption
C_T	Charge transfer
e^-	Electron
H^+	Proton
e	Elementary charge
m_e	Electron mass
m_I	Mass of the *I*th nucleus
Z_I	Atomic number of the nucleus
r_i	Position vector of the *i*th electron
R_J	Position vector of the *j*th nucleus
Gt	Gigatonne
nm	Nanometre
m^2g^{-1}	Square metres per gram
~	Approximately
C=C	Olefinic double bond
P=O	Phosphoryl bond
C=O	Carbonyl bond

ABSTRACT

The rapid increase in atmospheric carbon dioxide (CO_2) emissions due to industrialization and fossil fuel consumption has created an urgent need for efficient carbon capture, storage, and utilization technologies. In this thesis, first-principles-based density functional theory (DFT) methods have been employed to investigate porous metal-organic frameworks (MOFs) and covalent organic frameworks (COFs) materials for CO_2 capture and electrochemical CO_2 reduction reaction (CO_2RR). The first part of the work focuses on a molecular-level investigation of CO_2 adsorption on various pristine and Li-decorated MOF linkers, using DFT and the second-order Møller-Plesset (MP2) methods. The results reveal that the Li-decoration significantly enhances the CO_2 binding enthalpy through strong physisorption interactions, primarily driven by electrostatic and polarization effects. The second part explores sulfur-linked cobalt phthalocyanine (CoPc)-based COFs for electrochemical CO_2 reduction toward C_1 products. The electronic structure and catalytic activity studies demonstrate that the framework engineering through sulfur-containing linkages strongly influences catalytic selectivity and promotes efficient CH_4 formation. The final part extends the investigation to a copper phthalocyanine (CuPc)-based MOF for selective electrochemical CO_2 reduction toward both C_1 and C_2 products. The CuPc MOF exhibits favorable catalytic pathways for ethanol (C_2H_5OH) formation owing to efficient stabilization of key intermediates and enhanced C-C coupling. Overall, this work provides valuable mechanistic insights into porous framework engineering for carbon capture and CO_2 conversion technologies.

Chapter 1

Introduction

This chapter presents an overview of the increasing carbon dioxide (CO_2) emissions and their environmental impact, emphasizing the need for effective mitigation strategies such as carbon capture, utilization, and storage (CCUS). It introduces porous crystalline materials, particularly metal-organic frameworks (MOFs) and covalent organic frameworks (COFs), highlighting their design principles, key properties and applications. The role of organic linkers in controlling framework structure and functionality has been discussed here along with an overview of metallophthalocyanine (MPc)-based MOFs and COFs for CO_2 electroreduction. The research gaps, motivation, and objectives of the thesis are also outlined, followed by a brief summary of the contributions and organization of the thesis.

1.1 Global CO_2 emissions and environmental impact

The rapid expansion of the world's population and the accelerated industrial development have led to an increased rise in global energy demand, causing serious challenges in sustainable economic development.[1] The excessive dependence on fossil fuels to meet this demand has significantly increased CO_2 emissions, contributing to devastating environmental consequences. The increased atmospheric CO_2 levels have closely related to the global warming, glaciers melting, rising sea levels, ocean acidification, biodiversity loss, and the increasing frequency of extreme weather events, all of which threaten the ecosystems and human livelihoods in worldwide.[2] Since the beginning of the industrial revolution in the early 1800s, atmospheric CO_2 concentrations have risen dramatically from 280 ppm to more than 425 ppm in 2025, primarily attributed to anthropogenic activities and industrial emissions.[3] Therefore, to mitigate long-term climate risks, stabilizing and reducing CO_2 concentrations have become a global priority. However, the transition toward alternative energy sources that can completely replace fossil fuels remains challenging, escalating concerns about the future of the planet and its living species. Furthermore, it is predicted by the Intergovernmental Panel on Climate Change (IPCC) that the CO_2 concentration will reach by 950 ppm by the end of this century, which will bring about dramatic changes in the earth's atmospheric chemistry and it would be very harmful for our society.[4–6] Therefore, there is an urgent need to develop effective technologies and strategies to

control and reduce atmospheric CO_2 concentrations and slow down global climate change.

1.2 CO_2 capture, utilization, and storage

Carbon capture, utilization, and storage (CCUS) have become a key technological strategy for mitigating greenhouse gas emissions and facilitating the transition to carbon-neutral energy systems. This set of decarbonization techniques involves removing CO_2 from the atmosphere or from industrial flue gases, followed by its transport for either long-term storage or productive use. CCUS offers a viable mitigation pathway for existing power plants and energy-intensive industrial facilities, which could otherwise release nearly 600 Gt of CO_2 over the next fifty years.[7] These hard-to-decarbonize industries generally include steel, cement, and chemical manufacturing. Furthermore, CCUS is generally considered to be among the most economically feasible methods of generating low-carbon hydrogen. Therefore, meeting mid-century carbon neutrality targets is considered to be highly unlikely without the widespread use of CCUS technologies.[7–9] The performance of CO_2 capture processes strongly depends on the properties of the adsorbent materials used. An ideal adsorbent typically exhibits high CO_2 uptake and selectivity, low isosteric heat of adsorption (Q_{st}) to enable energy-efficient regeneration, excellent recyclability, strong thermal and chemical stability, rapid adsorption/desorption kinetics, and cost-effectiveness.[10] Current CO_2 separation techniques include solvent-based absorption, solid-state chemical adsorption, porous material adsorption, cryogenic distillation, and membrane separation.[11] Among these, adsorption-based systems employing advanced porous sorbents have attracted considerable attention due to their high efficiency and reduced energy requirement. However, despite technological advancements, the challenges towards ECR remain. The linear molecular structure and strong C=O bonds render CO_2 thermodynamically stable and kinetically inert, making its activation and catalytic conversion energetically demanding. Therefore, designing materials with tunable structural and electronic properties is essential to overcome the thermodynamic and kinetic barriers associated with CO_2 capture and reduction.

1.3 Porous crystalline organic frameworks

A porous material can be categorized as a solid structure with rich pores and a high specific surface area.[10] Over the years, porous materials have evolved from

conventional inorganic materials such as zeolites and molecular sieves to organic-inorganic hybrid materials like metal-organic frameworks (MOFs) and further to fully organic porous materials, including covalent organic frameworks (COFs). These different classes of porous materials have been considered as the most promising candidates for CCUS application.[12–14] Molecular sieves are synthetic hydrated aluminosilicates with high adsorption capacity, strong selectivity, and high temperature resistance that have attracted research interest for CO_2 adsorption.[15–17] The adsorption behavior of molecular sieves primarily arises from physical interactions such as weak van der Waals (vdW) forces, and because of the strong electrostatic field within the pores, it shows a strong affinity toward polar and unsaturated molecules. However, their relatively small pore size (typically below 2 nm) and purely inorganic framework limit functional tunability and restrict the directional design of materials for specific applications.[18–20] Natural zeolite is the earliest known porous material, and a naturally occurring aluminosilicate ore discovered by Swedish mineralogist Cronstedt in 1756 that boils when heated.[21] The reversible absorption-dehydration behavior, high thermal and chemical stability, good mechanical strength, and CO_2 adsorption capacity and selectivity make it attractive for CO_2 capture applications.[22–24] However, natural zeolites readily adsorb water, which significantly reduces their CO_2 capture performance under humid conditions. In addition, the non-uniform pore size distribution leads to poor CO_2 capture performance at both low and high pressures, thereby limiting its large-scale industrial applications.[17,24,25] To address these limitations, crystalline porous framework materials have gained increasing attention because of their high surface areas, structural tunability, and design flexibility. Among them, MOFs and COFs have emerged as two important classes of reticular materials widely explored for CO_2 capture and catalytic conversion. MOFs are constructed from metal ions or metal-containing secondary building units (SBUs) that are coordinated to organic linkers (linkages or bridging ligands) via coordination bonds, offering structural diversity and accessible metal sites that are beneficial for adsorption and catalysis.[26] In contrast, COFs are composed entirely of light elements connected by strong covalent bonds, resulting in lightweight structures with high thermal stability and well-defined porosity.[27] Despite their differences in bonding nature and composition, both MOFs and COFs possess ordered porous structures, tunable pore environments, and modular design strategies, making them highly promising materials for efficient CO_2 capture and conversion.

1.3.1 Metal organic frameworks

Metal-organic frameworks (MOFs) are crystalline porous materials composed of metal ions or metal clusters (secondary building units, SBUs) interconnected by multidentate organic ligands to form extended one, two, or three-dimensional networks.[28–31] The concept of coordinate polymers dates back to the 1960s; however, significant advances were realized in the mid-1990s when Prof. Omar M. Yaghi and co-workers introduced the term "metal-organic frameworks" and demonstrated the rational design of highly porous crystalline MOF-5, as depicted in Figure 1.1.[32,33] The development of MOFs was driven by the principle of reticular chemistry, which involves the assembly of predetermined molecular building blocks through strong metal-ligand coordination bonds into extended periodic structures.[34,35] This approach enables the predictable formation of structures with predefined geometries through the rational assembly of secondary building units and organic linkers. MOFs represent a highly versatile class of porous materials that have been extensively explored for gas storage, separation, and catalytic applications. Their adjustable pore size, tunable pore opening, and easy functionalization enable precise control over structural and chemical properties, allowing systematic variation of both metal nodes and organic linkers to tune pore size, functionality and topology. Owing to these properties, MOFs exhibit exceptionally high internal surface areas and porosity, with some structures achieving record-breaking Brunauer-Emmett-Teller (BET) surface areas among porous materials. Unlike conventional coordination polymers, MOFs exhibit permanent porosity and retain their structural integrity even after removal of guest molecules, which is critical for practical adsorption applications.[34] The large pore volume and well-defined channels in MOFs facilitate efficient gas adsorption and selective separation from mixtures of gases. The presence of open metal sites and functionalized pore environments significantly enhances host-guest interactions, especially for quadrupolar molecules such as CO_2. In particular, their structural diversity and tailorable functionality of MOFs make them strong candidates for CO_2 capture and separation compared to conventional adsorbents.[34,36,37] These advantages have positioned MOFs as one of the most promising materials for advanced gas storage and carbon capture applications.

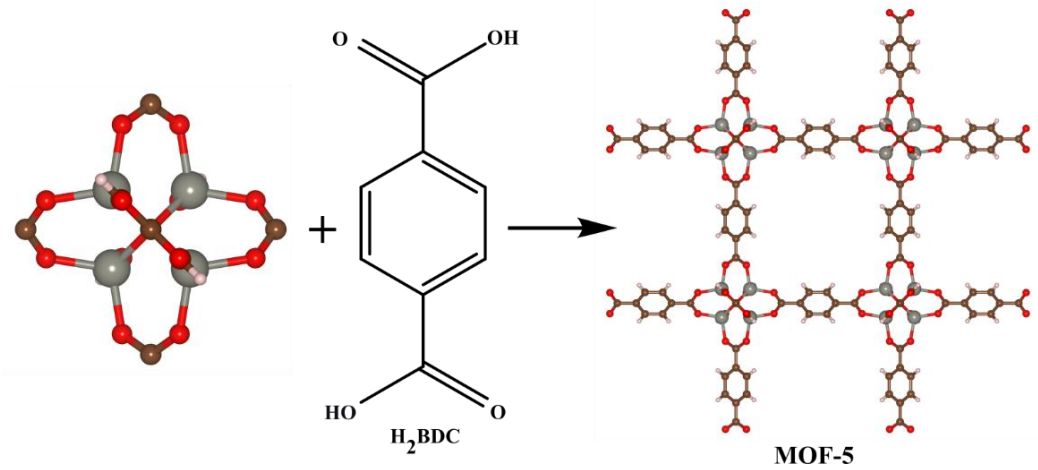


Figure 1.1 The structural illustration of MOF-5, showing coordination between the metal node and the organic linker.[32] The atomic color scheme is as follows: carbon (brown), oxygen (red), hydrogen (linen), and metal centers (grey).

1.3.2 Covalent organic frameworks

Covalent organic frameworks (COFs) are crystalline porous materials composed entirely of light elements (e.g., C, H, B, O, and N) linked through strong covalent bonds to form extended two- or three-dimensional periodic networks.[27] The development of COFs was enabled by the principles of reticular chemistry, which allow the rational assembly of predefined organic building blocks into ordered frameworks with predictable structures.[38] A breakthrough in this field was reported in 2005 by Yaghi and co-workers, who synthesized the first two-dimensional COFs i.e., COF-1 and COF-5 via boronic acid condensation reactions, as depicted in Figure 1.2, followed by the extension to three-dimensional structures such as COF-102 in 2007, thereby significantly expanding the structural diversity of these materials.[39,40] The left-hand panels in Figure 1.2 illustrate the chemical building units and corresponding condensation reactions, with atomic symbols represented in black for improved readability, whereas the right-hand panels show the resulting porous framework structures. COFs represent a unique class of porous materials distinguished by their low density, high surface area, and structural tunability. Their well-defined and periodic structures enable precise control over pore size, shape and topology. This modular design approach allows systematic variation of organic linkers and their chemistry, facilitating the incorporation of functional groups within the pore walls. Unlike many amorphous porous organic polymers (POPs), COFs exhibit long-range crystallinity and permanent porosity, retaining their ordered structures even after the removal of guest

molecules. The presence of uniformly distributed and tailorable pore environments in COFs plays a crucial role in governing host-guest interactions. In particular, functionalization of the pore surface enhances selective adsorption of gas molecules, such as CO_2. The combination of high porosity, structural regularity, and chemical tunability makes COFs highly attractive for a wide range of applications, including gas storage and separation, catalysis, optoelectronics, and energy-related processes.[36,40–42]

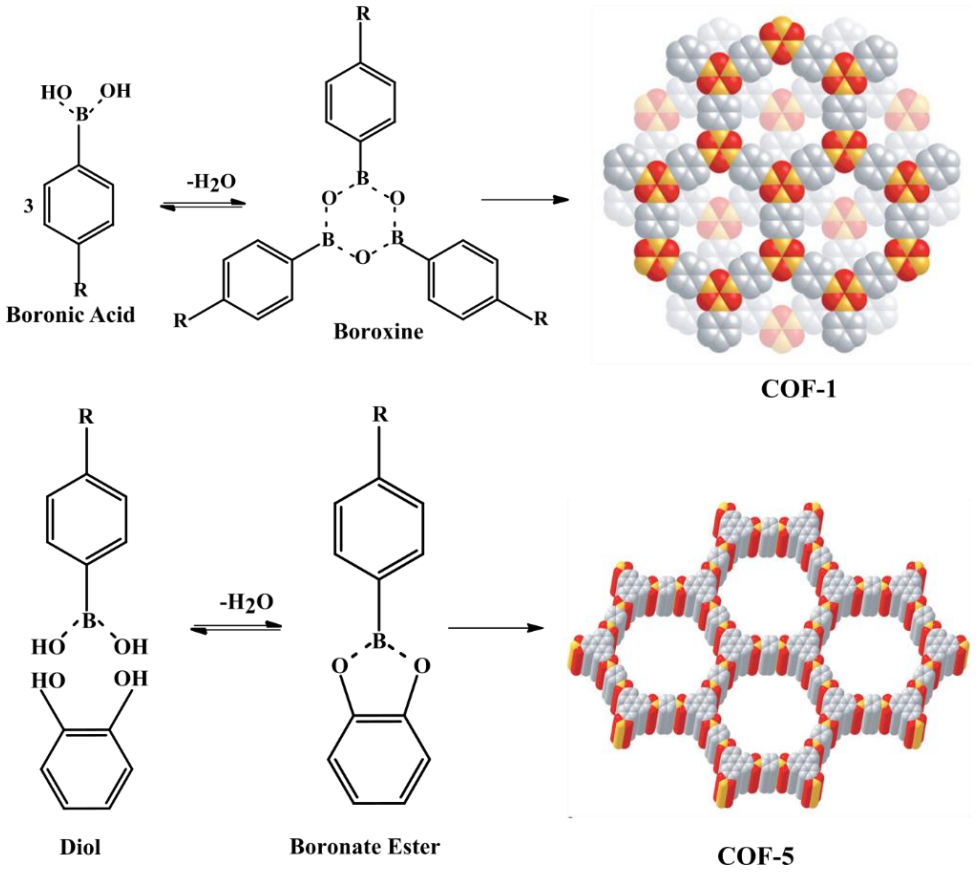


Figure 1.2 The schematic representation of the formation and porous structures of COF-1 and COF-5, illustrating the constituent organic building units and their connectivity within the extended framework.[39] The atomic colour scheme used in the molecular models is as follows: carbon (grey), oxygen (red), hydrogen (white), and boron (yellow).

1.4 Role of linkers in forming MOFs and COFs

Organic linkers or ligands play an important role in the formation and functionality of MOFs, as they bridge metal ions (clusters) to generate extended porous frameworks. The diversity in linker design, including variations in size, geometry, and functional groups, enables the formation of a wide range of MOF structures with distinct topologies and properties. Importantly, linkers not only determine the structural

features such as crystallinity, porosity, stability, and flexibility, but also govern the chemical environment within the pores, influencing host-guest interactions and application-specific performance.[43] Based on their functional groups, MOF linkers, as depicted in Figure 1.3, can be broadly classified as follows:

- **Carboxylate-based linkers**

  Carboxylate linkers are the most extensively employed in MOF synthesis due to their strong coordination ability with metal ions through deprotonation, forming stable metal-carboxylate bonds.[44] In addition to coordination, carboxylate groups can participate in hydrogen bonding as both donors and acceptors, influencing framework assembly, crystallinity, and pore structure.

- **Nitrogen-based linkers**

Nitrogen-containing linkers, including azines, azoles, and amines, provide versatile coordination environments and allow fine-tuning of framework structures.[45] Their coordination flexibility enables control over structural arrangements and pore chemistry.

- **Phosphate-based linkers**

Phosphate linkers from strong metal-oxygen bonds, which enhance the structural robustness and stability of MOFs.[46] The presence of polar P=O groups also modifies the chemical behavior of the framework.

- **Sulfonic acid-functionalized linkers**

Sulfonic acid (-SO_3H) linkers introduce strong Brønsted acidic sites and electron-rich sulfur centers, contributing to the development of polar frameworks and influencing intermolecular interactions during the structural formation.[47]

- **Hydroxyl-functionalized linkers**

Hydroxyl groups facilitate hydrogen-bonding interactions and contribute to the formation of hydrophilic environments within the framework.[48] They can act as both hydrogen bond donors and acceptors, influencing structural arrangement and stability.[49]

- **Halogen-functionalized linkers**

Halogenated linkers, particularly fluorinated ones, are used to modify the polarity and surface properties of MOFs. The presence of highly electronegative atoms affects intermolecular interactions and framework formation.[50]

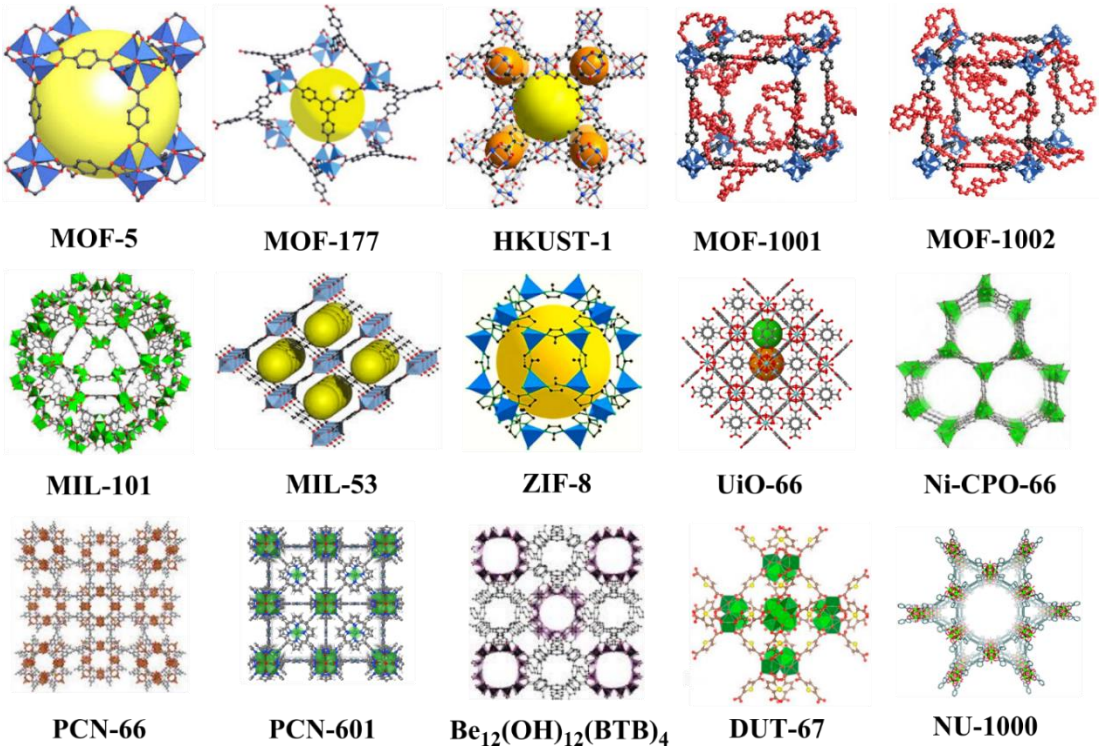


Figure 1.3 The MOFs with various structures, porosity and topology synthesized depending on the kinds of linkers.[32,51–59]

Again, organic linkers play an important role for COFs, as they undergo polymerization through covalent bond-forming reactions to generate highly ordered porous structures. The nature and the type of the linker formed are crucial in determining key properties such as crystallinity, pore structure, stability, and functionality. Variations in linker design, including size, geometry, and functional groups, allow the formation of diverse COF structures with distinct properties.[60] Based on the type of condensation reactions involved, COF linkages, as depicted in Figure 1.4, can be broadly classified as follows:

- **Boronate ester linkers**

These linkers are formed by the condensation of boronic acids with diols. Due to their planar and reversible nature, highly crystalline COFs are typically obtained.[39]

- **Boroxine linkers**

The linkers are generated through the self-condensation of boronic acids, resulting in cyclic planar structures that are commonly used in the formation of 2D COFs.[39]

- **Imine linkers**

Imine linkers are formed via the condensation of amines and aldehydes and are known to provide structural versatility and good crystallinity.[61]

- **Hydrazone linkers**

These linkers are produced from the reaction of aldehydes with hydrazides and are considered to enhance framework stability and rigidity.[62]

- **Azine linkers**

Azine linkers are derived from hydrazine and aldehydes and are generally used in the formation of frameworks with relatively smaller pore sizes.[63]

- **Imide linkers**

These linkers are formed from reactions between amines and anhydrides under increased temperature and are characterized by low reversibility and high structural stability.[64]

- **Olefin (C=C) linkers**

These linkers are obtained via condensation reaction and are known to yield fully π-conjugated structures.[65]

- **1,4-Dioxin linkers**

These linkers are generated through the condensation of fluorinated aromatic compounds and are used in the formation of chemically stable structures.[66]

Thus, organic linkers play a central role in the formation and functionality of both MOFs and COFs. In MOFs, linkers coordinate with metal ions to direct the coordination environment, topology, pore structure, and overall stability of the framework. In contrast, in COFs, linkers are interconnected through covalent bonds where their geometry, length and functional groups govern the formation of specific linkage types and the resulting structural features. In both porous materials, linker design critically influences pore size, topology, and the internal chemical environment, which in turn determines key properties such as adsorption behavior, electronic properties, and catalytic activity. Therefore, rational design and functionalization of linkers remain

fundamental to tailoring MOFs and COFs for applications in gas storage, separation, catalysis, and energy-related fields.

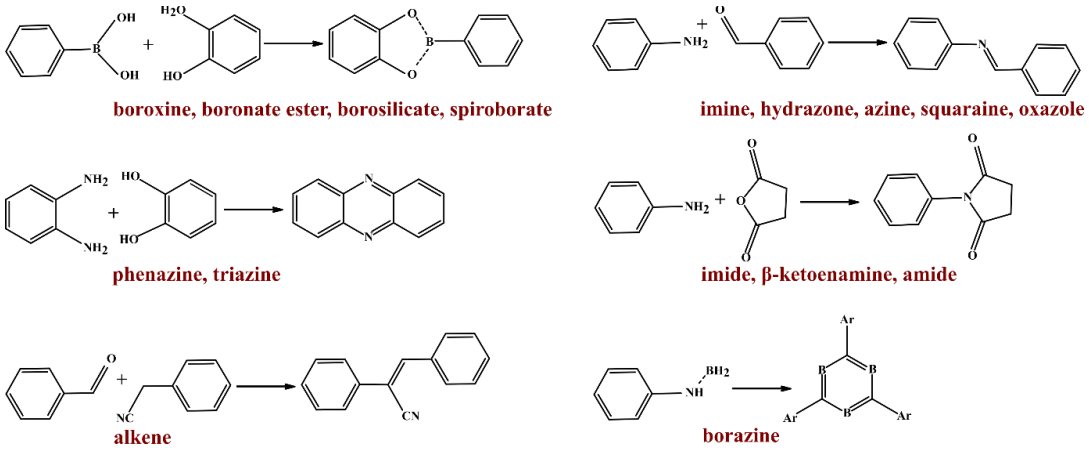


Figure 1.4 Various linkages formed by COFs linkers for the synthesis of COFs.

1.5 Properties of porous materials (COFs and MOFs)

In recent decades, the development of reticular chemistry has enabled the rational design and synthesis of an extraordinary number of porous crystalline materials, including more than 100,000 MOFs and over 570 COFs.[67] Since the pioneering work of Yaghi and his co-workers in introducing COFs in 2005 and earlier breakthroughs in MOFs, these materials have emerged as a versatile class of porous solids with precisely controlled structures. Their periodic and modular structures allow systematic tuning of physiochemical properties, leading to exceptional porosity, ultrahigh surface area, structural diversity, and tunable functionality. These properties of MOFs and COFs, as depicted in Figure 1.5, are discussed below in detail:

- **Crystalline structure**

One of the most distinctive features of both MOFs and COFs is their highly ordered crystalline nature. Unlike many conventional porous materials that are amorphous, these materials possess long-range periodic structures, where building blocks are arranged in a well-defined and repeating manner. The crystalline arrangement facilitates uniform pore distribution and well-defined channels, which are essential for predictable mass transport, adsorption, and catalytic behavior. In MOFs, crystallinity arises from the coordination between metal nodes and organic linkers, forming periodic three-dimensional networks. In COFs, the use of strong covalent bonds leads to highly ordered two-or three-dimensional structures. The ability to obtain crystalline

frameworks with tunable topology and symmetry is a key advantage that distinguishes MOFs and COFs from other porous materials and promotes their performance in gas storage, separation, catalysis, and optoelectronic applications.[68]

- **High porosity**

Permanent porosity is one of the defining properties of both the porous materials, MOFs and COFs. Permanently porous materials retain their rigid framework structure even after the removal of guest molecules from their internal cavities without undergoing collapse. In both MOFs and COFs, the presence of well-defined and periodically arranged pore channels enables efficient accommodation of gases, ions, or small molecules, which is particularly advantageous for energy storage and environmental applications.[69] Compared to conventional porous materials such as zeolites, MOFs, and COFs typically exhibit significantly larger pore volumes and broader pore size tunability, which in turn contributes to enhanced adsorption capacity and diffusion properties.[27]

- **High surface area**

A primary feature distinguishing MOFs and COFs from other porous materials is their exceptionally high BET surface area. These materials commonly exhibit surface areas ranging from 1000 to 10,000 m^2g^{-1}.[70] When gases are introduced into these porous materials, adsorption preferentially occurs at high-affinity surface sites within the pores rather than through intermolecular gas interactions. Consequently, the ultrahigh internal surface area significantly enhances gas uptake capacity, making MOFs and COFs highly promising candidates for CO_2 capture, hydrogen storage, and methane adsorption.

- **Framework stability**

Framework stability in MOFs and COFs can be categorized into chemical, thermal, mechanical, and structural stability. Chemical stability refers to resistance against degradation under acidic, basic, or aqueous conditions. Thermal stability is another critical parameter, with many MOFs and COFs retaining structural integrity up to ~600 ºC. Mechanical stability is defined as resistance to external stress, varies depending on the bonding nature. Structural stability, which describes retention of framework integrity upon guest removal, is essential for maintaining permanent porosity. The inherent rigidity and strong bonding networks in well-defined MOFs and COFs enable

prolonged operation under demanding conditions, making them suitable for industrial applications.[71]

- **Breathing behavior**

A distinctive property observed primarily in MOFs is their dynamic structural flexibility, commonly referred to as "breathing behavior". Certain MOFs can reversibly adjust their pore size and shape in response to external stimuli such as gas adsorption, solvent presence, temperature, or applied pressure. This flexibility enhances guest-host interactions and improves storage efficiency. The breathing phenomenon, combined with large surface area and tunable porosity, renders MOFs particularly attractive for gas storage, sensing and separation applications in sustainable energy technologies.[72] Although COFs are generally more rigid due to strong covalent bonding, recent studies have reported flexible COF systems exhibiting limited structural adaptability.

- **Tunable porous structure**

The modular design principles underlying MOFs and COFs allow precise tuning of structural and intrinsic properties. By modifying secondary building units (SBUs), varying organic linker length, or introducing functional groups through post-synthetic modification, it is possible to tailor pore size, surface chemistry, and electronic properties. Strategies such as metal doping, heteroatom incorporation, and transition-metal intercalation further expand their functional scope. In MOFs, variations of metal nodes (e.g., Zn, Cu, Zr, Fe, Co, etc.) and organic linkers generate immense structural diversity. In COFs, the selection of different linkage chemistries, such as boronate ester, imine, or β-ketoenamine, allows control over stability and conjugation. This tunability enables optimization of adsorption selectivity, catalytic activity, and charge transport properties, making both materials highly adaptable for targeted applications in gas separation, catalysis, and electrochemical energy conversion.[73]



Figure 1.5 Properties of MOFs and COFs.

1.6 Applications of MOFs and COFs

The unique structural and chemical features of MOFs and COFs, such as high porosity, tunable pore environments, and structural versatility, have enabled their application across a wide range of fields. Their ability to selectively interact with guest molecules, combined with tunable functionality, makes them highly attractive for diverse technological and industrial applications. The key applications of these materials are depicted in Figure 1.6 and are as follows:

- **Gas storage and separation**

MOFs and COFs are extensively studied for gas storage and separation due to their high surface area, tunable pore sizes, and structural versatility. They enable efficient adsorption of gases such as H_2, CH_4, CO_2, and N_2 under moderate conditions, offering

advantages over conventional storage techniques.[74] The separation of gas mixtures is governed by factors such as pore size distribution, shape selectivity, and host-guest interactions. However, many gas molecules possess similar kinetic diameters; therefore, enhancing selectivity often requires functionalization of organic linkers or modification of metal nodes. In particular, the presence of open metal sites and polar functional groups significantly improves adsorption affinity toward specific gases.[75] Such tunable interactions make MOFs and COFs highly effective for applications in gas purification, carbon capture, and energy storage.

- **Vapor sorption**

The well-defined porous structures of MOFs and COFs make them highly suitable for vapor sorption applications. Their large surface area and adjustable pore environment enable efficient adsorption of water vapor and various organic vapors. The sorption behavior is strongly influenced by the polarity, pore size, and surface functionality of the framework, allowing selective uptake of specific vapors. This property is particularly important for applications such as humidity control, adsorption-based cooling systems, and solvent recovery. Furthermore, the reversible adsorption-desorption properties of these materials contribute to their long-term usability in cyclic processes.[76]

- **Catalysis**

MOFs and COFs have emerged as versatile platforms for heterogeneous catalysis due to their ordered structures and high density of accessible active sites. Catalytic activity can originate from metal nodes, functional organic linkers, or encapsulated catalytic species within the pores. Their tunable structures allow precise control over reaction environments, facilitating improved activity, selectivity, and stability. These materials have been applied in a wide range of reactions, including oxidation, reduction, and CO_2 conversion into value-added chemicals. Additionally, their porous nature promotes efficient mass transport of reactants and products, enhancing overall catalytic performance.[67]

- **Biomedical applications**

The unique structural features of MOFs and COFs, including high porosity and the ability to encapsulate functional molecules, have led to their exploration in biomedical applications. These materials have been investigated for drug delivery, imaging, and

therapeutic purposes, where controlled release and targeted delivery are crucial. The pore structure enables high drug loading capacity, while surface functionalization improves biocompatibility and stability in physiological environments. Although challenges related to toxicity and long-term stability remain, ongoing research continues to expand their potential in biomedical fields.[77]

- **Sensing**

MOFs and COFs are promising candidates for sensing applications due to their selective adsorption properties and tunable electronic structures. They can detect a variety of gases, vapors, and small molecules through measurable changes in optical, electrical, or luminescent properties. The sensitivity and selectivity of these materials can be enhanced by incorporating specific functional groups or metal centers that interact preferentially with target analytes. This makes them suitable for environmental monitoring, industrial safety, and the detection of hazardous substances.[78]

- **Electronic and ionic conduction**

Certain MOFs and COFs exhibit electronic and ionic conductivity owing to their ordered frameworks and the presence of conjugated pathways or mobile ions. These properties make them attractive for applications in energy storage and conversion devices such as batteries, supercapacitors, and fuel cells. Conductivity can be tuned through structural design, incorporation of conductive guest species, or modification of linkers. Despite their generally lower conductivity compared to traditional materials, ongoing developments are improving their performance for practical applications.[67]

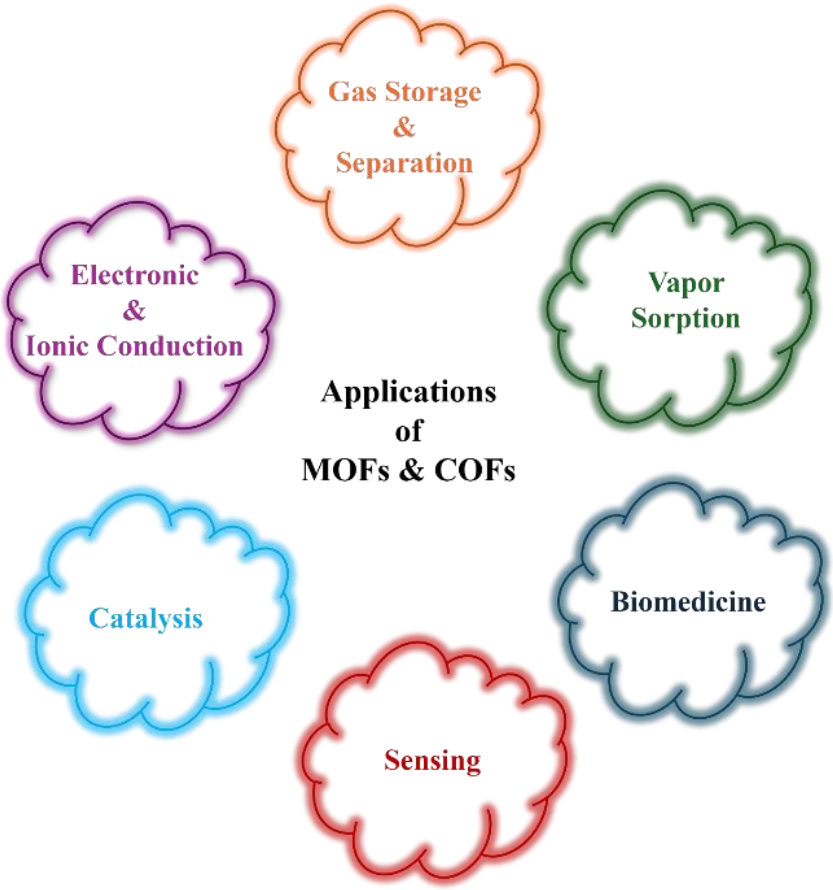


Figure 1.6 Applications of MOFs and COFs.

1.7 Metallopthacyanine (MPc)

Metallophthalocyanine (MPc) based materials have emerged as a prominent class of functional molecular systems due to their unique combination of structural definition, electronic versatility, and broad applicability in catalysis and energy related processes. Structurally, phthalocyanine consists of four isoindole subunits forming a rigid, planar macrocycle with an 18-π electron conjugated system and a central N_4 coordination activity.[79,80] In its metal-free form (H_2Pc), the two inner hydrogen atoms can be replaced by a wide range of metal ions, generating metal phthalocyanines (MPcs).[81] The central N_4 site stabilizes transition metal ions in well-defined coordination environments, making MPcs attractive models of M-N-C active sites. A key advantage of MPcs lies in their high degree of tunability, where both the central metal ion and peripheral substituents can be systematically modified to tailor electronic structure, adsorption strength, and catalytic activity. This molecular-level control makes MPcs particularly suitable for electrochemical applications such as CO_2 reduction reaction (CO_2RR), oxygen reduction reaction (ORR), and hydrogen evolution reaction (HER),

where the nature of the active site critically determines performance. Transition metals such as iron (Fe), cobalt (Co), nickel (Ni), copper (Cu), and zinc (Zn) phthalocyanines have been extensively investigated as CO_2RR electrocatalysts.[82] The catalytic activity strongly depends on the identity of the central metal. For example, CoPc has been shown to exhibit an optimal *CO binding energy at the Co center, enabling high selectivity toward CO formation during CO_2RR.

Beyond discrete molecular catalysts, MPcs have been incorporated into extended crystalline porous structures, including MOFs and COFs. In these materials, MPc units are integrated through well-defined linkages to form ordered porous structures. Compared to isolated MPc modules, MPc-based MOFs and COFs offer several advantages for CO_2RR, such as extended π-conjugation and improved charge transport, high surface area and porosity that enhance CO_2 adsorption and mass transfer, and uniformly distributed, accessible M-N_4 active sites within a rigid structure.[83] The layered stacking of MPc units with strong π-π interactions further facilitates electron delocalization and improves electrochemical performance.[84] As a result, MPc-based MOFs and COFs have emerged as a promising heterogenous electrocatalysts that combine the molecular precision of phthalocyanines with the structural stability and tunability of crystalline porous materials. These features make them particularly attractive platforms for designing efficient and selective CO_2RR catalysts.

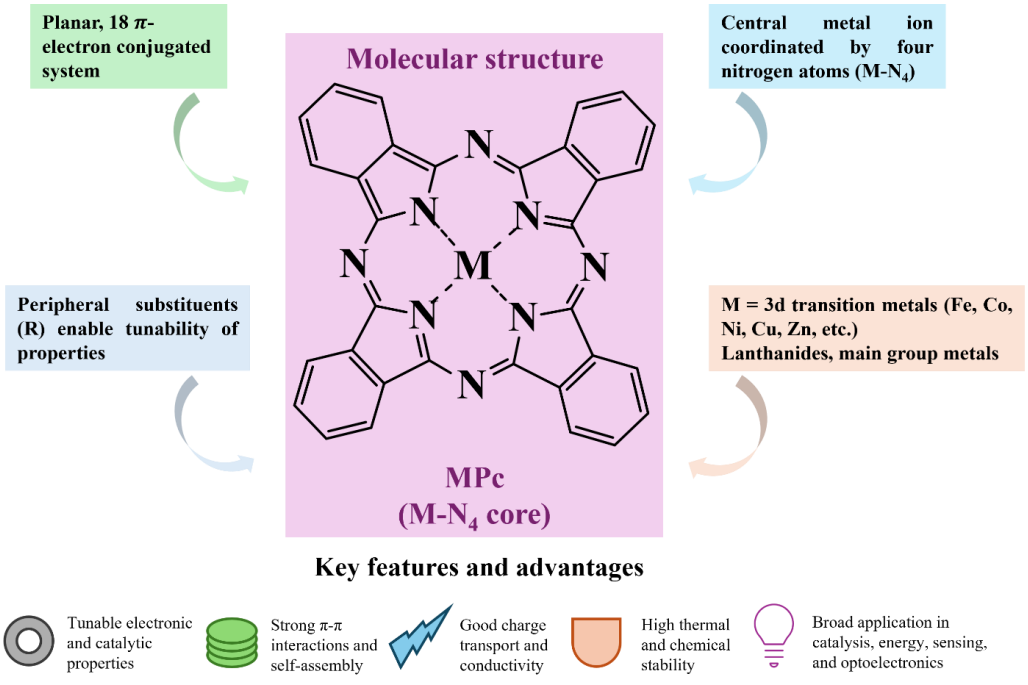


Figure 1.7 The molecular structure, features and advantages of metallophthalocyanine (MPc).

1.8 CO_2RR on MPc-based MOFs and COFs

To rationally design efficient catalysts towards CO_2 reduction, it is crucial to understand the different reaction pathways that yield both the desired and competing products. The CO_2RR mechanism generally comprises three fundamental steps: (i) adsorption of CO_2 molecules onto a catalyst surface; (ii) cleavage of C-O and/or the formation of C-H bonds, which is particularly intricate and involves multielectron transfer pathways yielding different products, and (iii) the rearrangement and desorption of these products. Depending on the transfer of protons (H^+) and electrons (e^-), CO_2 can be reduced into a broad spectrum of products, including formic acid (HCOOH), carbon monoxide (CO), methane (CH_4), methanol (CH_3OH), ethanol (C_2H_5OH), ethylene (C_2H_4), and many others. Most efforts are primarily directed towards converting CO_2 into C_1 products such as CO, CH_3OH, and CH_4. However, these C_1 products have low volumetric energy densities and require high energy consumption. In contrast, C_2 products like ethanol (C_2H_5OH) and ethylene (C_2H_4) are more valuable and in higher demand, making the conversion of CO_2 to C_2 products more attractive. Despite this, converting CO_2 to C_2 products is more complex due to the high energy required for C-C coupling. Thus, owing to the several advantages, we explored a few reaction mechanism pathways for both C_1 and C_2 products, as discussed below:

- **C_1 product**

In general, the electrochemical conversion of CO_2 to C_1 product (here, methane (CH_4)) proceeds through an eight-proton-coupled electron transfer (PCET) mechanism. The reaction begins with the first PCET step, yielding the carboxyl (*COOH) intermediate. This *COOH intermediate can subsequently be reduced to either *HCOOH or *CO, with the latter potentially desorbing to release CO as a product. When CO desorption is unfavorable, additional PCET steps occur, forming intermediates such as *COH and *CHO, which then drive the reaction toward alternative products and pathways. During the CH_4 production pathway, the *CO intermediate first reduces to either a formyl (*CHO) or a *COH intermediate. These intermediates are then protonated to form CH_4. The *CHO intermediate undergoes two protonation steps to produce a methanol (*CH_3OH) intermediate attached to the surface or may undergo desorption to produce a free CH_3OH molecule. Meanwhile, the *COH intermediate can be protonated and dehydrated to form *C, which can be protonated multiple times to yield CH_4. The asterisk (*) indicates that these species are adsorbed on the active site of the catalysts,

and the thin arrow represents the transfer of a pair of electrons and protons, i.e., $H^+ + e^-$ [1]. All other possibilities for CO_2RR to C_2 are depicted in Figure 1.8.

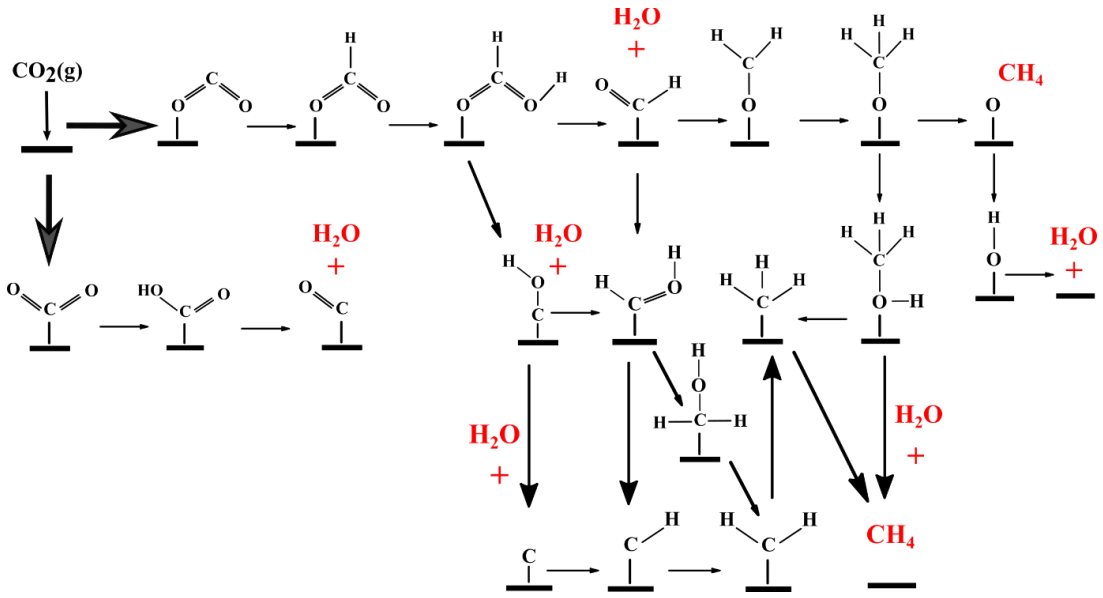


Figure 1.8 Possible pathways for CO_2 reduction into CH_4.

- **C_2 product**

The reaction routes for CO_2 conversion into C_2 products involve 12 PCET steps and 11 distinct hydrogenated carbon-oxygen intermediates. The process begins with the adsorption of two CO_2 molecules on the active site of the catalysts, and upon two protonation steps, the CO_2 molecules get reduced to *2CO intermediates and the desorption of two water molecules. This *2CO intermediate serves as the key intermediate for C_2 formation, and subsequent *CO reduction is essential for diversifying the product distribution. A pivotal stage in this route is C-C coupling, which arises from the interaction between *CO and C_1-derived intermediates such as *COH, and *CHO. The C-C bond is most likely established after *CO is further reduced to either *COH or *CHO. Once one of the adsorbed *CO intermediates transforms into *COH or *CHO, two possible pathways enable C-C bond formation: the *COH intermediate undergoes an additional proton-electron transfer, generating *C and *CO intermediates that remain coordinated to the active center and interact with a water molecule (H_2O). This *C and *CO intermediate couple to form *CCO intermediate, and the subsequent H^+/e^- additions proceed to preserve the C-C double bond. The other possibility is that *CHO is further reduced to *CH after the transfer of two H^+/e^- pairs and then coupled with *CO to produce *CHCO, which on further

reduction produces the C_2 products. The subsequent step involves protonation of the surface-bound carbon atom in *CHCO, followed by an additional protonation at the same carbon site to generate CH_2CO, which is then further reduced to *CH_2CHO. The next proton-electron transfer is a critical stage, as it directs the pathway toward the formation of C_2H_4 and C_2H_5OH. An alternative route to C_2H_4 proceeds via protonation of the carbon atom bound to oxygen, producing transient *OCHCH and *$OCHCH_2$ intermediates. In this case, the C-O bond undergoes rapid cleavage, releasing C_2H_4 and leaving behind an adsorbed *O species. This *O intermediate is subsequently hydrogenated to *OH and finally converted to H_2O. All other possibilities for CO_2RR to C_2 are depicted in Figure 1.9.

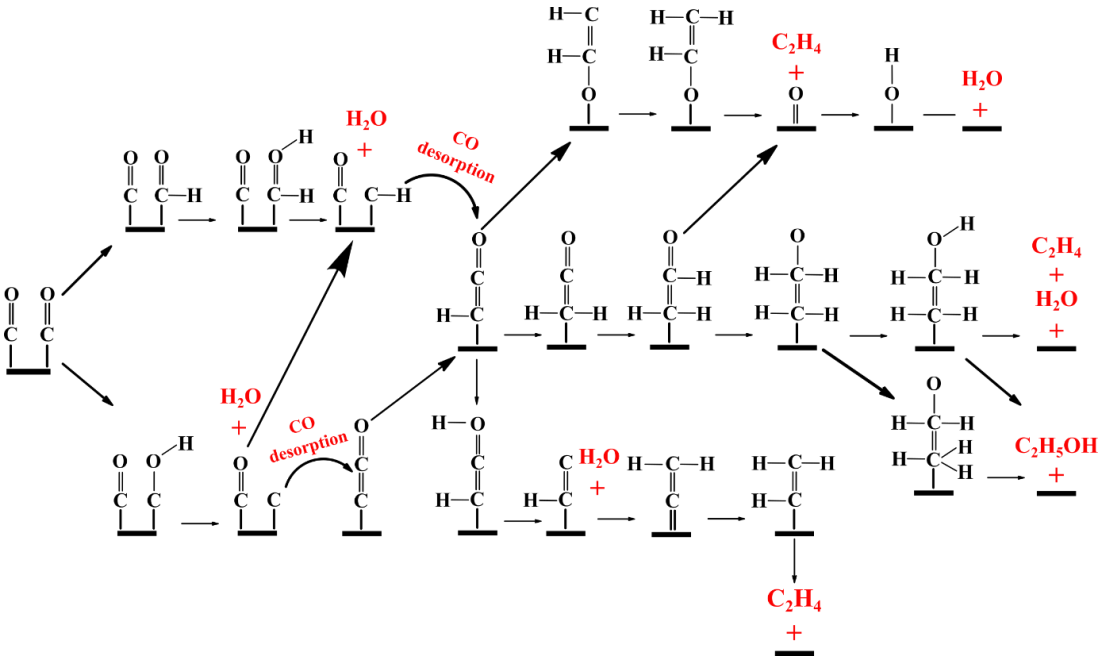


Figure 1.9 Possible pathways for CO_2 reduction into C_2H_4 and C_2H_5OH.

1.9 Research gap and motivation

The rapid increase in atmospheric CO_2 has driven the search for advanced porous materials which can both capture and convert the CO_2 efficiently. Among these, COFs and MOFs have gained considerable attention owing to their tunable pores and flexible structures. From a CO_2 adsorption perspective, most studies on CO_2 capture in MOFs have focused on surface area and metal-node interactions; the role of organic linkers in modulating CO_2 adsorption remains comparatively unexplored. Beyond capture, the catalytic reduction of CO_2 using these porous frameworks introduces additional

complexities. MPcs are well-defined molecular catalysts for CO_2 electroreduction due to their redox-active metal centers and tunable electronic structures. However, when incorporated into extended COF or MOF structures, the catalytic behavior changes. A critical research gap lies in correlating the CO_2 adsorption energetics with catalytic activation pathways. An efficient CO_2 reduction requires an optimal balance, i.e., CO_2 must bind strongly enough to be activated but not so strongly that products cannot be desorbed. A systematic computational study linking adsorption energy, charge transfer, and intermediate stabilization within MPc-based frameworks remains limited. The effect of the linker and different metal centers on reaction energetics and product selectivity within periodic frameworks also remains unexplored.

The main objective of the present thesis is to theoretically design and investigate novel porous COFs and MOFs for CO_2 capture and their catalytic conversion. The work aims to provide fundamental insights into the adsorption behavior of MOF linkers, electronic, structural, and catalytic properties of the designed frameworks for CCUS applications.

The specific objectives of the present thesis are:

- To investigate the role of organic bridging linkers of MOFs toward CO_2 adsorption and to investigate the effect of Lithium (Li) decoration on the binding enthalpy.
- To examine the electrocatalytic activity of sulfur-linked MPc-based COFs for CO_2 reduction to C_1 products.
- To examine the electrocatalytic activity of copper-containing MPc-based MOF for CO_2 reduction to C_1 and C_2 products.

Toward these objectives, this thesis offers new theoretical and computational design principles for CO_2 adsorption on linkers that can be integrated to form novel MOFs and evaluates the structural stability, adsorption energies, and catalytic reaction pathways of MPc-based COFs/MOFs towards CO_2RR. By integrating adsorption studies with catalytic reduction analysis, this work provides the fundamental understanding required for the design of next-generation porous materials for sustainable CCUS technologies.

1.10 Contribution from the present thesis

The following contributions addressing the rational design of COFs and MOFs for CO_2 adsorption and sustainable electroreduction have been made towards the preparation of this thesis:

- **CO_2 adsorption on MOF linkers**

This work provides a detailed non-periodic investigation of CO_2 adsorption on various functionalized MOF linkers using the first-principles density functional theory (DFT) and second-order Møller-Plesset (MP2) methods. Here, Li decoration is demonstrated as an effective strategy to significantly enhance the CO_2 binding strength while maintaining the reversible adsorption. By evaluating the change in binding enthalpy (ΔH), energy decomposition analysis (EDA), and frontier molecular orbitals (FMO), the study elucidates the dominant role of electrostatic and polarization interactions in governing the physisorption behavior, thereby offering rational design principles for developing novel MOFs with improved carbon capture performance.

- **CO_2 reduction to C_1 products on sulfur-based MPc COFs**

This work provides an understanding of CO_2 electroreduction in MPc-based COFs by systematically investigating the CoPc frameworks with sulfur-containing linkages using periodic DFT calculations. Through the detailed investigation of equilibrium geometries, electronic properties, i.e., band structure and density of states, and Gibbs free energy profile, the study establishes a relation between framework design and catalytic selectivity towards methane (CH_4), thereby contributing to the rational design of efficient CO_2 reduction electrocatalysts.

- **CO_2 reduction to C_1 and C_2 products on copper-based MPc MOF**

This work further extends the catalytic investigation to a CuPc-Cu-O MOF system, demonstrating its potential for CO_2 reduction toward both C_1 and C_2 products. Using hybrid period DFT calculations, the structural, electronic, and reaction energetics of the MOF were evaluated, revealing its semiconductor nature and favorable CO_2RR towards ethanol (C_2H_5OH) formation. The study provides a mechanistic insight into multi-carbon product formation and highlights the role of MPc-based MOF designing in enhancing catalytic efficiency and selectivity, thereby contributing to the development of next-generation electrocatalysts for sustainable energy conversion.

Overall, this thesis contributes to the rational design of porous materials for CCUS by bridging adsorption studies with catalytic conversion mechanisms, thereby advancing theoretical and computational understanding of COFs and MOFs as multifunctional materials for sustainable energy applications.

1.11 Organization of the thesis

- **Chapter 2** describes the theory and methodology used in the present thesis, highlighting the fundamental principles of quantum physics and the applications of computational quantum chemistry. It presents the theoretical background and computational methods used to investigate the CO_2 adsorption and catalytic reduction in porous COFs and MOFs.

- **Chapter 3** focuses on the non-periodic investigation of CO_2 adsorption on functionalized MOF linkers, including Li-decorated complexes using DFT and MP2 methods. It elucidates the adsorption energetics and interaction mechanisms for improved carbon capture design.
- **Chapter 4** investigates the electrochemical reduction of CO_2 to C_1 products using MPc-based COFs with sulfur-containing linkages through periodic DFT calculations. The study evaluates the structural and electronic properties, along with the reaction energetics, to elucidate the influence of linker engineering on catalytic selectivity and performance.
- **Chapter 5** explores the performance of a CuPc-Cu-O MOF towards electrochemical CO_2 reduction through periodic DFT calculations, focusing on its structural, electronic and catalytic properties for C_1 and C_2 products. The study evaluates the reaction energetics to elucidate the mechanism governing selectivity toward methane (CH_4), ethylene (C_2H_4), and ethanol (C_2H_5OH) production.

- **Chapter 6** summarizes the major findings and conclusions of the present thesis, highlighting the role of linker functionalization, metal active centers, and electronic structure in governing CO_2 adsorption and electrochemical reduction in MOF- and COF-based materials. It also outlines future research perspectives, including experimental validation, advanced linker engineering, multiscale computational simulations, exploration of alternative metal centers for selective

C_{2+} product formation, and the development of porous materials for carbon capture and direct air capture (DAC) applications.

1.12 References

[1] N. F. Attia, M. Jung, J. Park, H. Jang, K. Lee, H. Oh, Flexible nanoporous activated carbon cloth for achieving high H_2, CH_4, and CO_2 storage capacities and selective CO_2/CH_4 separation, Chem. Eng. J. 379 (2020) 122367.

[2] J. H. Park, J. Yang, D. Kim, H. Gim, W. Y. Choi, J. W. Lee, Review of recent technologies for transforming carbon dioxide to carbon materials, Chem. Eng. J. 427 (2022) 130980.

[3] https://www.downtoearth.org.in/climate-change/carbon-dioxide-emissions-to-hit-4296-ppm-in-may-2025-highest-in-over-2-million-years.

[4] https://www.ipcc-data.org/observ/ddc_co2.html

[5] M. Ding, R. W. Flaig, H. L. Jiang, O. M. Yaghi, Carbon capture and conversion using metal-organic frameworks and MOF-based materials, Chem. Soc. Rev. 48 (2019) 2783-2828.

[6] L. Zhang, Z. J. Zhao, J. Gong, Nanostructured materials for heterogeneous electrocatalytic CO_2 reduction and their related reaction mechanisms, Angew. Chem. Int. Ed. 56 (2017) 11326-11353.

[7] S. Chen, J. Liu, Q. Zhang, F. Teng, B. C. McLellan, A critical review on deployment planning and risk analysis of carbon capture, utilization, and storage (CCUS) toward carbon neutrality, Renew. Sustain. Energy Rev. 167 (2022) 112537.

[8] L. Rosa, M. Mazzotti, Potential for hydrogen production from sustainable biomass with carbon capture and storage, Renew. Sustain. Energy Rev. 157 (2022) 112123.

[9] B. Liu, X. Zheng, Q. Zhang, X. Pan, B. Mclellan, Drivers of global metal footprint during 1995-2013, J. Clean. Prod. 256 (2020) 120467.

[10] X. Wang, H. Liu, J. Zhang, S. Chen, Covalent organic frameworks (COFs): A promising CO_2 capture candidate material, Polym. Chem. 14 (2023) 1293-1317.

[11] E. Hanson, C. Nwakile, V. O. Hammed, Carbon capture, utilization, and storage (CCUS) technologies: Evaluating the effectiveness of advanced CCUS solutions for reducing CO_2 emissions, Results in Surfaces and Interfaces 18 (2025) 100381.

[12] S. Kitagawa, Future porous materials, Acc. Chem. Res. 50 (2017) 514-516.

[13] J. Yu, A. Corma, Y. Li, Functional porous materials chemistry, Adv. Mater. 32 (2020) 2006277.

[14] Z. Chen, K. O. Kirlikovali, K. B. Idrees, M. C. Wasson, O. K. Farha, Porous materials for hydrogen storage, Chem 8 (2022) 693716.

[15] J. Y. S. Lin, Molecular sieves for gas separation, Science 353 (2016) 121-122.

[16] H. Richter, H. Voss, N. Kaltenborn, S. Kämnitz, A. Wollbrink, A. Feldhoff, J. Caro, S. Roitsch, I. Voigt, High-flux carbon molecular sieve membranes for gas separation, Angew. Chem. Int. Ed. 56 (2017) 7760-7763.

[17] C. Toro, J. M. Buriak, The "holey" grail: Zeolites and molecular sieves, Chem. Mater. 30 (2018) 5519-5520.

[18] X. Song, L. Wang, X. Ma, Y. Zeng, Adsorption equilibrium and thermodynamics of CO_2 and CH_4 on carbon molecular sieves, Appl. Surf. Sci. 396 (2017) 870-878.

[19] Y. Park, D. K. Moon, D. Park, M. Mofarahi, C. H. Lee, Adsorption equilibria and kinetics of CO_2, CO, and N_2 on carbon molecular sieve, Sep. Purif. Technol. 212 (2019) 952-964.

[20] Y. Yamane, M. T. Miyahara, H. Tanaka, High-performance carbon molecular sieves for the separation of propylene and propane, ACS Appl. Mater. Interfaces 14 (2022) 17878-17888.

[21] A. M. Alotaibi, An overview of zeolites: From historical background to diverse applications, Molecules 30 (2025) 4036.

[22] J. Jiang, J. Yu, A. Corma, Extra-large-pore zeolites: Bridging the gap between micro and mesoporous structures, Angew. Chem. Int. Ed. 49 (2010) 3120-3145.

[23] W. Fan, M. Dong, Regulation of zeolite particle morphology, Science 375 (2022) 29.

[24] L. H. Chen, M. H. Sun, Z. Wang, W. Yang, Z. Xie, B. L. Su, Hierarchically structured zeolites: From design to application, Chem. Rev. 120 (2020) 11194-11294.

[25] X. Li, J. E. Remias, J. K. Neathery, K. Liu, NF/RO faujasite zeolite membrane-ammonia absorption solvent hybrid system for potential post-combustion CO_2 capture application, J. Memb. Sci. 366 (2011) 220-228.

[26] J. Wang, Y. Wang, H. Hu, Q. Yang, J. Cai, From metal-organic frameworks to porous carbon materials: Recent progress and prospects from energy and environmental perspectives, Nanoscale 12 (2020) 4238-4268.

[27] Y. Song, S. Ma, Pore engineering in metal-organic frameworks and covalent organic frameworks: strategies and applications, Chem. Sci. 16 (2025) 11740-11767.

[28] N. Stock, S. Biswas, Synthesis of metal-organic frameworks (MOFs): Routes to various MOF topologies, morphologies and composites, Chem. Rev. 112 (2012) 933-969.

[29] H. Li, M. Eddaoudi, M. O'Keeffe, O. M. Yaghi, Design and synthesis of an exceptionally stable and highly porous metal-organic framework, Nature 402 (1999) 276-279.

[30] G. Férey, Hybrid porous solids: Past, present, future, Chem. Soc. Rev. 37 (2008) 191-214.

[31] H. Furukawa, K. E. Cordova, M. O'Keeffe, O. M. Yaghi, The chemistry and applications of metal-organic frameworks, Science 341 (2013) 1230444.

[32] O. M. Yaghi, G. Li, Mutually interpenetrating sheets and channels in the extended structure of [Cu(4,4′-bpy)Cl], Angew. Chem. Int. Ed. Engl. 34 (1995) 207-209.

[33] O. M. Yaghi, H. Li, Hydrothermal synthesis of a metal-organic framework containing large rectangular channels, J. Am. Chem. Soc. 117 (1995) 10401-10402.

[34] C. Pettinari, F. Marchetti, N. Mosca, G. Tosi, A. Drozdov, Application of metal-organic frameworks, Polym. Int. 66 (2017) 731-744.

[35] O. M. Yaghi, M. O'Keeffe, N. W. Ockwig, H. K. Chae, M. Eddaoudi, J. Kim, Reticular synthesis and the design of new materials, Nature 423 (2003) 705-714.

[36] X. Zhang, M. Yan, P. Chen, J. Li, Y. Li, H. Li, X. Liu, Z. Chen, H. Yang, S. Wang, J. Wang, Z. Tang, Q. Huang, J. Lei, T. Hayat, Z. Liu, L. Mao, T. Duan, X. Wang, Emerging MOFs, COFs, and their derivatives for energy and environmental applications, Innov. 6 (2025) 100778.

[37] M. Usman, N. Iqbal, T. Noor, N. Zaman, A. Asghar, M. M. Abdelnaby, A. Galadima, A. Helal, Advanced strategies in metal-organic frameworks for CO_2 capture and separation, Chem. Rec. 22 (2022) e202100230.

[38] H. L. Nguyen, Reticular design and crystal structure determination of covalent organic frameworks, Chem. Sci. 12 (2021) 8632-8647.

[39] A. P. Côté, A. I. Benin, N. W. Ockwig, M. O'Keeffe, A. J. Matzger, O. M. Yaghi, Porous, crystalline, covalent organic frameworks, Science 310 (2005) 1166-1170.

[40] S. Y. Ding, W. Wang, Covalent organic frameworks (COFs): From design to applications, Chem. Soc. Rev. 42 (2013) 548-568.

[41] P. Singh, P. N. Dave, Advancements in covalent organic framework-based nanocomposites: Pioneering materials for CO_2 reduction and storage, Greenhouse. Gas. Sci. Technol. 14 (2024) 914-938.

[42] X. Feng, X. Ding, D. Jiang, Covalent organic frameworks, Chem. Soc. Rev. 41 (2012) 6010-6022.

[43] Z. C. Kampouraki, D. A. Giannakoudakis, V. Nair, A. H. Bandegharaei, J. C. Colmenares, E. A. Deliyanni, Metal organic frameworks as desulfurization adsorbents of DBT and 4,6-DMDBT from Fuels, Molecules 24 (2019) 4525.

[44] M. Kim, H. S. Lee, D. H. Seo, S. J. Cho, E. C. Jeon, H. R. Moon, Melt-quenched carboxylate metal-organic framework glasses, Nat. Commun. 15 (2024) 1174.

[45] A. V. Desai, S. Sharma, S. Let, S. K. Ghosh, N-donor linker based metal-organic

frameworks (MOFs): Advancement and prospects as functional materials, Coord. Chem. Rev. 395 (2019) 146-192.

[46] S. Ondrušová, M. Kloda, J. Rohlíček, M. Taddei, J. K. Zaręba, J. Demel, Exploring the isoreticular continuum between phosphonate- and phosphinate-based metal-organic frameworks, Inorg. Chem. 61 (2022) 18990-18997.

[47] S. A. A Razavi, A. Morsali, Linker functionalized metal-organic frameworks, Coord. Chem. Rev. 399 (2019) 213023.

[48] J. Liu, J. Peng, G. Chen, F. Lai, L. Dong, H. Ji, K. Chai, Hydroxyl-functionalized linker endows an ultra-microporous aluminum based metal-organic framework with electronegative site for enhancing ethane/ethylene separation, Sep. Purif. Technol. 351 (2024) 128116.

[49] M. Sadakiyo, T. Yamada, H. Kitagawa, Hydroxyl group recognition by hydrogen-bonding donor and acceptor sites embedded in a layered metal-organic framework, J. Am. Chem. Soc. 133 (2011) 11050-11053.

[50] D. S. Zhang, Z. Chang, Y. F. Li, Z. Y. Jiang, Z. H. Xuan, Y. H. Zhang, J. R. Li, Q. Chen, T. L. Hu, X. H. Bu, Fluorous metal-organic frameworks with enhanced stability and high H_2/CO_2 storage capacities, Sci. Rep. 3 (2013) 3312.

[51] Y. L. Zhao, L. Liu, W. Zhang, C. H. Sue, Q. Li, O. S. Miljanić, O. M. Yaghi, J. F. Stoddart, Rigid-strut-containing crown ethers and [2]catenanes for incorporation into metal-organic frameworks, Chem. Eur. J. 15 (2009) 13356-13380.

[52] H. Furukawa, M. A. Miller, O. M. Yaghi, Independent verification of the saturation hydrogen uptake in MOF-177 and establishment of a benchmark for hydrogen adsorption in metal-organic frameworks, J. Mater. Chem. 17 (2007) 3197-3204.

[53] C. H. Hendon, A. Walsh, Chemical principles underpinning the performance of the metal-organic framework HKUST-1, Chem. Sci. 6 (2015) 3674-3683.

[54] M. Y. Zorainy, M. G. Alalm, S. Kaliaguine, D. C. Boffito, Revisiting the MIL-101 metal-organic framework: design, synthesis, modifications, advances, and recent applications, J. Mater. Chem. A 9 (2021) 22159-22217.

[55] S. Tomar, V. K. Singh, Review on synthesis and application of MIL-53, Mater. Today Proc. 43 (2021) 3291-3296.

[56] K.S. Park, Z. Ni, A.P. Côté, J.Y. Choi, R. Huang, F.J. Uribe-Romo, H.K. Chae, M. O'Keeffe, O.M. Yaghi, Exceptional chemical and thermal stability of zeolitic imidazolate frameworks, Proc. Natl. Acad. Sci. U.S.A. 103 (2006) 10186-10191.

[57] F. Drache, V. Bon, I. Senkovska, C. Marschelke, A. Synytska, S. Kaskel, Postsynthetic inner-surface functionalization of the highly stable zirconium-based metal-organic framework DUT-67, Inorg. Chem. 55 (2016) 7206-7213.

[58] K. Wang, X. L. Lv, D. Feng, J. Li, S. Chen, J. Sun, L. Song, Y. Xie, J. R. Li, H. C. Zhou, Pyrazolate-based porphyrinic metal-organic framework with extraordinary base-resistance, J. Am. Chem. Soc. 138 (2016) 914-919.

[59] T. C. Wang, N. A. Vermeulen, I. S. Kim, A. B. F. Martinson, J. F. Stoddart, J. T. Hupp, O. K. Farha, Scalable synthesis and post-modification of a mesoporous metal-organic framework called NU-1000, Nat. Protoc. 11 (2016) 149-162.

[60] K. Geng, T. He, R. Liu, S. Dalapati, K. T. Tan, Z. Li, S. Tao, Y. Gong, Q. Jiang, D. Jiang, Covalent organic frameworks: Design, synthesis, and functions, Chem. Rev. 120 (2020) 8814-8933.

[61] F. J. U. Romo, J. R. Hunt, H. Furukawa, C. Klöck, M. O'Keeffe, O. M. Yaghi, A crystalline imine-linked 3-D porous covalent organic framework, J. Am. Chem. Soc. 131 (2009) 4570-4571.

[62] F. J. U. Romo, C. J. Doonan, H. Furukawa, K. Oisaki, O. M. Yaghi, Crystalline covalent organic frameworks with hydrazone linkages, J. Am. Chem. Soc. 133 (2011) 11478-11481.

[63] S. Manzoor, M. A. Younis, Y. Yao, Q. Tariq, N. Sultana, X. Ling, C. Qiu, Azine-linked covalent organic frameworks: recent developments in synthesis and functional applications, Chem. Commun. 62 (2026) 2020-2036.

[64] Q. Fang, Z. Zhuang, S. Gu, R. B. Kaspar, J. Zheng, J. Wang, S. Qiu, Y. Yan, Designed synthesis of large-pore crystalline polyimide covalent organic frameworks, Nat. Commun. 5 (2014) 4503.

[65] T. Wang, Y. Zhang, Z. Wang, Y. Chen, P. Cheng, Z. Zhang, Olefin-linked

covalent organic frameworks: synthesis and applications, Dalton Trans. 52 (2023) 15178-15192.

[66] B. Zhang, M. Wei, H. Mao, X. Pei, S. A. Alshmimri, J. A. Reimer, O. M. Yaghi, Crystalline dioxin-linked covalent organic frameworks from irreversible reactions, J. Am. Chem. Soc. 140 (2018) 12715-12719.

[67] R. Freund, O. Zaremba, G. Arnauts, R. Ameloot, G. Skorupskii, M. Dincă, A. Bavykina, J. Gascon, A. Ejsmont, J. Goscianska, M. Kalmutzki, U. Lächelt, E. Ploetz, C. S. Diercks, S. Wuttke, The current status of MOF and COF applications, Angew. Chem. Int. Ed. 60 (2021) 23975-24001.

[68] R. Nakatani, T. Irie, S. Das, Q. Fang, Y. Negishi, Converging the complementary traits of metal-organic frameworks and covalent organic frameworks, ACS Appl. Mater. Interfaces 17 (2025) 24701-24729.

[69] K. Endo, S. Canossa, F. Heck, D. M. Proserpio, M. S. Istek, F. Stemmler, J. V. Slageren, S. Hartmann, A. Hartschuh, B. V. Lotsch, Crystalline porous frameworks based on double extension of metal-organic and covalent organic linkages, Nat. Synth. 4 (2025) 603-613.

[70] O. K. Farha, I. Eryazici, N. C. Jeong, B. G. Hauser, C. E. Wilmer, A. A. Sarjeant, R. Q. Snurr, S. T. Nguyen, A. Ö. Yazaydın, J. T. Hupp, Metal-organic framework materials with ultrahigh surface areas: Is the sky the limit?, J. Am. Chem. Soc. 134 (2012) 15016-15021.

[71] I. J. Kang, N. A. Khan, E. Haque, S. H. Jhung, Chemical and thermal stability of isotypic metal-organic frameworks: Effect of metal ions, Chem. Eur. J. 17 (2011) 6437-6442.

[72] M. Alhamami, H. Doan, C. H. Cheng, A review on breathing behaviors of metal-organic frameworks (MOFs) for gas adsorption, Materials 7 (2014) 3198-3250.

[73] Q. G. Zhai, X. Bu, C. Mao, X. Zhao, L. Daemen, Y. Cheng, A. J. R. Cuesta, P. Feng, An ultra-tunable platform for molecular engineering of high-performance crystalline porous materials, Nat. Commun. 7 (2016) 13645.

[74] C. Jiang, X. Wang, Y. Ouyang, K. Lu, W. Jiang, H. Xu, X. Wei, Z. Wang, F. Dai, D. Sun, Recent advances in metal-organic frameworks for gas

adsorption/separation, Nanoscale Adv. 4 (2022) 2077-2089.

[75] Ü. K. Demir, A. Goldman, L. Esrafili, M. Gharib, A. Morsali, O. Weingart, C. Janiak, Coordinatively unsaturated metal sites (open metal sites) in metal–organic frameworks: design and applications, Chem. Soc. Rev. 49 (2020) 2751-2798.

[76] H. Furukawa, F. Gándara, Y. B. Zhang, J. Jiang, W. L. Queen, M. R. Hudson, O. M. Yaghi, Water adsorption in porous metal-organic frameworks and related materials, J. Am. Chem. Soc. 136 (2014) 4369-4381.

[77] M. H. Nematollahi, E. Mostafavi, S. Iravani, Covalent organic frameworks and metal-organic frameworks against pathogenic viruses and antibiotic-resistant bacteria: Diagnostic and therapeutic applications, J. Environ. Chem. Eng. 11 (2023) 109652.

[78] Y. Zhao, Emerging applications of metal-organic frameworks and covalent organic frameworks, Chem. Mater. 28 (2016) 8079-8081.

[79] W. Fan, Z. Duan, W. Liu, R. Mehmood, J. Qu, Y. Cao, X. Guo, J. Zhong, F. Zhang, Rational design of heterogenized molecular phthalocyanine hybrid single-atom electrocatalyst towards two-electron oxygen reduction, Nat. Commun. 14 (2023) 1426.

[80] O. A. Melville, B. H. Lessard, T. P. Bender, Phthalocyanine-based organic thin-film transistors: A review of recent advances, ACS Appl. Mater. Interfaces 7 (2015) 13105-13118.

[81] S. Yang, Y. Yu, X. Gao, Z. Zhang, F. Wang, Recent advances in electrocatalysis with phthalocyanines, Chem. Soc. Rev. 50 (2021) 12985-13011.

[82] J. H. Zagal, S. Griveau, J. F. Silva, T. Nyokong, F. Bedioui, Metallophthalocyanine-based molecular materials as catalysts for electrochemical reactions, Coord. Chem. Rev. 254 (2010) 2755-2791.

[83] Z. Li, Z. Zhou, M. Sun, T. Wu, Q. Lu, L. Lu, B. Chen, C. H. Chan, H. H. Wong, B. Huang, A mechanism review of metal phthalocyanines as single-atomic catalysts in electrochemical energy conversion, Chem. Sci. 16 (2025) 14019-14037.

[84] X. Wang, S. Sun, J. Yao, H. Wan, R. Ma, W. Ma, Two-dimensional metallophthalocyanine nanomaterials for electrocatalytic energy conversion, Energy Environ. Mater. 7 (2024) e12709.

Chapter 2

Theoretical Background and Computational Approaches

This chapter presents the theoretical background and computational methodologies employed in the studies. The chapter begins with the fundamental principles of quantum mechanics (QM) and theoretical chemistry, focusing on the formulation and solutions of the many-body Schrödinger equation. It introduces key electronic-structure methods, including the Hartree and Hartree-Fock approximations, post-Hartree-Fock approaches, and DFT methods, with an emphasis on the Hohenberg-Kohn theorems and the Kohn-Sham formalism. The role of exchange-correlation functionals, including modern and widely used formulations, has been discussed in the context of accurately describing electronic interactions. The chapter further explains the importance of basis sets in both ab initio and DFT calculations, mainly for periodic and extended systems. Computational models and descriptors related to catalytic systems, such as cluster and slab models, are also outlined here. Finally, the software packages and numerical techniques used to perform electronic structure calculations, geometry optimizations, and property calculations have been described, providing a theoretical foundation for the results presented in the subsequent chapters.

2.1 Fundamentals of quantum mechanics and electronic structure theory

Quantum mechanics (QM) provides the fundamental foundation for understanding the behavior of electrons in atoms, molecules, and solids. The pioneering work of Schrödinger and Heisenberg in the early twentieth century established the principles required to describe electronic motion at the atomic scale. In QM, condensed matter physics and materials science, the properties of a system are obtained by solving the time-independent Schrödinger equation, which governs the behavior of interacting electrons and nuclei.

For a system containing multiple electrons, the Schrödinger equation includes terms corresponding to the kinetic energy of electrons, electron-nucleus interactions, and electron-electron repulsions. The interactions between electrons make the many-body Schrödinger equation too difficult to solve computationally, except for very simple systems. To simplify this problem, the Born-Oppenheimer (BO) approximation is

commonly employed, in which the nuclear and electronic motions are separated due to their large mass difference. This approximation allows the electronic structure to be solved for fixed nuclear positions, forming the basis of most quantum mechanical calculations.[1]

Despite this simplification, solving the electronic Schrödinger equation for many-electron systems remains challenging due to the exponential increase in computational complexity with system size. Consequently, a variety of approximate electronic structure methods have been developed to obtain reliable solutions with manageable computational cost. These methods form the foundation of modern electronic structure theory and are discussed in the following sections, beginning with the Hartree and Hartree-Fock approaches and progressing toward density-based formulations such as DFT methods.

2.1.1 Many-body Schrödinger equation

The Schrödinger equation constitutes the fundamental basis of QM and forms the foundation of theoretical chemistry, basic solid state physics, and materials science. It provides a complete quantum mechanical description of the behavior of electrons and nuclei in atomic, molecular, and solid-state systems. The state of a quantum system is described by a wave function, denoted by Ψ, which contains all the information required to determine the physical properties of the system. For stationary states, the time-independent Schrödinger equation is expressed as:

$$\hat{H}\Psi(r,R) = E\Psi(r,R) \quad \ldots(2.1)$$

where $\hat{H}$ represents the total Hamiltonian operator of the system, $\Psi(r,R)$ denotes the many body wavefunction, and E is the corresponding energy eigenvalue. Here,

$$r = \left(r_1, r_2, \ldots\ldots, r_{N_e}\right) \quad \ldots(2.2)$$

represents the collective spatial coordinates of all electrons, while

$$r = \left(R_1, R_2, \ldots\ldots, R_{N_n}\right) \quad \ldots(2.3)$$

denotes the collective spatial coordinates of all nuclei, where N_e and N_n represent the total numbers of electrons and nuclei, respectively. The Hamiltonian operator includes

the kinetic energies of electrons and nuclei along with the electron-electron, electron-nucleus, and nucleus-nucleus Coulomb interactions.

For a molecular system containing N electrons and M nuclei, the total Hamiltonian includes the kinetic energy of electrons and nuclei, as well as the Coulomb interactions among all charged particles. The kinetic energy operator is given by:

$$\hat{T} = -\sum_{i=1}^{N} \frac{\hbar^2}{2m_e} \nabla_i^2 - \sum_{I=1}^{M} \frac{\hbar^2}{2m_I} \nabla_I^2 \quad \ldots (2.4)$$

where m_e and m_I denote the masses of the electron and the I^{th} nucleus, respectively, and ∇_i^2 and ∇_I^2 are the Laplacian operators acting on the electronic and nuclear coordinates.

The potential energy term arises from Coulomb interactions between electron-electron, nucleus-nucleus, and electron-nucleus pairs and can be written as:

$$\hat{V} = \frac{e^2}{4\pi\varepsilon_0} \sum_{i=1}^{N-1} \sum_{j=i+1}^{N} \frac{1}{|r_i - r_j|} + \frac{e^2}{4\pi\varepsilon_0} \sum_{I=1}^{M-1} \sum_{J=I+1}^{M} \frac{Z_I Z_J}{|R_I - R_J|} - \frac{e^2}{4\pi\varepsilon_0} \sum_{i=1}^{N} \sum_{I=1}^{M} \frac{Z_I}{|r_i - R_I|} \ldots (2.5)$$

where N and M represent the total numbers of electrons and nuclei, respectively. The indices i, j refer to electrons, whereas I, J refer to nuclei. The position vectors r_i, r_j represent the positions of the i^{th} and j^{th} electrons, respectively, while R_I, R_J denote the positions of the I^{th} and J^{th} nuclei, respectively. Here, Z_I and Z_J represent the atomic numbers of the corresponding nuclei, e denote the elementary charge, and ε_0 is the permittivity of free space. The first and second terms describe the electron-electron and nucleus-nucleus repulsive interactions, respectively, whereas the third term represents the attractive interactions between electrons and nuclei.

Combining the kinetic and potential energy terms, the complete many-body Schrödinger equation for the system can be written as:

$$\hat{H}\Psi(r_1, \ldots, r_N; R_1, \ldots, R_M) = E_{tot}\Psi(r_1, \ldots, r_N; R_1, \ldots, R_M) \quad \ldots (2.6)$$

where E_{tot} denotes the total energy of the system corresponds to the many body wavefunction Ψ.

In principle, solving this equation yields complete information about the ground state and excited state properties of the system. In practice, however, the explicit inclusion of electron-electron interactions makes the many-body Schrödinger equation analytically unsolvable for but the simplest systems. The computational cost increases rapidly with the number of electrons, rendering exact solutions infeasible for most molecular and condensed-phase systems. Consequently, further approximations are required to make the problem tractable, leading to the development of practical electronic structure methods discussed in the following sections.

2.1.2 Born-Oppenheimer approximation

The direct solution of the many-body Schrödinger equation for molecular systems is extremely challenging due to the simultaneous treatment of electronic and nuclear motions. A major simplification is achieved through the Born-Oppenheimer (BO) approximation, introduced by Professor Max Born and Professor J. Robert Oppenheimer in 1927.[2] This approximation exploits the large difference in mass between nuclei and electrons, which results in nuclei moving much more slowly compared to electrons. As a result, electronic motion can be treated independently of nuclear motion to a very good approximation.

Within the Born-Oppenheimer approximation, the total wavefunction of a molecular system is expressed as a product of an electronic wavefunction and a nuclear wavefunction. The electronic Schrödinger equation is solved by assuming that the nuclei are fixed at given positions, leading to

$$\hat{H}_e \Psi_e(r_1, r_2, \dots, r_N; \{R\}) = E_e(\{R\}) \Psi_e(r_1, r_2, \dots, r_N; \{R\}) \quad \dots (2.7)$$

where $\hat{H}_e$ is the electronic Hamiltonian operator, r_i denotes the electronic coordinates, and $(\{R\})$ corresponds to the electronic energy and depends parametrically on the nuclear coordinates.

Once the electronic problem is solved, the resulting electronic energy defines a potential energy surface on which the nuclei move. The nuclear motion is then described by a separate nuclear Schrödinger equation,

$$\hat{H}_n(\{R\}) \Phi(\{R\}) = E_n \Phi(\{R\}) \quad \dots (2.8)$$

where $\widehat{H}_n$ is the nuclear Hamiltonian operator and $\Phi(\{R\})$ is the nuclear wavefunction. This equation governs the vibrational and rotational motion of nuclei within the electronic potential energy surface.

Although the nuclei are treated as fixed during electronic structure calculations, their motion is not entirely absent in real molecular and solid-state systems. Nevertheless, owing to the considerably larger masses of nuclei compared to electrons, the Born-Oppenheimer approximation provides an accurate description of electronic motion for many molecular and solid-state systems and forms the foundation of modern electronic structure theory.

Under this approximation, the electronic Hamiltonian for a many-electron system[3] can be expressed in atomic units as:

$$\widehat{H}_e = -\frac{1}{2}\sum_{i=1}^{N}\nabla_i^2 - \sum_{i=1}^{N}\sum_{I=1}^{M}\frac{Z_I}{|r_i - R_I|} + \sum_{i=1}^{N-1}\sum_{j=i+1}^{N}\frac{1}{|r_i - r_j|} \qquad \ldots(2.9)$$

where, $\widehat{H}_e$ represents the electronic Hamiltonian, N and M denote the total numbers of electrons and nuclei, respectively, and ∇_i^2 is the Laplacian operator acting on the coordinates of the i^{th} electron. The indices i and j refer to electrons, whereas I denotes a nucleus. The position vectors r_i and r_j represent the positions of the corresponding electrons, while R_I denotes the position of the I^{th} nucleus, with Z_I representing its atomic number. The first term describes the kinetic energy of electrons, the second term represents the attractive interactions between all electrons and nuclei, and the third term accounts for electron-electron repulsive interactions.

This separation of electronic and nuclear motion significantly reduces the complexity of the many-body problem and provides the basis for most quantum mechanical methods, including Hartree-Fock (HF) and DFT methods discussed in the subsequent sections.

2.1.3 Need for approximate solutions

Despite the simplifications introduced by the Born-Oppenheimer approximation, the exact solution of the electronic Schrödinger equation is feasible only for very simple systems. This difficulty arises primarily from the electron-electron interaction term in

the many-electron Hamiltonian, which couples the motion of all electrons and leads to a highly correlated many-body problem. As the number of electrons increases, the complexity of the system grows rapidly, making exact numerical solutions computationally unfeasible. To address this challenge, approximate methods are employed to reduce the complexity while retaining the essential physics of electronic interactions. A common strategy is the independent-electron approximation, in which electrons are assumed to move in an effective potential generated by the nuclei and other electrons, thereby reducing many-body problems to a set of tractable one-electron equations.

The HF method provides a fundamental wavefunction-based approach, where the many-electron wavefunction is approximated by a single Slater determinant, ensuring proper antisymmetry with respect to electron exchange. Although the HF method accounts for exchange interactions exactly, it neglects electron correlation effects, which can lead to significant quantitative errors in total energies and reaction energetics. In contrast, the DFT method offers a computationally efficient alternative by using electron density as the central quantity. According to the Hohenberg-Kohn theorems, the ground-state properties of a many-electron system are uniquely determined by its electron density. In practical implementations, such as the Kohn-Sham (KS) formulation, the interacting many-electron system is mapped onto a system of non-interacting electrons moving in an effective potential. The accuracy of DFT calculations depends largely on the choice of the exchange-correlation functional, which approximates the complex many-body effects arising from electron exchange and correlation.

These approximate approaches form the foundation of modern electronic structure theory and enable the practical study of complex molecular and periodic systems. In this work, both the wavefunction and density-based methods are employed to investigate the CO_2 adsorption and conversion processes.

2.2 Hartree and Hartree-Fock theory

The Hartree and Hartree-Fock (HF) methods are the earliest and most fundamental wavefunction-based approaches developed to approximate solutions to the many-electron Schrödinger equation. These methods are based on the independent-electron

approximation, in which each electron is assumed to move in an effective potential generated by the nuclei and the average influence of all other electrons.[4]

In the Hartree method, the total many-electron wavefunction is expressed as a product of single-electron orbitals:

$$\Psi(r_1, r_2, \dots, r_N) = \prod_{i=1}^{N} \Psi_i(r_i) \quad \dots (2.10)$$

This mean-field approximation reduces the many-body problem to a set of coupled one-electron equations solved self-consistently. The effective potential experienced by an electron is described by the Hartree potential:

$$V_H(r_i) = \sum_{i \neq j} \int \frac{|\Psi_j(r_j)|^2}{|r_i - r_j|} dr_j \quad \dots (2.11)$$

However, this formulation does not satisfy the antisymmetric requirement of the electronic wavefunction and neglects electron spin, leading to a violation of the Pauli exclusion principle.

The Hartree-Fock method improves upon this by representing the total wavefunction as a Slater determinant of spin orbitals:

$$\Psi_{HF} = \frac{1}{\sqrt{N!}} \begin{vmatrix} \Psi_1(1) & \Psi_2(1) & \dots & \Psi_N(1) \\ \Psi_1(2) & \Psi_2(2) & \dots & \Psi_N(2) \\ \vdots & \vdots & \ddots & \vdots \\ \Psi_1(N) & \Psi_2(N) & \dots & \Psi_N(N) \end{vmatrix} \quad \dots (2.12)$$

This determinant ensures antisymmetric of the wavefunction and introduces exchange interactions between electrons of the same spin.

By applying the variational principle to this determinant, a set of coupled integro-differential equations, known as the Hartree-Fock equations, is obtained:

$$\hat{F}\Psi_i = \varepsilon_i \Psi_i \quad \dots (2.13)$$

where $\hat{F}$ is the Fock operator and ε_i are the orbital energies. These equations are solved iteratively using the self-consistent field (SCF) procedure until convergence in energy and electron density is achieved.

Despite its rigorous treatment of exchange interactions, the HF method neglects dynamic electron correlation arising from the instantaneous motion of electrons. As a result, it often overestimates the total energies and may inadequately describe weak interactions and reaction energetics. The missing correlation energy is defined as:

$$E_{corr} = E_{exact} - E_{HF} \quad \ldots (2.14)$$

Due to these limitations, more advanced approaches such as DFT have been developed. By using electron density as the central quantity and incorporating exchange-correlation effects through appropriate functionals, DFT provides a more accurate and computationally efficient manner for studying molecular and periodic systems.

2.3 Density functional theory

The density functional theory (DFT) method is a quantum mechanical approach used to describe the electronic structure of many-electron systems by employing the electron density as the fundamental variable.[5] The theoretical foundation of DFT is provided by the Hohenberg-Kohn theorems, which establish that the ground-state electron density uniquely determines all ground-state properties of a system and the correct density minimizes the total electronic energy. To enable practical calculations, the Kohn and Sham approach maps the interacting many-electron system onto an equivalent system of non-interacting electrons moving in an effective potential. This formulation makes the DFT computationally efficient while retaining many essential many-body effects through the exchange-correlation functional. Due to its favorable balance between accuracy and efficiency, DFT is widely used for studying molecular and periodic systems,[6] particularly in applications involving adsorption, surface reactions, and catalytic processes.

2.3.1 Hohenberg-Kohn theorems

The Hohenberg-Kohn (HK) theorems, proposed in 1964, form the theoretical basis of DFT by establishing the electron density as the fundamental variable for describing the ground-state properties of many-electron systems. These theorems demonstrate that the complex many-body wavefunction is not required to determine ground state observables.

The first HK theorem states that the ground-state electron density $\rho(r)$ uniquely determines the external potential $V_{ext}(r)$, and consequently all ground-state properties of the system. The total energy can therefore be expressed as a function of density:

$$E[\rho] = T[\rho] + V_{ee}[\rho] + \int V_{ext}(r)\rho(r)dr \quad \ldots (2.15)$$

where $T[\rho]$ is the kinetic energy functional and $V_{ee}[\rho]$ represents electron-electron interactions. These two terms are universal functionals, while the external potential term depends on the specific system.

The second HK theorem introduces a variational principle, stating that the true ground-state density minimizes the total energy functional.

$$E[\rho'] \geq E[\rho_{GS}] \quad \ldots (2.16)$$

where ρ_{GS} is the exact ground-state electron density. Consequently, ground-state energy is obtained by minimizing the energy functional with respect to the electron density.

$$E_{GS} = \min_{\rho} E[\rho] \quad \ldots (2.17)$$

Together, the HK theorems establish a one-to-one correspondence between the ground-state electron density and all ground-state properties of a many-electron system. However, since the exact forms of the kinetic and electron-electron interaction functionals are unknown, practical implementations of DFT rely on suitable approximations, motivating the development of the Kohn-Sham formalism.

2.3.2 Kohn-Sham formalism

Within the Born-Oppenheimer approximation, the nuclei are treated as fixed, generating an external potential $V(r)$ in which the electron moves. The interacting many-electron Hamiltonian is given by:

$$\hat{H} = \sum_{i=1}^{N}\left(-\frac{\hbar^2}{2m_e}\nabla_i^2 + V(r_i)\right) + \sum_{i=1}^{N-1}\sum_{j=i+1}^{N} U(r_i, r_j) \quad \ldots (2.18)$$

where, N denotes the total number of electrons, m_e is the electron mass, and $U(r_i, r_j)$ represents the interaction between electrons i and j.

In density functional theory (DFT), the electron density $\rho(r)$ serves as the fundamental variable for describing the ground-state properties of a many-electron system. It represents the electron number density at position r and is obtained by integrating the squared magnitude of the normalized many-electron wavefunction over the coordinates of the remaining electrons. Mathematically, the electron density is expressed as:

$$\rho(r) = N \int |\Psi(r, r_2, \dots, r_N|^2 \, d^3r_2 \dots d^3r_N \qquad \dots (2.19)$$

According to the Hohenberg-Kohn theorem, the ground-state electron density uniquely determines all ground-state properties, including the total energy, which can be expressed as a functional density,

$$E[\rho] = T[\rho] + U[\rho] + \int V(r)\rho(r)d^3r \qquad \dots (2.20)$$

Kohn and Sham introduced an auxiliary system of non-interacting electrons that yield the same ground state density as the interacting system. The total energy functional is written as:

$$E[\rho] = T_s[\rho] + \int V(r)\rho(r)d^3r + \frac{1}{2}\int \frac{e^2\rho(r)\rho(r')}{|r - r'|}d^3r d^3r' + E_{xc}[\rho] \qquad \dots (2.21)$$

where $T_s[\rho]$ is the kinetic energy of the non-interacting electrons, the third term represents the Hartree electrostatic energy, and $E_{xc}[\rho]$ is the exchange-correlation energy functional that accounts for all many-body effects beyond the classical Coulomb interaction and non-interacting kinetic energy.

Minimization of this energy functional with respect to the density leads to the Kohn-Sham single particle equations:

$$\left[-\frac{\hbar^2}{2m}\nabla^2 + V_s(r)\right]\Phi_i(r) = \varepsilon_i\Phi_i(r) \qquad \dots (2.22)$$

where the effective potential $V_s(r)$ is given by:

$$V_s(r) = V(r) + \int \frac{e^2\rho(r')}{|r-r'|}d^3r' + V_{XC}(r) \quad \ldots (2.23)$$

With the exchange-correlation potential defined as:

$$V_{XC}(r) = \frac{\delta E_{XC}[\rho]}{\delta\rho(r)} \quad \ldots (2.24)$$

The electron density is reconstructed from the Kohn-Sham orbitals as:

$$\rho(r) = \sum_{i}^{occ} |\Phi_i(r)|^2 \quad \ldots (2.25)$$

Since V_{XC} depends explicitly on the electron density, the Kohn-Sham equations must be solved self-consistently. This is achieved through an iterative procedure in which an initial guess for the density is used to construct V_s, the Kohn-Sham equations are solved to obtain updated orbitals, and a new density is generated. The process is repeated until convergence is reached.

The Kohn-Sham formalism thus provides an efficient and accurate method for treating interacting many-electron systems by reducing the complex many-body problem to a set of self-consistent single-particle equations, with all many-body effects incorporated through the exchange-correlation functional.[7]

2.3.3 Exchange-correlation functionals

In DFT, the exchange-correlation (XC) energy functional $E_{XC}[\rho]$ accounts for all many-body effects beyond the on-interacting kinetic energy and the classical electrostatic (Hartree) interaction. It incorporates exchange effects arising from the antisymmetry of the electronic wavefunction and correlation effects associated with electron-electron repulsion beyond the mean-field approximation. Although the Hohenberg-Kohn theorems guarantee the existence of such a functional, its exact analytical form is unknown in real systems, necessitating practical approximations. Consequently, the accuracy and predictive power of DFT calculations are strongly determined by the choice of XC functional.[8]

In practical implementations, the XC energy is commonly expressed as:

$$E_{XC}[\rho] = \int \varepsilon_{XC}\big(\rho(r)\big)d^3r \qquad \ldots (2.26)$$

and the corresponding XC potential is incorporated into the Kohn-Sham equations through a self-consistent procedure. Approximations to the $E_{XC}[\rho]$ are generally classified into local, semi-local, and non-local forms.

- **Local density approximation (LDA)**

The local Density Approximation (LDA) is the simplest and earliest XC approximation, in which the XC energy at each point in space is approximated by that of a homogeneous electron gas with the same local density. The LDA functional is given by:

$$E_{XC}^{LDA}[\rho] = \int \rho(r)\ \varepsilon_{XC}^{HEG}\big(\rho(r)\big)d^3r \qquad \ldots (2.27)$$

Despite its local nature, LDA provides reasonable descriptions of ground-state properties for systems with slowly varying electron densities, such as simple metals and bulk solids. However, it ends up over binding atoms and performs poorly for molecular systems, surfaces, and materials with rapidly varying densities or strong electron correlation.[9] The spin-polarized extension of LDA is known as the Local Spin Density Approximation (LSDA).

- **Generalized gradient approximation (GGA)**

The generalized Gradient Approximation (GGA) improves upon LDA by including the gradient of the electron density, allowing a better description of inhomogeneous systems. In GGA, the XC energy is written as:

$$E_{XC}^{GGA}[\rho] = \int \rho(r)\varepsilon_{XC}^{GGA}[\rho(r), \nabla\rho(r)]d^3\,r \qquad \ldots (2.28)$$

GGA functionals significantly enhance the accuracy of molecular geometries, binding energies, and ground-state energies compared to LDA. Widely used GGA functionals include PBE, $PW91$, $BLYP$, and $Becke88$.[10] While GGA performs well for most chemical bonding situations, it still fails to accurately capture long-range weak van der Waals interactions and tends to underestimate semiconductor band gaps. These limitations have motivated the development of more advanced approaches, such as meta-GGA and hybrid functionals, which further improve accuracy by incorporating additional physical information.[11]

- **Hybrid functionals**

Hybrid functionals were introduced in the early 1990s to improve the accuracy of DFT by partially incorporating the exact Hartree-Fock (HF) exchange into the XC functional. While HF theory treats exchange explicitly, conventional Kohn-Sham DFT includes exchange and correlation only through approximate functionals. Using the adiabatic connection formalism, the XC energy in hybrid DFT can be expressed as a linear combination of HF exchange and DFT exchange-correlation contributions:

$$E_{XC}^{hybrid} = C_{HF} E_X^{HF} + C_{DFT} E_{XC}^{DFT} \quad \ldots (2.29)$$

where C_{HF} and C_{DFT} are mixing coefficients. The inclusion of exact exchange reduces self-interaction errors and improves the description of electronic structure, reaction energetics, and localized states.

Among hybrid functionals, the Becke three-parameter Lee-Yang-Parr ($B3LYP$) functional is one of the most widely used.[12–14] It combines Becke's three-parameter exchange functional with the Lee-Yang-Parr correlation functional and is given by

$$E_{XC}^{B3LYP} = E_{XC}^{LDA} + c_0(E_X^{HF} - E_X^{LDA}) + c_X \Delta E_X^{B88} + E_C^{VWN3} + c_C (E_C^{LYP} - E_C^{VWN3}) \ldots (2.30)$$

where $c_0, c_X,$ and c_C are empirically optimized parameters. The $B3LYP$ functional provides a balanced treatment of exchange and correlation and has demonstrated reliable performance for molecular geometries, electronic properties, and reaction energetics.[15,15] In the present thesis, $B3LYP$ was employed together with dispersion corrections to accurately account for long-range van der Waals interactions, which are not described by standard DFT functionals.

2.3.4 van der Waals interactions and dispersion corrections

van der Waals (vdW) interactions are weak, long-range forces originating from instantaneous fluctuations in electron density that give rise to transient multipoles. These interactions are essential for accurately describing non-covalent phenomena such as interlayer binding in layered materials, molecular adsorption on surfaces, and physisorption processes.[16,17] In systems involving adsorbate-surface interactions, vdW interactions play a decisive role in determining structural stability and adsorption energetics.

Standard $DF\ XC$ functionals, including the LDA and GGA, are inherently limited in describing vdW interactions. This shortcoming arises from the non-local nature of dispersion forces, whereas the commonly used XC functionals are local or semi-local in form.[18] Consequently, dispersion interactions are either poorly described or absent in conventional DFT calculations, necessitating the inclusion of explicit vdW corrections for improved accuracy.[19,20] To address this limitation, several dispersion-corrected DFT schemes have been developed, among which the semi-empirical $DFT-D$ methods proposed by Grimme are widely used in the modern computational studies. In these approaches, the total energy is expressed as the sum of the conventional Kohn-Sham DFT energy and an additional dispersion correction term:

$$E_{total} = E_{KS-DFT} + E_{disp} \quad \ldots (2.31)$$

The dispersion energy E_{disp} accounts for long-range electron correlation effects and asymptotically follows an attractive R^{-n} dependence, where R is the interatomic distance. The simplest scheme, $DFT-D2$, includes only pairwise R^{-6} terms with fixed dispersion coefficients. An improved formulation, $DFT-D3$, incorporates both R^{-6} and R^{-8} contributions and allows the dispersion coefficients to depend on the local environment, leading to enhanced accuracy and transferability. Additionally, the $D3$ method includes a damping function to smoothly suppress the dispersion correlation at short interatomic distances, thereby avoiding double counting of interactions already described by the XC functional.

In the present thesis, dispersion interactions were treated using the $B3LYP-D3$ method, in which Grimme's $D3$ dispersion correction is combined with the hybrid $B3LYP\ XC$ functional. This approach enables a reliable description of both electronic structure and long-range vdW interactions in adsorption processes and porous materials.

2.3.5 Møller-Plesset second-order perturbation theory (MP2)

Second-order Møller-Plesset perturbation theory (MP2) provides an important correlation to the HF ground state energy by accounting for electron correlation effects through Rayleigh-Schrödinger perturbation theory, where the zeroth-order Hamiltonian is defined as a sum of one-electron Fock operators.[21] MP2 is widely used due to its relatively simple formulation and its ability to recover a significant portion of dynamic

correlation, including dispersion interactions that are essential for describing noncovalent systems. It is also applicable to condensed-phase systems using periodic boundary conditions and is incorporated into double-hybrid density functionals via MP2-like correlation terms derived from KS orbitals.[22]

Despite these advantages, MP2 is computationally more demanding than HF and conventional DFT. Additionally, it typically demands larger basis sets for convergence. To address these limitations, several methods have been developed, including Second-Order Møller–Plesset Perturbation Theory (MP2), local MP2 (LMP2), Laplace-transformed MP2, resolution-of-identity MP2 (RI-MP2), and explicitly correlated methods (F12-MP2), which reduce computational cost and improve basis-set convergence. However, MP2 calculations for large systems (> 50 heavy atoms) remain challenging, necessitating efficient parallel algorithms. Recent developments, such as the Gaussian and plane wave (GPW) MP2 method, improve scalability by avoiding four-center electron repulsion integrals and employing fast Fourier transforms for efficient evaluation. These advances enable large-scale MP2 calculations with improved computational efficiency and parallel performance on modern high-performance computing systems.[23]

2.3.6 Basis sets

In practical electronic structure calculations, molecular orbitals (MO) are represented as linear combinations of atomic basis functions using the linear combination of atomic orbitals ($LCAO$) approach:

$$\Psi_a = \sum_{i=1}^{n} c_{ai}\Phi_i \qquad \ldots (2.32)$$

Slater-type orbitals ($STOs$) accurately describe atomic orbitals due to their correct exponential decay, but their computational cost is high. Therefore, Gaussian-type orbitals ($GTOs$), given by:

$$\eta_{GTO} = Nx^l y^m z^n e^{-ar^2} \qquad \ldots (2.33)$$

are widely adopted owing to their computational efficiency.[24] To compensate for the inadequate shape of individual $GTOs$, particularly near the nucleus, contracted

Gaussian functions ($CGFs$) are employed, where several primitive Gaussians are linearly combined:

$$\eta_{\tau}^{CGF} = \sum_{a} d_{a\tau}\, \eta_{a}^{GTO} \quad \ldots (2.34)$$

Basis sets are often constructed using a split-valence scheme, in which valence orbitals are described by multiple basis functions to enhance flexibility, while core orbitals are treated with fewer functions for efficiency. Such basis sets are classified as double-zeta, triple-zeta, and higher, depending on the number of functions used to represent valence orbitals. The widely used basis set families, such as the Pople and Dunning series, provide a good balance between computational cost and accuracy and are therefore commonly employed in molecular electronic structure calculations. The study carried out in the present thesis used well-established basis sets to ensure both computational efficiency and reliable results.

2.4 Quantum physics and materials science calculations

In recent years, continuous improvements in computational facilities have considerably enhanced the capability of quantum mechanical calculations. The steady growth in computational resources, together with methodological developments, such as parallel processing and the widespread adoption of DFT, has led to more efficient and reliable approaches for investigating chemical systems. As a result, molecular systems containing many atoms can be studied with reasonable computational cost and accuracy. These advancements have broadened the applicability of computational quantum physics and materials science across various scientific disciplines, including , condensed matter physics, chemical engineering, organic and inorganic chemistry, and biochemistry.[25,26] The use of realistic molecular models has become increasingly common, allowing theoretical studies to address systems that are directly comparable to experimental conditions. At present, computational investigations are frequently carried out alongside experimental work. Theoretical calculations help interpret experimental observations by providing detailed information on electronic structures, reaction energetics, and possible mechanistic pathways. In particular, transition states and reaction intermediates, which are often difficult to characterize experimentally, can be examined through computational methods. Moreover, calculated results can help in predicting trends and guiding the design of subsequent experiments. This

complementary relationship between theory and experiment has strengthened the role of computational chemistry in modern research.[26] To evaluate the structural, electronic, and adsorption properties of the systems presented in the thesis, several computational parameters and analysis methods were employed, as described below:

2.4.1 Binding enthalpy

The binding enthalpy (ΔH) of gas adsorption was evaluated to quantify the strength of interaction between the adsorbate molecule and the adsorbent (host system).[27] This was achieved by performing geometry optimizations of the isolated host, adsorbate and the corresponding adsorbate-host complex at the same level of theory.

After obtaining the optimized equilibrium structures, the binding enthalpy was calculated using the following expression:

$$\Delta H_{ads} = H_{(host+adsorbate)} - [H_{host} + H_{adsorbate}] \quad \ldots (2.35)$$

where $H_{(host+adsorbate)}$ represents the total enthalpy of the optimized adsorption complex, H_{host} is the enthalpy of the isolated host system, and $H_{adsorbate}$ corresponds to the enthalpy of the isolated gas molecule.

A negative value of ΔH indicates an exothermic adsorption process, while increasingly negative values signify stronger binding between the adsorbate and the host.[28] Binding enthalpy is therefore a key parameter for assessing the adsorption capability of porous and molecular materials. The total enthalpy (H) of each system was obtained by incorporating the electronic energy, zero-point vibrational energy (ZPE), and thermal vibrational contributions according to:

$$H = E_{elec} + ZPE + H_{vib} \quad \ldots (2.36)$$

Finally, the binding enthalpy was determined by taking the difference between the enthalpy of the adsorbed complex and the sum of the enthalpies of the isolated components.

2.4.2 Energy decomposition analysis (EDA)

Energy Decomposition Analysis (EDA) is a theoretical approach based on electronic structure calculations, in which the total interaction energy between two or more

fragments is partitioned into individual energy components with clear physical meaning. This method is useful for understanding the nature of intermolecular interactions by identifying the relative contributions of different interaction mechanisms. The EDA proposed by Su and Li, popularly known as the localized molecular orbital energy decomposition analysis (LMO-EDA) has been used to identify the contribution of different energy components to the total interaction energy.[29] In the case of LMO-EDA, the total interaction energy (ΔE_{int} or ΔH_{bind}) of a system contains the contribution from electrostatic (ΔE_{els}), exchange (ΔE_{exc}), repulsion (ΔE_{rep}), polarization (ΔE_{pol}), and dispersion (ΔE_{dis}) energy components, given by:

$$\Delta H_{bind} = \Delta E_{els} + \Delta E_{exc} + \Delta E_{rep} + \Delta E_{pol} + \Delta E_{dis} \quad \ldots (2.37)$$

Each term in the LMO-EDA has its own significance. The electrostatic interaction (ΔE_{els}) is understandable in terms of Coulomb's law, which prevents the molecular orbitals from mixing. The exchange interaction (ΔE_{exc}) is caused by electron exchange and molecular delocalization. When two non-bonded atoms approach each other closely, their electron clouds begin to overlap. This overlap leads to strong electron-electron repulsion, resulting in an increase in repulsion energy (ΔE_{rep}). The polarization energy change (ΔE_{pol}) is produced by polarizing the wave function of each monomer in response to the electric field of the other monomer. In molecules, the oscillators are coupled when they are close to each other. Because of the coupled fluctuating dipoles, the dispersion interactions (ΔE_{dis}) also known as electrostatic interactions have been considered in the present computation.

By decomposing the interaction energy into these components, EDA provides a quantitative idea for analyzing the physical origin of molecular interactions. This makes it a useful tool for interpreting interaction trends and supporting the analysis of adsorption and binding phenomena in computational studies.

2.4.3 Natural bond orbital (NBO) analysis

Natural Bond Orbital (NBO) analysis provides a detailed orbital-based description of the electronic structure by transforming the delocalized wavefunction into a set of localized orbitals that closely correspond to classical chemical bonding concepts.[30] This approach is particularly useful for analyzing both intra- and intermolecular interactions, as it enables clear identification of bonding patterns, charge distributions,

and electron delocalization effects. In addition, the electronic properties are examined using frontier molecular orbital (FMO) analysis. The energies of the highest occupied molecular orbital ($HOMO$) and lowest unoccupied molecular orbital ($LUMO$) determine the electron-donating and accepting tendencies of a system, respectively. The energy gap ($E_g = HOMO - LUMO$) serves as an important indicator of chemical stability and reactivity, with larger gaps corresponding to greater stability. According to the FMO theory, chemical reactivity is primarily governed by interactions between the $HOMO$ of a donor and the $LUMO$ of an acceptor, which are crucial for understanding charge transfer processes and reaction mechanisms.

2.4.4 Computational hydrogen electrode (CHE) model

The concept of the Computational Hydrogen Electrode (CHE), developed by Professor Jens K. Nørskov and co-workers in the mid-2000s,[31] has profoundly influenced the field of computational electrocatalysis. The CHE model provides an elegant and efficient means of incorporating electrode potential effects into the DFT based electrocatalytic studies. The CHE model has been widely adopted to map reaction pathways, determine limiting potentials, and analyze activity trends in electrochemical processes such as CO_2 reduction, hydrogen evolution and oxygen reduction.[32] It is now regarded as a foundational methodology for theoretical as well as computational studies of heterogeneous electrocatalysis. In this model, the thermodynamics of proton-electron transfer steps are referred to the equilibrium between a proton-electron pair and molecular hydrogen, thereby the explicit treatment of solvated protons and electrons is avoided. The equivalence of their chemical potential (μ) at standard conditions is expressed as:

$$\mu(H^+) + \mu(e^-) = \frac{1}{2}\mu(H_2) \quad \ldots (2.38)$$

Under an applied electrode potential U, the free energy of an electron is shifted, and the chemical potential (μ) of the proton-electron pair becomes:

$$\mu(H^+ + e^-) = \frac{1}{2}\,\mu(H_2) - eU \quad \ldots (2.39)$$

The CHE model uses the reversible hydrogen electrode (RHE) as a reference, where the chemical potential of a proton-electron pair is related to half the chemical potential

of molecular hydrogen at equilibrium. At an electrode potential of 0 V versus RHE, the proton-electron pair and half a hydrogen molecule have equivalent chemical potentials. A more negative electrode potential favors reduction reactions by increasing the thermodynamic driving force for electron transfer.

This treatment enables the evaluation of potential dependent reaction energetics using conventional DFT calculations. The Gibbs free energy (G) of each intermediate is obtained by incorporating vibrational and entropic corrections into the DFT electronic energy:

$$G = E_{DFT} + E_{ZPE} + \int C_v dT - T\Delta S \quad \ldots (2.40)$$

Accordingly, the change in Gibbs free energy (ΔG) of an elementary step involving n electron transfer is calculated as:

$$\Delta G = \Delta E + \Delta E_{ZPE} - T\Delta S + neU \quad \ldots (2.41)$$

The calculated Gibbs free-energy changes provide insights into the thermodynamic feasibility of individual proton-electron transfer steps along the proposed electrochemical reaction pathways. By considering the successive reaction intermediates, a Gibbs free-energy profile can be constructed to examine the energetic requirements of the proposed electrochemical reaction mechanism. The relative free energies of different intermediates provide insights into the thermodynamically favorable and unfavorable reaction steps and allow comparisons among alternative reaction pathways.

In addition to the free energy analysis, adsorption energies of reaction intermediates are evaluated to understand their interaction strength with the catalyst surface using:

$$\Delta E_{ads} = E_{total} - (E_{adsorbate} + E_{adsorbent}) \quad \ldots (2.42)$$

where E_{total} represents the total energy of the adsorbed system, while $E_{adsorbent}$ and $E_{adsorbate}$ correspond to the energies of the adsorbent and intermediates respectively. Together, these expressions provide a systematic framework for evaluating the thermodynamic feasibility of electrochemical reaction pathways,

examining the relative stability of reaction intermediates, and understanding their interactions with the catalyst surface.

2.5 Software

The research work presented in this thesis was carried out using various widely recognized computational software packages. These include:

2.5.1 Gaussian 16

Gaussian 16 represents a modern and widely used version of the Gaussian series of electronic structure programs.[33] It is extensively utilized by researchers in chemistry, condensed matter physics, chemical engineering, atomic and molecular physics, biochemistry, and materials science. Built on the principles of QM, Gaussian 16 enables the prediction of molecular energies, optimized geometries, vibrational frequencies, and a wide range of molecular properties of diverse chemical systems. The software is applicable to both stable molecules and reactive intermediates that are difficult or impossible to study experimentally, such as reactive intermediates and transition states. It provides efficient geometry optimization and enables the identification and characterization of stationary points on the potential energy surface (PES). Frequency calculations are used to confirm whether a structure corresponds to a minimum or a transition state. In addition, intrinsic reaction coordinate (IRC) calculations allow the determination of reaction pathways connecting reactants and products through transition structures, thereby offering a complete description of reaction mechanisms and energy profiles.

Gaussian 16 provides access to a variety of computational methods, including HF, DFT, MP2, and coupled cluster approaches. A wide range of XC functionals and basis sets are available, allowing the appropriate level of theory to be selected depending on the system under investigation. It is compatible with a variety of computational environments, including single-processor systems, multicore processors, clusters, and GPU-based platforms. The results can be visualized using GaussView6.1, which provides an intuitive graphical interface for analyzing molecular structures and spectra.

Input file in Gaussian 16

The input file for Gaussian 16 is written as an ASCII text file consisting of the following sections:

- *Link 0 commands:* locate and name scratch files
- *Route section (# lines):* specifies the calculation type, method, and options (terminated by a blank line).
- *Title section:* provides a brief description of the calculation (blank line-terminates). The following characters should be avoided in the title section: @ # ! _ - \
- *Molecular specification:* defines charge, multiplicity, and atomic coordinates.
- *Optimal additional sections:* additional input required for specific calculations

```
%Chk=heavy                          #Link 0 section
#HF/6-31G9d) Opt Freq Test          # Route section
Opt job                             # Title section
0  1                                # Molecule specification section
atomic coordinates
3 8                          Add a bond and an angle to the internal
2 1 3                        Coordinates used during geom. opt.
```

2.5.2 GAMESS

The General Atomic and Molecular Electronic Structure System ($GAMESS$) is a versatile quantum physics and materials science software package developed for performing *ab initio* molecular electronic structure calculations.[34] It provides a broad range of theoretical methods for studying molecular systems at different levels of approximation. For larger molecular systems, GAMESS offers the Fragment Molecular Orbital (FMO) approach, which partitions the system into smaller fragments to reduce computational cost. A wide variety of internally stored basis sets, effective core potentials ($ECPs$), and model core potentials are available, allowing calculations across much of the periodic table. The program supports parallel execution, enhancing

computational efficiency for demanding calculations. Visualization and input preparation can be performed using external tools such as *MacMolPlt* and *Avogadro*.

Input Structure in GAMESS

A GAMESS input file is written in a structured format using keyword groups delimited by **$** and **$END**. The major sections typically include:

- **$CONTRL**: Specifies the type of wavefunction, calculation method, charge, multiplicity, coordinate system, and run type (e.g., energy, gradient).
- **$SYSTEM**: Defines computational resources such as memory and time limits.
- **$SCF**: Controls SCF convergence criteria and related options.
- **$BASIS**: Specifies the basis set either through built-in definitions or user-defined input.
- **$GUESS**: Defines the initial guess for molecular orbitals.
- **$DATA**: Contains title, symmetry specification, and molecular geometry.

A representative example of a water molecule is shown below:

```
 $CONTRL SCFTYP=RHF MULT=1 RUNTYP=GRADIENT COORD=UNIQUE
      UNITS=BOHR $END
     $SYSTEM TIMLIM=1 $END
     $SCF         DIRSCF=.TRUE. NCONV=9 $END
     $BASIS   GBASIS=N31 NGAUSS=6 NDFUNC=1 NPFUNC=0 $END
     $GUESS   GUESS=HUCKEL $END
     $DATA
TEST H2O MOLECULE
   C
   1
   O      8.0  0.0000000000  0.0000000000  0.0000000000
   H      1.0  1.4748637392  1.0778200416  0.0000000000
   H      1.0 -1.4748637392  1.0778200416  0.0000000000
    $END
```

In this structure, **$CONTRL** defines the computational method and run type, **$SCF** sets the convergence threshold, **$BASIS** specifies the basis set, and **$DATA** provides the molecular geometry and symmetry information.

2.5.3 CRYSTAL 23

CRYSTAL 23 program, an *ab initio* quantum mechanical package specifically developed for the study of crystalline systems, performs the periodic electronic

structure calculations.[35] The code enables the evaluation of ground-state energies, energy gradients, electronic wave functions, and a wide range of derived properties for periodic materials. It supports both HF and KS DFT Hamiltonians, incorporating appropriate XC functionals. The program is designed to treat systems of different dimensionalities within a unified formalism, including molecules (0D), polymers (1D), slabs and surfaces (2D), and fully periodic crystals (3D). A distinct feature of CRYSTAL 23 is the representation of single particle wave functions as Crystalline Orbitals (COs). These orbitals are expanded as linear combinations of Bloch functions (BFs), which are constructed from localized Atomic Orbitals (AOs). These AOs themselves are expressed as linear combinations of Gaussian-type functions (GTFs). This atom-centered Gaussian basis set approach enables efficient and accurate treatment of periodic systems.

This program incorporates automatic handling of spatial symmetry, providing access to 230 space groups, 80 layer groups, 99 rod groups, and 45 point groups. The program allows the construction and modification of a variety of structures, including bulk crystals, 2D slabs, 1D nanorods, polymers with helical symmetry, and 0D clusters derived from periodic structures. Additional capabilities include lattice distortion, supercell generation with defects, and the creation of special structures such as nanotubes and fullerenes. These features make the software particularly suitable for studying structural, electronic, and vibrational properties of extended systems.

Input file in CRYSTAL 23

A representative example of a 3D material is shown below:

CoPc-DNDS-COF	# Title Line
CRYSTAL	# Dimensionality of the system
0 0 0	# Crystallographic information (3D only)
83	# Symmetry group number
20.3331 3.4404	# Lattice Parameters
20	# Number of atoms in the asymmetric unit

```
6     0.29546   0.53343   0.00000
6     0.36412   0.44690   0.00000
6     0.76261   0.43038   0.00000          # Atomic numbers and coordinates
6     0.82254   0.46501   0.00000
7     0.11877   0.57092   0.00000
6     0.05993   0.53470   0.00000
9     0.76162   0.37717   0.00000
6     0.70454   0.53343   0.00000
6     0.63588   0.44690   0.00000
6     0.23739   0.43038   0.00000
6     0.17746   0.46501   0.00000
16    0.88123   0.57092   0.00000
6     0.94007   0.53470   0.00000
9     0.23838   0.37717   0.00000
7     0.40457   0.50000   0.00000
7     0.38393   0.61607   0.00000
6    -0.00000   0.56889   0.00000
1     0.00003   0.37215   0.00000
1     0.11900   0.63100   0.00000
27    0.50000   0.50000   0.00000
```

```
OPTGEOM
FULLOPTG                               # Keywords for geometry optimization
MAXCYCLE
800
ENDOPT
END
```

```
6 8
0 0 6 2.0 1.0
13575.349682 0.00022245814352
2035.2333680 0.00172327382520
463.22562359 0.00892557153140
131.20019598 0.03572798450200
42.853015891 0.11076259931000
```

15.584185766 0.24295627626000 0 0 2 2.0 1.0 6.2067138508 0.41440263448000 2.5764896527 0.23744968655000 0 0 1 0.0 1.0 0.4941102000 1.00000000000000 0 0 1 0.0 1.0 0.1644071000 1.00000000000000 0 2 4 2.0 1.0 34.697232244 0.00533336578050 7.9582622826 0.03586410909200 2.3780826883 0.14215873329000 0.8143320818 0.34270471845000 0 2 1 0.0 1.0 0.5662417100 1.00000000000000 0 2 1 0.0 1.0 0.2673545000 1.00000000000000 0 3 1 0.0 1.0 0.8791584200 1.00000000000000 99 0	# Basis sets for non-equivalent atoms
# Optional keywords	
END	# End of basis set input section
SHRINK 0 8 4 4 4	# Reciprocal space integration parameters
# Optional keywords	
END	# End of SCF input section

2.5.4 Chemcraft1.8

Chemcraft1.8 is a graphical software package developed for the visualization and analysis of quantum chemical calculations.[36] Although it does not perform electronic structure calculations itself, it provides a convenient interface for preparing input files

and interpreting results generated by widely used quantum physics and materials science programs. The software is primarily designed to work with packages such as GAMESS and Gaussian, while also supporting other computational codes through the import and export of atomic coordinates in standard text formats. Chemcraft is compatible with both Windows and Linux operating systems. One of the principal features of Chemcraft is its ability to generate three-dimensional molecular representations from atomic coordinate data. It allows interactive examination and modification of structural parameters, including bond lengths, bond angles, and dihedral angles. This capability facilitates structural analysis prior to and after geometry optimization.

Chemcraft also provides extensive tools for visualizing computational output files from programs such as *GAMESS, Gaussian, NWChem, ADF, Molpro, Dalton, Jaguar, ORCA, and Q-Chem*. Optimized geometries and intermediate structures obtained during geometry optimization can be displayed individually or as an animated sequence. The software enables visualization of vibrational modes, graphical representation of nuclear gradients, and depiction of molecular orbitals using isosurfaces or colored contour planes. In addition, it supports the visualization of vibrational and electronic spectra, including results from time-dependent DFT (TDDFT) calculations. Convergence behavior of SCF cycles can also be examined through graphical plots. The software further allows the generation of high-quality images suitable for publication. Various display modes, labelling options, and graphical adjustments can be applied to produce clear and informative structural representations. In addition, Chemcraft includes utilities that simplify input file preparation. These include tools for constructing Z-matrices, generating input files with user-defined or non-standard basis sets, and converting molecular orbital information from output files into formats suitable for subsequent calculations.

2.5.5 GaussView6.1

GaussView6.1 is a graphical user interface designed to facilitate calculations performed with Gaussian 16.[37] The program provides an integrated environment for constructing or importing molecular structures, preparing input files, submitting calculations, and analyzing computational results. Although the electronic structure calculations are carried out by Gaussian, GaussView1.6 significantly simplifies their

setup and interpretation. The software enables the construction and editing of molecular geometries through an interactive graphical interface. Structural parameters such as bond lengths, bond angles, and dihedral angles can be examined and modified prior to calculation. It also supports the preparation of input files for a wide range of computational methods and basis sets available in Gaussian. The program also generates plots of spectroscopic data, including vibrational, vibronic, and NMR spectra, facilitating interpretation of computed results.

Electronic structure properties can be visualized using surfaces or contour representations. Molecular orbitals, electron density, spin density, and electrostatic potential distributions can be displayed as isosurfaces or mapped onto electron density surfaces. These representations help in understanding charge distribution, bonding characteristics, and molecular reactivity. In addition, GaussView1.6 provides animation capabilities for dynamic processes. Normal vibrational modes, geometry optimization steps, and intrinsic reaction coordinate (IRC) pathways can be animated, enabling visualization of structural changes and molecular motion during chemical transformations. Overall, GaussView1.6 serves as an effective tool for molecular modeling, input generation, and graphical analysis of Gaussian calculations, thereby enhancing the efficiency and clarity of computational studies.

2.5.6 VESTA

Visualization for Electronic and Structural Analysis (VESTA) is a widely used three-dimensional visualization program for analyzing crystal structures, volumetric data, and related properties.[38] It enables the graphical representation of structural models such as ball-and-stick, space-filling, and polyhedral forms, allowing clear interpretation of atomic arrangements and bonding environments. The software is particularly designed for visualizing periodic systems, including crystalline materials, and supports multiple file formats generated from computational and experimental studies.

In addition to structural visualization, VESTA provides advanced capabilities for displaying volumetric data such as electron density, electrostatic potential, and wave functions through isosurfaces, contour maps, and two-dimensional slices. It allows superposition of structural and electronic information within a single framework, facilitating a deeper understanding of structure-property relationships. The program also supports the analysis of geometric parameters such as bond lengths, bond angles,

and coordination environments, making it a powerful tool for interpreting results obtained from electronic structure calculations. Furthermore, VESTA includes tools for detailed structural analysis, such as the calculation and visualization of bond lengths, bond angles, coordination polyhedral, and lattice planes. It also allows manipulation of structures through rotation, translation, and scaling in three dimensions, offering flexibility in examining complex systems. Its user-friendly graphical interface and compatibility with multiple operating systems make it an effective tool for both visualization and interpretation of computational results in materials science, condensed matter physics and chemistry.

2.6 References

[1] A. Szabo, N. S. Ostlund, Modern quantum chemistry: Introduction to advanced electronic structure theory, Dover Publications, 1996. https://books.google.co.in/books?id=6mV9gYzEkgIC.

[2] B. T. Sutcliffe, R. G. Woolley, On the quantum theory of molecules, J. Chem. Phys. 137 (2012) 22A544.

[3] P. Echenique, J. L. Alonso, A mathematical and computational review of Hartree–Fock SCF methods in quantum chemistry, Mol. Phys. 105 (2007) 3057-3098.

[4] C. D. Sherrill, An introduction to Hartree-Fock molecular orbital theory, Georg. Inst. Technol. (2000) 1-8.

[5] R. O. Jones, Density functional theory: Its origins, rise to prominence, and future, Rev. Mod. Phys. 87 (2015) 897-923.

[6] F. Giustino, Materials modelling using density functional theory: properties and predictions, 2014. https://api.semanticscholar.org/CorpusID:118018414.

[7] F. M. Bickelhaupt, E. J. Baerends, Kohn-Sham Density Functional Theory: Predicting and Understanding Chemistry, 15 (2000) 1-86.

[8] J. P. Perdew, K. Burke, Y. Wang, Generalized gradient approximation for the exchange-correlation hole of a many-electron system, Phys. Rev. B 54 (1996) 16533-16539.

[9] R. O. Jones, O. Gunnarsson, The density functional formalism, its applications and prospects, Rev. Mod. Phys. 61 (1989) 689-746.

[10] L. He, F. Liu, G. Hautier, M. J. T. Oliveira, M. A. L. Marques, F. D. Vila, J. J. Rehr, G. M. Rignanese, A. Zhou, Accuracy of generalized gradient approximation functionals for density-functional perturbation theory calculations, Phys. Rev. B 89 (2014) 064305.

[11] J. P. Perdew, J. A. Chevary, S. H. Vosko, K. A. Jackson, M. R. Pederson, D. J. Singh, C. Fiolhais, Atoms, molecules, solids, and surfaces: Applications of the generalized gradient approximation for exchange and correlation, Phys. Rev. B 46 (1992) 6671-6687.

[12] A. D. Becke, Density-functional exchange-energy approximation with correct asymptotic behavior, Phys. Rev. A 38 (1988) 3098-3100.

[13] C. Lee, W. Yang, R. G. Parr, Development of the Colle-Salvetti correlation-energy formula into a functional of the electron density, Phys. Rev. B 37 (1988) 785-789.

[14] B. Miehlich, A. Savin, H. Stoll, H. Preuss, Results obtained with the correlation energy density functionals of becke and Lee, Yang and Parr, Chem. Phys. Lett. 157 (1989) 200-206.

[15] J. T. Rives, W. L. Jorgensen, Performance of B3LYP density functional methods for a large set of organic molecules, J. Chem. Theory Comput. 4 (2008) 297-306.

[16] A. Tkatchenko, Current understanding of van der Waals effects in realistic materials, Adv. Funct. Mater. 25 (2015) 2054-2061.

[17] A. M. Reilly, A. Tkatchenko, van der Waals dispersion interactions in molecular materials: beyond pairwise additivity, Chem. Sci. 6 (2015) 3289-3301.

[18] F. Ortmann, F. Bechstedt, W. G. Schmidt, Semiempirical van der Waals correction to the density functional description of solids and molecular structures, Phys. Rev. B 73 (2006) 205101.

[19] M. Lee, B. Kim, M. Sim, M. Sogal, Y. Kim, H. Yu, K. Burke, E. Sim, Correcting dispersion corrections with density-corrected DFT, J. Chem. Theory Comput. 20

(2024) 7155-7167.

[20] J. Binns, M. R. Healy, S. Parsons, C. A. Morrison, Assessing the performance of density functional theory in optimizing molecular crystal structure parameters, Acta Cryst. B 70 (2014) 259-267.

[21] C. Møller, M. S. Plesset, Note on an approximation treatment for many-electron systems, Phys. Rev. 46 (1934) 618-622.

[22] D. Cremer, Møller–Plesset perturbation theory: From small molecule methods to methods for thousands of atoms, WIREs Comput. Mol. Sci. 1 (2011) 509-530.

[23] M. D. Ben, J. Hutter, J. VandeVondele, Second-order Møller–Plesset perturbation theory in the condensed phase: An efficient and massively parallel Gaussian and plane waves approach, J. Chem. Theory Comput. 8 (2012) 4177-4188.

[24] A. L. Magalhães, Gaussian-type orbitals versus Slater-type orbitals: A Comparison, J. Chem. Educ. 91 (2014) 2124-2127.

[25] M. Bursch, J. M. Mewes, A. Hansen, S. Grimme, Best-practice DFT protocols for basic molecular computational chemistry**, Angew. Chem. Int. Ed. 134 (2022) e202205735.

[26] T. Sperger, I. A. Sanhueza, F. Schoenebeck, Computation and experiment: A powerful combination to understand and predict reactivities, Acc. Chem. Res. 49 (2016) 1311-1319.

[27] S. Pakhira, J. L. M. Cortes, Quantum nature in the interaction of molecular hydrogen with porous materials: Implications for practical hydrogen storage, J. Phys. Chem. C 124 (2020) 6454-6460.

[28] N. Sinha, S. Pakhira, H_2 physisorption on covalent organic framework linkers and metalated linkers: A strategy to enhance binding strength, Mol. Syst. Des. Eng. 7 (2022) 577-591.

[29] P. Su, H. Li, Energy decomposition analysis of covalent bonds and intermolecular interactions, J. Chem. Phys. 131 (2009) 014102.

[30] B. D. Dunnington, J. R. Schmidt, Generalization of natural bond orbital analysis to periodic systems: Applications to solids and surfaces via plane-wave density functional theory, J. Chem. Theory Comput. 8 (2012) 1902-1911.

[31] J. K. Nørskov, J. Rossmeisl, A. Logadottir, L. Lindqvist, J. R. Kitchin, T. Bligaard, H. Jónsson, Origin of the overpotential for oxygen reduction at a fuel-cell cathode, J. Phys. Chem. B 108 (2004) 17886-17892.

[32] F. A. Pedersen, T. Bligaard, J. Rossmeisl, J. Greeley, Tribute to Jens K. Nørskov, J. Phys. Chem. C 129 (2025) 1025-026.

[33] M. J. Frisch, G. W. Trucks, H. B. Schlegel, G. E. Scuseria, M.A. Robb, J. R. Cheeseman, G. Scalmani, V. Barone, G. A.Petersson, H. Nakatsuji, X. Li, M. Caricato, A. V. Marenich,J. Bloino, B. G. Janesko, R. Gomperts, B. Mennucci, H. P.Hratchian, J. V. Ortiz, A. F. Izmaylov, J. L. Sonnenberg, Williams, F. Ding, F. Lipparini, F. Egidi, J. Goings, B. Peng,A. Petrone, T. Henderson, D. Ranasinghe, et al., Gaussian 16A.03. Wallingford, CT, 2016.

[34] M. W. Schmidt, K. K. Baldridge, J. A. Boatz, S. T. Elbert, M. S. Gordon, J. H. Jensen, S. Koseki, N. Matsunaga, K. A. Nguyen, S. Su, T. L. Windus, M. Dupuis, J. A. Montgomery, General atomic and molecular electronic structure system, J. Comput. Chem. 14 (1993) 1347-1363.

[35] A. Erba, J. K. Desmarais, S. Casassa, B. Civalleri, L. Donà, I. J. Bush, B. Searle, L. Maschio, L. E. Daga, A. Cossard, C. Ribaldone, E. Ascrizzi, N. L. Marana, J. P. Flament, B. Kirtman, CRYSTAL23: A program for computational solid state physics and chemistry, J. Chem. Theory Comput. 19 (2023) 6891-6932.

[36] Chemcraft - graphical software for visualization of quantum chemistry computations. Version 1.8, build 682. https://www.chemcraftprog.com

[37] R. Dennington, T. Keith, and J. Millam, Semichem Inc., Shawnee Mission, KS, GaussView, Version 6.1.1, 2019.

[38] K. Momma, F. Izumi, VESTA 3 for three-dimensional visualization of crystal, volumetric and morphology data, J. Appl. Cryst. 44 (2011) 1272-1276.

Chapter 3

Organic Bridging Linkers of MOFs for Enhanced CO_2 Adsorption

Research on MOFs has attracted considerable interest in materials science due to their high surface area, tunable porosity, and diverse applications in gas storage and separation. However, the weak interaction between the gas molecules and MOFs limits their practical application. This chapter focuses on the design and modification of organic bridging linkers in MOFs to enhance CO_2 adsorption performance. A series of pristine and functionalized 1,4-benzene dicarboxylate (BDC) organic ligands or linkers, including its fluorinated and chlorinated derivatives, as well as 1,4-naphthalene dicarboxylate (NDC) linker, have been systematically investigated. In addition, Li-decoration is employed as an effective strategy to improve the interaction strength between the CO_2 molecule and the linkers. The equilibrium geometries, binding enthalpy (ΔH), energy decomposition analysis (EDA), and frontier molecular orbital (FMO) analysis have been studied using the first principles-based dispersion corrected DFT (i.e., DFT-D). The binding enthalpy has also been evaluated at the MP2 level of theory. The results provide detailed insights into the role of functionalization and metal decoration in tuning the adsorption behavior, and offer valuable guidance for the rational design of efficient and stable MOF-based materials for CO_2 capture applications.

3.1 Introduction

MOFs are a class of crystalline nanoporous materials that have been used for several applications, such as gas storage and separation processes, catalysis, sensing, etc.[1–3] The ability of the MOF materials to be synthesized with different bridging linkers/ligands and metal ions/clusters provides enormous flexibility in the design of these porous materials with tunable pore size, pore volume, and high surface area.[4,5] As a class of MOFs, IRMOFs have the potential to be used as an excellent adsorbent. The first member of the MOF family (i.e., IRMOF-1) was synthesized using Zn_4O as a metal node and benzenedicarboxylate (BDC) as an organic linker, and has been widely investigated for storage of H_2, CO_2, and CH_4.[6–8] The other member of the IRMOF family are formed either by replacing the benzene ring with larger aromatic rings or the C and H atoms of the rings with heteroatoms and functional groups respectively. It has

been found that among the various IRMOFs-n (n = 3, 6, 8, 11, 18) studied, the CO_2 adsorption capacity of IRMOF-1 is highest and hence pristine IRMOF-1 acts as an excellent adsorbent for CO_2.[9] Liu et al. studied the CO_2 adsorption at eight different positions of IRMOF-1 with three orientations of CO_2, suggesting the side position with CO_2 parallel attack at the hydrogen side of the linker edge is the most favorable adsorption site.[8] Yang et al. revealed that MOFs with larger surface area and free volume have CO_2 high storage capacity.[10] Moreover, Torrisi et al. used DFT to study CO_2 interactions with functionalized aromatic molecules, guiding the design of linkers with enhanced CO_2 adsorption energy.[11,12] These studies suggest that interaction energy, positions, and orientations of the gas molecule, along with the organic linkers of the MOF materials, contribute to understanding the adsorption mechanism of CO_2 and designing novel MOFs with their applications in high uptake. However, due to the low reactivity (interaction energy) of the adsorbate or linker's surface, the adsorption of CO_2 on the pristine MOF linkers belongs to the weak physical adsorption, limiting the practical application of MOF as an adsorbent material. According to findings from earlier research, altering the adsorbate surface through techniques like metal doping or decoration, chelation, functionalization, and ligand/linker modification boosts the chemical reactivity of the substrate and strengthens the interaction between the gas molecules and the linker-based materials.[13–20] MOF synthesized with benzenetricarboxylate (BTC) and benzenedicarboxylate (BDC) linkers are known for their high thermal and hydrolytic stability and possess intrinsic porosity which have shown enhanced binding strength with the frameworks, resulting in a significant amount of CO_2 adsorption. Aprea et al. reported the isosteric heat of CO_2 adsorption (Q_{st}) on polymeric copper(II) benzene-1,3,5-tricarboxylate (Cu-BTC) MOF to be 25.9 kJ/mol.[21] Another study by Liu et al reported CO_2 adsorption for a series of functionalized MIL-47-X (where X = -Cl, -Br, $-CH_3$, $-CF_3$, OH, OCH_3) containing BDC as their constituent organic linker reached a maximum Q_{st} value of -24.99 kJ/mol.[22] Besides increased strength of interaction, targeting high stability will likely establish MOFs as the next generation of materials for practical CO_2 capture. Using fluorinated ligands is an effective approach for creating a highly stable, rigid, and multidimensional framework with a well-crystalline phase.[23,24] The -F moiety attached either to the ligand or trapped within the pores helps to stabilize the MOFs and acts as a structure-directing agent that influences the final topology of MOFs.[25]

In this work, we have computationally designed eight MOFs linkers i.e., 1,4-benzene dicarboxylate (BDC), 3-fluoro 1,4-benzene dicarboxylate (FBDC), 3,6-difluoro 1,4-benzene dicarboxylate (DFBDC-1), 2,3-difluoro 1,4-benzene dicarboxylate (DFBDC-2), 2,3,5,6-tetrafluoro 1,4-benzene dicarboxylate (TFBDC), 3,6-dichloro 1,4-benzene dicarboxylate (DClBDC-1), 2,3-dichloro 1,4-benzene dicarboxylate (DClBDC-2), and 1,4 naphthalene dicarboxylate (NDC) using molecular cluster model systems. This work studies the effect of fluorine and chlorine substitution at center and side positions of the linker on CO_2 adsorption, predict the interaction strength and guides the designing of hydrophobic MOFs. Although some studies have been conducted for CO_2 adsorption in fluorinated MOFs, the effect of the number and position of the -F and -Cl on the organic bridging linkers of MOFs using the molecular cluster model has not been reported previously. Here, we employed the first principles-based hybrid periodic DFT method with van der Waals (in short vdW) corrections (i.e., Grimme's D3 dispersion corrections) to calculate the equilibrium geometries of the complexes. The single-point energy of the equilibrium structures of the systems considered has been computed by both the DFT (B3LYP-D3) and second-order Møller-Plesset Theory (MP2) methods. The study of binding enthalpy (ΔH) shows the weak interaction of the CO_2 molecule with the pristine linkers, so the strategy of Li-decoration has been used to see its effect on the ΔH value. We computationally found that among all the complexes, CO_2 adsorption at the center position of the Li-decorated BDC, FBDC, DClBDC-1 and side position of the BDC, FBDC, DFBDC-1, and DFBDC-2 shows a strong physisorption interaction, which is essentially required for facile CO_2 release. Further to explain the interaction mechanism and find the contribution from different energy components to the ΔH value, the Energy Decomposition Analysis (EDA) was performed, and both the electrostatic and polarization energy components were found to be the most dominant ones. Also, to check the stability of the complexes, Frontier Molecular Orbital (FMO) analysis was performed at the equilibrium structure of the complexes, which shows a strong interaction, and it was found that the complexes remained stable even after Li decoration.

3.2 Computational details

The mechanism of CO_2 adsorption on the linkers has been investigated by employing the first principles-based unrestricted hybrid DFT. The equilibrium structures, geometries, energies of the molecular orbital, and the contribution of different energy

components to the relative enthalpy (ΔH) of the complexes were obtained by employing the B3LYP method with Grimme's 3rd order dispersion corrections, i.e., B3LYP-D3, implemented in the Gaussian 16 suite code.[26] To incorporate the long-range weak vdW dispersion effects between the atoms of the complexes, Grimme's dispersion corrections parameter (-D3) has been added with the DFT approach (i.e., B3LYP-D3), which is necessary for the weakly bound systems.[27–33] The hybrid B3LYP functional has been widely used for geometry optimization of systems containing metal atoms in their constitution, providing an accurate description and fair indication of the interaction energy.[34] We further calculated the ΔH at the second-order Møller Plesset (MP2) level of theory, which is a more accurate *ab initio* method. We took the relaxed structures obtained from the B3LYP-D3 method and calculated the single-point energies at the MP2 level to obtain the ΔH value. The correlation consistent polarization valence triple- ζ quality Gaussian basis set (cc-pVTZ) has been used for defining the atomic orbitals of all the atoms in the linkers.[35] This basis set is advantageous over other basis sets as it contains a higher basis function for each atom and gives much better results with high accuracy in the calculations. Using the same methods and basis sets, frequency (i.e., harmonic vibrational analysis) and thermodynamic calculations were performed to obtain the value of ΔH and confirm the stable geometry of the complexes. All the structures were optimized without any symmetrical constraints, and the optimized minimum-energy structures were confirmed to be stationary points on the potential energy surface. The equilibrium structures of all the complexes were visualized by using ChemCraft.[36] We used GaussView 6.1[37] for the pictorial representation of various adsorption sites, and this is a graphical interface implemented in Gaussian16.

The relative or binding enthalpy (ΔH) calculation includes geometry optimizations of the pristine/pure and Li-decorated linkers with one CO_2 molecule adsorbed to the center and side positions. After obtaining the equilibrium structure, the values of ΔH were calculated using the same B3LYP-D3 and MP2 methods. Also, the equilibrium geometries were further used to perform the localized molecular orbital energy decomposition analysis (LMO-EDA) using the General Atomic and Molecular Electronic Structural System "GAMESS" suite code.[38] Further, energies of the highest occupied molecular orbital (HOMO) and lowest unoccupied molecular orbital (LUMO) collectively known as Frontier Molecular Orbital (FMO) has been calculated

to find the stability of the complexes. The temperature and pressure were kept at 298.15 K and 1.0 atm, respectively, for all the calculations.

3.3 Molecular systems design and adsorption sites

The linkers studied here contain the basic building unit of the first synthesized MOF-5 (or IRMOF-1) material i.e., 1,4-benzene dicarboxylate (in short BDC) ligand or linker with halogen group elements attached to different positions of the BDC linker. These linkers contain hydrogen (H), carbon (C), oxygen (O), Fluorine (F), and Chlorine (Cl) atoms as their constituent atoms. BDC is a benzene ring with a carboxyl group attached at the para positions of the ring commonly known as 1,4-benzene dicarboxylate. FBDC is 3-fluoro 1,4-benzene dicarboxylate, where one fluorine is attached at the meta position of the BDC linker. DFBDC-1 and DFBDC-2 are difluoro 1,4-benzene dicarboxylate with two fluorine atoms attached to different positions of the BDC linker. In the case of DFBDC-1, one fluorine atom is attached at the meta and the other is at the ortho position (i.e., 3,6-difluoro 1,4-benzene dicarboxylate) whereas, in the case of DFBDC-2, one fluorine is attached at the ortho while the other is at the meta position of the BDC ring (i.e., 2,3-difluoro 1,4-benzene dicarboxylate). TFBDC is 2,3,5,6-tetrafluoro 1,4-benzene dicarboxylate ligand which is formed by attaching four fluorine atoms at both the ortho and meta positions. DClBDC-1 and DClBDC-2 are dichloro 1,4-benzene dicarboxylate with two chlorine atoms attached to different positions of the BDC linker. In the case of DClBDC-1, one chlorine is attached at the meta position while the other is at the ortho position (i.e., 3,6-dichloro 1,4-benzene dicarboxylate) whereas, in the case of DClBDC-2, one chlorine is attached at the ortho position while the other is at the meta position (i.e., 2,3-dichloro 1,4-benzene dicarboxylate) of the BDC ring. NDC is 1,4 naphthalene dicarboxylate which is formed by a fused pair of benzene rings with carboxylate groups attached to the para positions. All the linkers considered in this work are depicted in Figure 3.1.

In the present work, the COOH groups attached to the linkers act as an excellent substitute for ligand modification for CO_2 adsorption. The high density of surface (-COOH) groups enhances the physisorption behavior with the increase in binding energy value. This effect is attributed to the lone pair donation of the oxygen in the group and carbon in the CO_2, and by hydrogen bond interactions of the acidic protons and the oxygen of CO_2.[39] Furthermore, the introduction of polar functional groups

such as -F, -Br, -Cl, -OH, -OOH, -NO_2, and -SO_3 in the organic linkers of MOFs can enhance CO_2 capacity, which is the result of interactions between the dipole of the polar functional group and the quadrupole moment of CO_2.[40] MOFs functionalized with -F and -Cl are effective approaches to introduce strong CO_2 adsorption sites on MOFs that can increase the binding affinity between the sorbents and CO_2. The F atoms are characterized by their high electronegativity and low polarizability, resulting in a highly polar C-F bond with a significant negative charge on the F atom as well as the hydrophobic nature of this bond. Consequently, fluorinated organic ligands are used in MOFs to enhance gas framework interaction due to the high porosity of the C-F bond and to increase water stability and hydrophobicity by incorporating F atoms into the pores.[41] While the F atom is the most commonly used halogen in the functionalized MOFs, Cl atom atoms are occasionally used as alternatives in the side chains of MOF aromatic skeletons to improve gas adsorption performance.

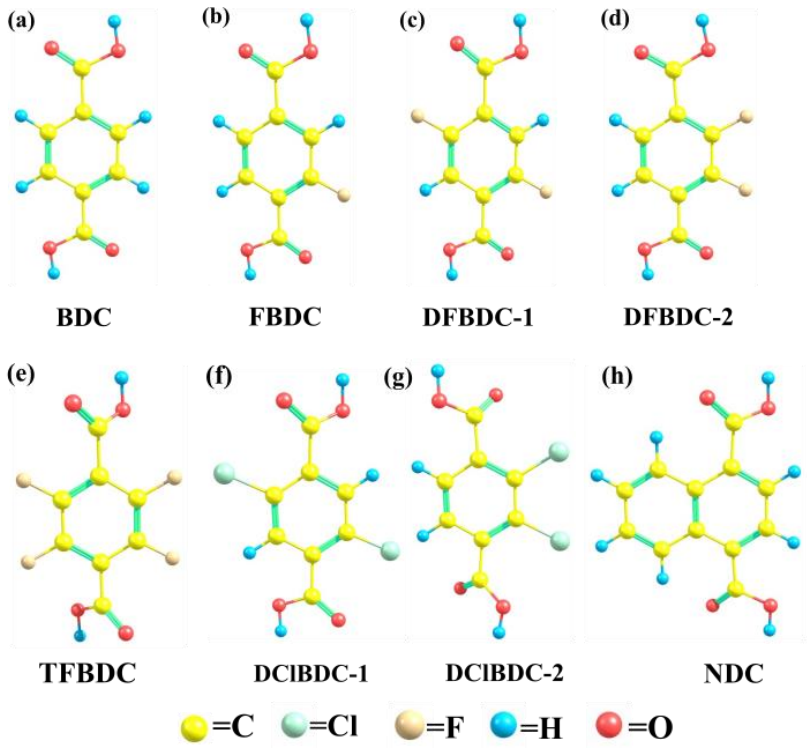


Figure 3.1 The equilibrium structures of the pure MOF's linkers: (a) 1,4-benzene dicarboxylate (BDC), (b) 3-fluoro 1,4-benzene dicarboxylate (FBDC), (c) 3,6-difluoro 1,4-benzene dicarboxylate (DFBDC-1), (d) 2,3-difluoro 1,4-benzene dicarboxylate (DFBDC-2), (e) 2,3,5,6-tetrafluoro 1,4-benzene dicarboxylate (TFBDC), (f) 3,6-dichloro 1,4-benzene dicarboxylate (DClBDC-1), (g) 2,3-dichloro 1,4-benzene dicarboxylate (DClBDC-2), and (h) 1,4 naphthalene dicarboxylate (NDC).

Understanding the adsorption mechanism in a porous material requires knowledge of the adsorption sites of the adsorbate, so we chose the center and side positions of the linkers as the adsorption sites. We carried out to obtain the equilibrium structures of other adsorption sites, unfortunately, the structures were not thermodynamically stable as they contain the imaginary frequency with the positive value of the relative enthalpy. For each system, the CO_2 molecule was placed perpendicularly to the center and side position of the pure and Li-decorated linkers. Figure 3.2 depicts the orientation of the CO_2 molecule for its adsorption at the center and side positions of the BDC linker.

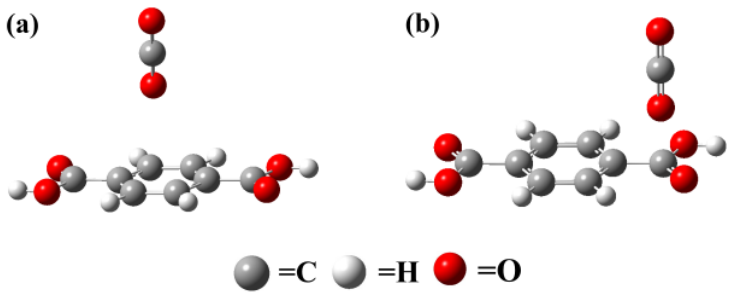


Figure 3.2 The adsorption of CO_2 molecule at the (a) center, and (b) side position of the BDC linker.

3.4 Results and discussion

3.4.1 Binding enthalpy

The change of enthalpy (ΔH) is one of the deciding parameters in determining the stability of any hypothetical compound or complex system. A negative value of ΔH suggests that the structure is thermodynamically stable and can be synthesized experimentally. Here, the adsorption of CO_2 at the center and side positions of both the pristine and Li-decorated linkers have been investigated. At first, the adsorption of CO_2 on all the pristine linkers was studied and the strength of their interactions was investigated. CO_2 molecule moved away from its original center and side positions after geometry optimization. The equilibrium geometries of the complexes are shown in Figure 3.3. In this case, the computed value of ΔH lies in the range of -8.07 to -14.09 kJ/mol computed by the B3LYP-D3 method, while the value lies between -6.76 to -13.98 kJ/mol obtained by the MP2 method. It should be noted here that both the B3LYP-D3 and MP2 methods provide similar values of the ΔH within the range of DFT error. The computed values of ΔH are negative, which also indicates the stability and exothermic nature of the adsorption processes. These values of ΔH indicate that CO_2 weakly interacts with the pristine linkers via vdW forces where the π electrons of

the benzene ring constituting the linkers attract the positively charged carbon atom of CO_2. It is observed that CO_2 adsorption at the center and side positions of the FBDC, DFBDC-1, DFBDC-2, TFBDC linkers, and side position of the DClBDC-2, and center position of the NDC linkers shows favorable physisorption behavior with the value of ΔH in the range of -12.05 kJ/mol to -14.09 kJ/mol. The highest binding configuration is observed for the NDC linker with one of the O atoms of CO_2 pointing towards the center of the six-membered ring, and this structure has the ΔH value of -14.09 and -13.98 kJ/mol computed by the B3LYP-D3 and MP2 methods, respectively. This low negative value of ΔH indicates the large amount of CO_2 adsorption, and it is due to the increased surface area of the NDC linker as it contains one extra benzene ring as compared to the other linkers. It is interesting to observe that the CO_2 adsorption at the side position of the NDC linker has the ΔH value -9.39 kJ/mol and -6.76 kJ/mol computed by the B3LYP-D3 and MP2 methods respectively. This difference in ΔH value at the center and side position of the NDC linker is due to the surface area available for CO_2 adsorption and different kinds of interactions. In contrast, the side position of the NDC linker has less available area available for the interaction of CO_2 with the linker and hence the values of relative enthalpy have increased as compared to the value at the center position. In the case of fluorine atoms attached at the ortho and meta position of the BDC linker, the value of ΔH increases (or CO_2 adsorption strength decreases) with the number of fluorine atoms. The increase in the number of fluorine atoms reduces the surface area and pore volume of the linker along with a minor decrement in the CO_2 adsorption.[42] The same is observed for the FBDC, DFBDC-1, DFBDC-2, and TFBDC linkers where the value of ΔH increases with the number of fluorine atoms. This increased value of ΔH is consistent with the fluorinated triazine framework, where CO_2 uptake capacity decreased upon increasing the fluorine content, mainly due to the high molecular weight of the fluorine atom.[43] It is also observed that the value of ΔH increases with the attached chlorine atoms at the ortho and meta position of the BDC linker forming DClBDC-1 and DClBDC-2 and as a result, it decreases the CO_2 adsorption strength. Thus, we can say that CO_2 adsorption at the center and side position of both the DFBDC-1 and DFBDC-2 linkers is more favorable than DClBDC-1 and DClBDC-2 linkers.

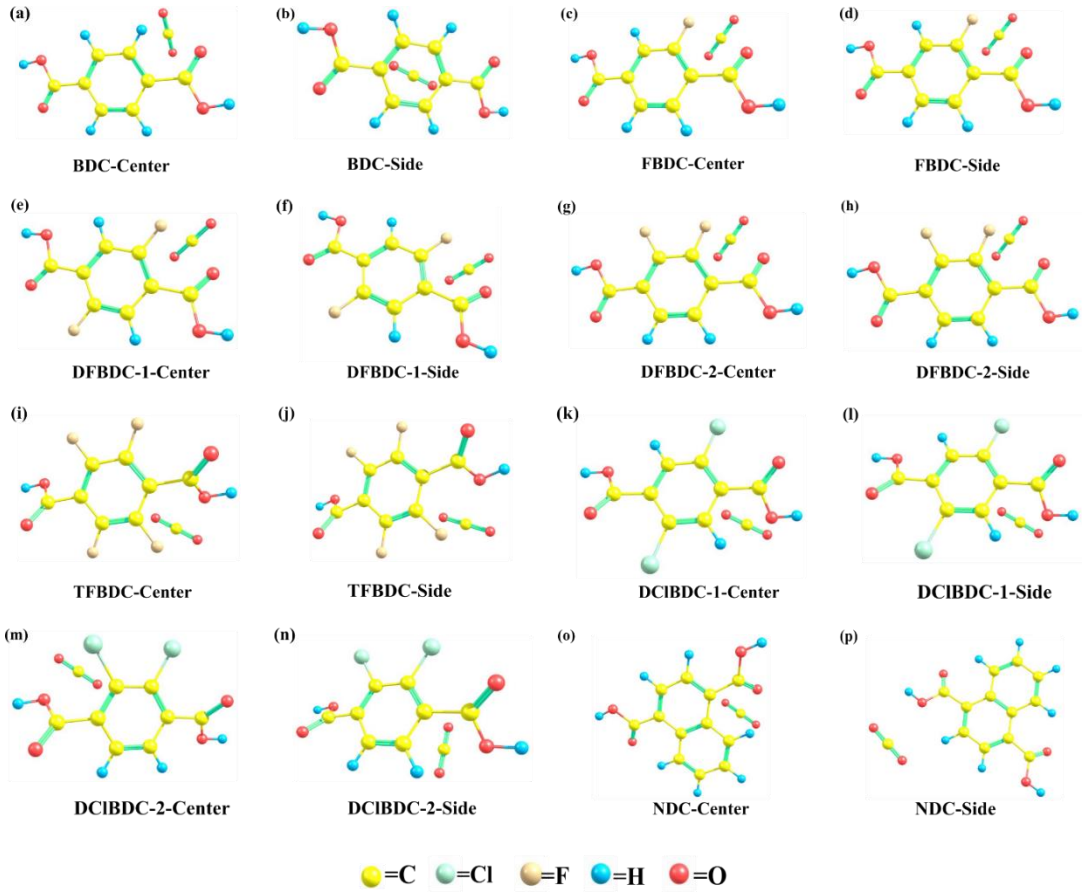


Figure 3.3 Equilibrium structures of both the pristine linkers and the adsorbed CO_2 at the center and side positions of the linkers: (a) BDC-Center, (b) BDC-Side, (c) FBDC-Center, (d) FBDC-Side, (e) DFBDC-1-Center, (f) DFBDC-1-Side, (g) DFBDC-2-Center, (h) DFBDC-2-Side, (i) TFBDC-Center, (j) TFBDC-Side, (k) DClBDC-1-Center, (l) DClBDC-2-Side, (m) DClBDC-2-Center, (n) DClBDC-2-Side, (o) NDC-Center, and (p) NDC-Side.

It is observed that the CO_2 adsorption at both the center and side positions of the FBDC, DFBDC-1, DFBDC-2, TFBDC linkers, and the side position of the DClBDC-2 and the center position of the NDC linkers shows favorable physisorption behavior, while both the center and side position of the BDC and DClBDC-1 and side position of the NDC linker are not showing favorable physisorption. This behavior of the linkers is attributed to the amount of charge transfer that takes place between the linker and the CO_2 molecule. Thus, to further understand the adsorption process, the charge transfer (C_T) between the linkers and the CO_2 molecule was calculated using Mulliken Population Analysis (MPA), and the corresponding values are also presented in Table 3.1. The positive value of C_T denotes the transfer of electrons from the linker to the CO_2 molecule, while the negative value denotes the electron transfer from the CO_2 molecule to the linker.[44] The values of binding enthalpy (ΔH) and charge transfer (C_T) have a

strong relation. The values of C_T during CO_2 adsorption at both the center and side positions of the FBDC, DFBDC-1, DFBDC-2, and TFBDC linkers are -0.016e, -0.015e, -0.014e, and -0.010e, respectively, corresponding to their values of ΔH lying in between the range of -13.34 kJ/mol to -12.05 kJ/mol, and thus, they show favorable physisorption nature. CO_2 adsorption at the center and side positions of the DClBDC-2 depends on the position of the chlorine atoms attached to the primary BDC linker. The center position shows a value of ΔH about -9.95 kJ/mol and a C_T value of -0.009e, while the side position has a value of -12.38 kJ/mol with a C_T value of -0.005e. The weak CO_2 adsorption at both the center and side positions of the BDC and DClBDC-1 linkers and the side position of the NDC linker is attributed to the low C_T value. The values of C_T during the CO_2 adsorption at the side position of both the BDC and NDC are 0.004e and 0.008e respectively, indicating the transfer of charge from the linker to the CO_2 molecule and therefore this result suggests that the nature of the adsorption is mainly electrostatic interactions.

Table 3.1 The charge transfer (C_T) of CO_2 at the center and side positions of the pristine and Li-decorated organic linkers.

Linkers	Position	C_T (e) Pure	C_T (e) Li-decorated
BDC	Center	-0.004	0.153
	Side	0.004	0.153
FBDC	Center	-0.016	0.156
	Side	-0.016	0.156
DFBDC-1	Center	-0.015	-0.016
	Side	-0.015	0.158
DFBDC-2	Center	-0.014	-0.014
	Side	-0.014	0.158
TFBDC	Center	-0.010	-0.015
	Side	-0.010	-0.015
DClBDC-1	Center	-0.007	0.159
	Side	-0.007	-0.013
DClBDC-2	Center	-0.009	-0.014
	Side	-0.005	-0.009
NDC	Center	-0.009	-0.011
	Side	0.008	-0.011

Next, we performed Li-decoration on the pristine linkers to see their effect on the binding strength (ΔH) of the CO_2 molecule. Due to the strong affinity of positively charged metal ions to the adsorbing gases, this strategy has been widely implemented for hydrogen storage.[19,45–48] Moreover, the choice of metal ions and their coordination environment plays a crucial role in the performance of MOF for CO_2 adsorption. The introduction of a very low coordination number for a metal ion (CN=2) in the simulation can be a useful strategy. This approach can induce interactions that may not be possible in the crystal structure of a MOF with a higher coordination number. The low coordination number of Li metal ions can lead to the creation of unsaturated or open metal sites. The presence of open metal sites corresponds to high CO_2 uptake, which is due to strong CO_2-metal interaction.[49] The adsorption of Li atoms on all the linkers forming Li-decorated complexes was studied by fully optimizing the structures, with Li atoms originally positioned near the O atoms of the COOH group attached to the six-atom carbon ring (C_6H_4 units). After geometry optimization, the lithium atom preferred to be in a position between the two neighboring oxygen atoms. The Li atoms decorated on each side of the linkers carry an average charge value of approximately +0.2e/Li atom to +0.3e/Li atom, suggesting the transfer of charges from the Li atoms to the linkers. To further investigate CO_2 capture, we optimized the structures with CO_2 positioned at both the center and side positions as was performed for the pristine linkers. The strong interaction of CO_2 with the linkers resulted in higher enthalpy of adsorption, which can be attributed to the large quadrupole moment of CO_2 as well as the presence of coordinatively unsaturated metal (Li) sites. Moreover, the structures were a little distorted after geometry optimization, which is attributed to the transfer of charges from the Li atoms to the linkers. The equilibrium geometries of the complexes are shown in Figure 3.4.

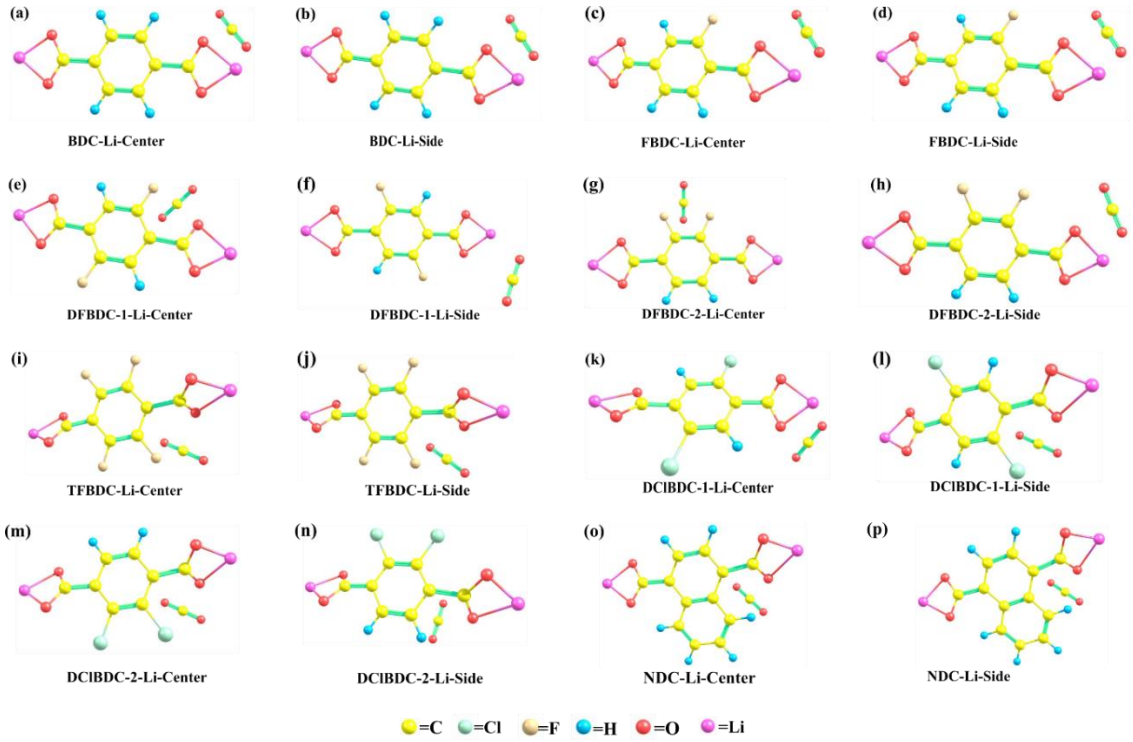


Figure 3.4 Equilibrium structures of the Li-decorated linkers and the adsorbed CO_2 at the center and side positions: (a) BDC-Li-Center, (b) BDC-Li-Side, (c) FBDC-Li-Center, (d) FBDC-Li-Side, (e) DFBDC-1-Li-Center, (f) DFBDC-1-Li-Side, (g) DFBDC-2-Li-Center, (h) DFBDC-2-Li-Side, (i) TFBDC-Li-Center, (j) TFBDC-Li-Side, (k) DClBDC-1-Li-Center, (l) DClBDC-2-Li-Side, (m) DClBDC-2-Li-Center, (n) DClBDC-2-Li-Side, (o) NDC-Li-Center, and (p) NDC-Li-Side.

Based on the computed results of CO_2 adsorption on the Li-decorated linkers, it is observed that the value of ΔH at both the center and side positions of the BDC and FBDC linkers has increased significantly. The side position of the DFBDC-1, DFBDC-2, and the center position of the DClBDC-1 linker are observed to have a drastic change in the ΔH value after Li-decoration. We find a reasonable quantitative agreement between our data calculated by both the methods and the experimentally synthesized M_2(dobdc) MOF systems.[50,51] This increment in ΔH is due to the large amount of charge transfer between the complexes. The center and side positions of the BDC and FBDC linker have the C_T value of 0.153e and 0.156e respectively, as provided in Table 3.1. Also, the values of C_T at the side positions of the DFBDC-1 and DFBDC-2 are 0.158e, while the center position of DClBDC-1 has a C_T value of 0.159e. This positive value of C_T indicates the charge transfer from the linker to the CO_2 molecule, indicating their high CO_2 adsorption at the center position and the possibility of their implementation in future porous MOF material. The CO_2 adsorption at the center

positions of DFBDC-1, DFBDC-2, and the side position of the DClBDC-1 linker exhibits ΔH values of -16.85 kJ/mol, -11.25 kJ/mol, and -16.85 kJ/mol. These values are attributed to the C_T values of -0.016e, -0.014e, and -0.013e respectively. It is further observed that the value of ΔH for the Li-decorated linkers with fluorine and chlorine attached at the ortho and meta positions does not follow the same trend as is observed in the case of pristine linkers. CO_2 adsorption at the center and side positions of both the TFBDC and DClBDC-2, as well as the center position of the DFBDC-1, DFBDC-2, and the side position of DClBDC-1 shows the reversible physisorption. This behavior is evident from the calculated values of ΔH, which is below the higher limit of physisorption. It is further noticed that the CO_2 adsorption at the center and side positions of the FBDC linker shows an approximate value of ΔH exceeding the higher limit of physisorption (i.e., 20 kJ/mol), while still lying below the lower range of chemisorption (i.e., 50 kJ/mol). The same behavior of CO_2 interaction is observed for the side position of the DFBDC-1, DFBDC-2, and the center position of DClBDC-1 linkers. These ΔH values indicate a strong physisorption behavior and thus, the process of adsorption and desorption are reversible at room temperature. The values of ΔH during CO_2 adsorption at the center and side positions of the linkers computed by both the B3LYP-D3 and MP2 methods are shown in Figure 3.5, respectively. Moreover, it is observed that the decoration of Li atoms on the NDC linkers does not influence the ΔH value much which was observed for the other Li-decorated linkers, despite its large surface area. Thus, we can say that the contribution of Li-atoms to the CO_2 adsorption of the NDC linker is not as significant as is observed for the other Li-decorated linkers showing favorable physisorption behavior. CO_2 adsorption at the center and side positions of the NDC linker have an equal amount of C_T value. Also, the hybridization between the CO_2 molecule and the Li atoms is weak, which indicates that the interaction between the CO_2 molecule and the linker originates mainly from the electrostatic ion and quadrupole moment of the CO_2 molecule and a major part of the electron/charge density comes from the atoms constituting the pristine NDC linker, which is depicted under the NBO analysis section. These negative value of ΔH indicates that the practical formation of porous materials using these linkers can be possible, and the present calculations suggests for synthesizing the MOFs with the application for CO_2 capture experimentally. These linkers show strong affinity with the CO_2 molecule and hence can be used as an efficient adsorbent for the future designing of an ideal porous material, especially MOFs.

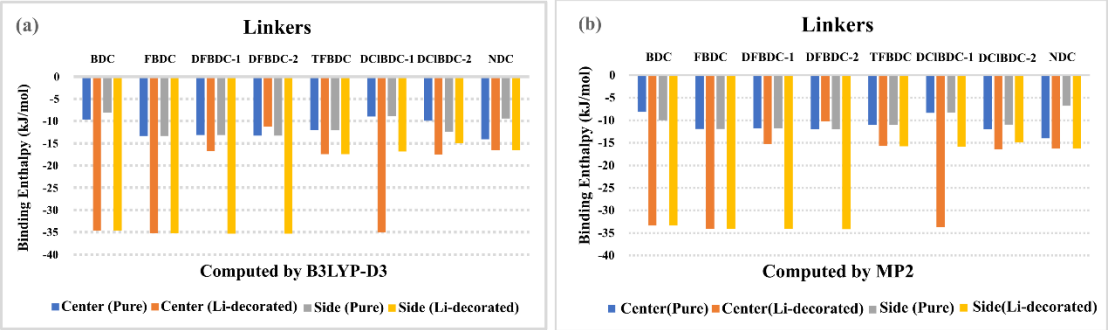


Figure 3.5 The binding enthalpy (ΔH) value of the adsorbed CO_2 molecule at the center and side positions of both the pure and Li-decorated linkers computed by the (a) B3LYP-D3, and (b) MP2 method.

Based on the above discussion, it can be stated here that the CO_2 adsorption on the Li-decorated linkers shows strong physisorption behavior with the ΔH lying below the chemisorption range, and these linkers are excellent candidates for CO_2 adsorption. This significant increase in the binding strength can probably be attributed to the combination of the high electrostatic interaction of CO_2 to the Li-atoms and the polar fluorinated and chlorinated pore surface of the framework. The main purpose of this study is to suggest the synthesis and predict the properties of these linkers towards CO_2 capture, and none of the linkers studied here have been integrated into a MOF or synthesized experimentally. However, the calculated vibrational frequencies and binding enthalpies predict that the systems are thermodynamically stable. Both the frequency analysis and binding enthalpy have been shown to demonstrate a material's stability and a posteriori synthesis in previous works.[13,14] The Li-decoration gives an accurate representation of the effect of metal units on the organic linkers. Indeed, increasing the length of the organic linkers results in a higher surface area of MOFs with enhanced gas adsorption. Nevertheless, extending the organic linker often compromises the stability of the MOFs. When CO_2 molecules are desorbed, there is a tendency for the system to partially or entirely collapse, resulting in reduced porosity or even non-porous frameworks. Consequently, creating a more stable MOF framework with increased porosity remains a significant challenge. Moreover, it is important to acknowledge that CO_2 adsorption in practical applications always takes place in the presence of water. Thus, hydrophobic frameworks are ideal for capturing CO_2 in humid environments. Despite water's large dipole moment causing it to interact more strongly with most frameworks than CO_2, the hydrophobic nature of some MOFs enables them to minimize competitive water adsorption. In this regard, selecting MOFs known for their high chemical and thermal stability will be crucial in the future. Thus, we expect

these linkers can be integrated into MOFs which will have a potential application in CO_2 capture and the present work will guide the researchers to synthesize these materials which may be readily fabricated experimentally in the future for industrial applications.

Pore volume is another crucial factor in evaluating the porosity of MOFs. Consequently, designing MOFs with high porosity and creating effective methods to preserve and utilize their pore space has been a key focus in MOF research. Organic linkers are crucial in forming pore structures and by functionalizing these linkers, the pore parameters (i.e., pore size and shape, pore volume, and surface area) of the MOFs can be systematically modified to improve their selectivity and adsorption strength towards a particular gas.[52] MOF-5 (or IRMOF-1) serves as a classic example of using isoreticular control to create various pore sizes through the judicious selection of organic linkers. Some highly porous MOFs for the adsorption of gases with their organic linkers, pore volume, and surface area are provided in Table 3.2.

Table 3.2 Some IRMOFs with their constituent linkers, and pore parameters (Brunauer-Emmett-Teller (BET) and Langmuir surface area, and pore volume).

MOFs	linker	surface area ($m^2\ g^{-1}$)	pore volume ($cm^3\ g^{-1}$)	ref
IRMOF-1	BDC	2205 (BET)	1.22	[53]
IRMOF-3	2-NH_2-BDC	1568 (BET)	1.07	[53]
IRMOF-6	Cyclobutyl-BDC	2516 (BET)	1.14	[54,55]
IRMOF-8	2,6-NDC	1021 (BET)	0.39	[56]
MIL-101(Cr)	BDC	5500 (Langmuir)	1.9	[57]

3.4.2 Energy decomposition analysis (EDA)

EDA is one of the quantitative methods based on electronic structure calculations that tell about the contribution of various energy components/terms to the total interaction energy or binding enthalpy. It provides a better understanding of the factors involved in molecular interactions. The result of this analysis helps us to predict the properties of an interacting molecular system which are difficult to analyze experimentally. Here, EDA has been performed for CO_2 adsorption at the side position of the BDC, FBDC, DFBDC-1, and DFBDC-2 linkers after obtaining the equilibrium structures. The contribution from different energy components to the total ΔH is shown in Figure 3.6. Our study shows that the components of electrostatic, exchange, repulsion, polarization,

and dispersion energies contribute to the total ΔH value for all the systems considered in the present investigation. Through this EDA, it is found that these complexes are effectively stabilized by electrostatic as well as polarization energy components, and thus are the main contributing components in the total ΔH. The contribution from exclusion and dispersion energy components to ΔH value was also found to be considerable. The repulsion energy term shows a positive contribution to the energy which is obvious due to Pauli's exclusion principle. Thus, it is observed that among all the energy components, the electrostatic energy term is the most dominant one as depicted in Figure 3.6.

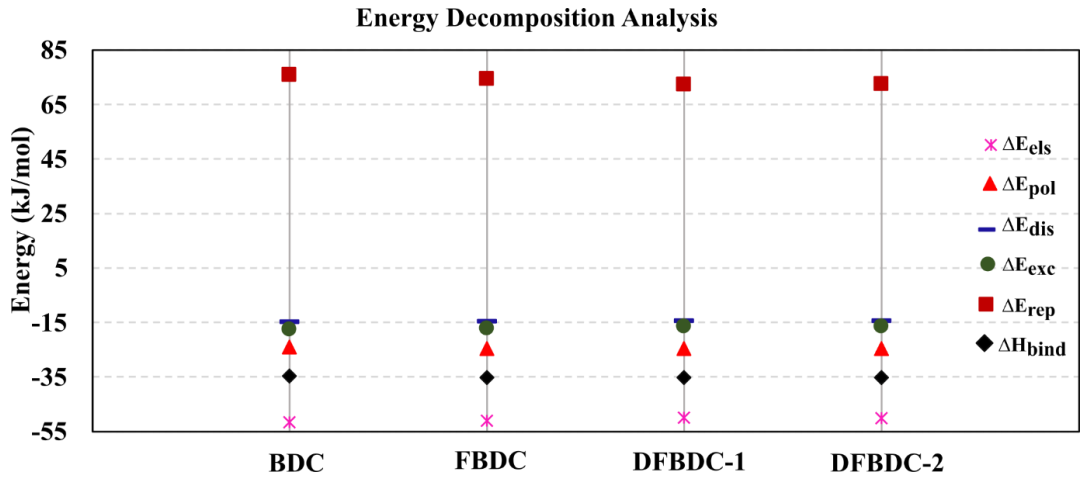


Figure 3.6 The Energy Decomposition Analysis (EDA) of CO_2 adsorption at the side position of the linkers. The electrostatic energy, polarization energy, dispersion energy, exchange energy, repulsion energy, and binding enthalpy are represented by ΔE_{els}, ΔE_{pol}, ΔE_{dis}, ΔE_{exc}, ΔE_{rep}, and ΔH_{bind} respectively. The units are expressed in kJ/mol.

3.4.3 Frontier molecular orbital (FMO)

To provide additional support to our calculated results and understand the interaction between the orbitals of adsorbed CO_2 and the organic linkers, we have extended our study to investigate the overlapping of molecular orbitals. The frontier molecular orbital analysis (FMO) was used to determine the energies of the highest occupied molecular orbital (HOMO) and lowest unoccupied molecular orbital (LUMO) levels. The HOMO and LUMO are collectively known as Frontier Molecular Orbital (FMO).[58] The difference in energies of the HOMO-LUMO gives an energy gap (E_g) which explains the stability as well as charge transfer taking place within the complex. The high value of E_g indicates the high kinetic stability and low chemical reactivity of the complex and hence chemically harder.[59] Since the physisorption process is a very weak

interaction, to explain CO_2 physisorption in the Li-linker complexes, there is a need for HOMO-LUMO energy gap and orbitals interactions. The HOMO is associated with bonding orbitals (σ) with more electrons, and LUMO is associated with anti-bonding orbitals (σ*) that doesn't have any electrons at the ground state.

This analysis was performed for all the linkers with adsorption of CO_2 molecule at the side positions of the linkers. For both the pure and Li-decorated linkers, we investigated the E_g value by calculating the energy difference between the HOMO and LUMO after CO_2 adsorption at the side position of the linkers. The computed energies of HOMO and LUMO of all the linkers and the energy gap between them are shown in Figure 3.7. It is observed from Figure 3.7 that there is a very small difference between the energy gap of FMO in the pure and Li-decorated linkers, however, the energy gaps of the Li-decorated linkers are higher than the pure linkers, which proves that the complexes remained stable even after the Li-decoration. For comparison, the HOMO and LUMO energies of the isolated CO_2 molecule were calculated to be -10.34 and 0.736 eV, respectively, corresponding to a HOMO-LUMO energy gap of 11.08 eV. The values of E_g of the BDC, FBDC, DFBDC-1, and DFBDC-2 complexes are 5.33eV, 5.09eV, 4.83 eV, and 4.97 eV, respectively. Among all the complexes showing strong binding affinity, the highest HOMO-LUMO gap (5.33 eV) is observed for the BDC linker where the energy of the HOMO and LUMO are -6.69 and -1.37 eV, respectively. The lowest value of HOMO-LUMO is observed for DFBDC-1 linker and the HOMO-LUMO energy gap is about 4.83 eV. The chances of electrons going from HOMO to LUMO decrease as the difference between the energies of FMO increases. Hence these high values of the energy gap of the BDC, FBDC, DFBDC-1, and DFBDC-2 organic linkers demonstrate higher kinetic stability of the complexes.

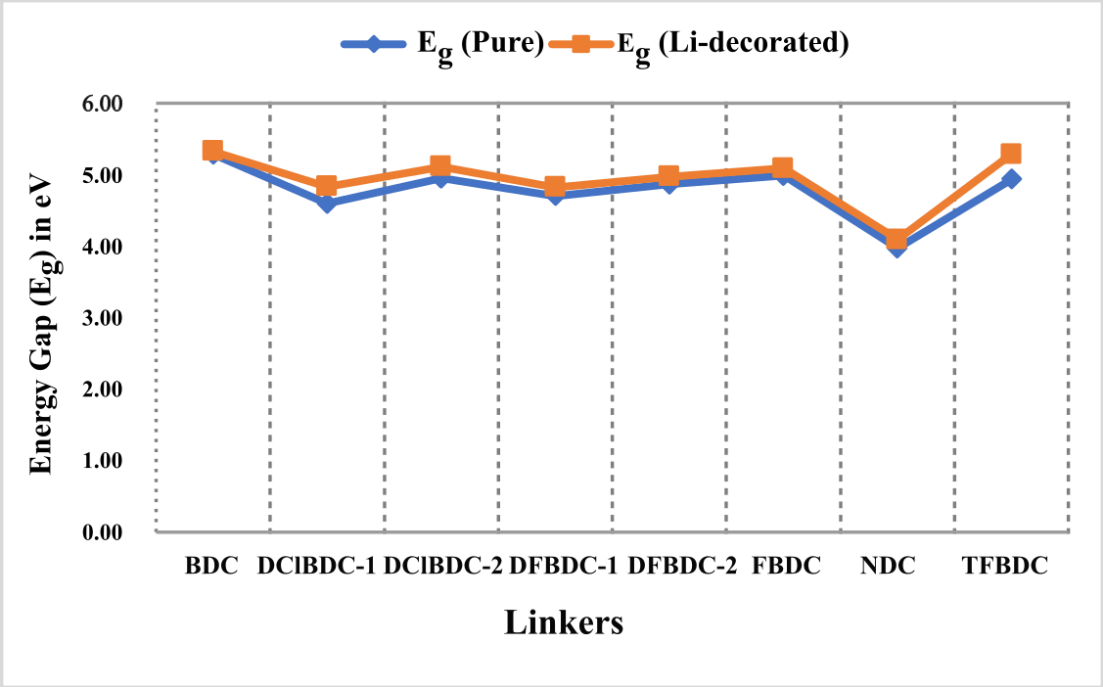


Figure 3.7 The energy gap (E_g) between the HOMO and LUMO of both the pure and Li-decorated linkers. The energies are expressed in eV.

Next, Natural Bond Orbital (NBO) analysis was performed to observe the interaction between the orbitals of the CO_2 molecule, Li atoms, and the organic linkers. Figure 3.8 shows the overlapping of the orbitals of both the pure and Li-decorated linkers with the adsorbed CO_2 molecule. Figure 3.8(a)-(e) shows the orbital overlapping of pure linkers with the adsorbed CO_2 molecule, where interaction is taking place between the ***p*** orbitals of C, O, and F atoms with the adsorbed CO_2 molecule. Similarly, Figure 3.8(f)-(j) shows the overlapping of Li-decorated linkers, where the ***s*** orbitals of Li and ***p*** orbitals of C, O, and F atoms are interacting with the ***p*** orbital of the CO_2 molecule. The positive wave function i.e., the up spin of the electrons or alpha electrons is indicated by the red color orbital, while the negative wave function i.e., the down spin of the electrons or beta electrons is indicated by the blue color orbital. It is observed from Figure 3.8 that the ***s*** orbital of Li and ***p*** orbitals of the C, O, and F atoms in the pure and Li-decorated linkers are interacting with the ***p*** orbital of the CO_2 molecule. These molecular interactions show that the CO_2 molecule is strongly adsorbed on the side position of the BDC, FBDC, DFBDC-1, and DFBDC-2 linkers. It is observed from Figure 3.8 that for CO_2 adsorption at the side position of the NDC linker, a major part of the electron/charge density comes from the atoms constituting the pristine NDC linker.

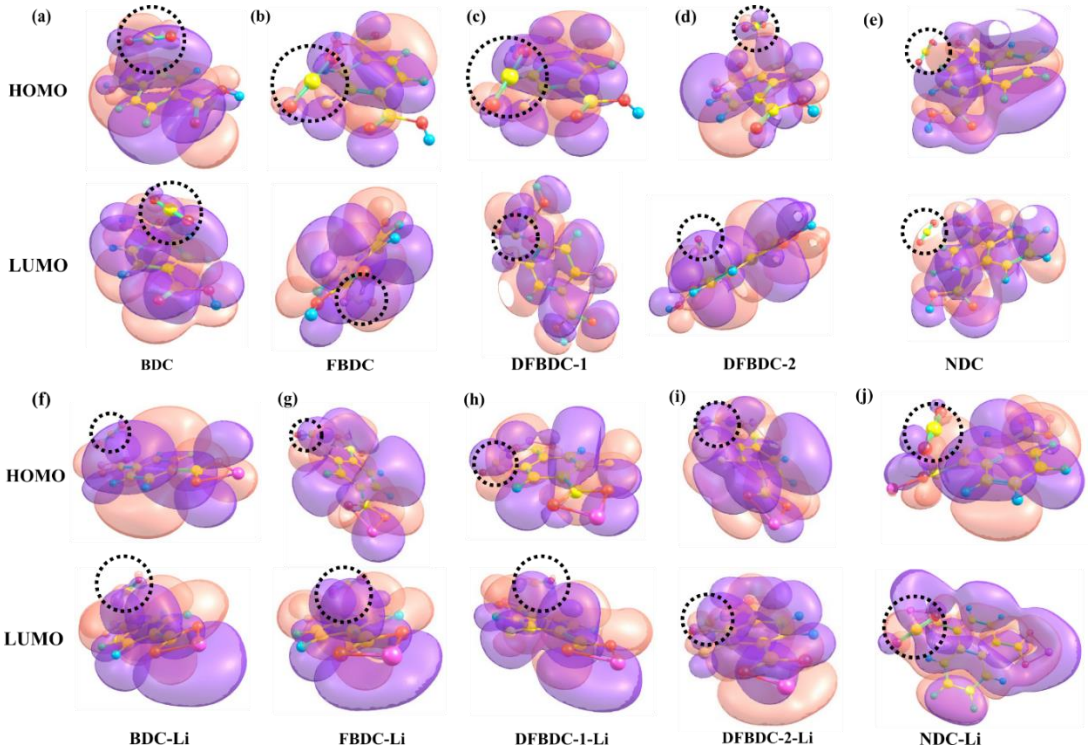


Figure 3.8 The HOMO-LUMO projections of CO_2 adsorption at the side position of pure and Li-decorated linkers (a) BDC linker, (b) FBDC linker, (c) DFBDC-1 linker, (d) DFBFC-2 linker, (e) NDC linker, (f) BDC-Li-decorated linker, (g) FBDC-Li-decorated linker, (h) DFBDC-1-Li-decorated linker, and (i) DFBDC-2-Li-decorated linker, (j) NDC-Li-decorated linker.

Thus, it is clear from the above discussion that the kinetic stability of the complexes remained even after Li-decoration. The orbital overlapping of the CO_2 molecule and the BDC, FBDC, DFBDC-1, and DFBDC-2 linkers depicts a large amount of C_T value and is therefore responsible for the high binding enthalpy value. However, despite the large surface area, CO_2 adsorption on the Li-decorated NDC linker is low due to weak hybridization between the CO_2 molecule and the Li-atoms.

3.5 Conclusions

In this study, we computationally investigated the effects of fluorine and chlorine functionalization and Li decoration of MOF organic linkers on CO_2 adsorption using molecular models. The B3LYP-D3 and MP2 methods with the cc-pVTZ basis set were employed to evaluate CO_2 adsorption strength at the atomistic level, with both methods yielding reasonably consistent interaction energies. The results of our investigation revealed that the CO_2 adsorption at the center and side positions of the FBDC, DFBDC-

1, DFBDC-2, and TFBDC linkers, as well as the side position of the DClBDC-2, and the center position of the NDC linkers exhibit favorable physisorption behavior, while CO_2 adsorption at the center position of the Li-decorated BDC, FBDC, DClBDC-1 and side position of the BDC, FBDC, DFBDC-1, and DFBDC-2 linkers reflects a strong physisorption behavior, indicating Li decoration is an efficient approach in designing linkers with highly improved affinity. Furthermore, the result of the EDA reveals that the contribution from both the electrostatic and polarization energy terms to the ΔH is the most dominant one. The high energy gap (E_g) of the complexes revealed their kinetic stability even after Li-decoration. The present study deals only with the organic linkers of MOFs for CO_2 adsorption. However, the use of isolated organic linkers presents certain limitations, including the absence of metal sites, framework-induced interactions, and structural confinement effects. Moreover, the adsorption behavior of fluorinated and chlorinated linkers integrated into MOFs under different operating conditions needs to be investigated experimentally and computationally to assess their practical applicability in CO_2 capture. Thus, designing MOFs with high chemical and thermal stability is essential for CO_2 capture, particularly under humid conditions. The incorporation of hydrophobic linkers can enhance the hydrophobic nature of MOF frameworks, potentially improving their hydrothermal stability and CO_2 capture performance. We expect that the linkers investigated in this work will provide useful insights for developing stable MOF frameworks with improved CO_2 adsorption characteristics and hydrothermal stability. The molecular-level understanding of CO_2 adsorption and electronic interactions developed in this chapter provides an important basis for extending the investigation toward catalytic conversion in porous materials. Therefore, the subsequent chapter focuses on electrochemical CO_2 reduction using sulfur-linked MPc-based COFs to investigate the influence of framework engineering and electronic structure tuning on catalytic activity and product selectivity.

3.6 References

[1] H. Furukawa, K. E. Cordova, M. O'Keeffe, O. M. Yaghi, The chemistry and applications of metal-organic frameworks, Science 341 (2013) 1230444.

[2] M. H. Yap, K. L. Fow, G. Z. Chen, Synthesis and applications of MOF-derived porous nanostructures, Green Energy Environ. 2 (2017) 218-245.

[3] M. Ding, X. Cai, H. L. Jiang, Improving MOF stability: Approaches and applications, Chem. Sci. 10 (2019) 10209-10230.

[4] P. D. C. Dietzel, V. Besikiotis, R. Blom, Application of metal-organic frameworks with coordinatively unsaturated metal sites in storage and separation of methane and carbon dioxide, J. Mater. Chem. 19 (2009) 7362-7370.

[5] K. S. Walton, A. R. Millward, D. Dubbeldam, H. Frost, J. J. Low, O. M. Yaghi, R. Q. Snurr, Understanding inflections and steps in carbon dioxide adsorption isotherms in metal-organic frameworks, J. Am. Chem. Soc. 130 (2008) 406-407.

[6] E. Klontzas, A. Mavrandonakis, G. E. Froudakis, Y. Carissan, W. Klopper, Molecular hydrogen interaction with IRMOF-1: A multiscale theoretical study, J. Phys. Chem. C 111 (2007) 13635-13640.

[7] T. Düren, L. Sarkisov, O. M. Yaghi, R. Q. Snurr, Design of new materials for methane storage, Langmuir 20 (2004) 2683-2689.

[8] Y. Liu, J. Liu, M. Chang, C. Zheng, Theoretical studies of CO_2 adsorption mechanism on linkers of metal-organic frameworks, Fuel 95 (2012) 521-527.

[9] Z. Mai, D. Liu, Synthesis and applications of isoreticular metal-organic frameworks IRMOFs-n (n = 1, 3, 6, 8), Cryst. Growth Des. 19 (2019) 7439-7462.

[10] Q. Yang, C. Zhong, J. F. Chen, Computational study of CO_2 storage in metal-organic frameworks, J. Phys. Chem. C 112 (2008) 1562-1569.

[11] A. Torrisi, C. M. Draznieks, R. G. Bell, Impact of ligands on CO_2 adsorption in metal-organic frameworks: First principles study of the interaction of CO_2 with functionalized benzenes. I. Inductive effects on the aromatic ring, J. Chem. Phys. 130 (2009) 194703.

[12] A. Torrisi, C. M. Draznieks, R. G. Bell, Impact of ligands on CO_2 adsorption in metal-organic frameworks: First principles study of the interaction of CO_2 with functionalized benzenes. II. Effect of polar and acidic substituents, J. Chem. Phys. 132 (2010) 044705.

[13] S. Pakhira, J. L. M. Cortes, Quantum nature in the interaction of molecular hydrogen with porous materials: Implications for practical hydrogen storage, J. Phys. Chem. C 124 (2020) 6454-6460.

[14] N. Sinha, S. Pakhira, H_2 physisorption on covalent organic framework linkers and metalated linkers: A strategy to enhance binding strength, Mol. Syst. Des. Eng. 7 (2022) 577-591.

[15] A. Mavrandonakis, E. Klontzas, E. Tylianakis, G. E. Froudakis, Enhancement of hydrogen adsorption in metal-organic frameworks by the incorporation of the sulfonate group and Li cations. A multiscale computational study, J. Am. Chem. Soc. 131 (2009) 13410-13414.

[16] A. Mavrandonakis, E. Tylianakis, A. K. Stubos, G. E. Froudakis, Why Li doping in MOFs enhances H_2 storage capacity? A multi-scale theoretical study, J. Phys. Chem. C 112 (2008) 7290-7294.

[17] G. Lim, K. B. Lee, H. C. Ham, Effect of N-containing functional groups on CO_2 adsorption of carbonaceous materials: A density functional theory approach, J. Phys. Chem. C 120 (2016) 8087-8095.

[18] C. Gu, Y. Liu, W. Wang, J. Liu, J. Hu, Effects of functional groups for CO_2 capture using metal organic frameworks, Front. Chem. Sci. Eng. 15 (2021) 437-449.

[19] S. S. Han, W. A. Goddard, Lithium-doped metal-organic frameworks for reversible H_2 storage at ambient temperature, J. Am. Chem. Soc. 129 (2007) 8422-8423.

[20] Y. Liu, J. Liu, M. Chang, C. Zheng, Effect of functionalized linker on CO_2 binding in zeolitic imidazolate frameworks: Density functional theory study, J. Phys. Chem. C 116 (2012) 16985-16991.

[21] P. Aprea, D. Caputo, N. Gargiulo, F. Iucolano, F. Pepe, Modeling carbon dioxide adsorption on microporous substrates: Comparison between Cu-BTC metal-organic framework and 13X zeolitic molecular sieve, J. Chem. Eng. Data. 55 (2010) 3655-3661.

[22] S. Biswas, D. E. P. Vanpoucke, T. Verstraelen, M. Vandichel, S. Couck, K. Leus, Y. Y. Liu, M. Waroquier, V. V. Speybroeck, J. F. M. Denayer, P. V. D. Voort, New functionalized metal-organic frameworks MIL-47-X (X = -Cl, -Br, $-CH_3$, $-CF_3$, -OH, $-OCH_3$): Synthesis, characterization, and CO_2 adsorption

properties, J. Phys. Chem. C 117 (2013) 22784-22796.

[23] B. Mohan, Virender, R. Kadiyan, S. Kumar, V. Gupta, B. Parshad, A. A. Solovev, A. J. L. Pombeiro, K. Kumar, P. K. Sharma, Carbon dioxide capturing activities of porous metal-organic frameworks (MOFs), Microporous Mesoporous Mater. 366 (2024) 112932.

[24] B. Mohan, A. Kamboj, Virender, K. Singh, Priyanka, G. Singh, A. J. L. Pombeiro, P. Ren, Metal-organic frameworks (MOFs) materials for pesticides, heavy metals, and drugs removal: Environmental safety, Sep. Purif. Technol. 310 (2023) 123175.

[25] S. Kumar, B. Mohan, C. Fu, V. Gupta, P. Ren, Decoration and utilization of a special class of metal-organic frameworks containing the fluorine moiety, Coord. Chem. Rev. 476 (2023) 214876.

[26] M. J. Frisch, G. W. Trucks, H. B. Schlegel, G. E. Scuseria, M. A. Robb, J. R. Cheeseman, G. Scalmani, V. Barone, B. Mennucci, G. A. Petersson, et al., Gaussian, Inc., Wallingford CT, (2016).

[27] S. Grimme, Semiempirical GGA-type density functional constructed with a long-range dispersion correction, J. Comput. Chem. 27 (2006) 1787–1799.

[28] S. Grimme, J. Antony, S. Ehrlich, H. Krieg, A consistent and accurate *ab initio* parametrization of density functional dispersion correction (DFT-D) for the 94 elements H-Pu, J. Chem. Phys. 132 (2010) 154104.

[29] J. Hui, N. B. Schorr, S. Pakhira, Z. Qu, J. L. M. Cortes, J. R. López, Achieving fast and efficient K^+ intercalation on ultrathin graphene electrodes modified by a Li^+ based solid-electrolyte interphase, J. Am. Chem. Soc. 140 (2018) 13599-13603.

[30] S. Pakhira, J. L. M. Cortes, Intercalation of first row transition metals inside covalent-organic frameworks (COFs): A strategy to fine tune the electronic properties of porous crystalline materials, Phys. Chem. Chem. Phys. 21 (2019) 8785-8796.

[31] S. Pakhira, K. P. Lucht, J. L. M. Cortes, Dirac cone in two dimensional bilayer graphene by intercalation with V, Nb, and Ta transition metals, J. Chem. Phys.

148 (2018) 064707.

[32] Y. Lei, S. Pakhira, K. Fujisawa, X. Wang, O. O. Iyiola, N. P. López, A. L. Elías, L. P. Rajukumar, C. Zhou, B. Kabius, N. Alem, M. Endo, R. Lv, J. L. M. Cortes, M. Terrones, Low-temperature synthesis of heterostructures of transition metal dichalcogenide alloys ($W_xMo_{1-x}S_2$) and graphene with superior catalytic performance for hydrogen evolution, ACS Nano. 11 (2017) 5103-5112.

[33] S. Pakhira, J. L. M. Cortes, Tuning the Dirac cone of bilayer and bulk structure graphene by intercalating first row transition metals using first-principles calculations, J. Phys. Chem. C. 122 (2018) 4768-4782.

[34] X. B. Feng, N. M. Harrison, Electronic structure of $CaCuO_2$ from the B3LYP hybrid density functional, Phys. Rev. B 69 (2004) 132502.

[35] M. F. Peintinger, D. V. Oliveira, T. Bredow, Consistent Gaussian basis sets of triple-zeta valence with polarization quality for solid-state calculations., J. Comput. Chem. 34 (2013) 451-459.

[36] Chemcraft - graphical software for visualization of quantum chemistry computations. Version 1.8, build 682. https://www.chemcraftprog.com.

[37] R. Dennington, T. A. Keith, J. M. Millam, GaussView, Version 6.1.1, Semichem Inc., Shawnee Mission, KS, (2019).

[38] M. W. Schmidt, K. K. Baldridge, J. A. Boatz, S. T. Elbert, M. S. Gordon, J. H. Jensen, S. Koseki, N. Matsunaga, K. A. Nguyen, S. Su, T. L. Windus, M. Dupuis, J. A. Montgomery, General atomic and molecular electronic structure system, J. Comput. Chem. 14 (1993) 1347-1363.

[39] B. Petrovic, M. Gorbounov, S. M. Soltani, Influence of surface modification on selective CO_2 adsorption: A technical review on mechanisms and methods, Microporous Mesoporous Mater. 312 (2021) 110751.

[40] M. Ding, R. W. Flaig, H. L. Jiang, O. M. Yaghi, Carbon capture and conversion using metal-organic frameworks and MOF-based materials, Chem. Soc. Rev. 48 (2019) 2783-2828.

[41] S. A. A. Razavi, A. Morsali, Linker functionalized metal-organic frameworks,

Coord. Chem. Rev. 399 (2019) 213023.

[42] A. Shahtalebi, M. Mar, K. Guérin, S. K. Bhatia, Effect of fluorine doping on structure and CO_2 adsorption in silicon carbide-derived carbon, Carbon 96 (2016) 565–577.

[43] Z. Yang, S. Wang, Z. Zhang, W. Guo, K. Jie, M. I. Hashim, O. Š. Miljanić, D. E. Jiang, I. Popovs, S. Dai, Influence of fluorination on CO_2 adsorption in materials derived from fluorinated covalent triazine framework precursors, J. Mater. Chem. A 7 (2019) 17277-17282.

[44] F. Safari, M. Moradinasab, M. Fathipour, H. Kosina, Adsorption of the NH_3, NO, NO_2, CO_2, and CO gas molecules on blue phosphorene: A first-principles study, Appl. Surf. Sci. 464 (2019) 153-161.

[45] A. Blomqvist, C. M. Araújo, P. Srepusharawoot, R. Ahuja, Li-decorated metal-organic framework 5: A route to achieving a suitable hydrogen storage medium, Proc. Natl. Acad. Sci. U. S. A 104 (2007) 20173-20176.

[46] K. L. Mulfort, J. T. Hupp, Chemical reduction of metal-organic framework materials as a method to enhance gas uptake and binding, J. Am. Chem. Soc. 129 (2007) 9604-9605.

[47] Y. J. Choi, J. W. Lee, J. H. Choi, J. K. Kang, Ideal metal-decorated three dimensional covalent organic frameworks for reversible hydrogen storage, Appl. Phys. Lett. 92 (2008) 173102.

[48] D. Cao, J. Lan, W. Wang, B. Smit, Lithium-doped 3D covalent organic frameworks: High-capacity hydrogen storage materials, Angew. Chem. Int. Ed. 48 (2009) 4730-4733.

[49] M. K. Rana, H. S. Koh, J. Hwang, D. J. Siegel, Comparing van der Waals density functionals for CO_2 adsorption in metal organic frameworks, J. Phys. Chem. C 116 (2012) 16957-16968.

[50] W. L. Queen, M. R. Hudson, E. D. Bloch, J. A. Mason, M. I. Gonzalez, J. S. Lee, D. Gygi, J. D. Howe, K. Lee, T. A. Darwish, M. James, V. K. Peterson, S. J. Teat, B. Smit, J. B. Neaton, J. R. Long, C. M. Brown, Comprehensive study of carbon dioxide adsorption in the metal-organic frameworks M_2 (dobdc) (M =

Mg, Mn, Fe, Co, Ni, Cu, Zn), Chem. Sci. 5 (2014) 4569-4581.

[51] D. Yu, A. O. Yazaydin, J. R. Lane, P. D. C. Dietzel, R. Q. Snurr, A combined experimental and quantum chemical study of CO_2 adsorption in the metal-organic framework CPO-27 with different metals, Chem. Sci. 4 (2013) 3544-3556.

[52] Y. Zhao, H. Wu, T. J. Emge, Q. Gong, N. Nijem, Y. J. Chabal, L. Kong, D. C. Langreth, H. Liu, H. Zeng, J. Li, Enhancing gas adsorption and separation capacity through ligand functionalization of microporous metal-organic framework structures, Chem. Eur. J. 17 (2011) 5101-5109.

[53] D. Britt, D. Tranchemontagne, O. M. Yaghi, Metal-organic frameworks with high capacity and selectivity for harmful gases, Proc. Natl. Acad. Sci. U. S. A. 105 (2008) 11623-11627.

[54] J. L. C. Rowsell, O. M. Yaghi, Effects of functionalization, catenation, and variation of the metal oxide and organic linking units on the low-pressure hydrogen adsorption properties of metal-organic frameworks, J. Am. Chem. Soc. 128 (2006) 1304-1315.

[55] A. R. Millward, O. M. Yaghi, Metal-organic frameworks with exceptionally high capacity for storage of carbon dioxide at room temperature, J. Am. Chem. Soc. 127 (2005) 17998-17999.

[56] Y. Li, R. T. Yang, Significantly enhanced hydrogen storage in metal-organic frameworks via spillover, J. Am. Chem. Soc. 128 (2006) 726-727.

[57] M. Latroche, S. Surblé, C. Serre, C. M. Draznieks, P. L. Llewellyn, J. H. Lee, J. S. Chang, S. H. Jhung, G. Férey, Hydrogen storage in the giant-pore metal-organic frameworks MIL-100 and MIL-101, Angew. Chem. Int. Ed. 45 (2006) 8227-8231.

[58] H. Gao, Z. Liu, DFT study of NO adsorption on pristine graphene, RSC Adv. 7 (2017) 13082-13091.

[59] J. Aihara, Reduced HOMO-LUMO Gap as an index of kinetic stability for polycyclic aromatic hydrocarbons, J. Phys. Chem. A. 103 (1999) 7487-7495.

Chapter 4

Metallophthalocyanine-based COFs for CO_2 Reduction Reaction

This chapter focuses on the theoretical investigation of MPc-based COFs as efficient electrocatalysts for the CO_2 Reduction Reaction (CO_2RR). The two structurally analogous COFs, namely CoPc-DNDS-COF (in short DNDS) and CoPc-DSDS-COF (in short DSDS), incorporating sulfur-containing thiomorpholine and dithiine linkers, respectively, are systematically studied to understand their structural, electronic, and catalytic properties. The chapter presents the design strategy of these COFs, highlighting the role of ligand engineering in tuning the electronic properties and catalytic performance. Using the first principles-based periodic DFT-D method, both the 3D bulk structures and 2D monolayer slab are analyzed to explore their electronic band structures and density of states (DOS). Furthermore, the CO_2RR mechanism is investigated in detail by evaluating various reaction intermediates and their corresponding relative Gibbs free energy diagram. The study reveals distinct catalytic behaviors of the two COFs, where the DNDS exhibits high selectivity toward methane (CH_4) formation, while the DSDS favors carbon monoxide (CO) production. Overall, this chapter provides fundamental insights into the CO_2RR mechanism and demonstrates the potential of MPc-based COFs as tunable and efficient electrocatalysts for sustainable CO_2 reduction.

4.1 Introduction

The electrochemical CO_2 reduction reaction (CO_2RR) has been recognized as a promising approach to generate valuable products and mitigate CO_2 emissions and energy crises.[1,2] However, the sluggish kinetics and thermodynamic stability of CO_2, along with the competing hydrogen evolution reaction (HER), give rise to challenges in developing electrocatalysts with high selectivity and efficiency of CO_2RR.[3,4] In recent years, a variety of heterogeneous and homogeneous electrocatalysts have been developed for CO_2RR, however, the performance of these systems has yet to reach a level where they can be successfully implemented in industries for commercialization.[5–8] Metallophthalocyanine (MPc) acts as a class of electrochemically active organometallic homogeneous molecular catalysts for CO_2RR possessing significant advantages in structural tunability, chemical stability, and easy

availability.[9–12] However, challenges such as inefficient electron transfer, facile deactivation, and dependence on organic media hinder their practical utility.[13] In this regard, integrating MPc units into COFs offers a promising avenue for advancing electrochemical materials and has emerged as a prominent area of research interest.[14–18] MPc has been widely investigated for its redox properties and electrocatalytic activities.[19,20] The presence of metal ions in the MPc serves as a single atom catalytically active site for various chemical transformations, especially CO_2RR to hydrocarbons. Yae et al. developed new kinds of bimetallic phthalocyanine-based COFs (i.e., CuPcF_8-CoPc-COF and CuPcF_8-CoNPc-COF) containing dioxine linkages, which served as efficient electrocatalysts for CO_2RR.[21] Han et al. studied the electrocatalytic CO_2RR mechanism of two-dimensional polyimide-linked phthalocyanine-based COFs.[22] Linkages or organic bridging linkers play a crucial role in improving the magnetic, electronic, and optical properties of the COFs.[23,24] Until now, various linkages such as pyrazine, dioxine, cobalt (II) tetraaza [14] annulene, and piperazine have been utilized in the formation of MPc-derived COFs, influencing the band structure of the resultant materials. Therefore, increasing the family of MPc-based COFs by incorporating additional heterocyclic linkers presents a challenge and is highly desired for the sustainable development of energy technology. The integration of MPc units with sulfur-containing heterocycles within a single COF network through linkage chemistry engineering has not been reported before. Very recently, Yang et al. synthesized two novel CoPc-based COFs containing thiomorpholine and dithiine with their constituent linkers in CoPc-DNDS-COF and CoPc-DSDS-COF respectively.[25] The synthesis of these COFs were achieved via nucleophilic aromatic substitution reactions and the findings of their study indicated the conductive nature of the COFs, with well-defined and adjustable chemical structures, and act as a superb electrocatalyst for CO_2RR to produce CO molecule as a final product. Catalytic behavior was well-adjusted by altering the linkages via only one atom (i.e., the sulfur atom) such that the empty ***d***-orbital and the poor electronegativity of sulfur offers a chance to modify the electronic conjugation in materials featuring heterocycles. Cobalt phthalocyanine (CoPc) has gathered significant attention due to its superior activity and selectivity towards CO.[26,27] However, the detailed investigation of CoPc units combining with sulfur-containing heterocycles resulting in a COF material and its application in CO_2RR to methane (CH_4) has not been reported previously.

Herein, we report the distinctive catalytic properties of the previously synthesized COFs i.e., CoPc-DNDS-COF (in short DNDS) and CoPc-DSDS-COF (in short DSDS) as a heterogeneous molecular electrocatalyst for CO_2 reduction. As illustrated in Figure 4.1, these COFs are formed using Co-hexadecaflurophthalocyanine (CoPc) as the nodes and 2,5-diaminobenzene-1,4-dithiol (DNDS) or 1,2,4,5-benzenetetrathiol (DSDS) as their constituent organic linkers. The main emphasis of this work is to use the two systematic isoreticular structural analogs of 3D semiconductive COFs as electrocatalysts for efficient CO_2RR to methane (CH_4). At first, we examined the periodic unit cell of the 3D crystal structures of both the DNDS and DSDS COFs by thoroughly analyzing the structural and electronic properties using the QM periodic hybrid dispersion-corrected DFT (in short DFT-D) method. The bulk 3D crystal structure of both the DNDS and DSDS COFs shows an electronic band gap (E_g) of around 0.35 eV and 0.44 eV, respectively, computed by the DFT-D approach. To explore the reaction intermediates involved in the CO_2RR to CH_4, we have cleaved a (001) surface from the bulk 3D crystal structure and computationally designed a 2D monolayer slab structure for both the DNDS and DSDS COF materials. The study of the electronic band structure indicates that the value E_g of both the 2D DNDS and DSDS monolayers increases slightly, and these values are 1.49 eV and 1.64 eV, respectively, obtained by the same DFT-D method. After studying the electronic properties of both the DNDS and DSDS COF materials, we have examined the CO_2RR by investigating various reaction intermediates present on the surfaces of DNDS and DSDS monolayer COFs. The calculation of the Gibbs free energy (ΔG) indicates that most of the reaction intermediates are energetically and thermodynamically feasible. Our investigation revealed that DNDS monolayer has excellent electrocatalytic activity and selectivity for CO_2RR to CH_4, while the DSDS monolayer has selectivity towards desorption of CO molecule, which are consistent with experimental findings. The results of our study represent the potential of MPc-based COFs towards CO_2RR with high electrocatalytic activity and selectivity for the production of CO and CH_4.

4.2 Computational details

The periodic equilibrium structure (i.e., the structure of unit cells), optimized geometries, and electronic properties of both the 3-dimensional (3D) and two-dimensional (2D) monolayer slabs of the DNDS and DSDS COFs were achieved by

performing hybrid dispersion corrected periodic DFT, i.e., B3LYP-D3 method. All these computations were carried out using the *ab-initio* based CRYSTAL23 suite code[28] where the B3LYP-D3 method has been implemented. The accurate geometries, energy, electronic structure, and electronic properties were obtained by considering the weak van der Waals (vDW) interactions between the atoms and layers of both the 3D crystal structure and 2D monolayer slab, i.e., Grimme's 3rd order dispersion correction (-D3) has been added to the B3LYP DFT method (which is noted by B3LYP-D3 or DFT-D method throughout the chapter).[37–48] Triple-ζ valence with polarization (TZVP) quality Gaussian type basis sets were applied for the carbon (C), cobalt (Co), fluorine (F), hydrogen (H), nitrogen (N), oxygen (O), and sulfur (S) involved in the formation of both the bulk 3D crystal and 2D (slab) layer structures.

At first, after obtaining the equilibrium structures and geometries of both the bulk 3D crystal structures, the electronic properties, i.e., electronic band structures and total density of states (DOS) were computed at the same level of theory. Integrations inside of the first Brillouin zone were sampled on 4×4×16 Monkhorst-Pack[41] ***k***-mesh grids for the 3D crystal structure during geometry optimization and 20×20×20 Monkhorst-Pack ***k***-mesh grids for the calculations of electronic band structure and DOS. The band pathway for the 3D bulk crystal structures followed the high symmetry ***k***-points noted by: **Γ-K-M-H-A-L-M-Γ** followed by the original symmetry of the crystal. To investigate the contribution of the electron density of the cobalt (Co) atom in the total DOS, the partial DOS (PDOS) of the Co atom was computed and plotted in the present investigation. Further, the contribution of electron density from the ***d*** orbital of the Co atom in both the Co PDOS and the total DOS was also computed. Now, to explore the CO_2RR reaction mechanism, the 3D materials were cut into periodic 2D monolayer slabs. The height of the unit cell was kept at 500 Å (which considers that there is no periodicity in the z-direction in the 2D layer structure model in the *ab initio*-based CRYSTAL23 code. In other words, to accommodate the vacuum environment or provide enough distance to prevent unphysical forces from affecting periodic images (where proper 2D layer structure is reflected), the vacuum region in the z-axis was kept at ~ 500 Å in these computations.[42,43] For the 2D monolayers, electrostatic potential effects were included in the present calculations, which reveals that the energy for both the electronic band structure and DOS is determined with respect to vacuum (i.e., w.r.t. vac.) by using the "POTC" keyword implemented in CRYSTAL23 suite code. The equilibrium structures, geometries, and electronic properties, i.e., the electronic band

structures and total DOS of the 2D monolayer slabs were calculated using the same periodic hybrid B3LYP-D3 method. Integration across the first Brillouin zone was performed using the 4×4×1 Monkhorst k-mesh grids for 2D slabs, with band structure plotted along the highly symmetric **Γ-K-M-Γ** direction, yielding eight electronic bands around the Fermi energy level (E_F), consistent with the original symmetry of both the 2D DNDS and DSDS materials. The total DOS was computed using atomic orbitals from C, Co, F, H, N, and S atoms for both the 2D monolayer COFs. The electronic self-consistency criterion or the threshold for the convergence of energy, forces, and electron density was set to 10^{-7} a.u. during these calculations. For graphical representation and analysis of all the optimized structures including 3D bulk crystal structures, 2D monolayers, and reaction intermediates, a visualization code known as VESTA was used.[44]

4.3 Materials design

The origin of our material design depends on the reticular incorporation of molecular CO_2 electroreduction catalysts, metallophthalocyanines (MPcs), as a building block, resulting in the formation of conductive, porous, and extended framework network. The resulting COF materials, namely CoPc-DNDS-COF and CoPc-DSDS-COF consist of Co-hexadecafluorophthalocyanine (CoPc) as the nodes and the 2,5-diaminobenzene-1,4-dithiol (DNDS) or 1,2,4,5-benzenetetrathiol (DSDS) works as a bridging linker in the subject COFs, as illustrated in Figure 4.1. These specific building blocks based on MPcs were selected for two key reasons.[45] Firstly, MPcs are widely recognized molecular catalysts for CO_2 reduction whose activity and selectivity are strongly influenced by their metal centers. Secondly, the presence of functional groups with various heteroatoms adorning at the outer periphery of MPcs introduces an additional level of direct modification to the electronic properties of MPcs, facilitating electronic communication within the extensive conjugated framework. On the other hand, the catalytic behavior of the materials studied was well adjusted by altering the linker via only one atom, i.e., the sulfur (S) atom. We postulated that, based on the preceding design considerations, this ligand engineering with the MPc unit will enable us to systematically investigate the structure-property relationships of these materials category in the context of their catalytic performance using conductive framework materials, and will enable us to accomplish an efficient, hierarchical, and multifaceted tuning to the CO_2RR.

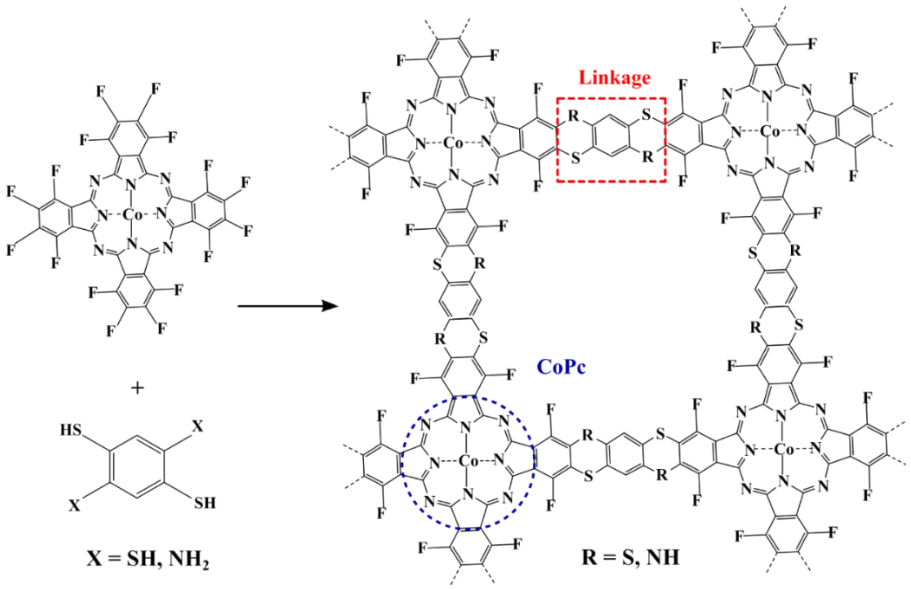


Figure 4.1 Illustration of the chemical structure of the COF materials, where X stands for SH and NH_2 group. The R with NH group in the resultant COF stands for the CoPc-DNDS-COF and S group stands for the CoPc-DSDS-COF. The metallophthalocyanine (MPc) part of the COF materials is shown by the dotted blue color circle, and the organic bridging linker part is shown by the dotted red color rectangle.

4.4 Results and discussion

4.4.1 Equilibrium geometries

The optimized equilibrium unit cell and electronic structure with the lattice parameters of both the 3D COFs (noted by CoPc-DNDS-COF and CoPc-DSDS-COF) were obtained by the hybrid B3LYP-D3 level of theory. The equilibrium geometries of the 3D DNDS COF have the tetragonal symmetry with space group P4/M, showing the cell parameters a = b = 20.79 Å and c = 3.50 Å, as shown in Figure 4.2 (a), while 3D DSDS COF has the tetragonal symmetry with space group P4/MMM, showing the cell parameters a = b = 21.29 Å and c = 3.55 Å. The equilibrium lattice parameters are consistent with the experimentally synthesized COFs.[22,25] In addition, we also calculated the framework properties (i.e., surface area, pore volume, and density) of the 3D bulk crystal structure of the DNDS and DSDS COFs using the same level of theory (i.e., B3LYP-D3). Equilibrium geometry, electronic band structure, total DOS, partial density of states (PDOS) of the Co atom, and the contributing component of the DOS of ***d***-orbital of the Co atom of both the 3D CoPc-DNDS and CoPc-DSDS COFs are shown in Figure 4.2 (a)-(e) and Figure 4.3 (a)-(e). The 3D bulk crystal structure of the DNDS and DSDS COFs have a surface area of 905.10 m^2/g and 900.01 m^2/g and pore volume of 0.24 cm^3/g and 0.25 cm^3/g, respectively. The higher surface area and pore width offer a much higher number of exposed single active sites. A large surface area

facilitates proton (H^+) and electron (e^-) transfer across the solid-liquid-gas boundaries, minimizing the CO_2RR to occur on a single atom. Moreover, utilizing extremely porous and stable substrates are crucial for enhancing catalytic efficiency and simultaneously reducing costs. Moreover, the densities of the 3D bulk crystal structure of DNDS and DSDS are 4.14 g/cm^3 and 3.92 g/cm^3, respectively. Now, to explore the CO_2RR mechanism, we have computationally designed a 2D monolayer slab of both the COFs, which has triclinic 2D layer symmetry (layer group number is 1). This 2D slab exhibits periodic symmetry in both the x and y directions, forming a triclinic 2D layer system with respect to the vacuum (w.r.t. vac.) space along the z-axis. The lattice parameters of these equilibrium 2D monolayer structures of the DNDS and DSDS are determined to be a = b = 20.71 Å and a = b = 21.25 Å obtained by the DFT-D method, which are in good agreement with the previous experimental results.[17] Equilibrium geometry, electronic band structure, total DOS, partial density of states (PDOS) of the Co atom, and the contributing component of the DOS of ***d***-orbital of the Co atom of both the 2D CoPc-DNDS and CoPc-DSDS COFs are shown in Figure 4.4 (a)-(e) and Figure 4.5 (a)-(e). Table 4.1 represents the equilibrium lattice parameters of the 3D bulk crystal structure and 2D monolayer slab of DNDS and DSDS COFs, indicating its space group symmetry, lattice constants (a, b, c), and interfacial angles (α, β, γ), bandgap (E_g), and state of the COFs calculated by the hybrid periodic DFT-D calculations.

Table 4.1 The equilibrium structural parameters (lattice constants and interfacial angles), space group symmetry, bandgap (E_g), and material state of the bulk 3D crystal structure and 2D monolayer of the DNDS and DSDS COFs.

Systems	**Lattice parameters (Å)**		**Interfacial angles (°)**		**Space group symmetry**	**Bandgap (eV)**	**Material state**
	a = b	**c**	**α = β**	**γ**			
DNDS (3D)	20.79	3.50	90°	90°	P4/M	0.35	Semiconductor
DSDS (3D)	21.29	3.55	90°	90°	P4/MMM	0.44	Semiconductor
DNDS (2D)	20.71	-	90°	-	P1	1.49	Semiconductor
DSDS (2D)	21.25	-	90°	-	P1	1.64	Semiconductor

4.4.2 Electronic properties

The electronic properties of a material are crucial for understanding its physical and chemical characteristics, as they represent the distribution of electrons across different energy levels and help in predicting the electrical behavior of the material. The equilibrium geometries, electronic band structure, energy bandgap (E_g), position of the E_F, and total DOS have been calculated to investigate the electronic/materials properties of the COFs, as illustrated in Figures 4.2 (a)-(c), 4.3 (a)-(c), 4.4 (a)-(c), and 4.5 (a)-(c). Most importantly, the experimentally synthesized catalysts were analyzed to understand their distinct electronic properties, which provided valuable insights into their catalytic performance. Using the B3LYP-D3 method, geometry optimization was carried out to obtain the equilibrium structure and to perform the electronic properties calculations (band structure, total DOS, contribution of Co atom and its ***d*** orbital to the total DOS) of both the 3D bulk crystal structures and 2D monolayer slab structures of the COFs. At first, using the original 3D space group symmetry of the 3D bulk crystal structures of DNDS and DSDS COFs, as shown in Figures 4.2 (a) and 4.3 (a), eight energy bands surrounding the Fermi Energy level (E_F) have been computed. These bands were plotted along a specific direction within the irreducible Brillouin zone, specifically selecting **Γ-K-M-H-A-L-M-Γ** high symmetric points followed by the original symmetry of the COFs. The electronic band from both regions comes closer towards the E_F, and hence the electronic properties computed by the DFT-D method reveal that both the DNDS and DSDS COFs have a semiconductor behavior with a value electronic band gap (E_g) of 0.35 eV and 0.44 eV, respectively, as illustrated in the band structure and total DOS as shown in Figures 4.2 (b), 4.2 (c), 4.3 (b), 4.3 (c). In the present study, the normalized electronic band structures have been plotted, i.e., the electronic bands have been computed and drawn with respect to the E_F. The present investigation reveals a substantial electron density surrounding the E_F, which helps to increase carrier (electrons) concentration and is beneficial to the charge transfer processes, thus facilitating the electrocatalytic CO_2RR. The presence of electron density around the E_F was confirmed by computing and drawing the DOS. The electronic states near the Fermi energy level (E_F) arise from the contributions of different constituent atoms of the DNDS and DSDS COF frameworks. The PDOS analysis further reveals that, among the electronic contributions originating from the Co atoms, the ***3d*** orbitals

provide the predominant contribution to the Co-projected DOS, as illustrated in Figures 4.2 (d)-(e) and 4.3 (d)-(e), respectively.

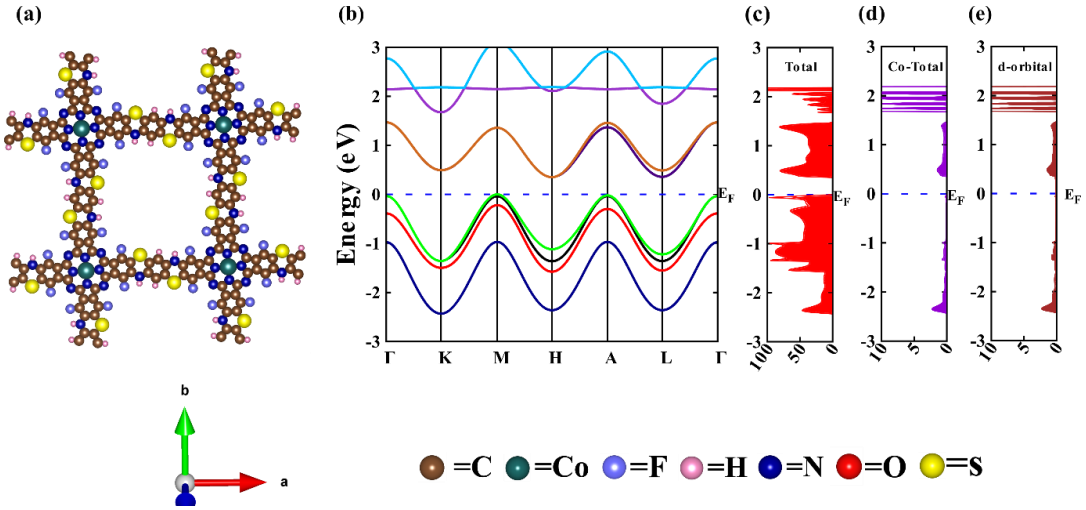


Figure 4.2 (a) Equilibrium geometry, (b) Electronic band structure, (c) Total DOS of the 3D CoPc-DNDS-COF, and Partial density of states (PDOS) of (d) Co atom, and (e) the contributing component of the DOS of ***d***-orbital of the Co atom.

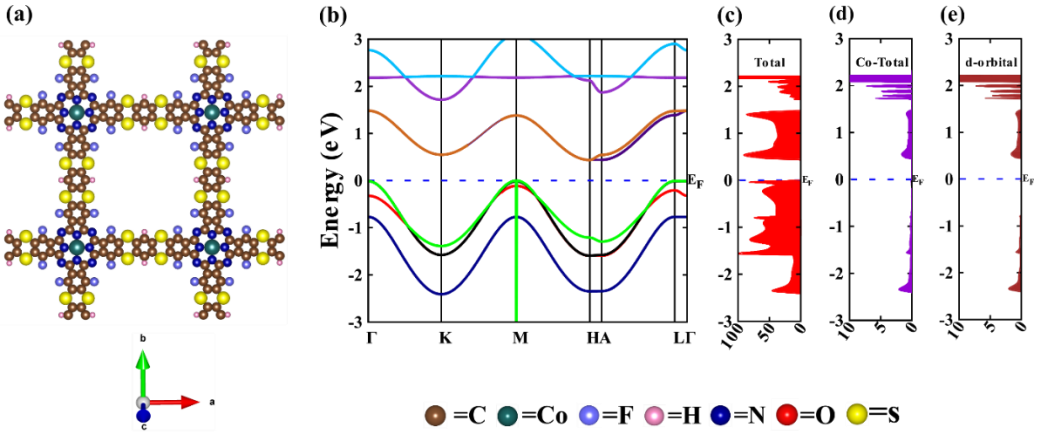


Figure 4.3 (a) Equilibrium geometry, (b) Electronic band structure, (c) Total DOS of the 3D CoPc-DSDS-COF, and Partial density of states (PDOS) of (d) Co atom, and (e) the contributing component of the DOS of ***d***-orbital of the Co atom.

Now, the electronic properties of the 2D monolayer of both the COFs have been computed to explore the electrocatalytic CO_2RR mechanism using the same DFT-D method. The present calculations show that the designed 2D monolayer of DNDS and DSDS COFs exhibit a semiconducting nature with an electronic bandgap (E_g) of 1.49 eV and 1.64 eV, respectively, as illustrated in Figures 4.4 (b) and 4.5 (b), suggesting their favorable electrical semi-conductivity and ensuring effective transfer throughout

the reaction mechanism. The calculated value of E_g is well consistent with the previously reported electronic energy band gap of CoPc COF, which has a value of 1.53 eV.[22] Also, these values are approximate to the band gap values obtained for the experimentally synthesized novel pyrazine (pz)-linked MPc based 2D COFs i.e., ZnPc-pz ~ 1.20 eV and CuPc-pz ~ 1.18 eV.[17] It is important to note that there is an increase in the E_g value of the 2D monolayers, as compared to the 3D bulk crystal structure of both the DNDS and DSDS COFs. This is because, as the linked unit size increases, the value of E_g of the unit decreases due to the reduction of quantum confinement, and as a result affects the electronic properties of the material.[46] To determine the electronic band structures at the equilibrium of the 2D monolayer of both the DNDS and DSDS COFs, a total of eight energy bands encompassing the E_F have been computed and plotted along a particular direction of irreducible Brillouin zone, specifically by selecting the high symmetric points **Γ-K-M-Γ**, as illustrated in Figures 4.4 (b) and 4.5 (b). The electronic band structure of both the 2D monolayer DNDS and DSDS COFs are notably flat, a characteristic frequently observed in porous materials like MOFs, COFs, and ZIFs.[53] This flatness results from the abundance of pores and cavities within the framework, mitigating interactions among neighboring atoms.[47] In other words, the calculation of valence and conduction bands (CB) represents the flat bands which is due to the localization of electron density. Despite the fact that the bands are almost flat, we can still gain valuable qualitative insights into the electronic structure of the 2D monolayer COFs. It should be mentioned here that the current computations have incorporated the electrostatic potential calculations, i.e., the energies of the band structure and total DOS are presented with respect to vacuum (w.r.t. vac.). For the DNDS COF, the E_F level was found to be approximately -4.32 eV, closely situated near the upper limit of the valence band (VB), while for the DSDS COF, the upper limit of the VB overlaps the E_F level situated at approximately -5.23 eV. Additionally, the band structure calculations for both the COFs were identified to have an indirect electronic E_g, which is subsequently validated by the total DOS calculations. In Figure 4.4 (c), the total DOS of the DNDS is illustrated, revealing that the maximum of the VB and the minimum of the CB are located at approximately -4.71 eV and -3.21 eV, respectively. Notably, the E_F level is positioned close to the maximum of the VB, while the minimum of the CB is approximately situated at -3.21 eV obtained by the DFT-D method. This discrepancy in energy level corresponds to the electronic band gap energy E_g, estimated to be around 1.49 eV. Moreover, the total DOS of the DSDS is illustrated in Figure 4.5

(c), indicating that the maximum of the VB and the minimum of the CB were observed at approximately -5.24 eV and -3.60 eV, respectively. Here, the E_F level overlaps the maximum of the VB, while the electron density at the minima of the CB is approximately 1.64 eV away from the E_F. This disparity in energies corresponds to the E_g value of 1.64 eV. The partial density of states (PDOS) calculations has been performed for both the 2D COFs to understand the availability of states for occupation in each case. The PDOS analysis of the Co atom suggests that a notable portion of the total DOS is attributed to the CB electron density, with the Co atom making a substantial contribution. In other words, the ***d***-orbitals electron density of the states of the Co atoms are the main contributing component to the total density of states of both the COFs considered in the present investigation. However, the involvement of the Co atom in the VB electron density is relatively less, as illustrated in Figures 4.4 (d) and 4.5 (d).

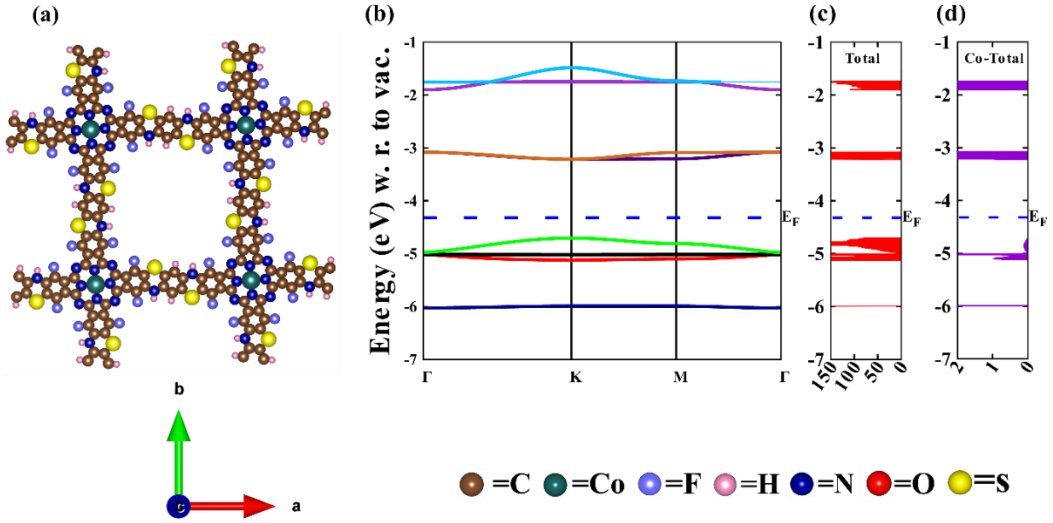


Figure 4.4 (a) Equilibrium geometry, (b) Electronic band structure, (c) Total DOS of 2D monolayer slab of the CoPc-DNDS-COF, and (d) Partial density of states (PDOS) of the Co atom.

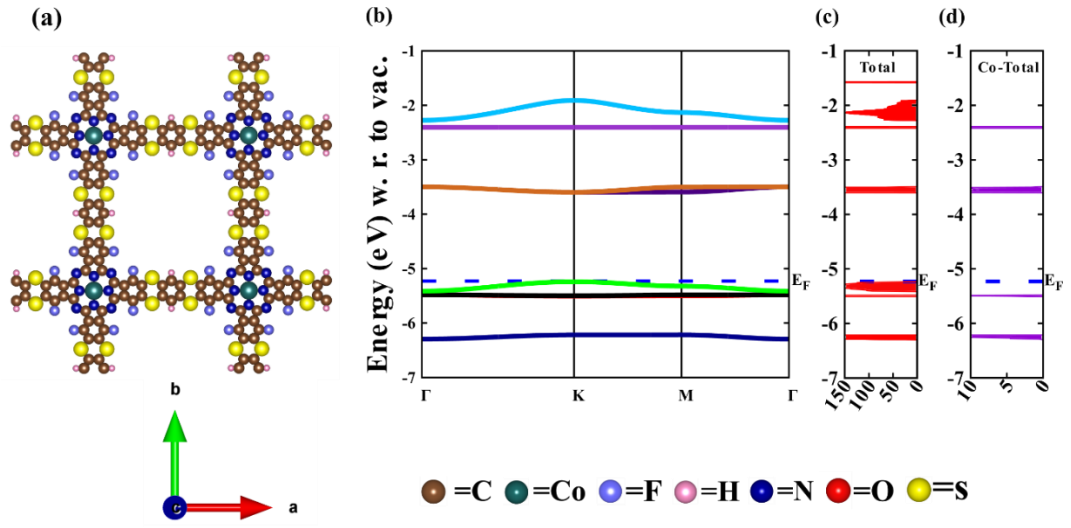


Figure 4.5 (a) Equilibrium geometry, (b) Electronic band structure, (c) Total DOS of 2D monolayer slab of the CoPc-DSDS-COF, and (d) Partial density of states (PDOS) of the Co atom.

Thus, the results of our finding suggest that both the 2D monolayers of DNDS and DSDS COFs exhibit characteristics of an indirect band gap semiconductor with an E_g value of 1.49 eV and 1.64 eV, respectively, obtained by the DFT-D method and thus, both the COFs may serve as favorable candidates for CO_2RR catalysts. It has been experimentally demonstrated that both the COFs studied here have the potential for electrocatalytic CO_2RR into carbon monoxide (CO). However, there has been a lack of theoretical and computational investigation about the catalytic activities of both the COFs studied into CO or CH_4. It should be noted here that until now, many research articles have shown electrocatalysts for the CO_2RR. However, only a few reports on CO_2RR on MPc-based COF, and MOF materials. This study fills the gap by investigating the catalytic mechanism of the 2D monolayers DNDS and DSDS COFs in facilitating the CO_2RR mechanism, providing a thorough analysis to support its potential as an effective electrocatalyst towards CO_2RR.

4.4.3 CO_2RR mechanisms

Understanding the affinity relationship between intermediates and surfaces is crucial for determining the free energy changes (ΔG) in the elementary reaction steps. Most of the studies have reported two electron transfer products such as CO and HCOOH during the CO_2RR. However, achieving highly efficient generation of valuable products through multiple proton-coupled electron transfers remains a scientific hurdle for COF-based materials in the electrocatalytic CO_2RR. One of the preferred reaction products

for CO_2RR on the 2D porous material is CH_4. The mechanism of CO_2RR to CH_4 at the cathode is an eight proton-electron ($8H^+/e^-$) transfer process. The initial elementary reaction typically involves the adsorption of gaseous reactants onto the catalyst surface, playing a pivotal role in determining the catalytic mechanism. Thus, we studied CO_2RR on the surface of the DNDS and DSDS COFs, starting from CO_2 adsorption. Using the B3LYP-D3 method, geometry optimization with harmonic vibrational analysis was carried out to determine the value of relative Gibbs free energy (ΔG) or the change of free energy of all the reaction intermediates involved in the CO_2RR steps, and to evaluate the catalytic activity of both the DNDS and DSDS COFs. A total number of eight possible reaction pathways of the CO_2RR towards CH_4 have been explored in the present study, and a possible reaction mechanism of the CO_2RR is proposed in Scheme 2. We have started with the analysis of the interaction between the key intermediates and the DNDS and DSDS surfaces i.e., at first, a CO_2 molecule was adsorbed on the surfaces of both the DNDS and DSDS COF materials and it is attached to the Co atoms of the DNDS and DSDS COFs. This leads to a proton-coupled electron transfer (PCET), resulting in the formation of *COOH intermediate. Subsequently, the *CO intermediate undergoes hydrogenation, yielding *CHO, $^*OCH_2$, and $^*OCH_3$ intermediates, and finally eight proton-electron transfer processes are involved in producing CH_4.

At first, we studied the catalytic activity on the surface of DNDS and the results of our calculations revealed that the 2D monolayer slab of DNDS exhibits the ability to spontaneously capture CO_2 molecules, as evidenced by their negative adsorption energy ($\Delta G_{CO_2} < 0\ eV$). The equilibrium geometries of the reaction intermediates for the most favorable pathway of CO_2RR into methane (CH_4) in the CO_2RR process on the surface of CoPc-DNDS-COF material computed by the DFT-D method are depicted in Figure 4.6. The calculated value of ΔG suggests that the lowest free energy pathway from CO_2 to CH_4 on the surface of DNDS is through $CO_2 \rightarrow$ *COOH $\rightarrow$ *CO $\rightarrow$ *CHO $\rightarrow$ *OCH_2 $\rightarrow$ *OCH_3 $\rightarrow$ *CH_3OH $\rightarrow$ *CH_3 $\rightarrow$ CH_4 (pathway 2, see Figure 4.7; where * represents the active site of the catalyst) by forming various reaction intermediates during the CO_2RR, suggesting that the production of methane is energetically more favorable than methanol. In the first proton-electron transfer process, the incoming pair of H^+/e^- may attack the carbon atom or the O atom of the CO_2 molecule to form *HCOO or carboxyl (*COOH) intermediate respectively. The value of ΔG computed by the DFT-D method indicates that the formation of *COOH (ΔG = 0.03 eV) is more

favorable than the *HCOO intermediate (ΔG = 1.11 eV). Next, the second pair of H^+/e^- may attack the O atom of the OH group in *COOH to form H_2O and *CO or carbon atom in *COOH to form formic acid (HCOOH). The active site-bound carbon monoxide (*CO) may either be desorbed from the electrode to generate free CO or proceed with further protonation. The value of ΔG required for CO desorption is 0.68 eV which is higher than the value of ΔG needed for the release of H_2O and *CO (-0.60 eV), indicating their higher selectivity towards *CO. Thus, the computed value of ΔG indicates that the formation of *CO is more stable than HCOOH (ΔG = 6.42 eV) or CO desorption, as depicted in Figure 4.7, and therefore, the process of protonation proceeds further. The *CO intermediate formed is considered as the beginning of the process of electrocatalytic reduction of CO_2 to methane and other C_{2+} products, and the adsorption energy of *CO is the descriptor of different products produced by the catalyst. In the present study, the computed value of ΔG required for the selectivity towards *CO is better than the energy observed for the previously synthesized COFs.[22] As the proton-electron happens sequentially, *CO is protonated to *CHO and *COH with the ΔG value of -0.16 eV and 1.96 eV, respectively. As for the possible pathway of CO_2RR, the calculated energy value manifests a lower energy barrier for yielding the *CHO intermediate instead of yielding *COH species. In fact, the calculated free energy of *CHO, $*OCH_2$, and $*OCH_3$ are -0.16 eV, -0.53 eV, and 0.15 eV, respectively (as depicted in Figure 4.7) indicating that the hydrogenation pathway is preferred over desorption. Both the $*OCH_2$ and $*OCH_3$ species are vital intermediates of CO_2 electroreduction to CH_4. Again, protonation of $*OCH_3$ either leads to the formation of methanol (CH_3OH) either attached to the surface or may desorb from the surface. The calculated value of CH_3OH desorption (ΔG = 0.17 eV) is unfavorable, thus $*CH_3OH$ undergoes further protonation to yield $*CH_3$ with an energy (ΔG) value of -1.0 eV. Lastly, $*CH_3$ is protonated to produce CH_4 with the value of ΔG approximately equal to -0.97 eV, consistent with the experimentally synthesized porous materials.[48–50] The corresponding structures of all the intermediates are shown in Figure 4.6, and the free energy diagram or potential energy surface (PES) representing the Gibbs free energies of the intermediates for all the eight reaction pathways on the surface of DNDS COF and at U = 0V are represented in Figure 4.7.

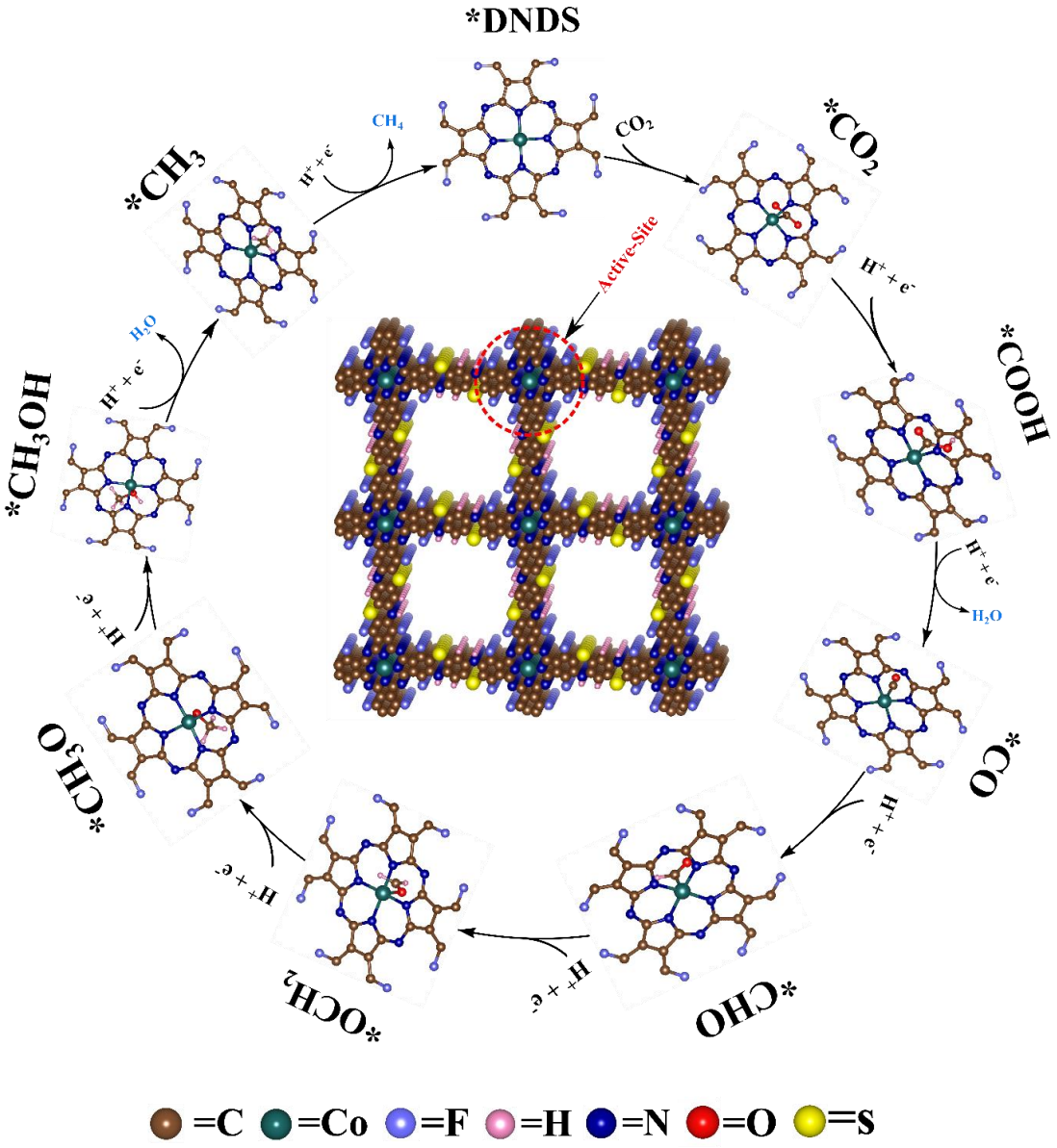


Figure 4.6 The equilibrium geometries of the reaction intermediates for the most favorable path of CO_2RR into methane (CH_4) in the CO_2RR process on the surface of CoPc-DNDS-COF material computed by the DFT-D method.

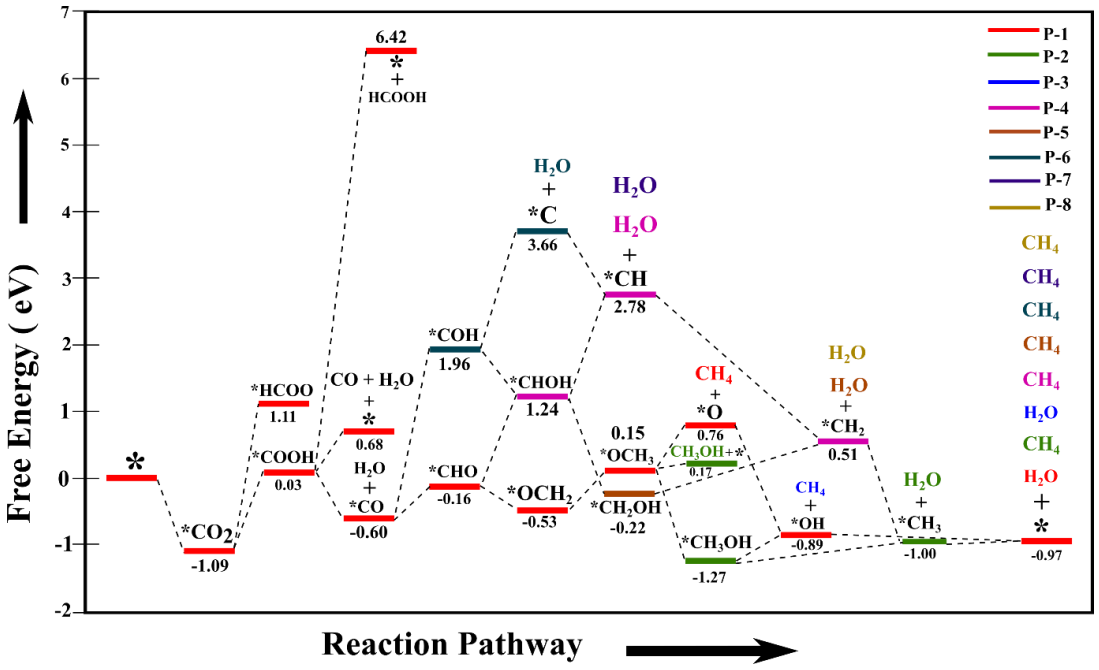


Figure 4.7 The free energy diagram computed by the DFT-D method (i.e., Gibbs free energy (ΔG in eV) profile) of all the eight pathways followed in CO_2 reduction reaction (CO_2RR) into methane (CH_4) at the surface of CoPc-DNDS-COF material.

To elucidate the mechanism of CO_2RR on the DSDS surface, we calculated the relative free energies along the typical pathways for the CO_2RR on Co sites. The initial step involved the adsorption of a CO_2 molecule on the Co site followed by the formation of the *COOH and *HCOO intermediates through the PCET process. The calculated value of ΔG associated with the formation of the *COOH and *HCOO intermediates were 1.32 eV and 9.10 eV, respectively, indicating that *COOH formation is thermodynamically more favorable than *HCOO under the considered reaction conditions. Subsequently, *COOH underwent another PCET process to transform into *CO intermediate or desorption of C_1 products like HCOOH and CO from the Co site of the catalyst. The simulated value of ΔG for the desorption of HCOOH is 6.42 eV, which is much higher than the energy required for the *CO formation, hence the reaction proceeds for the *CO intermediate formation or CO molecule desorption. The computed value of ΔG for the *CO intermediate is 0.76 eV, which is more than the energy barrier required for the CO desorption process (ΔG = 0.68 eV), indicating that the 2D monolayer of DSDS COF is much more favorable for CO desorption from the Co site of the catalyst. Thus, the results of our DFT calculations reveal that the DSDS surface is more prone to CO desorption rather than CH_4 reduction, consistent with the value of ΔG required for the desorption of the CO molecule of some experimentally

synthesized COFs.[22,25,49,51,52] The optimized structures of the intermediates involved in CO_2RR to CO desorption are depicted in the Figure 4.8, and the potential energy surface (PES) i.e., free energy diagram of the CO_2RR to the formation of CH_4 on the surface of DSDS is represented in Figure 4.9. The main objective of this work was to investigate whether these experimentally synthesized COFs can reduce CO_2 into CH_4 or not. The results of our findings match well with the experimental report of effectively reducing the CO_2 into CO on the surface of DSDS COF material, while our DFT calculations suggest that the DNDS COF can effectively reduce CO_2 into CH_4. Although direct experimental data on our specific material remains limited, some of the previously reported COFs emphasize the crucial role of DFT calculations combined with experiments in investigating reaction mechanisms for C_1 and C_2 products.[53–55] The mechanistic aspects of CO_2RR to CH_4 on the surface of a single atom catalyst and an organic frameworks shows an approximate values of ΔG about -3.0 eV and -1.0 eV, respectively,[54,56] suggesting that the simulated reactions in the current study are thermodynamically feasible and can occur on a long length scale.

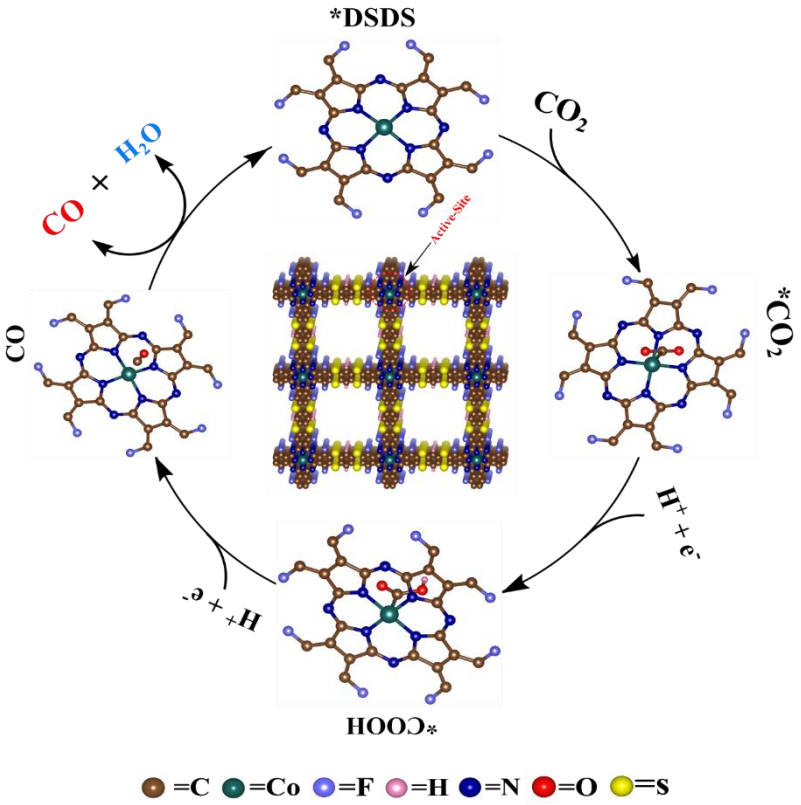


Figure 4.8 The equilibrium geometries of the reaction intermediates involved in the electrochemical reduction of CO_2 into carbon monoxide (CO) on the surface of CoPc-DNDS-COF material computed by the DFT-D method.

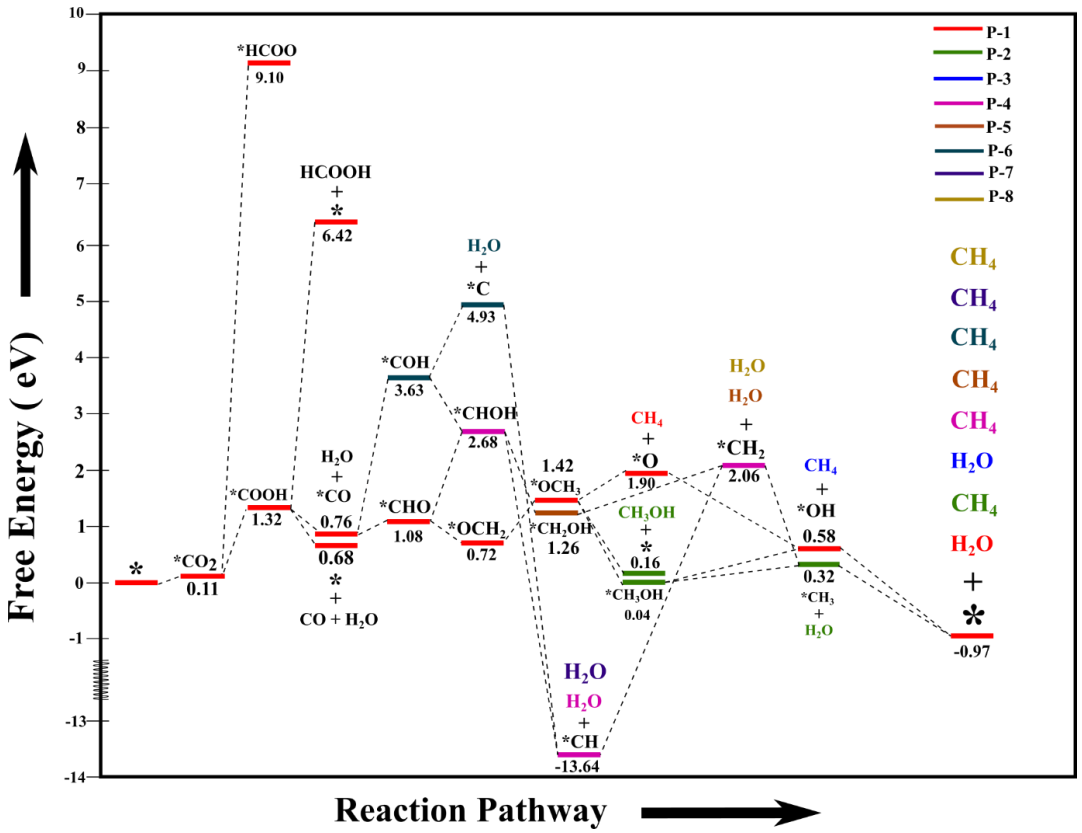


Figure 4.9 The free energy diagram computed by the DFT-D method (i.e., Gibbs free energy (ΔG in eV) profile) of all the eight pathways followed in CO_2 reduction reaction (CO_2RR) into carbon monoxide (CO) and methane (CH_4) at the surface of CoPc-DNDS-COF material.

An important challenge in the CO_2RR to hydrocarbons and alcohols is the rate of competing reaction, HER. For CO_2RR, the binding of the CO_2 needs to be strong enough for the molecule to be firmly attached to the surface, and the differential adsorption energy of $^*H$ must be small enough to prevent the predominant occurrence of the side reaction i.e., hydrogen gas formation (H_2 evolution). In CO_2RR, the first step of CO_2 molecule adsorption is a critical step during the entire catalytic process, while for the HER process to occur, $^*H$ adsorption plays a significant role in deciding whether the CO_2RR or the HER reaction mechanism will take place. Hence, we calculated the free energy change (ΔG) of the $^*H$ and $^*CO_2$ steps on the surface of DNDS and DSDS COFs. Based on simulated results, for the case of DNDS COF, the calculated value of ΔG for *H (H is adsorbed on the active site of the catalysts) is -0.57 eV, which is much higher than the ΔG value observed for $^*CO_2$ (-1.09 eV), while for the case of DSDS COF, the calculated value of ΔG for *H is 0.89 eV, and for that of $^*CO_2$ is 0.11 eV. These calculated values of *H and $^*CO_2$ indicate the hindrance to the occurrence of HER on both the COF surfaces.

4.4.4 Spin density

To elucidate the CO_2 adsorption behavior and uncover the origin of the fast rate of hydrogenation in CO_2RR to CH_4, the electron spin density for the reaction intermediates was analyzed to reveal the CO_2RR mechanism. We attribute the excellent CO_2RR performance of the DNDS COF to the electron-rich Co atom, which effectively adjusts the local electron density of the active Co sites, thereby enhancing the adsorption of reactant molecules and facilitating electron transfer to the intermediates, as evidenced in Figure 4.10. The spin density arises from the transfer of electrons between the electrocatalyst and intermediates through bonding interactions, influencing the catalytic activity by modulating the electronic properties of the active sites. The strength of these bonds correlates with the extent of electrons (charges) transferred, which is a key factor influencing the catalytic kinetics, particularly the adsorption and desorption of intermediates. Consequently, the spin density analysis helps to investigate the density of electrons, which is the difference between the α electron density and the β electron density. These electronic densities (i.e., α and β) are often visualized as isodensity surfaces or isosurfaces which are useful for investigating systems with unpaired electrons. Electronic spin density is positive in areas where an electron is more likely to be found in the α spin state referred to as up-spin, and negative where an electron is more likely to be found in the β spin state referred to as down-spin.[57] The transfer of electrons between the adsorbed intermediates and the Co atom also revealed their strong interaction. Figure 4.10 (a)-(i) shows the electron spin densities of the reaction intermediates, where a large amount of charge transfers from the substrate to the Co atom, making the Co atom negatively charged. These negatively charged Co atoms are considered to be active sites in the CO_2RR catalytic process**.** Moreover, it is observed that the N atom in the Pc ligand plays an important role in adsorbing and activating the CO_2 molecule. The electron delocalization causes an increase in electron density on the CoPc surface, which modulates the adsorption energy of $^*COOH$, $^*CHO$, $^*CH_2OH$, and $^*CH_3$ intermediates, while facilitating the desorption energy of $^*CO$, $^*OCH_2$, and $^*CH_3OH$ from the catalyst surface. This process ultimately promotes the CO_2RR to CH_4.

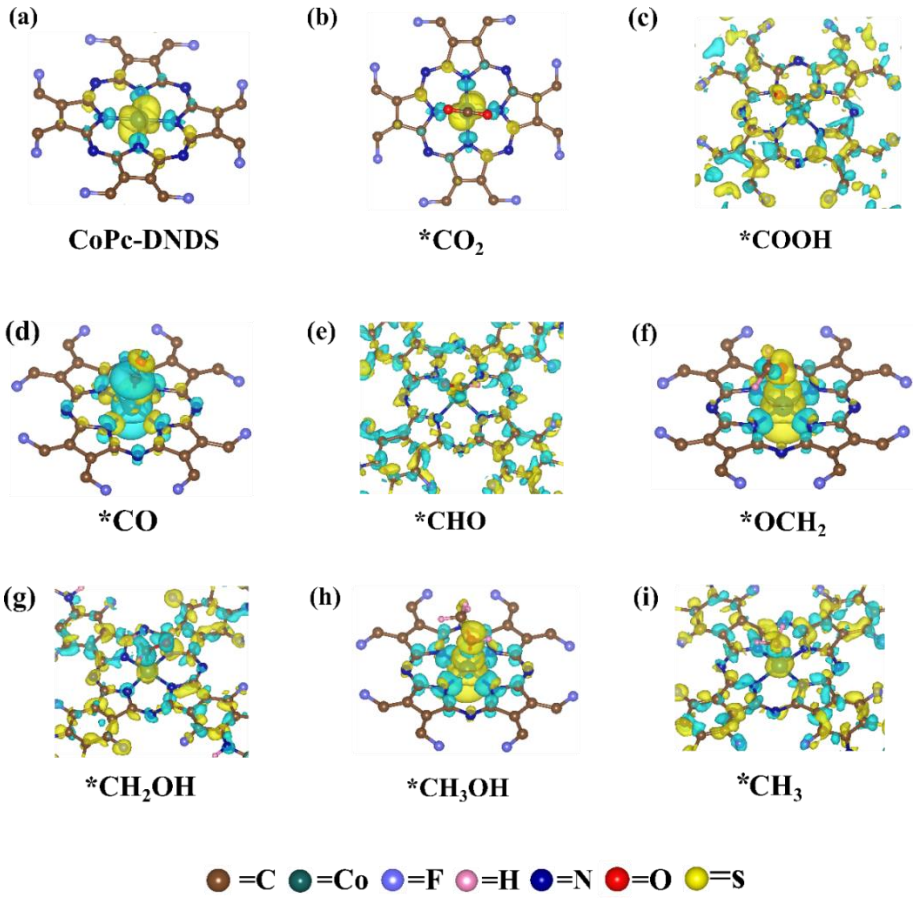


Figure 4.10 Electron spin density of all the intermediates adsorbed on the DNDS surface during CO_2 reduction into CH_4; (a) CoPc-DNDS surface; (b) *CO_2; (c) *COOH; (d) *CO; (e) *CHO; (f) *OCH_2; (g) *CH_2OH; (h) *CH_3OH; and (i) *CH_3. The yellow region represents the positive part of the wave function i.e., α spin, while the sky blue region represents the negative part of the wave function i.e., β spin. The * asterisk represents that the species (intermediate) is adsorbed on the surface of CoPc-DNDS-COF.

4.5 Conclusions

In summary, we have systematically investigated the critical roles of thiomorpholine, and dithiine linkages coordinated with the MPc unit in the activity and selectivity of the CoPc-DNDS and CoPc-DSDS COFs for the CO_2RR to CO and CH_4 using the DFT-D method. The equilibrium structure, geometry, and electronic properties of the 3D COFs have been achieved by employing the first principles-based hybrid DFT method. The study of the electronic properties revealed that the band gap of the 3D DNDS and DSDS COFs are 0.35 and 0.44 eV respectively. The 2D monolayer slab structures of both the COFs were computationally designed to explore the CO_2RR mechanism and their structural and electronic properties calculations found that the 2D monolayer structure of DNDS is an indirect bandgap of 1.49 eV, and that of the DSDS monolayer has a

bandgap of 1.64 eV, indicating the semiconducting behavior of both the COFs. The catalytic performance of the 2D monolayer COFs has been explored by computing the energy barriers corresponding to the change in Gibbs free energy (ΔG) during the CO_2RR mechanism on the Co site of the catalysts. The analysis of the electrocatalytic activity indicated that DNDS efficiently reduces CO_2 to CH_4 with a value of ΔG approximately equal to -0.97 eV, whereas DSDS favors CO desorption with a value of ΔG equal to 0.68 eV. The excellent catalytic activity of the DNDS COF is due to the presence of a sufficiently strong interaction between the reaction intermediates and the Co atom attached to the MPc unit, which facilitates the protonation of *CO, leading to the generation of CH_4 on the DNDS surface, as evident by the spin density of the intermediates. The results of our findings highlight the potential of a novel MPc group of low-cost and abundant electrocatalysts for producing CH_4 from CO_2. Moreover, our research demonstrates the great potential of using porous conductive COFs for the electrochemical conversion of CO_2 to CH_4 and paves the way for the design of high-performance CO_2 reduction catalysts through linkage engineering by strategically addressing the ideal combinations of metallophthalocyanines (MPc) with sulfur-containing linkages. The insights obtained from the catalytic activity and selectivity of sulfur-linked MPc-based COFs in this chapter further motivated the exploration of porous frameworks capable of promoting multi-carbon product formation during the CO_2RR. The present study primarily focused on the selective C_1 product, particularly CH_4 formation; however, the subsequent chapter extends the investigation toward Cu-based MPc MOF for the electrochemical reduction of CO_2 into both C_1 and higher valued C_2 products. This transition provides broader insights into the role of metal centers and structural engineering in regulating catalytic pathways and product selectivity in porous electrocatalysts.

4.6 References

[1] R. B. Lin, B. Chen, Reducing CO_2 with stable covalent organic frameworks, Joule 2 (2018) 1030-1032.

[2] S. Lin, C. S. Diercks, Y. B. Zhang, N. Kornienko, E. M. Nichols, Y. Zhao, A. R. Paris, D. Kim, P. Yang, O. M. Yaghi, C. J. Chang, Covalent organic frameworks comprising cobalt porphyrins for catalytic CO_2 reduction in water, Science 349 (2015) 1208-1213.

[3] Z. Weng, J. Jiang, Y. Wu, Z. Wu, X. Guo, K. L. Materna, W. Liu, V. S. Batista, G. W. Brudvig, H. Wang, Electrochemical CO_2 reduction to hydrocarbons on a heterogeneous molecular Cu catalyst in aqueous solution, J. Am. Chem. Soc. 138 (2016) 8076-8079.

[4] H. Bao, Y. Qiu, X. Peng, J. Wang, Y. Mi, S. Zhao, X. Liu, Y. Liu, R. Cao, L. Zhuo, J. Ren, J. Sun, J. Luo, X. Sun, Isolated copper single sites for high-performance electroreduction of carbon monoxide to multicarbon products, Nat. Commun. 12 (2021) 238.

[5] Y. S. Wei, M. Zhang, R. Zou, Q. Xu, Metal-organic framework-based catalysts with single metal sites, Chem. Rev. 120 (2020) 12089-12174.

[6] E. E. Benson, C. P. Kubiak, A. J. Sathrum, J. M. Smieja, Electrocatalytic and homogeneous approaches to conversion of CO_2 to liquid fuels, Chem. Soc. Rev. 38 (2009) 89-99.

[7] R. Francke, B. Schille, M. Roemelt, Homogeneously catalyzed electroreduction of carbon dioxide - methods, mechanisms, and catalysts, Chem. Rev. 118 (2018) 4631-4701.

[8] E. Zhang, T. Wang, K. Yu, J. Liu, W. Chen, A. Li, H. Rong, R. Lin, S. Ji, X. Zheng, Y. Wang, L. Zheng, C. Chen, D. Wang, J. Zhang, Y. Li, Bismuth single atoms resulting from transformation of metal-organic frameworks and their use as electrocatalysts for CO_2 Reduction, J. Am. Chem. Soc. 141 (2019) 16569-16573.

[9] Y. Pan, R. Lin, Y. Chen, S. Liu, W. Zhu, X. Cao, W. Chen, K. Wu, W. C. Cheong, Y. Wang, L. Zheng, J. Luo, Y. Lin, Y. Liu, C. Liu, J. Li, Q. Lu, X. Chen, D. Wang, Q. Peng, C. Chen, Y. Li, Design of single-atom Co-N_5 catalytic site: A robust electrocatalyst for CO_2 reduction with nearly 100% CO selectivity and remarkable stability, J. Am. Chem. Soc. 140 (2018) 4218-4221.

[10] X. Zhang, Z. Wu, X. Zhang, L. Li, Y. Li, H. Xu, X. Li, X. Yu, Z. Zhang, Y. Liang, H. Wang, Highly selective and active CO_2 reduction electrocatalysts based on cobalt phthalocyanine/carbon nanotube hybrid structures, Nat. Commun. 8 (2017) 14675.

[11] H. Takeda, C. Cometto, O. Ishitani, M. Robert, Electrons, photons, protons and earth-abundant metal complexes for molecular catalysis of CO_2 reduction, ACS Catal. 7 (2017) 70-88.

[12] N. Han, Y. Wang, L. Ma, J. Wen, J. Li, H. Zheng, K. Nie, X. Wang, F. Zhao, Y. Li, J. Fan, J. Zhong, T. Wu, D. J. Miller, J. Lu, S. T. Lee, Y. Li, Supported cobalt polyphthalocyanine for high-performance electrocatalytic CO_2 reduction, Chem 3 (2017) 652-664.

[13] N. Elgrishi, M. B. Chambers, X. Wang, M. Fontecave, Molecular polypyridine-based metal complexes as catalysts for the reduction of CO_2, Chem. Soc. Rev. 46 (2017) 761-796.

[14] C. Yang, K. Jiang, Q. Zheng, X. Li, H. Mao, W. Zhong, C. Chen, B. Sun, H. Zheng, X. Zhuang, J. A. Reimer, Y. Liu, J. Zhang, Chemically stable polyarylether-based metallophthalocyanine frameworks with high carrier mobilities for capacitive energy storage, J. Am. Chem. Soc. 143 (2021) 17701-17707.

[15] H. Zhong, M. Wang, M. G. Asl, J. Zhang, K. H. Ly, Z. Liao, G. Chen, Y. Wei, B. P. Biswal, E. Zschech, I. M. Weidinger, A. V. Krasheninnikov, R. Dong, X. Feng, Boosting the electrocatalytic conversion of nitrogen to ammonia on metal-phthalocyanine-based two-dimensional conjugated covalent organic frameworks, J. Am. Chem. Soc. 143 (2021) 19992-20000.

[16] X. F. Qiu, J. R. Huang, C. Yu, Z. H. Zhao, H. L. Zhu, Z. Ke, P. Q. Liao, X. M. Chen, A stable and conductive covalent organic framework with isolated active sites for highly selective electroreduction of carbon dioxide to acetate, Angew. Chem. Int. Ed. 61 (2022) e202206470.

[17] M. Wang, M. Ballabio, M. Wang, H. H. Lin, B. P. Biswal, X. Han, S. Paasch, E. Brunner, P. Liu, M. Chen, M. Bonn, T. Heine, S. Zhou, E. Cánovas, R. Dong, X. Feng, Unveiling electronic properties in metal-phthalocyanine-based pyrazine-linked conjugated two-dimensional covalent organic frameworks, J. Am. Chem. Soc. 141 (2019) 16810-16816.

[18] N. Huang, K. H. Lee, Y. Yue, X. Xu, S. Irle, Q. Jiang, D. Jiang, A stable and conductive metallophthalocyanine framework for electrocatalytic carbon

dioxide reduction in water, Angew. Chem. Int. Ed. 59 (2020) 16587-16593.

[19] F. Bedioui, S. Griveau, T. Nyokong, A. J. Appleby, C. A. Caro, M. Gulppi, G. Ochoa, J. H. Zagal, Tuning the redox properties of metalloporphyrin - and metallophthalocyanine-based molecular electrodes for the highest electrocatalytic activity in the oxidation of thiols, Phys. Chem. Chem. Phys. 9 (2007) 3383-3396.

[20] X. Wang, S. Sun, J. Yao, H. Wan, R. Ma, W. Ma, Two-dimensional metallophthalocyanine nanomaterials for electrocatalytic energy conversion, Energy Environ. Mater. 7 (2024) e12709.

[21] Y. Yue, P. Cai, K. Xu, H. Li, H. Chen, H. C. Zhou, N. Huang, Stable bimetallic polyphthalocyanine covalent organic frameworks as superior electrocatalysts, J. Am. Chem. Soc. 143 (2021) 18052-18060.

[22] B. Han, X. Ding, B. Yu, H. Wu, W. Zhou, W. Liu, C. Wei, B. Chen, D. Qi, H. Wang, K. Wang, Y. Chen, B. Chen, J. Jiang, Two-dimensional covalent organic frameworks with cobalt(II)-phthalocyanine sites for efficient electrocatalytic carbon dioxide reduction, J. Am. Chem. Soc. 143 (2021) 7104-7113.

[23] Y. Yue, H. Li, H. Chen, N. Huang, Piperazine-linked covalent organic frameworks with high electrical conductivity, J. Am. Chem. Soc. 144 (2022) 2873-2878.

[24] G. Xing, L. Chen, Linkages take charge, Nat. Synth. 1 (2022) 341-343.

[25] X. Yang, X. Li, M. Liu, S. Yang, Q. Niu, L. Zhai, Z. Jiang, Q. Xu, G. Zeng, Modulating electrochemical CO_2 reduction performance via sulfur-containing linkages engineering in metallophthalocyanine based covalent organic frameworks, ACS Mater. Lett. 5 (2023) 1611-1618.

[26] M. Wang, K. Torbensen, D. Salvatore, S. Ren, D. Joulié, F. Dumoulin, D. Mendoza, B. L. Kaiser, U. Işci, C. P. Berlinguette, M. Robert, CO_2 electrochemical catalytic reduction with a highly active cobalt phthalocyanine, Nat. Commun. 10 (2019) 3602.

[27] N. Corbin, J. Zeng, K. Williams, K. Manthiram, Heterogeneous molecular catalysts for electrocatalytic CO_2 reduction, Nano Res. 12 (2019) 2093-2125.

[28] R. Dovesi, A. Erba, R. Orlando, C. M. Zicovich-Wilson, B. Civalleri, L. Maschio, M. Rérat, S. Casassa, J. Baima, S. Salustro, B. Kirtman, Quantum-mechanical condensed matter simulations with CRYSTAL, Wiley Interdiscip. Rev. Comput. Mol. Sci. 8 (2018) e1360.

[29] A. D. Becke, Density-functional thermochemistry. III. The role of exact exchange, J. Chem. Phys. 98 (1993) 5648-5652.

[30] S. Pakhira, C. Sahu, K. Sen, A. K. Das, Can two T-shaped isomers of OCS-C_2H_2 van der Waals complex exist?, Chem. Phys. Lett. 549 (2012) 6-11.

[31] Y. Lei, S. Pakhira, K. Fujisawa, X. Wang, O. O. Iyiola, N. P. López, A. L. Elías, L. P. Rajukumar, C. Zhou, B. Kabius, N. Alem, M. Endo, R. Lv, J. L. M. Cortes, M. Terrones, Low-temperature synthesis of heterostructures of transition metal dichalcogenide alloys ($W_xMo_{1-x}S_2$) and graphene with superior catalytic performance for hydrogen evolution, ACS Nano 11 (2017) 5103-5112.

[32] S. Pakhira, J. L. M. Cortes, Intercalation of first row transition metals inside covalent-organic frameworks (COFs): A strategy to fine tune the electronic properties of porous crystalline materials, Phys. Chem. Chem. Phys. 21 (2019) 8785-8796.

[33] S. Pakhira, Rotational dynamics of the organic bridging linkers in metal-organic frameworks and their substituent effects on the rotational energy barrier, RSC Adv. 9 (2019) 38137-38147.

[34] S. Pakhira, K. P. Lucht, J. L. M. Cortes, Iron intercalation in covalent-organic frameworks: A promising approach for semiconductors, J. Phys. Chem. C 121 (2017) 21160-21170.

[35] S. Pakhira, K. P. Lucht, J. L. M. Cortes, Dirac cone in two dimensional bilayer graphene by intercalation with V, Nb, and Ta transition metals, J. Chem. Phys. 148 (2018) 064707.

[36] S. Pakhira, J. L. M. Cortes, Quantum nature in the interaction of molecular hydrogen with porous materials: Implications for practical hydrogen storage, J. Phys. Chem. C 124 (2020) 6454-6460.

[37] K. Parveen, S. Pakhira, Designing organic bridging linkers of metal-organic

frameworks for enhanced carbon dioxide adsorption, New J. Chem. 48 (2024) 13700-13714.

[38] S. Pakhira, D. Mandal, B. Mondal, A. K. Das, Theoretical study of spectroscopy, interaction, and dissociation of linear and T-shaped isomers of RgClF (Rg = He, Ne, and Ar) van der Waals complexes, Struct. Chem. 23 (2012) 681-692.

[39] S. Pakhira, A. K. Das, Spectroscopic properties, potential energy surfaces and interaction energies of RgClF (Rg = Kr and Xe) van der Waals complexes, Eur. Phys. J. D 66 (2012) 144.

[40] N. Sinha, S. Pakhira, H_2 physisorption on covalent organic framework linkers and metalated linkers: A strategy to enhance binding strength, Mol. Syst. Des. Eng. 7 (2022) 577-591.

[41] J. D. Pack, H. J. Monkhorst, "Special points for Brillouin-zone integrations"—a reply, Phys. Rev. B 16 (1977) 1748-1749.

[42] L. Yadav, S. Pakhira, Platinum-adsorbed defective 2D monolayer boron nitride: A promising electrocatalyst for O_2 reduction reaction, J. Mater. Chem. C 11 (2023) 15215-15232.

[43] D. Halba, S. Pakhira, Unraveling the O_2 Reduction Reaction on 2D Monolayer $LaNiO_3$ Perovskite, ACS Omega 9 (2024) 35614-35626.

[44] K. Momma, F. Izumi, VESTA 3 for three-dimensional visualization of crystal, volumetric and morphology data, J. Appl. Cryst. 44 (2011) 1272-1276.

[45] Z. Meng, J. Luo, W. Li, K. A. Mirica, Hierarchical tuning of the performance of electrochemical carbon dioxide reduction using conductive two-dimensional metallophthalocyanine based metal-organic frameworks, J. Am. Chem. Soc. 142 (2020) 21656-21669.

[46] Y. Zhou, Z. Wang, P. Yang, X. Zu, F. Gao, Electronic and optical properties of two-dimensional covalent organic frameworks, J. Mater. Chem. 22 (2012) 16964-16970.

[47] L. M. Yang, R. Pushpa, Tuning electronic and optical properties of a new class of covalent organic frameworks, J. Mater. Chem. C 2 (2014) 2404-2416.

[48] Y. R. Wang, H. M. Ding, X. Y. Ma, M. Liu, Y. L. Yang, Y. Chen, S. L. Li, Y. Q. Lan, Imparting CO_2 electroreduction auxiliary for integrated morphology tuning and performance boosting in a porphyrin-based covalent organic framework, Angew. Chem. Int. Ed. 61 (2022) e202114648.

[49] M. D. Zhang, D. H. Si, J. D. Yi, S. S. Zhao, Y. B. Huang, R. Cao, Conductive phthalocyanine-based covalent organic framework for highly efficient electroreduction of carbon dioxide, Small 16 (2020) 202005254.

[50] Y. Y. Liu, H. L. Zhu, Z. H. Zhao, N. Y. Huang, P. Q. Liao, X. M. Chen, Insight into the effect of the d-orbital energy of copper ions in metal-organic frameworks on the selectivity of electroreduction of CO_2 to CH_4, ACS Catal. 12 (2022) 2749-2755.

[51] X. Y. Dong, F. Q. Yan, Q. Y. Wang, P. F. Feng, R. Y. Zou, S. Wang, S. Q. Zang, A benzimidazole-linked bimetallic phthalocyanine-porphyrin covalent organic framework synergistically promotes CO_2 electroreduction, J. Mater. Chem. A 11 (2023) 15732-15738.

[52] S. Y. Chi, Q. Chen, S. S. Zhao, D. H. Si, Q. J. Wu, Y. B. Huang, R. Cao, Three-dimensional porphyrinic covalent organic frameworks for highly efficient electroreduction of carbon dioxide, J. Mater. Chem. A 10 (2022) 4653-4659.

[53] A. Singh, S. Barman, F. A. Rahimi, A. Dey, R. Jena, R. Kumar, N. Mathew, D. Bhattacharyya, T. K. Maji, Atomically dispersed Co^{2+} in a redox-active COF for electrochemical CO_2 reduction to ethanol: Unravelling mechanistic insight through operando studies, Energy Environ. Sci. 17 (2024) 2315-2325.

[54] P. Zhao, H. Jiang, H. Shen, S. Yang, R. Gao, Y. Guo, Q. Zhang, H. Zhang, Construction of low-coordination Cu-C_2 single-atoms electrocatalyst facilitating the efficient electrochemical CO_2 reduction to methane, Angew. Chem. Int. Ed. 135 (2023) e202314121.

[55] J. Cai, Q. Zhao, W. Y. Hsu, C. Choi, Y. Liu, J. M. P. Martirez, C. Chen, J. Huang, E. A. Carter, Y. Huang, Highly selective electrochemical reduction of CO_2 into methane on nanotwinned Cu, J. Am. Chem. Soc. 145 (2023) 9136-9143.

[56] Q. Zhao, Y. Wang, M. Li, S. Zhu, T. Li, J. Yang, T. Lin, E. P. Delmo, Y. Wang, J. Jang, M. Gu, M. Shao, Organic frameworks confined Cu single atoms and nanoclusters for tandem electrocatalytic CO_2 reduction to methane, SmartMat 3 (2022) 183-193.

[57] M. Savarese, É. Brémond, I. Ciofini, C. Adamo, Electron spin densities and density functional approximations: Open-shell polycyclic aromatic hydrocarbons as case study, J. Chem. Theory Comput. 16 (2020) 3567-3577.

Chapter 5

Metallophthalocyanine-based MOF toward CO_2 Reduction Reaction

This chapter presents a comprehensive theoretical and computational investigation of a copper phthalocyanine (CuPc) based MOF as an efficient electrocatalyst for CO_2RR toward both C_1 and C_2 products. The study focuses on understanding the fundamental mechanisms governing CO_2 activation, intermediate formation, and product selectivity using periodic DFT-D method. A 2D monolayer slab model of the CuPc framework is constructed to examine its structural stability, electronic properties, and catalytic performance. The chapter systematically analyses key reaction pathways leading to important products such as methane (CH_4), ethylene (C_2H_4), and ethanol (C_2H_5OH), with particular emphasis on the critical C-C coupling step responsible for C_2 product formation. The role of dual active sites, comprising Cu-N_4 centers and CuO_4 nodes, is highlighted in enhancing catalytic efficiency and promoting multi-carbon product formation. Furthermore, adsorption energies and reaction energetics of intermediates are evaluated to determine the most favorable pathways. The present findings reveal a strong preference for C_2H_5OH formation over C_2H_4, along with competitive CH_4 formation. Overall, this chapter provides valuable mechanistic insights and establishes design principles for developing advanced MOF-based electrocatalysts for selective CO_2 conversion into valuable fuels and chemicals.

5.1 Introduction

The electrochemical CO_2 reduction reaction (CO_2RR) powered by renewable energy has attracted considerable attention for its versatility in generating a wide range of C_1 and C_{2+} end products.[1] Nevertheless, CO_2RR faces formidable kinetic barriers, arising from challenges such as the competing H_2 evolution reaction (HER), the inherent stability of the C=O double bond, and the complexity of C-C dimerization.[2,3] Among the potential products, C_{2+} species are especially appealing owing to their superior energy density and economic significance. To date, elemental copper (Cu) and Cu-based catalysts have emerged as the most widely studied, largely because of their unique ability to facilitate C-C bond formation during CO_2 reduction.[4,5] The exceptional ability of Cu and Cu-based electrocatalysts to promote C-C coupling and generate C_{2+} products arises from their unique electronic

characteristics and *CO intermediate binding strength. Unlike noble metals such as Ag, Au, or Zn, which bind *CO too weakly, or transition metals such as Co, Ru, or Pt that bind *H too strongly, Cu achieves a balance that allows *CO to retain stably adsorbed while remaining reactive toward further reduction.[6] This optimal *CO adsorption facilitates the accumulation of *CO intermediates at adjacent Cu sites, enabling their dimerization to *OCCO, *OCCHO, or *OCCOH, a key step in forming C_{2+} species. Additionally, the local *CO concentration, mass transfer process and surface residence time play decisive roles in driving C-C coupling by enhancing the probability of *CO interaction with *CO, *COH, and *CHO intermediates on the catalyst interface.[7] Beyond this intrinsic *CO binding property, the superior performance of C-C coupling performance of the Cu-based systems has also been attributed to the coexistence of multiple oxidation states (Cu^0, Cu^+, Cu^{2+}) and their synergistic interfacial effects. Mixed-valence sites, particularly Cu^+/Cu^0 interfaces, can enhance the C_{2+} selectivity by simultaneously providing strong *CO adsorption (Cu^+) and favorable coupling environments (Cu^0).[8] Moreover, oxide-derived Cu catalysts with abundant grain boundaries, low coordination sites, and Cu(100)-type facets further promote *CO dimerization due to their high density of reactive centers and efficient charge transport.[9,10] Thus, to unravel the complexities of CO_2RR and improve catalyst design, it is essential to develop a thorough understanding of the underlying mechanism processes, particularly for optimizing Cu-based systems and identifying viable alternatives for C_{2+} production.[11]

Embedding MPc units into metal-organic frameworks (MOFs) and covalent organic frameworks (COFs) has emerged as an active area of research, primarily due to the presence of well-structured M-N_4 active sites that serve as an ideal platform for studying the catalytic behavior of M-N_4 single-atom catalysts (SACs).[12,13] In recent years, transition metal MPc-based porous materials have been widely investigated as an efficient electrocatalyst for CO_2RR.[14,15] In electrochemical CO_2 reduction, the majority of MPc compounds primarily yield CO as the main product,[16,17] however, molecular copper phthalocyanine (CuPc) is unique in exhibiting activity towards the formation of C_2H_4.[18] The C-C dimerization step is widely acknowledged as a key step in the conversion of CO_2 to C_{2+} products, and lowering the energy barrier associated with this process can enhance their formation. Computational studies have provided valuable insights into the initial C-C coupling steps and the factors that govern

the preference for C_2 over C_1 products. However, fewer studies have examined the elementary steps following C-C coupling, particularly the critical intermediates that influence the selectivity between ethylene and ethanol.[4,19–21] As ethylene is the predominant C_2 product, most theoretical investigations have focused on elucidating its formation mechanism. Recently, a few researchers have begun to address the energetics of ethanol pathways, and there is still no clear agreement on the competitive relationship between these two major C_2 products or on the intermediates at which their reaction pathways diverge. This lack of agreement complicates the efforts to rationally tune product distribution.

Herein, we present a theoretical and computational investigation of a 2D CuPc-Cu-O MOF (in short CuPc), highlighting its potential as an efficient electrocatalyst for CO_2RR into both C_1 (CH_4) and C_2 (C_2H_5OH, C_2H_4) products, offering a promising technological route for transforming CO_2 into valuable carbon-based fuels and chemicals. The MOF studied here was previously synthesized by Qiu et al.,[22] using 2,3,9,10,16,17,23,24-octahydroxyphthalo-cyaninato)copper(II) ($PcCu-(OH)_8$) as the linker and the square-planar CuO_4 units as the metal node, serving as a dual active site for the electrocatalytic reduction of CO_2RR into C_2H_4. The presence of two simultaneous active metal centers can result in enhanced catalytic performance due to unique electronic interactions occurring between the paired active sites.[23] Here, we have explored the potential of CuPc material for C_1 (methane) and C_2 (ethylene, ethanol) products by employing hybrid periodic DFT methods with van der Waals (vdW) dispersion corrections (i.e., Grimme's-D3 dispersion corrections, (in short DFT-D)). To probe the CO_2RR mechanism, a computational model of CuPc monolayer slab was constructed, and its equilibrium structures, along with intrinsic electronic properties including electronic band structure, density of states (DOS), and partial density of states (PDOS) were analyzed using the same DFT-D method. The designed monolayer exhibits a semiconducting nature with a low electronic bandgap (E_g) value of about 0.64 eV, suggesting its favorable electrical conductivity and ensuring effective transfer throughout the reaction mechanism. The investigation reveals that the CO_2RR on the CuPc surface favors the formation of the C_2 product i.e., C_2H_5OH, with a relative adsorption energy (ΔE_{ads}) of -2.76 eV, rather than the formation of C_2H_4 which has the value of ΔE_{ads} 2.11 eV, along with the remarkable electrocatalytic activity for CO_2 reduction to CH_4 with a ΔE_{ads} value of -2.28 eV.

5.2 Computational details

First, to investigate the reaction mechanism, a computational model of a 2D CuPc-Cu-O (in short CuPc) MOF monolayer was constructed, with a vacuum space exceeding 500 Å (i.e., there is no periodicity along the z-direction) to prevent interactions between neighboring layers. Next, the equilibrium geometry of the CuPc was obtained using first principles hybrid periodic DFT calculations, specifically the B3LYP functional, as implemented in *ab initio*-based CRYSTAL23 suite code.[24] Given the presence of numerous weak van der Waals (vdW) interactions both between CuPc layers and within the atomic frameworks, it was essential to account for dispersion effects. Thus, third-order semiempirical Grimme's (-D3) dispersion corrections were incorporated to account for these vdW contributions.[25–28] The B3LYP-D3 approach is well recognized for providing reliable thermochemical predictions in systems involving both covalent bonding and dispersion-dominated interactions. This method was further employed for geometry optimizations, as it yields densities and energies less prone to spin contamination compared to other methods.[29] In the CRYSTAL23[25] suite code, the atomic orbitals of the CuPc were described using localized Gaussian-type orbitals (GTOs), rather than plane waves, offering a more suitable basis for hybrid DFT-D calculations. During the geometry optimization and single-point energy calculations, the SPIN and SPINLOCK keywords were employed to define the unrestricted wave functions and to fix the total spin state of the CuPc, respectively. Additionally, the ATOMSPIN keyword was used to assign the individual spins of the active site Cu atom. In the present investigation, the H, C, N, O, and Cu atoms were described using the triple-ζ valence with polarization quality (TZVP) Gaussian type basis sets.[30] Thus, the B3LYP-D3 method with Gaussian-type basis sets yields results comparable to the high-level G_0W_0 calculations, which are labor-intensive and computationally expensive and not implemented in the CRYSTAL23 suite code.[25]

After achieving the equilibrium geometry of the CuPc, its electronic properties, including the band structures and total density of states (DOS) were computed at the same theoretical level. Monkhorst *k*-mesh grids were employed to compute the structural and electronic properties of CuPc, including geometry, DOS and band structure. For the CuPc layer, a 4×4×1 *k*-mesh grid with a resolution of $2\pi\times1/60$ $Å^{-1}$ was applied. In total, eight electronic bands near the Fermi level (E_F) were analyzed within the first Brillouin zone along the highly symmetric *k*-directions, i.e., **Γ-K-M-Γ**.

Contributions from the atomic orbitals of C, N, H, O, and Cu atoms were incorporated to compute the total orbital electron DOS. The band structure and DOS calculations were referred to the vacuum level, with electrostatic potential effects included through POTC calculations implemented in the CRYSTAL23 suite code.[31] The convergence criteria for ground state energy, as well as for geometry optimization, band structure, and DOS calculations, were set to 10^{-7} a.u. For the Visualization and analysis of the crystal structures, VESTA[32] was used.

5.3 Material details

The origin of this material design depends on stable, rigid, macrocyclic compounds with an 18 π-electron aromatic system, phthalocyanines (Pcs), known for their chemical and thermal stability. The central cavity of these compounds can be metalated to form metallophthalocyanines (MPcs).[33] These materials are intriguing for electrolysis due to their ability to incorporate various elements into the Pc core, possess a high density of N-donor sites, and their adaptable structure, enabling precise tuning of the catalytically active metal sites and the synergy between them.[34] Moreover, several characteristics make metallophthalocyanines promising candidates for electrocatalysis: (i) their extended π-conjugated system, (ii) the possibility of synthesizing MPcs with a wide range of elements across the periodic table, (iii) favorable electron transport capabilities, and (iv) the well-established correlations between catalytic behavior and quantum descriptors.[35] Keeping these points in mind, we studied the electrochemical CO_2RR of a previously synthesized MOF constructed using (2,3,9,10,16,17,23,24-octahydroxyphthalo-cyaninato)copper(II) as organic metallo-linker, represented by (CuPc-$(OH)_8$ combined with square-planar CuO_4 as the metal nodes, as illustrated in Figure 5.1. The electron-donating effect of the eight hydroxyl groups on the CuPc-$(OH)_8$ metallo-linker is expected to improve the coordination ability of the nitrogen atoms, thereby strengthening the Cu-N interaction.[36,37] As a result, it is predicted that combining CuPc-$(OH)_8$ with a CO-producing site will be highly promising for achieving both high selectivity and durability in the CO_2RR mechanism. In the CuPc-Cu-O, the four nitrogen atoms at the center of the phthalocyanine can bond with various metal atoms, allowing for atomic-level adjustments to the CuPc-Cu-O structure.

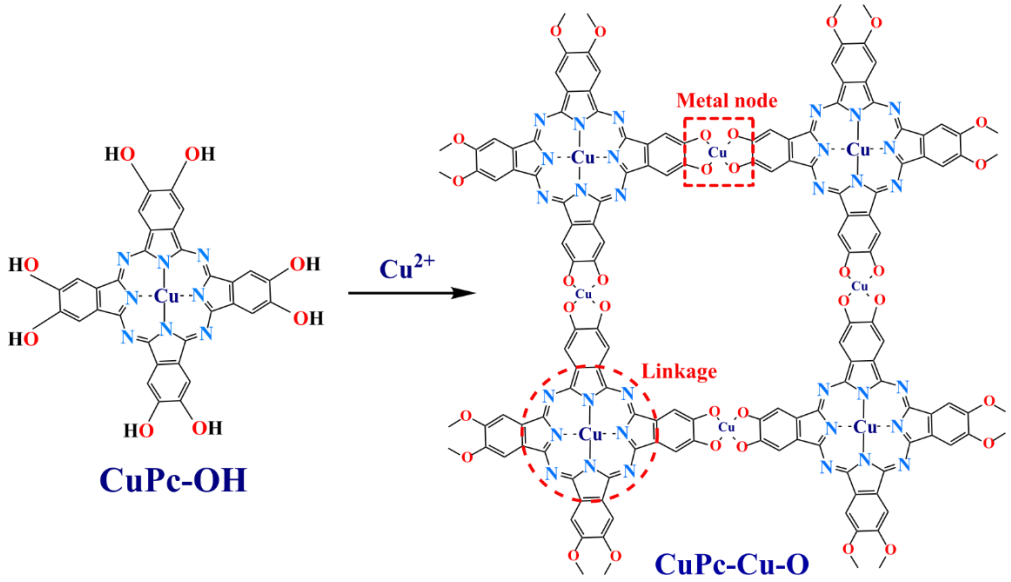


Figure 5.1 Illustration of the chemical structure of CuPc MOF material. The metal node and the linkage parts of the CuPc MOF are shown by the dotted red color rectangle and circle, respectively.

5.4 Results & discussion

5.4.1 Equilibrium geometry, structural and electronic properties

When 3D MOFs are used for CO_2RR, they exhibit slow charge and mass transfer, inefficient electron conductivity, and hindered gas diffusion, leading to higher resistance and reduced electrocatalytic performance.[38] Therefore, to understand the CO_2RR mechanism towards the formation of C_1 and C_2 products, we designed a 2D monolayer slab structure of the CuPc, whose chemical structure is illustrated in Figure 5.1. This 2D monolayer offers ultrahigh specific surface area, more exposed metal atoms with rich dangling bonds for higher catalytic activity, and increased carrier concentration through the vacancies, thereby improving electrical conductivity.[39,40] The DFT-D study reveals that the CuPc exhibits P4/MMM tetragonal layer symmetry (with a layer group number 61). This means that periodic symmetry is present along the x- and y-axes, representing the tetragonal 2D layer system, while along the z-axis, there is no symmetry, indicating a vacuum space in this direction. The active Cu atom in the pristine CuPc exhibits an oxidation state of 0, consistent with a Cu^0-like electronic configuration within the semiconducting $Cu\text{-}N_4$ coordination environment. The equilibrium geometry, electronic band structure, total density of states (DOS), and partial density of states (PDOS) of Cu atom's ***d***-subshell in the CuPc, achieved using the same DFT-D method, are depicted in Figure 5.2. Using hybrid periodic DFT-D calculations, we determined that the equilibrium lattice parameters are approximately a = b = 18.08 Å, and interfacial angles, i.e., $\alpha = \beta = \gamma = 90°$. The equilibrium structure of

the CuPc monolayer as depicted in Figure 5.2 (a), with their corresponding equilibrium lattice parameters including lattice constants (a and b), interfacial angles (α, β, and γ), layer group symmetry, average bond distance for Cu-N(a), N(a)-C, and N(b)-C atoms of the Pc unit of the linker, bandgap (Eg), and material state summarized in Table 5.1. These optimized bond lengths are estimated to have an uncertainty of approximately ±0.02 Å, which is consistent with the expected accuracy of the B3LYP-D3 method.[41] The electronic bandgap (i.e., E_g=0.65 eV) of the CuPc can be effectively tuned by optimizing structural parameters such as lattice constants and bond lengths, which directly influence the orbital overlap and electronic delocalization. A slight reduction in lattice constants enhances the spatial proximity between Cu centers and coordinating nitrogen atoms, strengthening ***π-d*** conjugation between the metal ***d***-orbitals and ligand ***π***-systems. This increased orbital overlap broadens the band dispersion, thereby narrowing the electronic bandgap and facilitating charge transport.[42,43] Similarly, a slight reduction in the Cu-N bond length enhances covalent interaction between Cu ***d***-orbitals and ***p***-orbitals of the N atom, leading to stronger electronic coupling within the CuPc framework. This increased orbital overlap broadens the electronic bands and promotes carrier delocalization across the conjugated plane, thereby reducing the electronic bandgap. The reduced electronic bandgap improves the electrical conductivity, facilitating more efficient electron transfer during CO_2RR, while maintaining the structural integrity.[44,45] Thus, a careful balance in lattice constants and bond lengths tuning can significantly improve the electrical conductivity and charge-transfer efficiency of the CuPc, ultimately promoting superior CO_2 reduction performance.

Table 5.1 The equilibrium structural parameters (lattice constants and interfacial angles), space group symmetry, bandgap (E_g), and material state of the 2D monolayer slab of the CuPc.

MOF	Lattice parameters (Å)	Interfacial angles (°)	Layer group symmetry	Average bond distance (Å)	Bandgap (eV)	Material state
	a = b	α = β = γ				
CuPc	18.08	90	61 and P4/MMM	Cu-N(a) =1.95, N(a)-C =1.38, and N(b)-C =1.33	0.65	Semiconductor

The performance of an electrocatalytic reaction is strongly influenced by the electronic conductivity of the catalyst, as efficient charge transfer is essential. To explore this, we computed the electronic properties, both the electronic band structures and density of states (DOS) of the CuPc using the same DFT-D approach. The band structure, plotted along the highly symmetric **Γ-K-M-Γ** path with respect to the vacuum (w.r.t vac.), as shown in Figure 5.2 (b), with the Fermi energy level (E_F) situated at -5.28 eV. The resulting band gap (E_g) for the CuPc was found to be 0.65 eV, consistent with the band gaps observed for previously reported COFs and MOFs.[15,46] This lower value of the electronic band gap (the energy gap between the VB and CB) helps to increase the conductivity of the structure and makes it easy to transmit the electrons from the VB to the CB. It was observed that two of the bands in the valence and conduction bands overlapped with each other near the E_F level, suggesting the existence of localized electronic states. Consequently, pronounced peaks appeared in the DOS near the band edges, arising from the high density of accumulated states. Also, the band structure calculations revealed that the bands are flat due to localization of electron density, a characteristic commonly observed in COFs and MOFs.[28,38] Two energy bands overlapped near the bottom of the CB, close to the E_F level, while the bands in the VB also overlapped at -5.73 eV. Also, the total density of states (DOS) representing the number of available electrons or hole states per unit volume at a given energy, was also evaluated, as it is crucial for understanding the carrier concentrations and distribution. The DOS, computed w.r.t the vacuum, revealed an absence of electron clouds in regions lacking energy bands, with only a minor electron density appearing slightly above the E_F level, as illustrated in Figure 5.2 (c). To examine the electronic contributions near E_F, we analyzed the Cu atom's ***d***-orbital electron density, as plotted in Figure 5.2 (d), which confirms that the ***d***-subshell electrons of Cu dominate the states around E_F in the total DOS. Hence, the Cu ***d***-orbital electron density plays a vital role in enhancing the catalytic performance of the CuPc, thereby boosting its overall efficiency in the CO_2RR mechanism. The analysis clearly shows that the Cu atom's ***d***-orbital makes the dominant contribution to the total DOS. Upon energy adsorption, holes are generated on the Cu atom, suggesting that it serves as an electron-rich active center. In addition, the phthalocyanine group, with its extended conjugation and multiple nitrogen atoms, enhances the electron density around the coordinated metal center, thereby facilitating ***d***-electron transfer. This leads to enhanced charge polarization and, consequently,

improved CO_2RR catalytic activity. Thus, the unique structural and electronic properties of the CuPc demonstrate their high potential for CO_2RR catalysis.

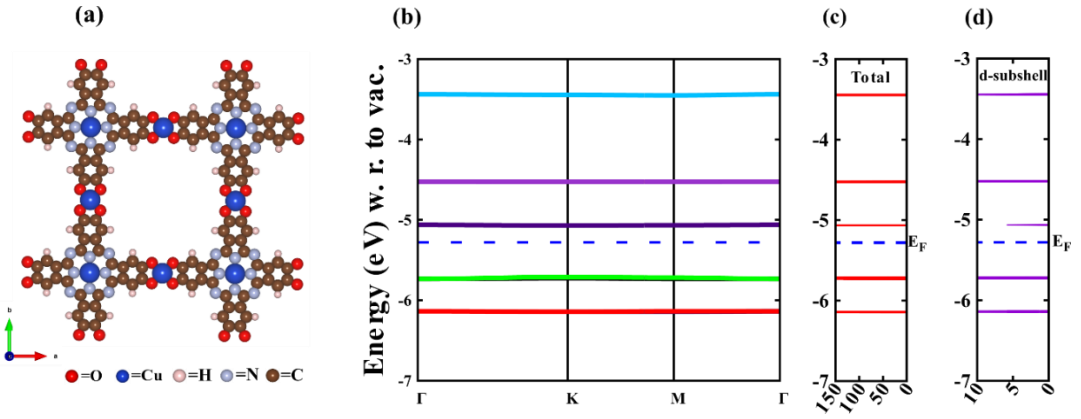


Figure 5.2 The (a) equilibrium geometry, (b) band structure, (c) total density of states (DOS), and (d) partial density of states (PDOS) of the Cu atom's d subshell of the CuPc.

Although MPc-based catalysts show good performance in the electroreduction of CO_2 to C_1 and C_2 products, their long-term stability remains a significant challenge. Therefore, to study the thermodynamic stability of the CuPc monolayer slab, we have calculated the binding energy ($\boldsymbol{E_b}$) (often denoted by formation energy), cohesive energy ($\boldsymbol{E_{coh}}$), and change in binding energy ($\boldsymbol{\Delta E_b}$) of the Cu atom on the CuPc using the expression provided below:

$$\boldsymbol{E_b = E_{CuPc} - E_{Pc} - E_{Cu}} \quad \textbf{(i)}$$

$$\boldsymbol{E_{coh} = [aE_H + bE_C + cE_{Cu} + dE_N + eE_O - E_{total}]/n} \quad \textbf{(ii)}$$

where $\boldsymbol{E_b}$ is the binding energy of the Cu atom on CuPc, $\boldsymbol{E_{CuPc}}$ and $\boldsymbol{E_{Pc}}$ are the total energies of CuPc with and without the Cu atom, respectively, and $\boldsymbol{E_{Cu}}$ corresponds to the energy of a single Cu atom. The cohesive energy ($\boldsymbol{E_{coh}}$) refers to that of the Cu metal atom, $\boldsymbol{E_{total}}$ stands for the total energy of CuPc in its stable crystal structures, whereas $\boldsymbol{E_H}$, $\boldsymbol{E_C}$, $\boldsymbol{E_{Cu}}$, $\boldsymbol{E_N}$, and $\boldsymbol{E_O}$ represent the energies of H, C, Cu, N, and O atoms, respectively. The terms a, b, c, d, and e indicate the number of corresponding H, C, Cu, N, and O atoms, with n being the total number of atoms within the unit cell. Thus, the change in binding energy ($\boldsymbol{\Delta E_b}$) is given by the expression:

$$\boldsymbol{\Delta E_b = E_b - E_{coh}} \quad \textbf{(iii)}$$

A negative value of $\boldsymbol{E_b}$ reflects the thermodynamic stability and practical feasibility of the system.[47] For the CuPc, the computed value of $\boldsymbol{E_b}$ was -3.59 eV, confirming both

its stability and the experimental viability of its synthesis, consistent with earlier reports on CO_2RR materials.[48,49] Also, the cohesive energy provides important insight into the structural robustness of catalysts during the electrocatalytic reduction process. The relatively high value of $\boldsymbol{E_{coh}}$ (6.73 eV/atom) for CuPc suggests strong interatomic bonding, thereby ensuring excellent structural integrity of the CuPc monolayer.[50] Furthermore, the calculated result of $\boldsymbol{\Delta E_b}$ (-10.32 eV) suggests that Cu atoms tend to stay uniformly distributed within the CuPc framework instead of aggregating into metallic clusters, confirming the stable atomic arrangement of Cu in the CuPc.

5.4.2 Reaction mechanisms

Understanding the mechanism of various product formations in the electrocatalytic CO_2 reduction is essential for developing efficient catalysts. We next examine the catalytic behavior of CuPc for CO_2 reduction to C_1 and C_2 products. The CO_2RR process is initiated by the adsorption and activation of a CO_2 molecule on the catalyst surface. Since the adsorption energy of intermediates strongly influences the reaction pathway, it plays a decisive role in determining the product selectivity. We first evaluated the adsorption strength of CO_2 on different active sites, namely the Cu atoms of the linker and metal node, and the nearby nitrogen atoms N(a) and N(b) within the linker, as shown in Figure 5.3. The DFT-D calculations revealed that the CO_2 adsorption at N(a) exhibited an adsorption energy of - 4.19 eV, while N(b) showed a value of - 4.12 eV. Moreover, CO_2 adsorption at the Cu atom of the metal node resulted in an adsorption energy value of - 4.18 eV, while that at the linker has an adsorption energy value of - 4.22 eV. The results indicated that CO_2 binds more strongly to the Cu atom of the linker than the other three sites, which is obviously due to the coordinatively unsaturated Cu sites present at the edges. This suggested that CO_2 molecules preferentially tend to be adsorbed at the Cu atom of the linker. Thus, in line with the minimum energy principle, CO_2 molecules preferentially adsorb and become activated at the Cu atom of the linker during the initial step of CO_2RR ($CO_2 + * \rightarrow *CO_2$-CuPc). It is noteworthy that in the CuPc, CO_2 adsorption at the Cu center (- 4.22 eV) and the adjacent N atom (- 4.19 eV) are nearly identical, reflecting a delicate balance of electronic and geometric effects. The Cu ***d***-orbitals interact with the $\boldsymbol{\pi^*}$ orbital of CO_2, while the neighboring N atom contributes through lone-pair donation, leading to cooperative stabilization. Such Cu-N synergy enhances electron delocalization and increases electron density around Cu active sites, thereby facilitating charge transfer and CO_2 activation.[51,52] Therefore,

the N atoms indirectly promote catalysis by modulating the Cu electronic environment and stabilizing intermediates through Cu-N cooperative interactions.

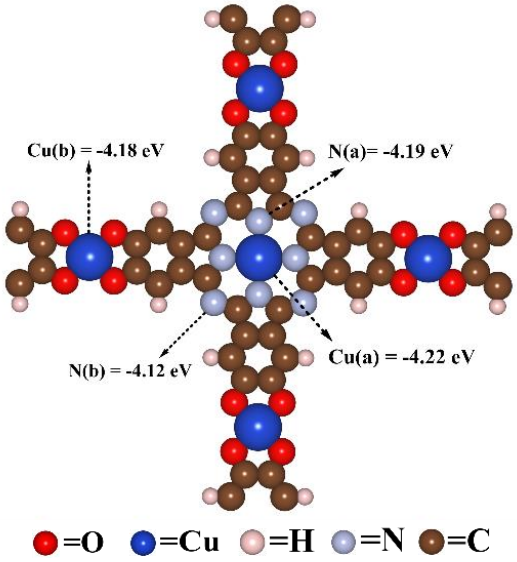


Figure 5.3 CO_2 adsorption at the various possible sites of CuPc.

Next, the study focused on elucidating atomic carbon as a critical surface intermediate that directs the selectivity of C_1 and C_2 products through different competing reaction routes. This mechanistic analysis is based on the adsorption energies of key intermediates obtained from the periodic DFT-D calculations in the present investigation. Due to the high computational cost, limited efficiency and robustness of transition-states (TS) searches in large periodic MOF frameworks, relative adsorption energy (ΔE_{ads}) was employed as a reliable thermodynamic descriptor to evaluate catalytic activity and pathway selectivity.[26,53–55] The intermediates along the CH_4 pathway were considered as the basis for C_2 product formation, where C-C coupling of *CO with either *COH or *CHO was identified as the first step toward generating C_2 products. Notably, the same intermediate can give rise to different products depending on their adsorption strength. For instance, when *CO binds weakly, it tends to be desorbed as CO gas; however, stronger adsorption enables further hydrogenation or C-C coupling, leading to hydrocarbons or C_2 products. Thus, a moderately higher *CO adsorption energy is necessary to retain *CO on the catalytic surface long enough to enable its further reduction into more complex hydrocarbons like CH_3OH, CH_4, C_2H_4, and C_2H_5OH.

- **CO_2 reduction to C_1 products**

The activation of CO_2 is crucial for CO_2RR due to the inert nature of CO_2 molecules. As discussed above, the Cu metal atom coordinated with the Pc unit was identified as the active site for CO_2RR. We began by examining CO_2 adsorption on the CuPc monolayer slab, where the calculated ΔE_{ads} was - 4.22 eV, indicating strong binding. The spontaneous CO_2 adsorption at the central Cu site facilitated the activation of CO_2 for subsequent reactions. Following this, we analyzed the reduction pathway of CO_2 toward four C_1 products: carbon monoxide (CO), formic acid (HCOOH), methanol (CH_3OH), and methane (CH_4). All the possible intermediates involved in CO_2RR to CH_4 are depicted in Figure 5.4-5.5, and their corresponding energies are shown through the potential energy surface (PES) diagram depicted in Figure 5.6. The most feasible reaction pathway for CO_2RR to CH_4 was discussed in this study, along with the competing reaction intermediates.

CO_2 reduction to *HCOOH intermediate: Generally, after two proton/electron transfers, the electrochemical reduction of CO_2 typically involves *HCOO, *COOH, *HCOOH, and *CO intermediates. If the catalyst's binding strength with the molecules is weak or the intermediate that follows *HCOOH and *CO is unstable, the resulting formation of *HCOOH and *CO will be the primary reduction products. However, hydrocarbons can eventually form if the *CO or *HCOOH intermediate undergoes hydrogenation. Thus, enhancing the interaction between the catalyst and key intermediates is an effective approach to enhance the performance of CO_2 electroreduction into hydrocarbons. After the first proton-electron transfer, the calculated values of ΔE_{ads} to form the *COOH and *HCOO intermediates were -5.69 eV and -3.14 eV, respectively, presenting a greater propensity for *COOH formation. Subsequently, the transfer of a second proton/electron pair to *COOH via proton-coupled electron transfer (PCET), produces either *CO or *HCOOH intermediates. These two *HCOOH and *CO intermediates were found to be competitive, as the *COOH intermediate could be protonated directly to form *HCOOH or can undergo C-O bond cleavage to yield *CO. The calculated value of ΔE_{ads} for the *CO intermediate (-3.49 eV) was considerably higher than that of *HCOOH (-5.07 eV), exhibiting improved selectivity towards *HCOOH over *CO. It is important to note here that these two intermediates may also desorb from the catalyst's active site, resulting in the release of CO and HCOOH molecules. However, the desorption of CO and HCOOH molecules required an E_{ads} value of 0.67 eV and 6.29 eV, respectively,

which were significantly higher than the value needed for the formation of the *HCOOH intermediate (-5.07 eV). In other words, the desorption of CO and HCOOH was endothermic, favoring further PCET processes through *HCOOH intermediate. The adsorption of all potential intermediates involved in the two-electron pathway on the surface of CuPc, along with their corresponding hydrogenation energies, are displayed in Figure 5.4 (a)-(f). Next, we investigated the possibility of generating hydrocarbon products, including methane and methanol, by evaluating whether the *HCOOH intermediate could undergo further hydrogenation to form *COH or *CHO intermediates.

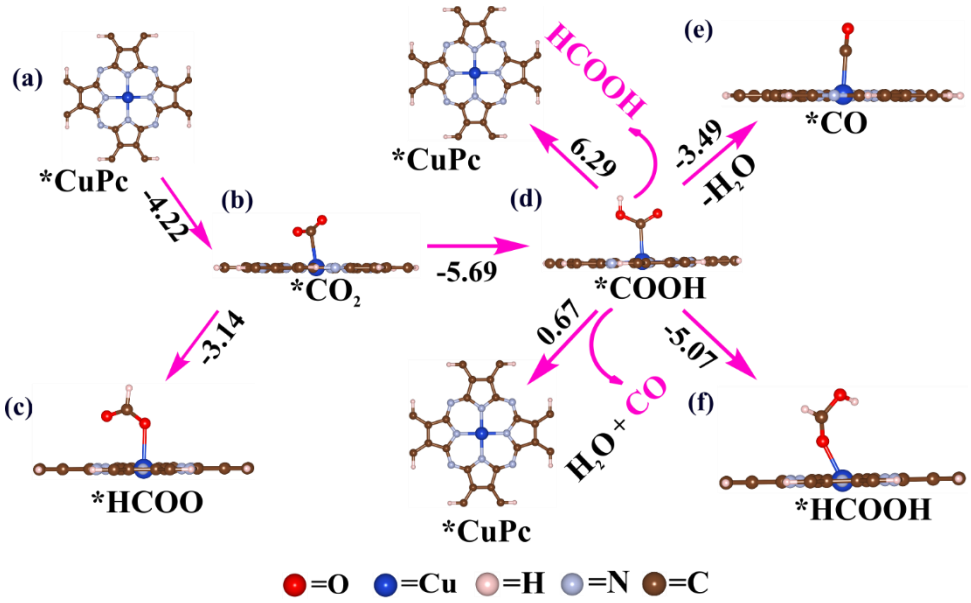


Figure 5.4 The equilibrium geometries of the possible reaction intermediates associated with the two-electron CO_2RR to *HCOOH intermediate on the CuPc surface, with (a) CuPc surface; and the intermediates: (b) *CO_2; (c) *HCOO; (d) *COOH; (e) *CO; and (f) *HCOOH.

***HCOOH reduction to methane:** In the advanced C_1 pathways, which involve hydrocarbons and alcohols beyond CO or HCOOH, further PCET of *HCOOH or *CO to *CHO (formyl) or *COH is considered a key step that influences both selectivity and reaction potential. Consequently, both the *COH and *CHO are the potential reaction intermediates for CH_3OH and CH_4 formation. The energy required for further hydrogenation of *HCOOH to *CHO intermediate was -1.77 eV, lower than the value achieved for *COH (-0.28 eV), indicating that the formation of *CHO intermediate was relatively facile. That is, it was more conducive to C hydrogenation to form *CHO than O hydrogenation to form *COH intermediate, and thus production proceeded through

*CHO intermediate. We optimized the stable adsorption structure of all the potential intermediates in the *HCOOH reduction to CH_4 on the CuPc surface, and the resulting stable configurations are shown in Figure 5.5 (a)-(o). The subsequent hydrogenation of *CHO resulted in the formaldehyde (*OCH_2), *CHOH, and *C formation, with the preferred pathway determined by the lowest energy requirement. The calculated ΔE_{ads} values indicated that formation of the *OCH_2 (-4.17 eV) reaction intermediate was more favorable than the *CHOH (-1.88 eV), and *C (-0.39 eV) with a water molecule. Thus, *OCH_2 was further reduced to *CH, methoxy (*OCH_3), and *CH_2OH intermediates with the value of ΔE_{ads} = -2.15 eV, -6.78 eV, and -6.88 eV, respectively, favoring the formation of the *CH_2OH intermediate. Next, the carbon-bound *CH_2OH intermediate can either undergo C-O bond cleavage to yield methane while leaving an adsorbed *O on the surface or accept a hydrogen at the carbon end of *CH_2OH to produce the methanol (*CH_3OH) intermediate. The *CH_2OH intermediate could also lead to the formation of *CH_2 intermediate with a H_2O molecule. Thus, the reduction of *CH_2OH was considered the critical step controlling the selectivity between methane (CH_4) and methanol (CH_3OH) production. After CH_4 was produced from the reduction of *CH_2OH, an adsorbed *O remained on the surface, which was subsequently reduced to H_2O via *OH intermediate. Alternatively, *CH_2OH could also be reduced to *CH_3OH to produce CH_4. The calculated value of ΔE_{ads} indicated that the hydrogenation of *CH_2OH to *CH_3OH was energetically favored, with a value of -8.37 eV, compared to the other intermediates. In simpler terms, the results of our DFT-D calculations indicate that the desorption of CH_4 from *CH_2OH exhibits a higher reaction energy, suggesting that generating CH_4 is thermodynamically challenging. Thus, it should be emphasized that CH_4 formation proceeds via the *CH_3OH intermediate. Now, the *CH_3OH intermediate could either desorb from the surface to produce CH_3OH or be further reduced to generate CH_4. As illustrated in Figure 5.6, the desorption energy of the CH_3OH (-1.09 eV) molecule was less negative than that of the *CH_3OH (-8.37 eV) intermediate formation. This suggests that the formation of the *CH_3OH intermediate is easier and more spontaneous. Now, *CH_3OH is further reduced to produce *CH_3 or *OH intermediates along with H_2O molecule and methane, respectively. However, the calculated values of ΔE_{ads} show the favorable formation of *OH intermediate (-3.73 eV) and CH_4 release over *CH_3. The *OH intermediate is further hydrogenated to produce H_2O and the active site of the catalyst with an ΔE_{ads} value of -2.28 eV. Each of these steps is thermodynamically feasible due to the low

energy barriers, and the ΔE_{ads} values are comparable with the previously reported linkage-based COF for CO_2RR to CH_4.[26] A clearer understanding of the adsorption energies of all possible intermediates and the product formation is obtained from the PES diagram depicted in Figure 5.6.

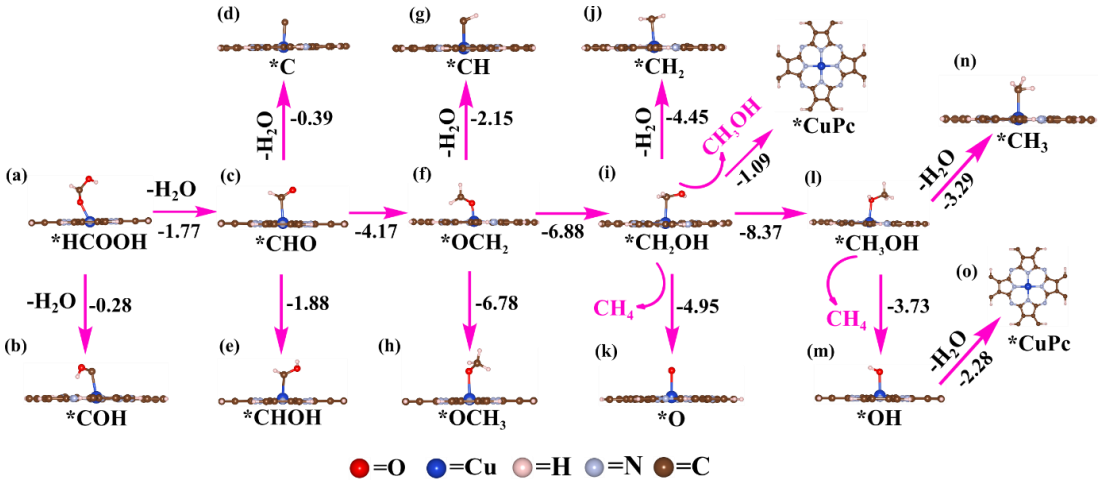


Figure 5.5 The equilibrium geometries of the possible reaction intermediates associated with the subsequent six-electron reduction of *HCOOH to CH_4 on the CuPc surface with intermediates: (a) *HCOOH; (b) *COH; (c) *CHO; (d) *C; (e) *CHOH; (f) *OCH_2; (g) *CH; (h) *OCH_3; (i) *CH_2OH; (j) *CH_2; (k) *O; (l) *CH_3OH; (m) *OH; (n) *CH_3; and (o) *CuPc.

The kinetics of the CO_2RR mechanism are incomplete without addressing the H_2 Evolution Reaction (HER) since hydrogen production is undesirable when the aim is to produce CO_2RR products. HER is typically a more kinetically favorable reaction and can therefore compete with CO_2RR, lowering its selectivity. To achieve efficient CO_2 adsorption and activation, the binding strength of CO_2 at the active site must surpass that of hydrogen (H) intermediate to suppress HER. To evaluate this, we performed additional DFT-D calculations to compare the ΔE_{ads} values of H and CO_2 on the Cu site of the linker. The computed ΔE_{ads} values showed that H adsorption (-3.98 eV) was weaker than CO_2 adsorption (-4.22 eV). These results suggest that the process of HER can be significantly prohibited on the CuPc-based MOF catalysts.

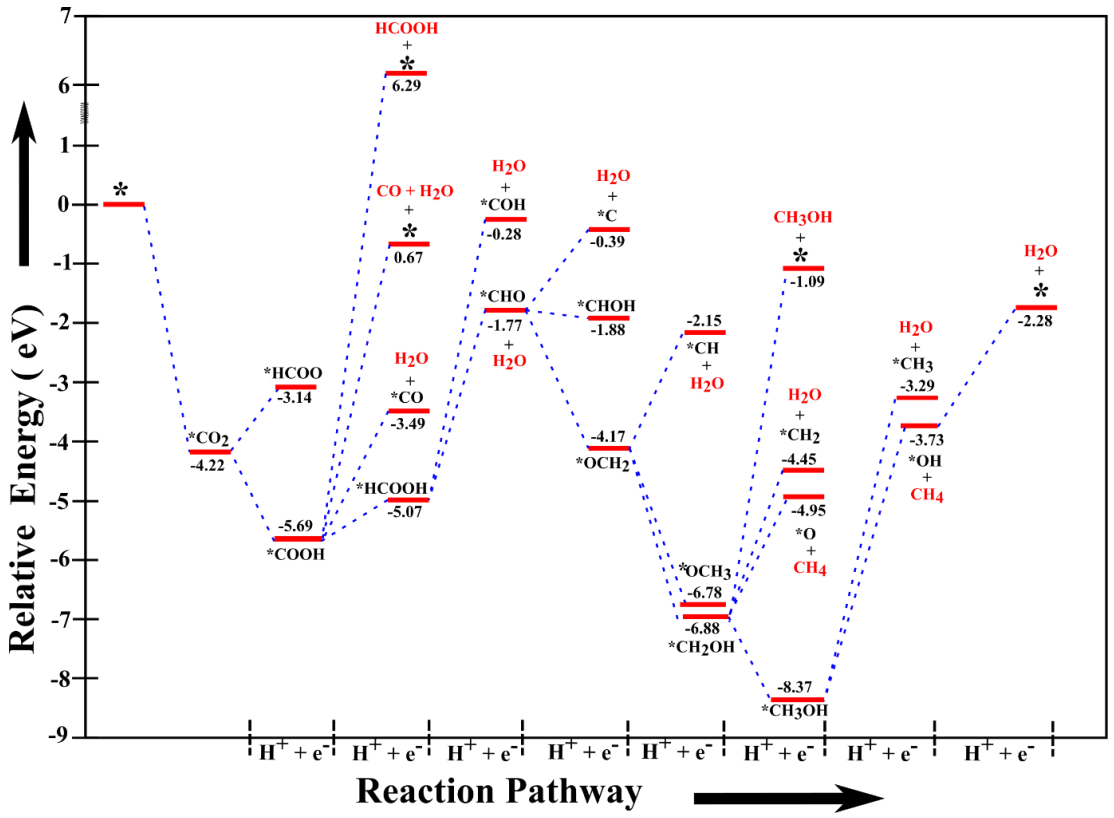


Figure 5.6 The potential energy surface (PES) diagram representing the ΔE_{ads} values for CO_2 reduction to CH_4 through various reaction intermediates on the CuPc surface at 0 V_{RHE}. The energies are expressed in eV.

- **CO_2 reduction to C_2 products**

The transformation of CO_2 into C_2 products such as C_2H_4 and C_2H_5OH depends on C-C coupling between *CO intermediates, which requires the synergy of two adjacent catalytic sites. Since copper-based catalysts are known to favor hydrocarbon formation, a CuPc-based MOF featuring a homogeneous Pc unit and spatially separated CuO_4 metal node as dual active sites emerge as a promising candidate for CO_2 reduction to C_2 compounds. The incorporation of Cu sites with lower coordination was found to enhance the binding energies of *CO and *CHO, while simultaneously lowering the energy barrier for C-C bond generation via OC-CHO coupling, thus promoting the formation of multi-carbon (C_{2+}) products. It is noteworthy that the pivotal step in CO_2 electroreduction toward C_2 products is the C-C coupling between adsorbed CO and CHO, however, the present study cannot stabilize the *COCO intermediate. Previous studies have demonstrated that when the arrangement of closely adjacent copper atoms is < 2.6 Å, such a short Cu-Cu distance is beneficial to the direct C-C coupling between two *CO intermediates (i.e., the *CO-*CO coupling to yield *OCCO).[51,56] In

contrast, MOFs with di- and tri- copper sites usually take the form of either *CO-*CHO or*CO-*COH coupling, instead of the *CO-*CO coupling, where the adjacent Cu-Cu sites are separated by ~ 3.3 Å to ~ 3.6 Å.[57–59] For the systems with even longer adjacent Cu-Cu distances (> 4Å), the migration of CO species for the C-C coupling is necessary during the reaction. For instance, in the Cu(111)@Cu-THQ system, the dual CuO_4 site acts as the CO source, while the Cu(111) surface provides stronger CO adsorption and reduction capability, promoting C-C bond formation and C_{2+} product generation.[60] Similarly, in the present CuPc featuring both CuO_4 and CuPc sites with the adjacent Cu-Cu separation distance of 9.04 Å, the C-C coupling is expected to occur via a similar mechanism, where a *CO intermediate desorbs and migrates to the *CHO site to enable dimerization.

CO_2 reduction to *2CO and *CHCO intermediates: Initially, two CO_2 molecules were adsorbed onto the active sites of CuPc, one binding to the Cu atom of the organic linker and the other to the metal node. The adsorption energy (ΔE_{ads}) value required for both the CO_2 molecules to get adsorbed on the active sites of the CuPc was -5.23 eV. After the adsorption of CO_2 molecules on each Cu atom, both the CO_2 molecules underwent hydrogenation and were reduced to two *COOH intermediates, followed by the proton-coupled electron transfer that produced *CO intermediates on each of the active sites with ΔE_{ads} values of -1.73 eV and -3.78 eV, respectively, along with the desorption of two H_2O molecules. CO is a crucial intermediate in the CO_2RR to produce C_2 compounds, so its binding energy plays a significant role in determining the product distribution. If a catalyst has low binding energy, CO desorbs from the surface, preventing C_2 products formation. In contrast, if the binding energy is too high, CO is retained too strongly, which can lead to catalyst poisoning. We observed that the transition from *CO-*CO to *COCO coupling, the calculated *COCO intermediate failed to stabilize on the active site as the Cu-Cu distance is 9.04 Å, and one *CO underwent hydrogenation to produce *COH or *CHO. The finding indicates that prior to C-C coupling, *CO intermediate bound to the linker undergoes additional hydrogenation, generating *CHO and *COH intermediates, while another *CO intermediate remains attached to the metal node. The ΔE_{ads} values required for the formation of *COH and *CHO together with the *CO intermediates were -0.52 eV and -1.95 eV, respectively, suggesting subsequent hydrogenation leading to C_2 (here ethylene and ethanol) primarily proceeds via the *CHO intermediate, consistent with

earlier reports.[22] All the possible intermediates involved in CO_2RR to C_2H_4 and C_2H_5OH are depicted in Figure 5.7-5.8, and their corresponding energies are shown through the PES diagram depicted in Figure 9. It is important to note that the conversion of CO_2 to C_2 compounds requires C-C bond formation between *CO and either *COH or *CHO, necessitating the cooperation of adjacent catalytic sites. Furthermore, the CuO_4 site with its square-planar configuration exhibits weak CO binding, meaning that *CO intermediates tend to desorb as CO gas rather than progressing toward hydrocarbon formation through further hydrogenation.[61,62] Therefore, the CO molecule on the metal node was desorbed and combined with *CHO to form *CCO and a H_2O molecule, while on the other hand, the *CHO intermediate before coupling with the *CO intermediate, underwent further hydrogenation to produce *CHOH. Next, the *CO intermediate present on the metal node coupled with the *CHOH intermediate, forming a *CHCO intermediate and a H_2O molecule, depicting that during the coupling process, the intermediates flipped, allowing the carbon atom to bind to the Cu atom of the linker. Therefore, the energies required for the formation of *CCO and *CHOH have been calculated, and the low value of ΔE_{ads} for the *CHOH intermediate (-3.06 eV) indicates its favorable formation over *CCO (-0.03 eV). The resulting stable configurations for CO_2 reduction to *2CO and *CHCO intermediates in the pathway of generating C_2 products are shown in Figure 5.7 (a)-(i).

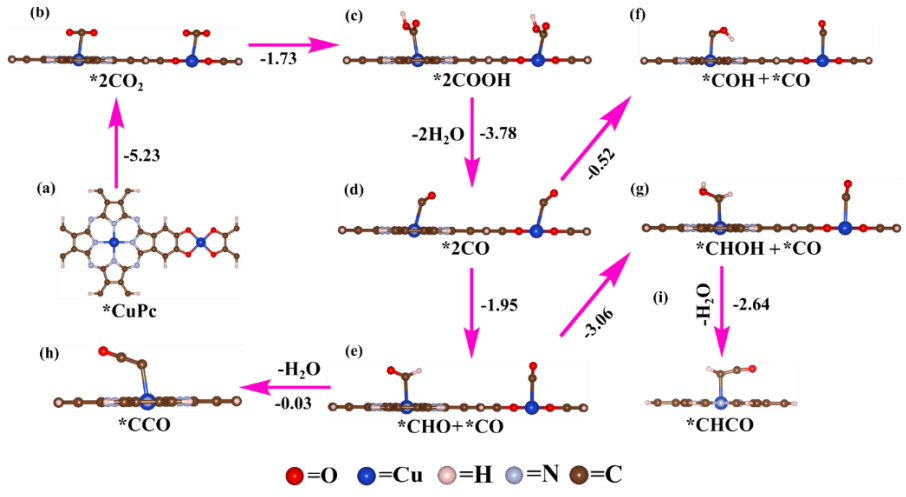


Figure 5.7 The equilibrium geometries of the possible reaction intermediates associated with the first seven-electron reduction of CO_2 to *CHCO intermediate on the CuPc surface with (a) CuPc surface; and intermediates: (b) *$2CO_2$; (c) *2COOH; (d) *2CO; (e) *CHO + *CO; (f) *COH + *CO; (g) *CHOH + *CO; (h) *CCO; and (i) *CHCO.

***CHCO reduction to ethylene and ethanol:** The *CHCO intermediate was further hydrogenated into various intermediates to finally produce C_2H_4 or C_2H_5OH, which then desorbed from the CuPc unit to yield C_2H_4 or C_2H_5OH. After *CO and *CHOH coupling to form *CHCO intermediate, the *CHCO intermediate was further reduced to form *CHCOH, *CH_2CO, and *OCHCH intermediates with ΔE_{ads} values of -3.83 eV, -4.90 eV, and -5.36 eV, respectively, confirming the favorable formation of the *OCHCH intermediate. Further reduction of *OCHCH led to the formation of the next key intermediates, including *CHC, *CH_2CHO, and *$OCHCH_2$, with ΔE_{ads} values of -1.23 eV, - 4.33 eV, and - 4.42 eV, respectively. These reaction steps are thermodynamically permissible, as indicated by their relatively low energy barriers. The *$OCHCH_2$ intermediate was subsequently subjected to hydrogenation to produce *CHCH, *CH_2CH_2O, and *O with C_2H_4 desorption. However, the computed values of ΔE_{ads} indicate that the C_2H_4 desorption and *CHCH formation are unfavorable, and hence, further reduction of the *CH_2CH_2O intermediate takes place. The resulting stable configurations of all the possible intermediates for *CHCO reduction to C_2 products are shown in Figure 5.8 (a)-(n).

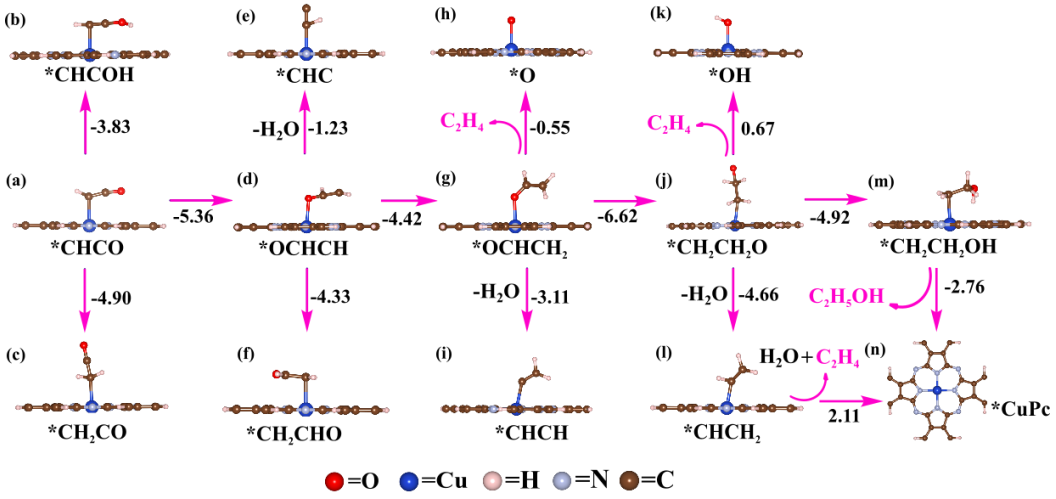


Figure 5.8 The equilibrium geometries of the possible reaction intermediates associated with the subsequent five-electron reduction of *CHCO toward C_2 Products (C_2H_4 and C_2H_5OH) on the CuPc surface with intermediates: (a) *CHCO, (b) *CHCOH; (c) *CH_2CO; (d) *OCHCH; (e) *CHC; (f) *CH_2CHO; (g) *$OCHCH_2$; (h) *O; (i) *CHCH; (j) *CH_2CH_2O; (k) *OH; (l) *$CHCH_2$; (m) *CH_2CH_2OH; and (n) CuPc surface.

Next, the *CH_2CH_2O intermediate was further hydrogenated to generate *OH with C_2H_4 desorption, *$CHCH_2$ with H_2O molecule, and *CH_2CH_2OH intermediate with the

ΔE_{ads} values of 0.67 eV, -4.66 eV and -4.92 eV, respectively, favoring the formation of *CH_2CH_2OH intermediate. This intermediate was further hydrogenated to produce C_2H_5OH at the catalytic active site, with a ΔE_{ads} value of -2.76 eV, consistent with the previously reported value for C_2 product,[63] and thus, indicating the exothermic nature and thermodynamic feasibility of C_2H_5OH desorption. It is noteworthy that, compared to *OH, the formation of the *$CHCH_2$ intermediate was more favorable, and subsequent hydrogenation of *$CHCH_2$ produced C_2H_4 at the catalytic active site, with a ΔE_{ads} of approximately 2.11 eV, as depicted through the PES in Figure 5.9, indicating the endothermic and thermodynamically unfavorable behavior. Particularly, to clarify the competition between these two C_2 products, we note that although both C_2H_4 and C_2H_5OH originate from the *CHCO intermediate, their subsequent hydrogenation steps proceed through distinct intermediates. A small variation in the adsorption energies of key intermediates (*OCHCH, *$OCHCH_2$, *CH_2CH_2O, CH_2CH_2OH, and *$CHCH_2$) governs the relative formation of C_2H_4 and C_2H_5OH, as illustrated in Figure 5.9. The route leading to CH_2CH_2OH formation is thermodynamically more favorable (ΔE_{ads} = - 4.92 eV) than that leading to $CHCH_2$ (ΔE_{ads} = - 4.66 eV) and C_2H_4 desorption (ΔE_{ads} = 0.67 eV), indicating that C_2H_5OH formation is exothermic and energetically preferred, whereas C_2H_4 desorption is endothermic and less favorable under the studied conditions. This mechanistic distinction rationalizes the observed preference for C_2H_5OH over C_2H_4 on the surface of CuPc and highlights the critical role of subtle energetic differences between intermediates in directing C_2 product selectivity. Thus, the detailed analysis of the reaction mechanism favors the formation of C_2H_5OH over C_2H_4, which agrees with the experimental results of PcCu-Cu-O MOF acting as a dual active site for C_2 products. The experimental work on PcCu-Cu-O MOF demonstrated a single C_2 product; however, our study reveals the various competing intermediates involved in the generation of C_2 products. A clearer picture of ΔE_{ads} values for all intermediates and competing pathways at a potential of U = 0 V Vs RHE is illustrated through the PES diagram depicted in Figure 5.9.

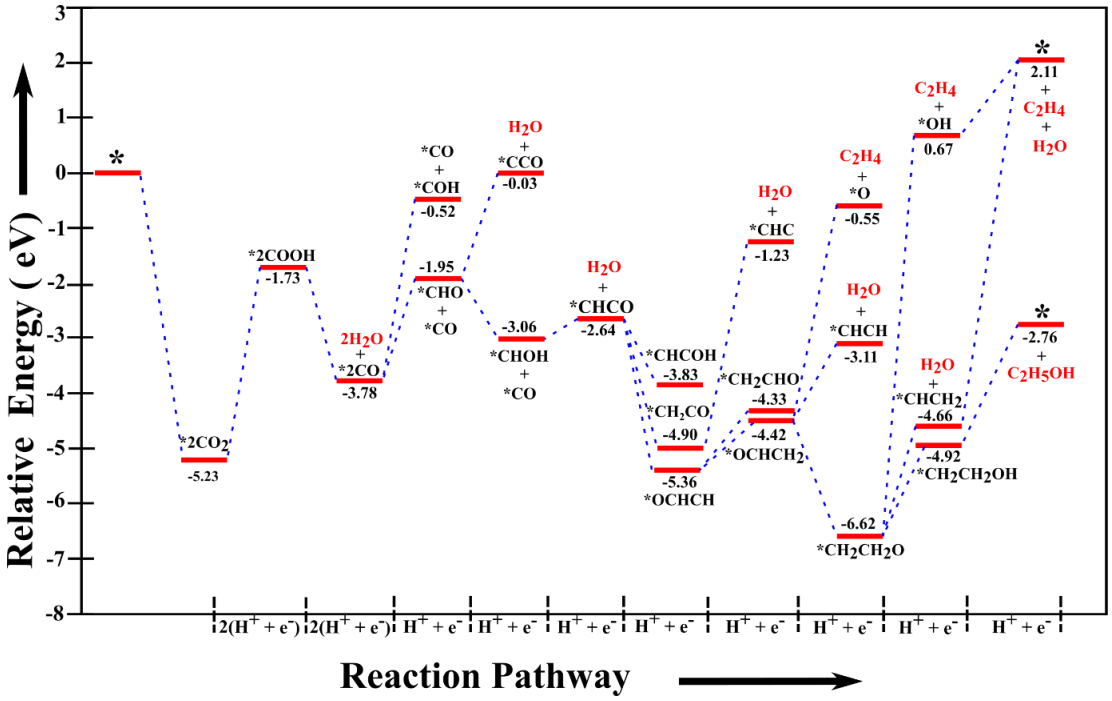


Figure 5.9 The potential energy surface (PES) diagram representing the ΔE_{ads} values for CO_2 reduction to C_2H_4 and C_2H_5OH through various reaction intermediates on the CuPc surface at 0 V_{RHE}. The energies are expressed in eV.

- **Competition between C_1 and C_2 products**

The proposed pathways for CO_2RR to C_1 products (CO, HCOOH, CH_3OH, and CH_4) and C_2 products (C_2H_4 and C_2H_5OH) commence with the reduction of CO_2 to *HCOOH and *CO, which served as pivotal surface intermediates directing subsequent PCET toward different reaction routes leading to C_1 and C_2 products. The further reduction of *HCOOH and *CO dimerization represents a competitive process. For the CH_4 production, *HCOOH reduction to *CHO and *COH intermediates takes place with ΔE_{ads} values of -1.77 eV and -0.28 eV, respectively, suggesting the favorable formation of *CHO intermediate, while for the C_2 product, *CO may be coupled with the *COH or *CHO to get C-C bond coupling. The C-C coupling in the present study proceeds after the formation of *COH and *CHO, and the results of our DFT-D calculations dictate that the formation of *CHO + *CO (-1.95 eV) is more favorable than the *COH + *CO intermediate (-0.52 eV). The next step involves the C-C coupling to form *CCO (-0.03 eV) or further hydrogenation of *CHO to yield *CHOH with *CO attached to the metal node with ΔE_{ads} value of -3.06 eV. The results propose a greater propensity for the occurrence of *CHOH + *CO, and further hydrogenation lead to *CHCO (-2.64 eV). Here, the two key intermediates after C-C coupling study are *CCO and *CHCO

with ΔE_{ads} values of -0.03 eV and -2.64 eV, respectively, suggesting favorable formation of *CHCO. Thus, results reveal that the energy barrier for *CO coupling is lower than that for the subsequent reduction of *CO to the *CHO (-1.77 eV) intermediate associated with C_1 product formation. Thus, CO_2 reduction to C_2H_5OH through *CHO intermediate is the most feasible one among the mechanisms investigated for both C_1 and C_2 products. All the calculated values of ΔE_{ads} are subject to an estimated uncertainty of approximately ±0.02 eV, which reflects the typical accuracy of the B3LYP-D3 method.[41]

5.4.3 Structural and chemical stability

The structural and chemical stability of the CuPc was examined to assess its robustness during CO_2RR. In our computational study, the CuPc framework with the adsorbed intermediates was fully optimized during geometry relaxation to accurately capture the equilibrium adsorption geometries and local electronic effects. The optimized adsorption geometries showed negligible structural distortion near the active Cu-N_4 center, and the local coordination environment around Cu remained intact. In other words, during the geometry optimization of the intermediates for C_1 and C_2 products, the optimized Cu-N(a) = 1.95 Å, N(a)-C = 1.38 Å, and N(b)-C = 1.33 Å bond lengths closely match with the optimized bond lengths of the pristine CuPc structure, suggesting that adsorption does not induce significant structural disturbance at the catalytic site. Moreover, the moderate and thermodynamically consistent adsorption energies further suggest that the Cu-N coordination framework remains intact during electron transfer and hydrogenation steps. Furthermore, previous studies have demonstrated that the strong in-plane Cu-N coordination and π-π interactions between layers of the MPc-based porous materials effectively prevent Cu aggregation and restacking during CO_2RR, maintain both structural and catalytic integrity.[22,63,64]

To further assess the chemical stability of the active sites, the Mulliken charge distribution of CuPc has been analyzed before and after the CO_2 adsorption obtained by the B3LYP-D3 method. This Mulliken charge analysis has been performed at the equilibrium geometries of the system. In pristine CuPc, the central Cu exhibits a charge of +0.64 e, consistent with a Cu(0)-like electronic character, and shows minimal variation after adsorption (+0.64 to -0.69 e). The adjacent N atoms also display only slight charge redistribution (-0.16 to -0.03 e), confirming that the oxidation state of Cu

remains effectively unchanged. The maintained Cu-N coordination and planar structure confirm that the Cu centers remain in the Cu^0 state throughout CO_2 adsorption, reflecting the electronic and structural robustness of the active site. These findings, consistent with previous reports,[65] demonstrate that the Cu-N framework remains both structurally and chemically stable throughout the CO_2 reduction process.

This study offers important mechanistic understanding of CO_2 electroreduction (CO_2RR) on MPc-based MOFs, with particular emphasis on the generation of C_2 products such as C_2H_5OH and C_2H_4. Using first principles periodic hybrid DFT-D calculations, the study reveals the energetic favorability of key reaction pathways and underscores the significance of the Cu-N_4 active site and synergistic interactions within the CuPc framework to enhance the electrocatalytic activity toward CO_2RR. Notably, the CuPc surface shows a thermodynamic preference for C_2H_5OH over other products, pointing toward its potential in selectively producing C_2 compounds. The structural and chemical stability of the CuPc remained stable during the reduction reaction. Overall, these insights establish a theoretical basis for the rational design of MOF-based electrocatalysts and contribute to advancing strategies aimed at improving both selectivity and efficiency in CO_2 conversion to valuable multi-carbon products.

5.5 Conclusions

In summary, we have provided mechanistic insights into CO_2 adsorption, activation, and reduction, along with the associated pathways leading to further reduced C_1 (CH_4) and C_2 (C_2H_4, C_2H_5OH) products, explored through first principles DFT-D (B3LYP-D3) calculations. The results of the electronic band structure calculations revealed a bandgap of 0.65 eV, while the density of states calculations indicated that the catalytic performance predominantly arises from the synergistic contributions of Cu atoms present with the nitrogen atom of the MPc unit of the 2D CuPc monolayer. Further calculations revealed that the Cu-N_4 complex in the CuPc has the lowest CO_2 adsorption energy, which indicates the fast proton/electron kinetics, and the negative value of binding energy (E_b = -3.59 eV) signifies the thermodynamic stability and experimental feasibility of the CuPc. Next, the periodic hybrid DFT-D calculations were subsequently conducted to reveal the detailed change in relative adsorption energy (ΔE_{ads}) profiles for each reaction intermediate during the catalytic activity of the CuPc towards major C_1 (CH_3OH, CH_4) and C_2 (C_2H_5OH and C_2H_4) products. The simulated

values of ΔE_{ads} revealed that among the two possible reaction pathways, the *HCOOH (-5.07 eV) pathway favored further hydrogenation over the *CO (-3.49 eV) pathway for CO_2RR to CH_4 (-2.28 eV) after the complete eight electron ($8e^-$) transfer. The CuPc surface preferentially promotes the C_2H_5OH formation over the C_2H_4, with a more favorable ΔE_{ads} value of -2.76 eV versus 2.11 eV, suggesting that the MPc-containing MOFs tend to favor C_2 over C_1 product formation. These findings offer new perspectives on improving the selectivity of CO_2 conversion toward C_1 and C_2 products and emphasize the importance of strategically designing highly efficient electrocatalysts for CO_2 electroreduction into valuable products. Overall, this work contributes to the advancement of carbon capture, utilization, and storage (CCUS) technologies by providing an atomistic-level understanding that can guide the rational design of next-generation electrocatalysts for efficient CO_2 conversion. We anticipate that this study will benefit both theoretical and experimental researchers working on the CO_2RR mechanism on the MPc-based catalysts and aid in the development of more effective CO_2RR systems.

5.6 References

[1] E. R. López, J. G. Loe, F. B. Moreno, T. R. Reina, J. A. Odriozola, Electrocatalytic CO_2 conversion to C_2 products: Catalysts design, market perspectives and techno-economic aspects, Renew. Sustain. Energy Rev. 161 (2022) 112329.

[2] X. Han, T. Zhang, J. Arbiol, Metal-organic framework-derived single atom catalysts for electrocatalytic reduction of carbon dioxide to C_1 products, Energy Adv. 2 (2023) 252-267.

[3] Y. Hu, M. Asif, J. Gong, H. Zeb, H. Lan, M. K. khan, H. Xia, M. Du, Mechanistic insights into C-C coupling in electrocatalytic CO_2 reduction reaction, Chem. Commun. 60 (2024) 10618-10628.

[4] F. C. Vallejo, M. T. M. Koper, Theoretical considerations on the electroreduction of CO to C_2 Species on Cu(100) electrodes, Angew. Chem. Int. Ed. 52 (2013) 7282-7285.

[5] S. Nitopi, E. Bertheussen, S. B. Scott, X. Liu, A. K. Engstfeld, S. Horch, B. Seger, I. E. L. Stephens, K. Chan, C. Hahn, J. K. Nørskov, T. F. Jaramillo, I. Chorkendorff, Progress and perspectives of electrochemical CO_2 reduction on

copper in aqueous electrolyte, Chem. Rev. 119 (2019) 7610-7672.

[6] F. A. Rollier, V. Muravev, A. Parastaev, R. C. J. van de Poll, J. M. J. J. Heinrichs, B. Ligt, J. F. M. Simons, M. C. Figueiredo, E. J. M. Hensen, Restructuring of Cu-based catalysts during CO electroreduction: Evidence for the dominant role of surface defects on the C_{2+} product selectivity, ACS Catal. 14 (2024) 13246-13259.

[7] J. Dai, J. Zhu, Y. Xu, X. Liu, D. Zhu, G. Xu, H. Liu, G. Li, Structural regulating of Cu-based metallic electrocatalysts for CO_2 to C_{2+} products conversion, ChemSusChem. 18 (2025) e202402184.

[8] Y. Yang, Z. Tan, S. Wang, Y. Wang, J. Hu, Z. Su, Y. Zhao, J. Tai, J. Zhang, Cu/Cu_2O nanocrystals for electrocatalytic carbon dioxide reduction to multi-carbon products, Chem. Commun. 59 (2023) 2445-2448.

[9] L. Wang, Y. Wu, Advancing electrocatalytic CO_2 reduction: Key strategies for scaling up to industrial applications, Nanoscale. 17 (2025) 16988-17003.

[10] S. Nilsson, J. N. E. Berch, D. Albinsson, J. Fritzsche, G. Mpourmpakis, C. Langhammer, The Role of grain boundary sites for the oxidation of copper catalysts during the CO oxidation reaction, ACS Nano. 17 (2023) 20284-20298.

[11] Y. Y. Birdja, E. P. Gallent, M. C. Figueiredo, A. J. Göttle, F. C. Vallejo, M. T. M. Koper, Advances and challenges in understanding the electrocatalytic conversion of carbon dioxide to fuels, Nat. Energy. 4 (2019) 732-745.

[12] T. N. Huan, N. Ranjbar, G. Rousse, M. Sougrati, A. Zitolo, V. Mougel, F. Jaouen, M. Fontecave, Electrochemical reduction of CO_2 catalyzed by Fe-N-C materials: A structure-selectivity study, ACS Catal. 7 (2017) 1520-1525.

[13] Y. C. Feng, X. Wang, D. Wang, Metal porphyrins and metal phthalocyanines as designable molecular model electrocatalysts, Mater. Chem. Front. 8 (2024) 228-247.

[14] M. Lu, M. Zhang, C. G. Liu, J. Liu, L. J. Shang, M. Wang, J. N. Chang, S. L. Li, Y. Q. Lan, Stable dioxin-linked metallophthalocyanine covalent organic frameworks (COFs) as photo-coupled electrocatalysts for CO_2 reduction, Angew. Chem. Int. Ed. 60 (2021) 4864-4871.

[15] Z. Meng, J. Luo, W. Li, K. A. Mirica, Hierarchical tuning of the performance of electrochemical carbon dioxide reduction using conductive two-dimensional metallophthalocyanine based metal-organic frameworks, J. Am. Chem. Soc. 142 (2020) 21656-21669.

[16] H. Zhong, M. G. Asl, K. H. Ly, J. Zhang, J. Ge, M. Wang, Z. Liao, D. Makarov, E. Zschech, E. Brunner, I. M. Weidinger, J. Zhang, A. V. Krasheninnikov, S. Kaskel, R. Dong, X. Feng, Synergistic electroreduction of carbon dioxide to carbon monoxide on bimetallic layered conjugated metal-organic frameworks, Nat. Commun. 11 (2020) 1409.

[17] Y. Hori, A. Murata, R. Takahashi, Formation of hydrocarbons in the electrochemical reduction of carbon dioxide at a copper electrode in aqueous solution, J. Chem. Soc. Faraday Trans. 1 85 (1989) 2309-2326.

[18] S. Kusama, T. Saito, H. Hashiba, A. Sakai, S. Yotsuhashi, Crystalline copper(II) phthalocyanine catalysts for electrochemical reduction of carbon dioxide in aqueous media, ACS Catal. 7 (2017) 8382-8385.

[19] H. Xiao, T. Cheng, W. A. Goddard, Atomistic mechanisms underlying selectivities in C_1 and C_2 products from electrochemical reduction of CO on Cu(111), J. Am. Chem. Soc. 139 (2017) 130-136.

[20] T. T. Zhuang, Z. Q. Liang, A. Seifitokaldani, Y. Li, P. D. Luna, T. Burdyny, F. Che, F. Meng, Y. Min, R. Q. Bermudez, C. T. Dinh, Y. Pang, M. Zhong, B. Zhang, J. Li, P. N. Chen, X. L. Zheng, H. Liang, W. N. Ge, B. J. Ye, D. Sinton, S. H. Yu, E. H. Sargent, Steering post-C–C coupling selectivity enables high efficiency electroreduction of carbon dioxide to multi-carbon alcohols, Nat. Catal. 1 (2018) 421-428.

[21] A. J. Garza, A. T. Bell, M. H. Gordon, Mechanism of CO_2 reduction at copper surfaces: Pathways to C_2 products, ACS Catal. 8 (2018) 1490-1499.

[22] X. F. Qiu, H. L. Zhu, J. R. Huang, P. Q. Liao, X. M. Chen, Highly selective CO_2 electroreduction to C_2H_4 using a metal-organic framework with dual active sites, J. Am. Chem. Soc. 143 (2021) 7242-7246.

[23] Y. Zhang, X. Zhang, L. Jiao, Z. Meng, H. L. Jiang, Conductive covalent organic frameworks of polymetallophthalocyanines as a tunable platform for electrocatalysis, J. Am. Chem. Soc. 145 (2023) 24230-24239.

[24] A. Erba, J. K. Desmarais, S. Casassa, B. Civalleri, L. Donà, I. J. Bush, B. Searle, L. Maschio, L. E. Daga, A. Cossard, C. Ribaldone, E. Ascrizzi, N. L. Marana, J. P. Flament, B. Kirtman, CRYSTAL23: A program for computational solid state physics and chemistry, J. Chem. Theory Comput. 19 (2023) 6891-6932.

[25] N. Sinha, K. Parveen, S. Pakhira, Synergistic Ni-doping in 2D monolayer molybdenum disulfide for enhanced electrocatalytic H_2 evolution, Int. J.

Hydrogen Energy 105 (2025) 1294-1308.

[26] K. Parveen, S. Pakhira, Unveiling the electrocatalytic activity of metallophthalocyanine-based covalent organic frameworks toward CO_2 reduction reaction, J. Phys. Chem. C 129 (2025) 2973-2987.

[27] H. Joshi, N. Sinha, K. Parveen, S. Pakhira, Unveiling the electrocatalytic activity of cobaloxime metallolinker in the UU-100(Co) metal-organic framework toward the H_2 evolution reaction: A DFT study, Energy Fuels 37 (2023) 19771-19784.

[28] K. Parveen, S. Pakhira, Designing organic bridging linkers of metal-organic frameworks for enhanced carbon dioxide adsorption, New J. Chem. 48 (2024) 13700-13714.

[29] J. Hui, N. B. Schorr, S. Pakhira, Z. Qu, J. L. M. Cortes, J. R. López, Achieving fast and efficient K^+ intercalation on ultrathin graphene electrodes modified by a Li^+ based solid-electrolyte interphase, J. Am. Chem. Soc. 140 (2018) 13599-13603.

[30] R. Nagaraj, S. Pakhira, K. Aruchamy, P. Thippeswamy, D. Mondal, K. Dharmalingm, N. S. Kotrappanavar, D. Ghosh, Catalyzing the intercalation storage capacity of aqueous zinc-ion battery constructed with Zn(II) preinserted organo-vanadyl hybrid cathode, ACS Appl. Energy Mater. 3 (2020) 3425-3434.

[31] J. Hui, S. Pakhira, R. Bhargava, Z. J. Barton, X. Zhou, A. J. Chinderle, J. L. M. Cortes, J. R. López, Modulating electrocatalysis on graphene heterostructures: Physically impermeable yet electronically transparent electrodes, ACS Nano. 12 (2018) 2980-2990.

[32] K. Momma, F. Izumi, VESTA 3 for three-dimensional visualization of crystal, volumetric and morphology data, J. Appl. Cryst. 44 (2011) 1272-1276.

[33] M. Urbani, M. E. Ragoussi, M. K. Nazeeruddin, T. Torres, Phthalocyanines for dye-sensitized solar cells, Coord. Chem. Rev. 381 (2019) 1-64.

[34] A. Kumar, V. K. Vashistha, D. K. Das, Recent development on metal phthalocyanines based materials for energy conversion and storage applications, Coord. Chem. Rev. 431 (2021) 213678.

[35] M. G. Walter, A. B. Rudine, C. C. Wamser, Porphyrins and phthalocyanines in solar photovoltaic cells, J. Porphyr. Phthalocyanines 14 (2010) 759-792.

[36] Z. Weng, Y. Wu, M. Wang, J. Jiang, K. Yang, S. Huo, X. F. Wang, Q. Ma, G. W. Brudvig, V. S. Batista, Y. Liang, Z. Feng, H. Wang, Active sites of copper-

complex catalytic materials for electrochemical carbon dioxide reduction, Nat. Commun. 9 (2018) 415.

[37] K. Zhao, X. Nie, H. Wang, S. Chen, X. Quan, H. Yu, W. Choi, G. Zhang, B. Kim, J. G. Chen, Selective electroreduction of CO_2 to acetone by single copper atoms anchored on N-doped porous carbon, Nat. Commun. 11 (2020) 2455.

[38] J. Albo, D. Vallejo, G. Beobide, O. Castillo, P. Castaño, A. Irabien, Copper-Based Metal-Organic Porous Materials for CO_2 Electrocatalytic Reduction to Alcohols, ChemSusChem 10 (2017) 1100-1109.

[39] D. Zhu, C. Guo, J. Liu, L. Wang, Y. Du, S. Z. Qiao, Two-dimensional metal-organic frameworks with high oxidation states for efficient electrocatalytic urea oxidation, Chem. Commun. 53 (2017) 10906-10909.

[40] J. Duan, S. Chen, C. Zhao, Ultrathin metal-organic framework array for efficient electrocatalytic water splitting, Nat. Commun. 8 (2017) 15341.

[41] N. Mardirossian, M. H. Gordon, Thirty years of density functional theory in computational chemistry: An overview and extensive assessment of 200 density functionals, Mol. Phys. 115 (2017) 2315-2372.

[42] C. Park, J. W. Baek, E. Shin, I. D. Kim, Two-dimensional electrically conductive metal-organic frameworks as chemiresistive sensors, ACS Nanosci. Au 3 (2023) 353-374.

[43] L. S. Xie, G. Skorupskii, M. Dincă, Electrically conductive metal-organic frameworks, Chem. Rev. 120 (2020) 8536-8580.

[44] M. Wang, R. Dong, X. Feng, Two-dimensional conjugated metal-organic frameworks (2D c-MOFs): Chemistry and function for MOFtronics, Chem. Soc. Rev. 50 (2021) 2764-2793.

[45] T. Tang, X. Bai, Z. Wang, J. Guan, Structural engineering of atomic catalysts for electrocatalysis, Chem. Sci. 15 (2024) 5082-5112.

[46] Z. Meng, R. M. Stolz, K. A. Mirica, Two-dimensional chemiresistive covalent organic framework with high intrinsic conductivity, J. Am. Chem. Soc. 141 (2019) 11929-11937.

[47] P. Das, B. Ball, P. Sarkar, Bifunctional electrocatalytic activity of two-dimensional metallophthalocyanine-based metal-organic-frameworks for overall water splitting: A DFT study, ACS Catal. 13 (2023) 16307-16317.

[48] G. Liu, Q. T. Trinh, H. Wang, S. Wu, J. M. A. Ramos, M. B. Sullivan, M. Kraft, J. W. Ager, J. Zhang, R. Xu, Selective and stable CO_2 electroreduction to CH_4

via electronic metal-support interaction upon decomposition/redeposition of MOF, Small 19 (2023) 2301379.

[49] J. Zhao, J. Zhao, F. Li, Z. Chen, Copper dimer supported on a C_2N layer as an efficient electrocatalyst for CO_2 reduction reaction: A computational study, J. Phys. Chem. C 122 (2018) 19712-19721.

[50] L. Fang, X. Cao, Z. Cao, Covalent organic framework with high capacity for the lithium ion battery anode: Insight into intercalation of Li from first-principles calculations, J. Phys. Condens. Matter 31 (2019) 205502.

[51] H. L. Zhu, J. R. Huang, P. Q. Liao, X. M. Chen, Rational design of metal-organic frameworks for electroreduction of CO_2 to hydrocarbons and carbon oxygenates, ACS Cent. Sci. 8 (2022) 1506-1517.

[52] C. Wang, Y. Zhang, F. Zhao, D. Zhao, J. Zhang, Design principles of metal phthalocyanine for electrochemical CO_2 reduction: From targeted molecular structures to atomic-level active sites, Small 21 (2025) 2502897.

[53] H. C. Huang, J. Li, Y. Zhao, J. Chen, Y. X. Bu, S. B. Cheng, Adsorption energy as a promising single-parameter descriptor for single atom catalysis in the oxygen evolution reaction, J. Mater. Chem. A 9 (2021) 6442-6450.

[54] X. Zhao, J. Wang, X. Niu, High-throughput screening approach for catalytic applications through regulation of adsorption energies via work function, Langmuir 40 (2024) 26532-26539.

[55] Y. Wang, W. Qiu, E. Song, F. Gu, Z. Zheng, X. Zhao, Y. Zhao, J. Liu, W. Zhang, Adsorption-energy-based activity descriptors for electrocatalysts in energy storage applications, Natl. Sci. Rev. 5 (2018) 327-341.

[56] G. Y. Duan, X. Q. Li, G. R. Ding, L. J. Han, B. H. Xu, S. J. Zhang, Highly efficient electrocatalytic CO_2 reduction to C_{2+} products on a poly(ionic liquid)-based Cu^0-Cu^I tandem catalyst, Angew. Chem. Int. Ed. 134 (2022) e202110657.

[57] D. S. Huang, H. L. Zhu, Z. H. Zhao, J. R. Huang, P. Q. Liao, X. M. Chen, A stable and low-cost metal-azolate framework with cyclic tricopper active sites for highly selective CO_2 electroreduction to C_{2+} products, ACS Catal. 12 (2022) 8444-8450.

[58] R. Wang, J. Liu, Q. Huang, L. Z. Dong, S. L. Li, Y. Q. Lan, Partial coordination-perturbed Bi-copper sites for selective electroreduction of CO_2 to hydrocarbons, Angew. Chem. Int. Ed. 60 (2021) 19829-19835.

[59] Y. F. Lu, L. Z. Dong, J. Liu, R. X. Yang, J. J. Liu, Y. Zhang, L. Zhang, Y. R.

Wang, S. L. Li, Y. Q. Lan, Predesign of catalytically active sites via stable coordination cluster model system for electroreduction of CO_2 to ethylene, Angew. Chem. Int. Ed. 133 (2021) 26414-26421.

[60] Z. H. Zhao, K. Zheng, N. Y. Huang, H. L. Zhu, J. R. Huang, P. Q. Liao, X. M. Chen, A Cu(111)@metal-organic framework as a tandem catalyst for highly selective CO_2 electroreduction to C_2H_4, Chem. Commun. 57 (2021) 12764-12767.

[61] H. L. Zhu, J. R. Huang, X. W. Zhang, C. Wang, N. Y. Huang, P. Q. Liao, X. M. Chen, Highly efficient electroconversion of CO_2 into CH_4 by a metal-organic framework with trigonal pyramidal $Cu(I)N_3$ active sites, ACS Catal. 11 (2021) 11786-11792.

[62] Y. Y. Liu, H. L. Zhu, Z. H. Zhao, N. Y. Huang, P. Q. Liao, X. M. Chen, Insight into the effect of the d-orbital energy of copper ions in metal-organic frameworks on the selectivity of electroreduction of CO_2 to CH_4, ACS Catal. 12 (2022) 2749-2755.

[63] Y. L. Yang, Q. Li, P. Liu, Q. Xu, Q. Y. Zeng, Y. X. Chen, Y. Q. Yang, H. T. Yang, F. Yu, Y. R. Wang, Y. Chen, Y. Q. Lan, Subtle tuning of catalytic well effect in phthalocyanine covalent organic frameworks for selective CO_2 electroreduction into C_2H_4, Adv. Mater. 37 (2025) 2415799.

[64] X. F. Qiu, J. R. Huang, C. Yu, Z. H. Zhao, H. L. Zhu, Z. Ke, P. Q. Liao, X. M. Chen, A stable and conductive covalent organic framework with isolated active sites for highly selective electroreduction of carbon dioxide to acetate, Angew. Chem. 134 (2022) e202206470.

[65] K. Yue, Y. Qin, H. Huang, Z. Lv, M. Cai, Y. Su, F. Huang, Y. Yan, Stabilized Cu^0 -Cu^{1+} dual sites in a cyanamide framework for selective CO_2 electroreduction to ethylene, Nat. Commun. 15 (2024) 7820.

Chapter 6

Conclusions and Future Perspectives

The major conclusions drawn from the research work carried out in the present thesis are highlighted in this chapter. Future perspectives and possible directions for further research on these novel porous MOF and COF-based materials for CO_2 capture, direct air capture (DAC), and electrochemical conversion are also discussed here.

6.1 Conclusions

This thesis presents a joint comprehensive theoretical and computational investigation into the rational design of porous materials for CCUS, with a particular focus on MOFs and COFs. Using a combination of non-periodic DFT, hybrid periodic DFT, and post-Hartree-Fock (HF) calculations, the thesis systematically has explored the adsorption and catalytic behavior of functionalized porous materials toward efficient CO_2 capture and electrochemical reduction. The overall objective of the thesis was to study the CO_2 adsorption strength, electronic properties, catalytic activity, and product selectivity in MOF and COF-based systems. The conclusions of the research work presented in the thesis are summarized below:

1. The thesis first examined the role of organic linkers in governing CO_2 adsorption behavior. A detailed non-periodic investigation of different functionalized MOF linkers demonstrated that linker engineering plays a decisive role in controlling adsorption energetics and host-guest interactions. In particular, the combined B3LYP-D3 and MP2 methods demonstrated that Li decoration significantly enhanced the binding enthalpy of CO_2 while maintaining reversible adsorption behavior. The EDA has revealed that the effects of both the electrostatic and polarization dominate the adsorption mechanism. Further, the FMO study has clarified the nature of charge distribution occurring during adsorption. These findings provide important molecular-level insights into the design of next-generation MOF linkers with improved CO_2 affinity and adsorption performance.
2. The second major contribution involved in investigating sulfur-linked MPc-based COFs for electrochemical CO_2 reduction to C_1 products. The periodic DFT calculations revealed the structural stability and semiconducting behavior of the COFs while elucidating the catalytic pathways associated with CH_4. The

study has demonstrated that sulfur-containing linkages effectively modulate the electronic structure and adsorption behavior of reaction intermediates, thereby influencing the catalytic selectivity and reaction energies. The calculated Gibbs free energy profiles have revealed favorable reaction pathways for CO_2 adsorption and proton-coupled electron transfer steps, confirming the catalytic potential of sulfur-linked CoPc COFs for selective CO_2 electroreduction. This work highlights the importance of linker engineering in tuning catalytic activity within extended porous materials.

3. The final part of the thesis focused on a CuPc-Cu-O MOF for electrochemical CO_2 reduction toward both C_1 (CH_4) and C_2 (C_2H_4, C_2H_5OH) products. Using hybrid periodic DFT calculations, the structural, electronic, and catalytic properties of the MOF were systematically analyzed. The results reveal favorable energetics for the formation of multi-carbon products, particularly C_2H5OH, indicating that the designed MOF provides suitable active sites and electronic environments for efficient C-C coupling. Mechanistic analysis has demonstrated that the Cu-centered active sites stabilize key intermediates involved in multi-electron-proton transfer processes, thereby promoting C_2 product formation. The work establishes that the extended porous framework facilitates charge transport and reactant accessibility, enhancing the catalytic efficiency of the system. These findings provide valuable mechanistic understanding for the rational design of MPc-based MOFs as efficient electrocatalysts for sustainable CO_2 conversion.

Overall, this thesis presents a strong theoretical understanding connecting adsorption behavior, electronic structure, and catalytic performance in porous MOFs and COFs. By integrating molecular-level adsorption studies with periodic catalytic investigations, the work provides fundamental insights into the design principles required for efficient CO_2 capture and electrochemical conversion. The systematic exploration of linker effects, metal-center activity, and structure engineering advances the understanding of how porous crystalline materials can be tailored for specific CCUS applications.

6.2 Future Perspectives

The present thesis provides a joint theoretical and computational foundation for the rational design of porous MOFs and COFs for CO_2 capture and electrochemical conversion. Although significant insights have been obtained regarding adsorption

energies, electronic properties, and catalytic pathways, several promising directions remain open for future exploration. The possible future perspectives emerging from this work are outlined below:

1. A major future direction involves the experimental realization and validation of the theoretically designed Li-decorated linkers into integrated MOFs. While the computational studies demonstrate favorable CO_2 adsorption, experimental synthesis would provide direct confirmation of the predicted performance.
2. Another important perspective is the exploration of a wide range of linker functionalization strategies, such as chelation, impregnation, and metal doping, to further tune the pore environment, adsorption strength, charge transport, and catalytic selectivity. Such modifications may lead to the development of porous materials with enhanced stability and improved catalytic efficiency under operating conditions.
3. The thesis primarily investigates equilibrium adsorption energies; however, future work could extend toward studies involving adsorption kinetics, diffusion behavior, cyclic regeneration performance, and simulations. Multiscale computational modelling combining DFT calculations with molecular dynamics (MD), grand canonical Monte Carlo (GCMC) simulations could provide deeper insights into CO_2 capture at operating conditions.
4. The investigation of different transition metal centers also presents an important research direction. In addition to Co and Cu, other metals such as Fe, Ni, Mn, Zn and bimetallic systems may exhibit unique catalytic properties for selective CO_2 reduction. The selective formation of C_{2+} products remains one of the most challenging aspects of CO_2 electroreduction. Therefore, future research may focus on understanding and controlling C-C coupling pathways in detail. The incorporation of dual or hetero metal active sites could further improve C-C coupling and promote the formation of higher-value multi-carbon products. In addition, advanced computational methods combined with machine learning methods may help identify descriptors governing intermediate stabilization and product selectivity, thereby accelerating the discovery of highly efficient electrocatalysts for multi-carbon products.
5. The outcomes of this thesis can be further extended toward advanced CCUS technologies, particularly in the rapidly growing field of direct air capture

(DAC). Since atmospheric CO_2 concentrations are ~420 ppm, DAC requires adsorbent materials with exceptionally high selectivity, reversible CO_2 binding, fast adsorption-desorption kinetics, and excellent stability under humid conditions. The insights from this thesis provide an important foundation for designing next-generation porous materials suitable for DAC applications.